NASA/TM-20240010950

Hybrid Thermally Efficient Core (HyTEC) HyTEC Phase 1—HTEBC
Final Report

Suresh Viswanathan
GE Aerospace, Evendale, Ohio

Reza Sarrafi-Nour, Julin Wan, Nick Antolino, Anant Setlur, and Andrea Vozar
GE Aerospace Research, Niskayuna, New York

Kang Lee, Bryan Harder, Mike Presby, Roy Sullivan, and Subodh Mital
Glenn Research Center, Cleveland, Ohio

January 2025

NASA STI Program Report Series

Since its founding, NASA has been dedicated to the advancement of aeronautics and space science. The NASA scientific and technical information (STI) program plays a key part in helping NASA maintain this important role.

The NASA STI program operates under the auspices of the Agency Chief Information Officer. It collects, organizes, provides for archiving, and disseminates NASA's STI. The NASA STI program provides access to the NTRS Registered and its public interface, the NASA Technical Reports Server, thus providing one of the largest collections of aeronautical and space science STI in the world. Results are published in both non-NASA channels and by NASA in the NASA STI Report Series, which includes the following report types:

- TECHNICAL PUBLICATION. Reports of completed research or a major significant phase of research that present the results of NASA programs and include extensive data or theoretical analysis. Includes compilations of significant scientific and technical data and information deemed to be of continuing reference value. NASA counterpart of peer-reviewed formal professional papers but has less stringent limitations on manuscript length and extent of graphic presentations.

- TECHNICAL MEMORANDUM. Scientific and technical findings that are preliminary or of specialized interest, e.g., quick release reports, working papers, and bibliographies that contain minimal annotation. Does not contain extensive analysis.

- CONTRACTOR REPORT. Scientific and technical findings by NASA-sponsored contractors and grantees.

- CONFERENCE PUBLICATION. Collected papers from scientific and technical conferences, symposia, seminars, or other meetings sponsored or cosponsored by NASA.

- SPECIAL PUBLICATION. Scientific, technical, or historical information from NASA programs, projects, and missions, often concerned with subjects having substantial public interest.

- TECHNICAL TRANSLATION. English-language translations of foreign scientific and technical material pertinent to NASA's mission.

Specialized services also include organizing and publishing research results, distributing specialized research announcements and feeds, providing information desk and personal search support, and enabling data exchange services.

For more information about the NASA STI program, see the following:

- Access the NASA STI program home page at http://www.sti.nasa.gov

NASA/TM-20240010950

Hybrid Thermally Efficient Core (HyTEC) HyTEC Phase 1—HTEBC
Final Report

Suresh Viswanathan
GE Aerospace, Evendale, Ohio

Reza Sarrafi-Nour, Julin Wan, Nick Antolino, Anant Setlur, and Andrea Vozar
GE Aerospace Research, Niskayuna, New York

Kang Lee, Bryan Harder, Mike Presby, Roy Sullivan, and Subodh Mital
Glenn Research Center, Cleveland, Ohio

National Aeronautics and
Space Administration

Glenn Research Center
Cleveland, Ohio 44135

January 2025

Acknowledgments

This material is based upon work supported by the National Aeronautics and Space Administration under contract Number 80GRC021CA005 with Ian Parks (NASA Glenn) as Contracting Officer and Michael Kulis (NASA Glenn) as Technical Monitor. The authors are grateful for the contributions of the following individuals at GE Aerospace, GE Aerospace Research, and NASA Glenn Research Center personnel who made significant contributions to the project and allowed for the successful execution and completion of the task objectives.

HTEBC Advancement Contributing Teams

GE Aerospace:

Suresh Viswanathan, Michael Guerette, Cameron Farley, Alex Ruschau, Glen Kirby, and Mano Manoharan

GE Aerospace Research:

Nicholas Antolino, Geoff Eadon, Joseph Foroughi, Quentin Fouliard, Claire Henderson, Lakshmi Krishnan, Caitlin Lambrecht, Carl Lester, Allan Northrup, Tracy Paxon, Vidya Ramaswamy, Enes Sales, Jose Sanchez, Anant Setlur, Scott Smith, Julin Wan, Reza Sarrafi-Nour, Anant Setlur, Andrea Vozar, Julin Wan, Michael Worku, Michael Barber, Lauri Le Tarte, Najafa Islam, Joseph Foroughi, Allan Northrop, Jared Weaver, and James Vartuli

NASA Glenn Research Center:

Bryan Harder, Michael Presby, Mike Kulis, Kang Lee, Roy M. Sullivan, Subodh Mital, Steven Arnold, Josh Stuckner, Carl Liebfried, Laura Evans, Amelia Wilson, Leland Hoffman, and Makoto Endo (QARE Rig modeling)

Level of Review: This material has been technically reviewed by technical management.

NASA STI Program/Mail Stop 050
NASA Langley Research Center
Hampton, VA 23681-2199

Contents

List of Figures

List of Tables

List of Acronyms

Acronym	Definition
AAVP	Advanced Air Vehicles Program
AME	Additive Manufacturing Engineering
ARMD	Aeronautics Research Mission Directorate
ASTM	American Society for Testing and Materials
BC	Bond Coat
BSAS	Barium Strontium Aluminosilicate
CFD	Computational Fluid Dynamics
CFM	50/50 joint company of GEA and Safran
CMAS	Calcium-Magnesium-Aluminum-Silicate
CMC	Ceramic Matrix Composite
CO	Carbon Monoxide
CTE	Coefficient of Thermal Expansion
CTQ	Critical to Quality
CUI	Controlled Unclassified Information
CVI	Chemical Vapor Infiltration
PIP	Polymer Impregnation and Pyrolysis
DoE	Design of Experiment
EBC	Environmental Barrier Coating
EIS	Entry Into Service
ESCORT	NASA GRC’s 1 Hz data acquisition system
FOD	Foreign Object Damage
GEA	General Electric Aerospace
GRC	Glenn Research Center
HE	Hybrid Electric
HfO_2	Hafnium oxide or Hafnia
$HfSiO_4$	Hafnium Silicate or Hafnon
HMI	Human Machine Interface
HPCR	High Pressure Combustor Rig
HPT	High Pressure Turbine
HSCT	High Steam Cyclic Test
HSCT-EPM	High Speed Civil Transport—Enabling Propulsion Materials
HT	High Temperature
HTCMC	High Temperature Ceramic Matric Composite
HTEBC	High Temperature Environmental Barrier Coatings
HTP	High Temperature & Pressure
HyTEC	Hybrid Thermally Efficient Core
IC	Intermediate Coat
JETS	Jet Engine Thermal Shock
KPP	Key Performance Parameter
LDI	Lean Direct Injector
LEAP	Leading Edge Aviation Propulsion
LPS	Liquid Phase Sintering
LuDS	Lutetium Di Silicate
LuMS	Lutetium Mono Silicate
LTAG	Long-Term Aspirational Goal
LWIR	Long Wavelength Infrared
MF	Magnification Factor

MI	Melt-Infiltrated
MO	Metal Oxide
NASA	National Aeronautics and Space Administration
NGNB	Next Gen Narrow Body
OML	Outer Mold Line
PLC	Programmable Logic Controller
PS-PVD	Plasma Spray-Physical Vapor Deposition
QARE	Quick Access Rocket Exhaust
RCA	Root Cause Analysis
REDS	Rare Earth Di Silicate
REMS	Rare Earth Mono Silicate
RES	Rare-Earth Silicates
RISE	Revolutionary Innovation for Sustainable Engines
ScDS	Scandium Di-silicate
SCFH	Standard Cubic Feet per Hour
ScMS	Scandium Mono-silicate
SEM	Scanning Electron Microscopy
Si	Silicon
SLM	Selective Laser Melting
TC	Top Coat
TGO	Thermally Grown Oxide
TPM	Technical Performance Measures
TRL	Technology Readiness Level
TTT	Transformational Tools and Technologies
TS	Thermal spray deposition methods
UEET	Ultra Efficient Engine Technology
UNFCCC	United Nations Framework Convention on Climate Change
VCAT	Variable Cycle Advanced Technology
YbDS	Ytterbium Di-Silicate

Executive Summary

GEA is developing next generation clean-sheet, sustainable aviation propulsion systems with higher efficiency, use of sustainable fuels and the ability to provide dual and/or hybrid electric propulsion and power. These new engine systems are expected to demand engine cores capable of much higher energy density, hence significant increase in the thermal efficiency, thermal load, and thermal management of first- and second-stage turbine components relative to those of the state-of-art LEAP and 9X engines are needed.

GEA has demonstrated multiple advanced gas turbine engine hot section component designs using Silicon-Carbide Ceramic Matrix Composite (SiC-SiC CMC) material. The current state-of-art CMC systems include Gen 2 Environmental Barrier Coatings for service life durability. The CMC-Gen2 EBC system technology has been successfully applied to the design and development of several components of high-pressure turbine hardware for advanced GEA CFM LEAP, GE 9X and military engine product hardware such as: combustor liners; turbine nozzles; turbine blades; turbine vanes & fairings. In the pursuit of higher material temperatures, GEA is maturing an alternative High Temperature Ceramic Matrix Composite (HTCMC) technology, based on an alternate Chemical Vapor Infiltration (CVI) process. HTCMC technology would be an enabler for achieving higher T3 and T4 operating conditions, increasing engine thermodynamic efficiency, which could effectively reduce the size and weight of the engine core.

The temperature capability of current generation Environmental Barrier Coating (EBC) systems in use on CMC components has a hard limit at the CMC-EBC interface driven by the melting point of the silicon bondcoat layer at 2550F. Therefore, GEA has been investigating novel material systems and concepts to overcome this hard limit. GEA recent advancements in this area have led to a novel composite bondcoat material system, which was successfully demonstrated under Navy VCAT program (ONR N0001410D0010). GEA-NASA HyTEC HTEBC program was designed to mature further the high-temperature EBC system including GEA's composite bondcoat system and NASA Glenn's high temperature EBC system. The program was able to advance several high-temperature EBC architectures further with successful sequential demonstrations under commercial engine relevant conditions in NASA QARE rig and NASA CE-5 rig tests for TRL-4 and TRL-5 qualifications, respectively.

In addition, modeling efforts were initiated thru collaborations between GEA and NASA Glenn Research teams under this program to develop tools to predict the durability of the HTEBC architectures and to guide future material and component design development efforts. The primary focus of the modeling work was the development of a physics-based oxidation kinetics model for the complex composite bondcoat system. The collaborative development efforts successfully devised a 1D model to assess the oxidation life durability criteria set for the program.

Three different HTEBC architectures - one from NASA Glenn and two from GEA Research - were evaluated in the program through laboratory tests and burner-rig testing in simulated environment at NASA Glenn Research Center. Three leading candidates, one from each architecture, successfully completed TRL-4 and TRL-5 laboratory tests in cyclic steam at 2700F for 1000 hours, cyclic thermal gradient/transient for 1000 cycles with EBC surface temperature of 3000F and CMC/EBC interface temperature corresponding to 2700F for 1000 cycles, and 3000F for 250 hours exposure in the atmospheric natural gas/oxygen burner rig (QARE) tests at NASA. The three HTEBC architectures were subsequently applied to CVI CMC airfoil test articles. The coated CMC articles were subjected to over 76 hours of exposure to ~3000F combustion gas in the high-pressure combustor rig at NASA Glenn Research Center CE-5 test facility. All three candidate systems successfully completed their combustion rig test and met all program TPM exit criteria for TRL-5.

1. Introduction

GEA pioneered the first commercial application of SiC-SiC Ceramic Matrix Composite in the first stage high-pressure turbine shroud (S1S) of GEA/CFM LEAP engine in 2016. Since their introduction into CFM LEAP engine, more than 250,000 CMC S1S components have been successfully produced and installed in the growing LEAP engine fleet. The LEAP engine fleet has now (as of January 2024) accumulated more than +49,000,000 flight hours (+22,000,000 flight cycles), establishing a successful and reliable track record for application of CMC components in next generation high-efficient jet engines. More recently (in 2020), GEA completed the FAA certification program of GE 9X engine, which relies on multiple CMC components in the construction of the high-pressure turbine architecture (combustor liners, stage-1 turbine shroud, stage-1 and stage-2 turbine nozzles). GE 9X engine is the sole-sourced power plant for Boeing 777X plane, the world's largest and most efficient twin engine widebody aircraft designed for seamless integration with Boeing's 777 and 787 fleet. GEA is currently producing GE 9X engines in preparation for Boeing 777X entry into service (EIS) in 2025.

The CMC components of LEAP and 9X engines are designed and fabricated using GEA Melt-Infiltrated (MI) SiC-SiC CMC material system with Gen2 Environmental Barrier Coating (EBC) systems applied to the CMC component surfaces. The maximum operability temperature of MI CMC components for long service design life demanded in commercial jet engines (+24,000 hours) is considered to be 2400F. This maximum temperature is largely set due to the melting point of the residual Si phase (T_m~2500F) that is present in the SiC matrix of MI SiC-SiC CMC system. Gen2 EBC systems rely on an oxidation barrier layer of Si (the so-called Si bondcoat) and the outer layers of the EBC architectures consisting of rare-earth silicates (RES). While Gen2 EBC systems are able to withstand surface temperatures up to 3000F, their long-life operability temperatures are primarily limited by the melting point of the Si layer (~2500F) and the oxidation kinetics of Si to SiO_2 (absent of other service environment threats such as CMAS (Calcium-Magnesium-Aluminum-Silicate).

Over the past decade, GEA has been developing next generation of SiC-SiC CMC and EBC systems for maximum service temperatures of 2700F and +3000F at the CMC-EBC interface and EBC surface, respectively. These next generation CMC and EBC systems are currently designated as HTCMC and HTEBC. The HTCMC development relies on the same prepreg processing methods and the use of uni-directional fiber plies to construct cross-ply architectures as those utilized in the construction of current generation MI CMC components. However, the SiC matrix of HTCMC system is formed via Chemical Vapor Infiltration (CVI) process, eliminating the residual free Si present in the MI CMC systems, and providing increased temperature capability.

HTCMCs are an enabling technology for advanced gas turbine engines. As has been the case for decades, each new generation of engines push core temperatures ever hotter to improve thrust and reduce fuel burn. Modern clean sheet and derivative engines feature temperatures higher than ever before at the compressor discharge, and in the combustor and turbines. Traditional materials require increasing cooling flows to accommodate these increases temperatures, potentially reducing the thermodynamic gains of higher cycle temperatures. New higher temperature materials provide performance improvement relative to the current MI system by allowing for even hotter cycles and/or less cooling air, thereby reducing fuel burn and emissions.

The NASA Aeronautics Research Mission Directorate (ARMD) is currently operating an integrated subsonic transport technology maturation program, called the Advanced Air Vehicles Program. A part of this program is the HyTEC project, which focuses on accelerating technology development for compact core technologies, with the objective of meeting the Key Performance Parameters (KPPs) shown in Table 1. As a part of this effort, GEA is under contract to mature HPT HTEBC technologies for the next generation of narrowbody transport engines.

Table 1: HyTEC Project KPPs

KPP#	KPP	Full Success Single Aisle ~2035 EIS	Minimum Success Single Aisle ~2035 EIS
KPP-1	Fuel burn reduction attributed to the high-power density core of the original equipment manufacturer's vision turbofan engine	10%	5%
KPP-2	Engine Bypass Ratio	>15	>12
KPP-3	Engine Overall Pressure Ratio (defined at top of climb)	>50	>45
KPP-4	Durability, measured in operating hours between major refurbishments	Exceed SOA by 5%	Meet SOA of baseline
KPP-5	Degree of hybridization measured by level of power extraction from the turbofan engine at altitude	20%	10%
KPP-6	High Pressure Compressor Exit Corrected Flow	< 3 lbm/s	<3.5 lbm/s

For the temperatures under consideration, the current Gen 2 EBC will not survive. For the HPT specific technologies, the relevant KPP for the contract is therefore KPP-4 (durability) that will enable maturation of the HTCMC/HTEBC material system.

2. Technology and Program Overview

NASA and GEA have extensive experience in developing and commercializing a 2400F CMC/EBC system for aircraft engines. This program builds upon GEA's existing system to develop and to achieve TRL-5 on a new HTEBC system with capability up to 3000F for use on HT CMC with capability up to 2700F.

2.1 GEA HTEBC Development: Background

The development of HTEBC system for HTCMC components has primarily focused on developing alternative oxidation barrier layers to address the temperature limit associated with the melting temperature of the Si layer of Gen2 EBC systems. The outer layer of HTEBC architectures would remain ideally the same as the Gen2 EBC or fully compatible with the existing RES EBC architecture and manufacturing technologies. Over the past decade GEA Research team has investigated several innovative HTEBC oxidation barrier concepts following these principles. The most promising concept that has emerged through these investigations since 2017 is a composite oxidation barrier layer concept. In this case, the oxygen barrier layer is constructed using mullite as the matrix with an oxygen-getter phase introduced in the mullite matrix as discrete second phase inclusions of Si-based non-oxide ceramic such as Si, SiC, Si_3N_4 or a metal silicide, M_xSi_y [28 and 29]. Figure 1 compares the architectures and the max temperature performance attributes expected for Gen2 EBC and HTEBC architectures. The choice of mullite as the matrix is based on its very low oxygen permeability (second to amorphous silica) amongst all refractory ceramic oxides and based on its relatively close thermal expansion matching with SiC system. The choice of the Si-based non-oxide second phase or the oxygen getter is primarily derived from the slow oxidation kinetic of Si and Si-based ceramics enabled by the low oxygen permeability of silica at high temperature. In addition, the silica phase formed on oxidation of the Si-based getter phase is thermo-chemically compatible with the mullite matrix at all temperatures below the SiO_2-Mullite pseudo-binary (or SiO_2-Al_2O_3 binary) system eutectic temperature of ~2900F. GEA Research has successfully demonstrated both the fabrication and the oxidation performance of the mullite-matrix composite oxidation barrier coatings on HTCMC substrates at 2700F in air and water-vapor atmosphere using both SiC and Si as the oxygen getter phases and thermal spray processing methods to deposit the coating layers.

With the invention of the composite oxygen barrier layer, thermo-chemical compatibility considerations and limits set the definition of the rest of the EBC architecture in contact with or in the proximity of this layer. While SiO_2-REDS system is generally thermo-chemically compatible up to T<~3000F, with the introduction of mullite or Al_2O_3 into the system the resulting ternary eutectic reactions in SiO_2-RE_2O_3-Al_2O_3 become highly relevant in limiting the refractoriness of the EBC architecture. With this recognition, the implementation of mullite-matrix composite oxygen barrier layer required changes to the rest of the (Gen2) EBC architecture to maintain performance temperature requirement of T=2700F at the HTCMC-HTEBC interface.

GEA investigated the temperature capability of both types of architectures in prior programs directed at potential applications of HTCMC components in military engine applications. Isothermal and cyclic steam oxidation tests were performed on bi-layered Mullite-Si/HfO_2 and Mullite-Si/REDS coatings at 2700F to investigate the performance capabilities of both material system/architectures. The bi-layered coating structures could be considered as representations of the tri-layered architectures, in which the intermediate $HfSiO_4$ and the surface layer of REMS formed in-situ during exposure to service environment at high temperatures. The investigations REMS demonstrated oxidation life capabilities of the composite bondcoat in both architectures in excess of 1000 hours in 90%H_2O-10%O_2 atmosphere. The steam oxidation tests also indicated the higher temperature capability of the HfO_2-based vs REDS-based HTEBC architecture.

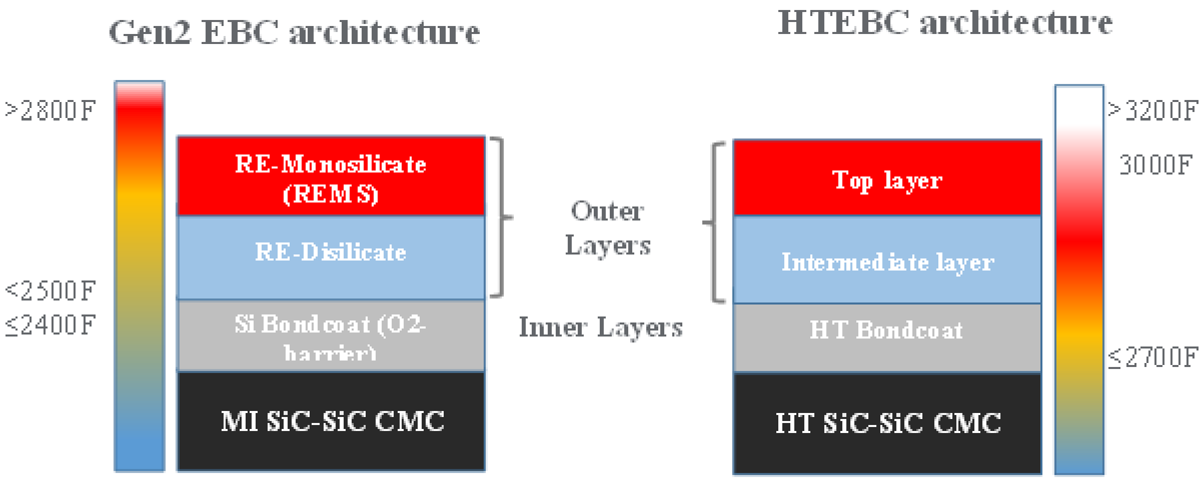

Figure 1: Comparison between Gen2 and HTEBC architectures, the expected service temperature requirements and limits.

With these positive observations, a strategy was set and drove internal GEA Research work to investigate methods to further improve and mature the HTEBC material systems and architectures. A primary focus was given to the coating layers deposited by the current thermal spray methods. A second focus in the material and process evaluations was directed to the effect of MO in quaternary systems and unintentional impurities in the thermo-chemical behavior and oxidation response of the composite bondcoat in contact with the outer layer. This was guided by the minimum eutectic temperature predictions for multiple pseudo binary Mullite-MO systems.

2.2 Coating Development Plan

2.2.1 GEA – NASA HyTEC program

Previous development efforts at GEA on HTEBC focused on short duration applications such as in military engines. GEA-NASA HyTEC HTEBC efforts focused on investigating the technology for applications in next generation aircraft engines. Based on prior HTEBC efforts at GEA and at NASA Glenn Research Center, the development efforts in this program focused on three model HTEBC architectures for future commercial applications such as in GEA's Next Gen Narrow Body, NGNB, as an entry propulsion system into the future hybrid electric engine core. The architectures included the HTEBC architectures from GEA and one EBC architecture from NASA as shown in Figure 2. The two GEA architectures were those developed in earlier GEA program with potential derivatives or alterations in the architecture to improve performance and durability as laid out for the HyTEC program. The NASA Glenn Research HTEBC architecture is labeled architecture 0 because of its similarity to GEA architecture 1 without composite bondcoat and the outer layer of either HfO_2 or rare-earth silicate. NASA had independently evaluated this architecture in their internal programs through steam oxidation test at temperatures not exceeding 2600F.

The EBC material and architecture development tasks of HyTEC program focused on baselining and evaluations of the three HTEBC architectures shown in Figure 2 under the test conditions based on operating condition guided by assumed NGNB/HyTEC engine cycle at the onset of the program.

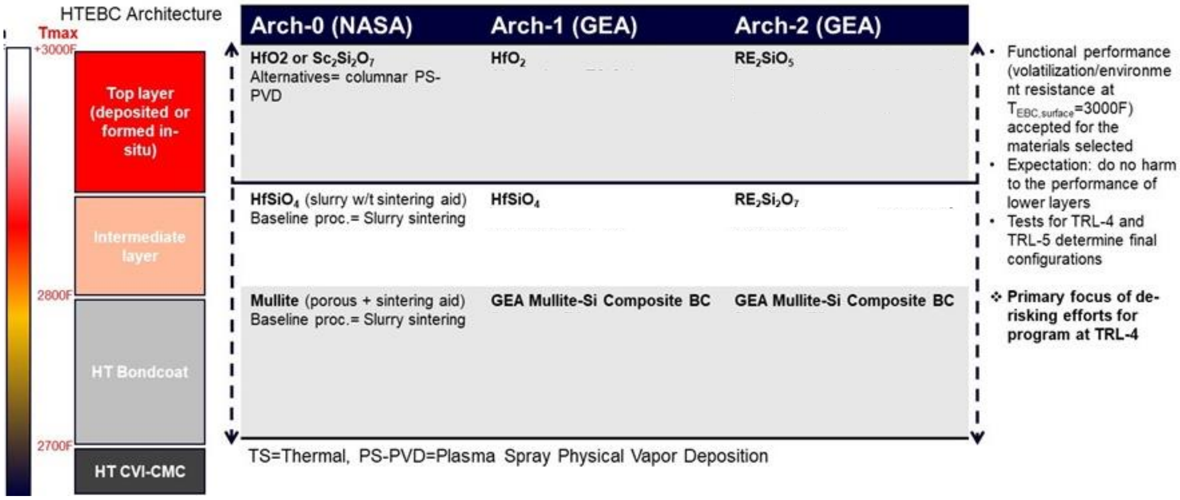

Figure 2: HTEBC architecture considered for GEA-NASA HTEBC HyTEC program.

2.2.2 HTCMC-HTEBC Performance Objectives

Previous development efforts of GEA HTCMC-HTEBC systems focused on relatively short service life but demanding operating conditions anticipated in next generation military propulsion systems. For the HyTEC development, vis-à-vis NGNB engine, the operating conditions of the engine may not be as severe, but the service & operability life requirements of commercial engines are expectedly far more demanding. Because NGNB/RISE/HyTEC propulsion systems are still in conceptual design studies, the engine operating cycles have not been sufficiently matured to drive detailed design of the component. Therefore, an existing iteration of NGNB engine cycle operation profile was used to guide selections of the test temperature and the selection of durations at maximum temperatures of the operating cycle for a notional Stage-1 HTCMC nozzle configuration. Using a notional 20,000 flight cycles to set the durability criteria for the HTEBC system, the total hot times during the takeoff and cruise conditions could be estimated to set the durability performance requirements as shown in Table 2. By treating the total takeoff and climb duration as one and under the takeoff conditions, the program exit criteria for successful HTEBC systems in laboratory TRL-4 and TRL-5 tests (such as steam oxidation and thermal gradient tests) shown in Table 3 and Table 4 were derived from 10% and 30%, respectively, engine cycle total combined take-off + climb durations noted in Table 2.

Table 2: Expected operating profile cycle for a notional HTCMC nozzle component of NGNB / HyTEC engine.

Engine cycle	EBC Surface Temperature	CMC Surface Temperature	Cycle duration	20k cycle durability	10% durability	30% durability
Takeoff + Climb	~2900F	~2700F	~5 min	~1667 hrs	~167 hrs	~500 hrs

With the HyTEC HTEBC maximum expected operating conditions at the surface in the range of 2800F-3000F, the cyclic steam, thermal gradient-cycle (JETS), atmospheric burner rig and high-pressure burner rig test conditions were defined through discussions between GEA and NASA program team. The test conditions defined within the scope and objectives of TRL-4/-5 evaluations of the program as well as the ownership of the executions of the test plans are shown in Table 3.

Table 3: HyTEC HTEBC program test scope, plans, and objectives

EBC Coupon Test	Notional Conditions	GE	NASA	TRL-4	TRL-5
High Steam Cyclic Test (HSCT)	T=2400F-2700F 90%H_2O-10%O_2 1h-cycle, 500 and 1000 cycles	▼	▼	Yes 10% mission durability (simulated)	Yes 30% mission durability (simulated)
Thermal Gradient & Cycle Tests	$T_{surface}$= 2800F-3000F $T_{bondcoat}$= 2500F-2700F 5 min hot cycle, up to 2000 cycles	▼	▼		
CMAS Exposure	$T_{surface}$= 2800F-3000F $T_{bondcoat}$= 2700F	▼	▼		
Atmospheric Burner Rig Test (QARE)	$T_{surface}$= 2800F-3000F $T_{bondcoat}$= 2500F-2700F p_{H2O} > 0.5 atm, 50 – 200hrs		▼		NA
High Pressure Combustor Rig Test	$T_{surface}$= 2800F-3000F $T_{bondcoat}$= 2500F-2700F p_{H2O} > 0.5 atm, 50 – 70hrs		▼	NA	Yes

The set of TPM requirements for this program in Table 4 were then created by combining the inputs from Table 2 and Table 3 to help establish clear TRL exit criteria from the HTEBC maturation activities.

Table 4: TPM requirements established for TRL exits.

Test	Criteria	Test Condition TRL-4 (for min success)	Test Condition TRL-5 (for full success)
Steam Oxidation	< 25% exposure of CMC	250 Hours at 2700F	1000 Hours at 2700F
Thermal Gradient	< 25% exposure of CMC		1000 Cycles at TC>2850F and BC>2700F
QARE Rig	< 25% exposure of CMC	250 Hours at 2700F	NA
Combustion Rig	< 33% exposure of CMC	NA	72 Hours
Assessment based on % exposure of CMC substrate area after test (measure by visual inspection at 200x)		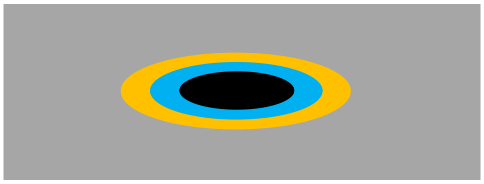	

2.3 HTCMC Substrates for HTEBC Development and Demonstration

2.3.1 HTCMC Coupons

Standard 8-ply HTCMC panels were fabricated and machined into different coupons as required for steam test and JETS. Twenty-six panels were made under this program to support development activities at both GEA and NASA-Glenn.

2.3.2 HTCMC Airfoils

HTCMC airfoils were designed and fabricated based on current established steps listed under section 2.3.2.1 and section 2.3.2.2. In total, seven airfoils were made under this program:

- One setup airfoil for coating trials (P/N: 16281)
- Two airfoils for rig testing of HTEBC Arch 0 (P/N: 16283 and 16286)
- Two airfoils for rig testing of HTEBC Arch 1 (P/N: 16282 and 16284)
- Two airfoils for rig testing of HTEBC Arch 2 (P/N: 16285 and 16287)

2.3.2.1 Design

To facilitate testing of the High Temp EBC in the NASA combustor rig, a design effort was required to adapt the HTMC material system for the existing rig design while facilitating the implementation of instrumentation to assess interior and exterior surface temperature in-situ. The airfoil design was based on a scaled-up version of ceramic airfoils that had previously been tested in the rig to reduce cost and complexity. This design is a symmetrical, thin-walled fairing, with a large internal cavity. The height and width of the airfoil were maximized within the confines of the test section in order to incorporate as much instrumentation within the cavity as possible. The images in Figure 3 show the key airfoil dimensions.

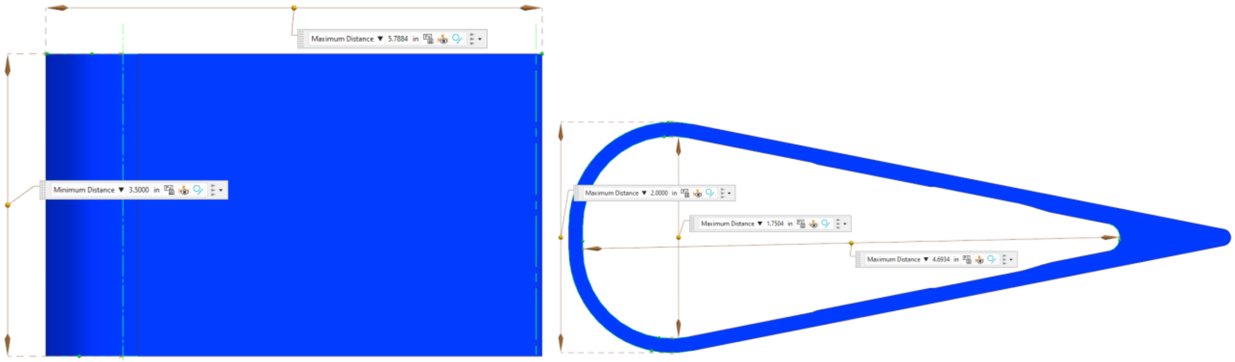

Figure 3 Design of CMC Airfoil

The airfoil wall thicknesses were assessed to determine capability to withstand the mechanical stresses due pressure differences in the flowpath and airfoil cavity. The airfoil walls and wishbone layout were not sized for stresses caused by thermal gradients due to the nature of the test and unknown thermal boundary conditions within the test section. The metallic insert that delivers cooling air and holds instrumentation during testing is shown in Figure 4. At nominal room temperature conditions, the minimum gap is 22 mils. The gap between the airfoil and the metallic insert closes to 13 mils at 1200F.

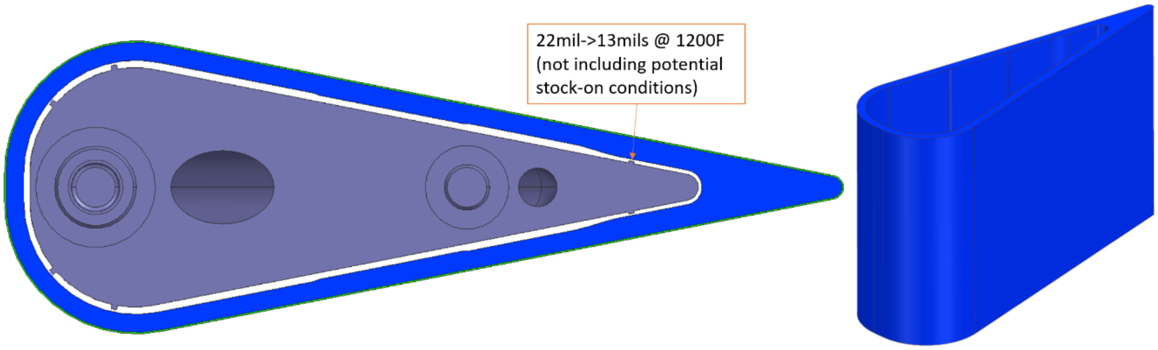

Figure 4: Planned mounting of Airfoil in CE-5 rig.

The mounting of the airfoil within the test section was done in the same manner as the previously tested smaller airfoils. Two water cooled copper plates were 3D printed with a shaped channel to sandwich the top and bottom faces of the symmetrical airfoil. A high temperature fabric was inserted between the airfoil and copper plate to limit leakage between the cavity and flowpath, as well as provide a more compliant surface between the mounting plate and the CMC.

2.3.2.2 Fabrication

The objective was to manufacture HTEBC coated CVI SiC/SiC CMC test articles to be tested by NASA in the high pressure combustor rig test setup discussed in the later sections of this report. The test article mimics an airfoil with a simplified 2D design. A quantity of 7 airfoils were produced. The manufacturing process, from preform definition through machining and inspection, is summarized below.

To prepare for manufacturing, the nominal test article was scaled 0.25 inches in the in-plane direction to create a stock on condition for final machining. This is shown in Figure 5 via where as-molded part is shown in red and the final machined part is shown in blue.

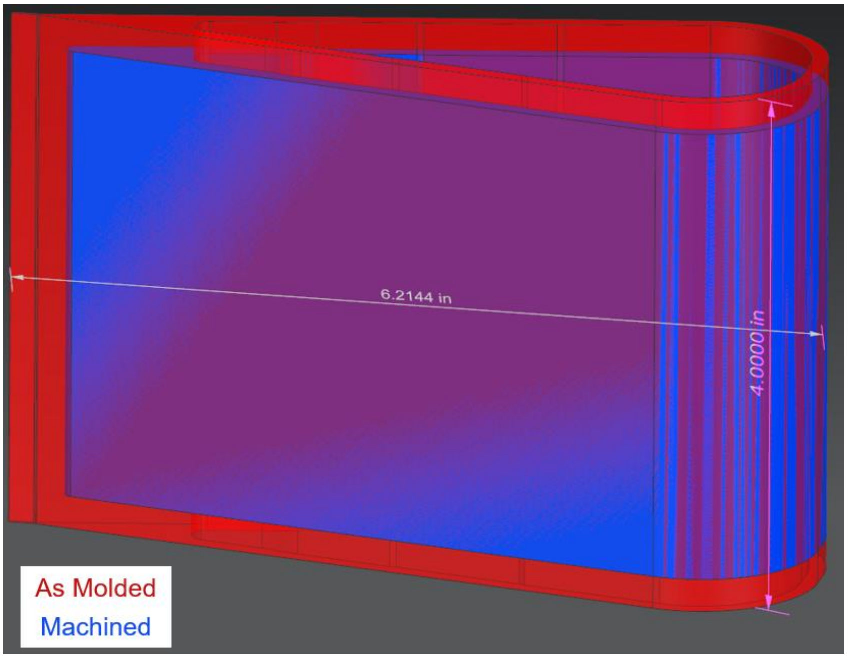

Figure 5: Test Article Preform and Machined Bodies.

From the 3D model, ply sheets were defined and flattened into 2D shapes using FiberSim to produce ply shapes for cutting fiber prepreg tapes. The 2D flat patterns are digitally laid out to control ply fiber direction within the area of a prepreg tape, and then automatically cut. These plies are then laid up and placed in hard tooling to define the outer mold line (OML). The part and tooling are then processed through an autoclave to laminate and consolidate the preform. The part is then processed through pyrolysis to convert organics, and finally a chemical vapor infiltration (CVI) process to densify the preform. Once infiltrated, the preform passes through dimensional and NDE inspections, final machining, and a final dimensional inspection, before proceeding to HTEBC deposition process.

3. HTEBC Development

3.1 GEA HTEBC Architectures 1 and 2 Development

3.1.1 Composite bondcoat composition optimization and oxidation kinetics evaluation

3.1.1.1 Initial bondcoat composition and processing evaluations

Improving the oxidation life of the composite mullite-Si bondcoat was a primary objective of the material development task in the HyTEC program. GEA broadly studied the processing and oxidation performance of mullite-Si bondcoats across these parameters:

- Bondcoat thermal spray conditions.
- Bondcoat composition, including Si level and the composition of the mullite matrix.
- Post-deposition annealing heat treatment conditions.
- Architecture 1 and 2 topcoats.

These oxidation experiments have been conducted at multiple temperatures and oxidant concentrations to allow for extrapolation towards conditions for a hypothetical engine cycle and TRL assessment.

In the mullite-Si composite bondcoat, oxidation life is presently defined as the approximate time when the Si getter particles are fully consumed. The general observation is that after full Si consumption, there is finite time (for example in 1-hr cyclic oxidation tests at 2700F/0.9atm H_2O-0.1atm O_2 conditions) before coating delamination from the CMC substrate is observed and proceeds to spallation. Figure 6 shows examples of a bi-layered EBC architecture including a mullite-Si composite bondcoat. The large vertical crack seen in the bondcoat (Figure 6), represents areas where more rapid oxidation occurs, during thermal exposures.

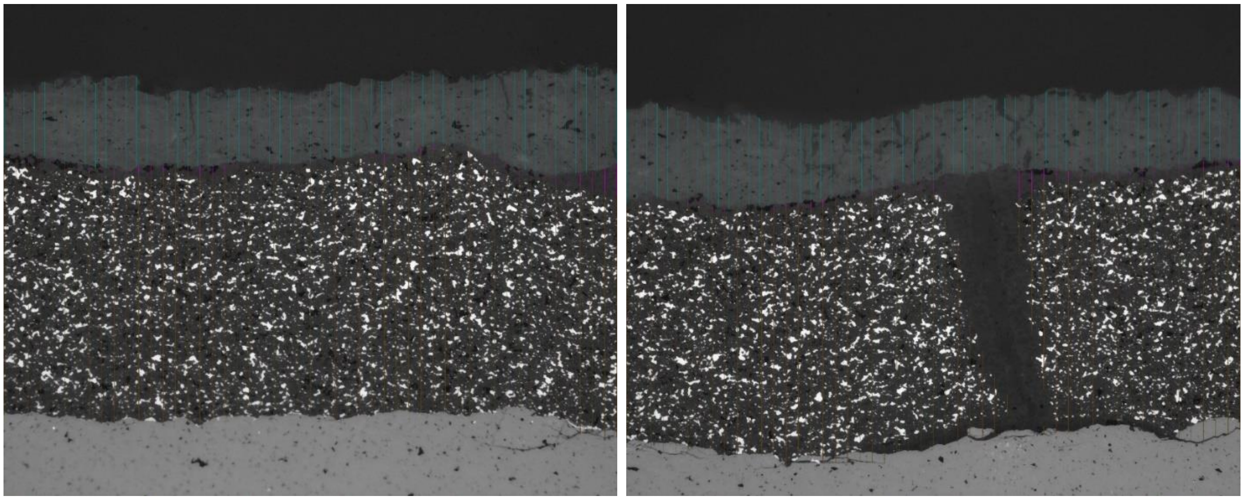

Figure 6: 200x optical micrograph of mullite-Si bondcoat after annealing heat treatment (Left) a typical section of the bondcoat, and (Right) an example region with a vertical crack in the bondcoat. The Si inclusions in the vicinity of the vertical crack have been oxidized to form a TGO layer.

GEA performed screening study across different bondcoat compositions and annealing heat treatment using a model Architecture 2 system using TS $Sc_2Si_2O_7$ (REDS) as model material for evolution. Flash IR method (thermal diffusivity) was used for efficacy to determine whether there were coating delaminations after oxidation testing with dark blue regions indicating delamination. The results of the screening study can be summarized as follows:

- Altering mullite compositions deteriorated the oxidation kinetics of silicon particles (samples B, C and E) in 2700F cyclic steam tests. These composition modifications could achieve only ~750 hours of oxidation life (marked by complete oxidation bondcoat) at 2700F in cyclic steam tests, short of the program expectations of 1000 hours of steam oxidation for TRL-5.
- Some of composition modifications had negative impacts in the as-deposited composite mullite-Si layer microstructure leading to discrete nodules with surrounding regions of high porosity (Figure 7). These regions and their proximity oxidized faster during subsequent thermal aging.

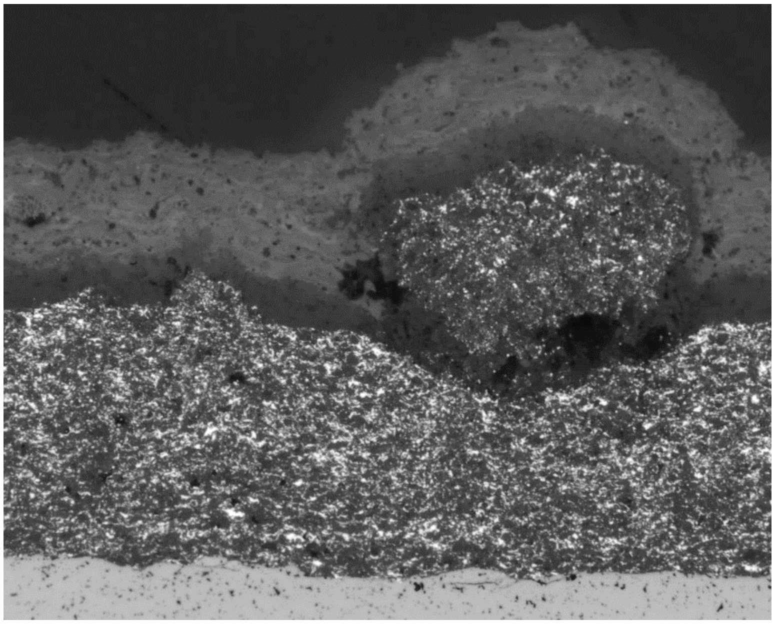

Figure 7: 200X optical image of an as-sprayed coating cross-section containing oxide dopants with a coating nodule with enhanced porosity in the vicinity of the nodule.

3.1.1.2 Optimization of bondcoat oxidation performance using Architecture 2 intermediate layers: microstructural metrics and composition evaluations

Increasing the Si level in the feedstock directly correlated to higher Si levels in the bondcoat after a baseline annealing heat treatment (Figure 8 and Table 5). Later experiments to further increase BC Si levels through higher Si in the feedstock did give higher Si in the as-sprayed state, but there was extensive Si loss after annealing heat treatment (Figure 9 and Table 5) with significantly higher residual porosity for bondcoats with much higher Si content in the as-sprayed state (Table 5).

Table 5: Comparison of Si-level and porosity as a function of Si level in the feedstock formulation of Mullite-Si/REDS coating samples.

Si-level in feedstock	Coating layer condition	Relative Si volume fraction	Porosity (SEM image analysis at 500X)
Low	As-sprayed	0.93	15.9%
Low	HT1	0.61	11.1%
High	As-sprayed	1.3	14.0%
High	HT1	1	9.6%

High	As-sprayed	2.19	7.3%
High	HT1	1.09	13.0%
Higher	As-sprayed	3.62	8.5%
Higher	HT1	0.9	20.5%
Highest	As-sprayed	5.33	6.9%
Highest	HT1	0.77	27.9%

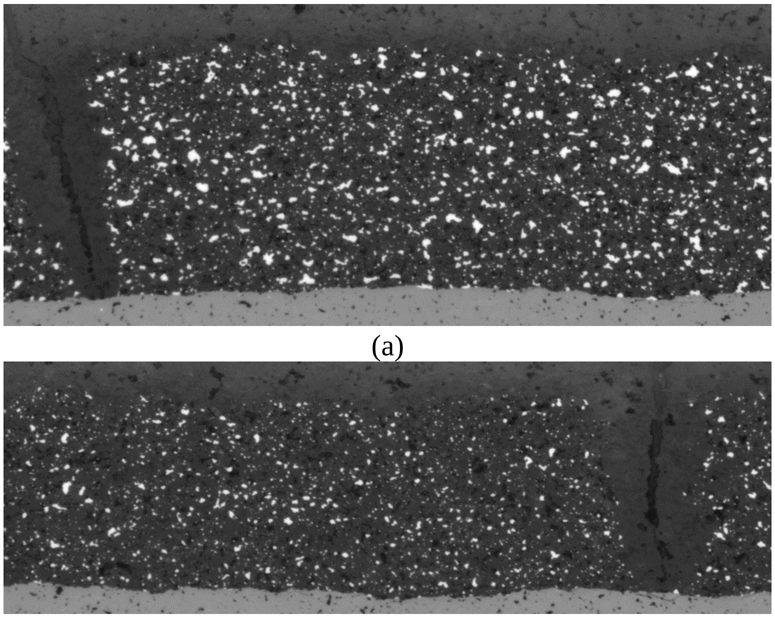
(a)

(b)

Figure 8: 200x optical microscope images of a mullite-Si bondcoat in a mullite-Si/mullite/ REDS architecture after annealing heat treatment HT1 with (a) high Si and (b) low Si content in the mullite-Si feedstock material.

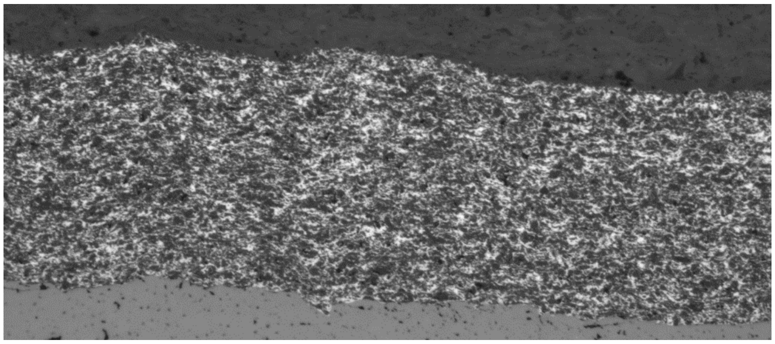

(a)

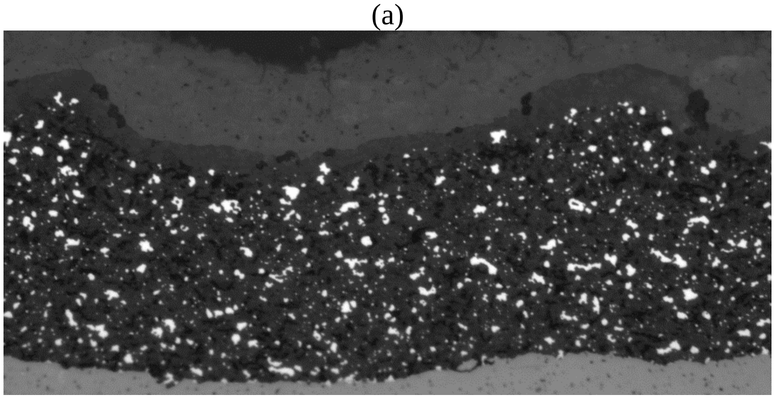

(b)

Figure 9: 200x optical microscope images of a mullite-Si bondcoat in a mullite-Si/mullite/ REDS architecture produced with the highest Si content evaluated in the feedstock material. (a) in the as-deposited state and (b) after HT1 annealing heat treatment.

We also screened different annealing heat treatment schedules, temperatures to determine if any changes in the annealing heat treatment could affect either Si retention. Higher temperature annealing heat treatments (denoted as HT2) led to more bondcoat consumption and a thicker reaction zone. Cyclic steam testing at 2700F showed almost complete Si consumption after 250 cycles (Figure 6 and Figure 10). Therefore, the initial oxidation study to meet TRL-4 and TRL-5 oxidation metrics utilized the baseline HT1 annealing heat treatment.

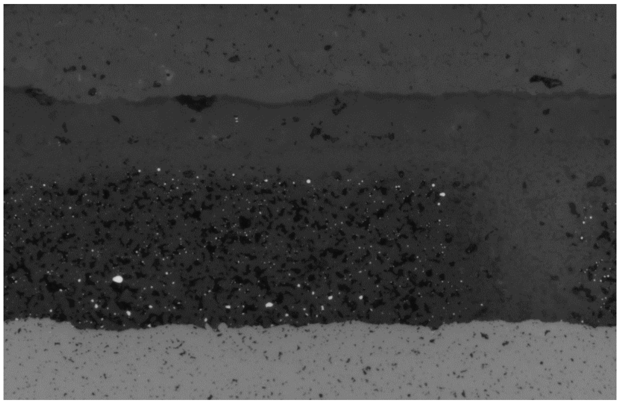

Figure 10: 200x optical micrograph of a mullite-low Si bondcoat in a mullite-Si/mullite/ REDS architecture after annealing heat treatment at HT2 temperatures and lower oxygen partial pressures and 2700F/250 cycle steam testing.

In cyclic steam oxidation tests (1 hr cycles, 0.9 atm H_2O-0.1 atm O2), GEA is able to fit the growth of the reaction layer/thermally-grown oxide (TGO) reasonably well to a parabolic relationship for short testing times (Figure 11).

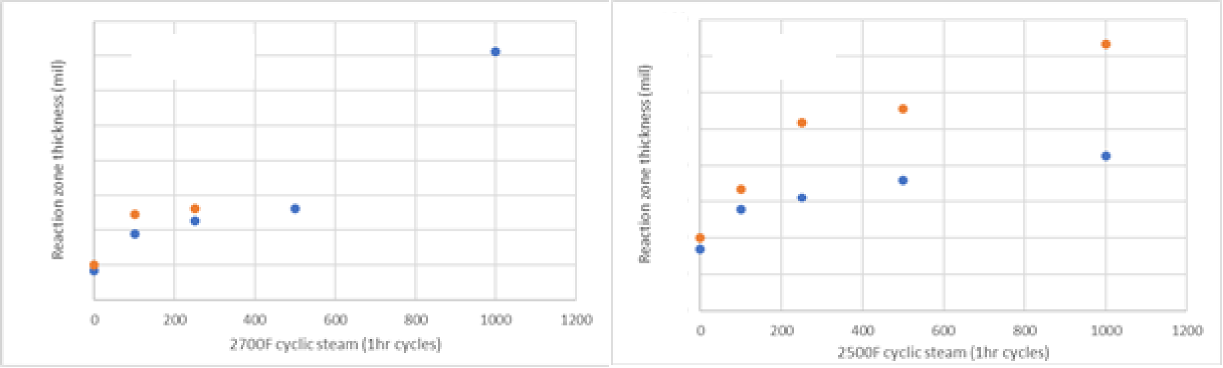

(a)

(b)

Figure 11: Observed TGO/reaction zone thickness versus time for mullite-Si bondcoats (orange points are low Si content, blue points are high Si content) in steam oxidation tests at (a) 2700F and (b) 2500F. The 2700F reaction zones thicknesses are not taken to longer times in the low Si sample due to nearly full Si consumption in the bondcoat.

HT1 annealing heat treat was designated as the baseline process based on prior experience. The annealing heat treatment schedules designated HT2, HT3, HT4 were investigated as alternative to HT1. The focused effort aimed at further improving oxidation response by annealing heat treatment modifications. Post heat-treatment image analysis comparing sister bondcoat test coupons with the baseline HT1 annealing heat treatment versus alternative heat treatment conditions showed varying degrees of total Si retentions in the bondcoat and varying thickness of TGO / reaction layer (Figure 12), although these differences are within one standard deviation of one another. Overall, the specimens with a HT4 heat treatment had better Si retention after steam test at 2700F for 1000 hrs (Figure 12). In summary, while our initial baseline HT1 heat treated coatings did meet the 1000 hrs steam testing life for TRL-5, the alternative annealing heat treatment such as HT4 could be utilized for rig test airfoil articles.

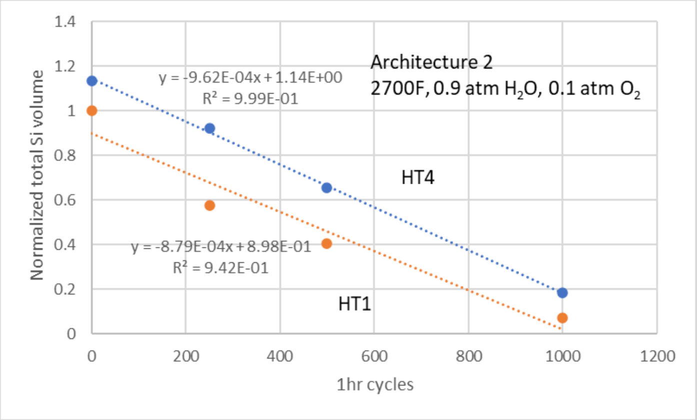

Figure 12: Comparison of Si retention for baseline and optimized heat treatments for a high Si-mullite bondcoat (blue=HT4 heat treatment, orange=HT1 heat treatment).

3.1.1.3 Mullite-Si bond coat for Architecture 1 intermediate layers

The oxidation studies were extended to Architecture 1 HTEBC system (HfO_2/$HfSiO_4$-based intermediate layer). Our initial expectations were that changing the intermediate layer composition from the model RE= REDS-based layer system to a $HfSiO_4$-based intermediate layer should not have any major impact on oxidation behavior beyond some observed crosstalk and silicate TGO interactions.

For oxidation tests, GEA used a thermal-sprayed $HfSiO_4$ layer. GEA refers to this thermal-sprayed material as the $HfSiO_4$ layer in this section. One issue in these HTEBC architecture test specimens was that the bondcoat had significantly lower Si volume fractions. The lower Si level contents appeared consistent across different HT conditions. The origin of this variability in the mullite-Si bondcoat layer is not known currently. Therefore, GEA can make only relative comparisons for short-term oxidation response as a function of intermediate layer compositions. GEA tests have been evaluated after 250 cycles of testing (Table 6). From initial image analysis of these bondcoats, the oxidation response of the bondcoats in Architecture 1 and Architecture 2 appeared to be similar. There is an apparently faster TGO/reaction layer growth in the coating architecture with a $HfSiO_4$ (Table 7).

Table 6: Bondcoat properties for a mullite-high Si bondcoat with a mullite barrier layer and a thermally-sprayed $HfSiO_4$ intermediate layer after annealing heat treatment and 250 cycles of oxidation testing. The relative Si values are versus an Architecture 2 mullite-high Si/TS REDS system.

Condition	TGO thickness	Relative Si VF	Porosity in Si-rich
After HT4 annealing heat treatment	60 μm	0.41	9.3%
+2500F 250cyc steam	78 μm	0.55	9.6%
+2700F 250cyc steam	121 μm	0.27	14.0%
+2700F 250cyc 100% O_2	85 μm	0.32	11.6%

Table 7: Comparison of various architectures for initial Si level and their approximate parabolic rate constant (K_p) for reaction zone/TGO growth for the mullite-Si bondcoat. This approximation for K_p assumes that any mullite barrier layer is permeable to oxidants.

Architecture	Annealing heat treatment	Relative Si vol. fract.	Oxidation	250 hrs K_p [mm^2/hr]
High Si/mull/REDS	HT1	1.0	2700F-steam	6.5
			2700F-dry	5.0
			2500F-steam	1.6
Low Si/mull/REDS	HT1	0.61	2700F-steam	9.1
			2700F-dry	5.5
			2500F-steam	3.9
High Si/REDS	HT1	1.09	2700F-steam	7.9
High Si/REDS	HT3	2.1	2700F-steam	4.7
High Si/mull/$HfSiO_4$	HT3	0.41	2700F-steam	24.6
			2700F-dry	6.6
			2500F-steam	4.1

GEA has also observed higher K_p values with TS REDS intermediate layers with low Si content in feedstock material versus high Si in GEA oxidation tests (Table 7 and Figure 13). Therefore, the effect of intermediate layer composition on bondcoat oxidation in cyclic steam and oxygen testing cannot be deconvoluted from experimental and measurement variability.

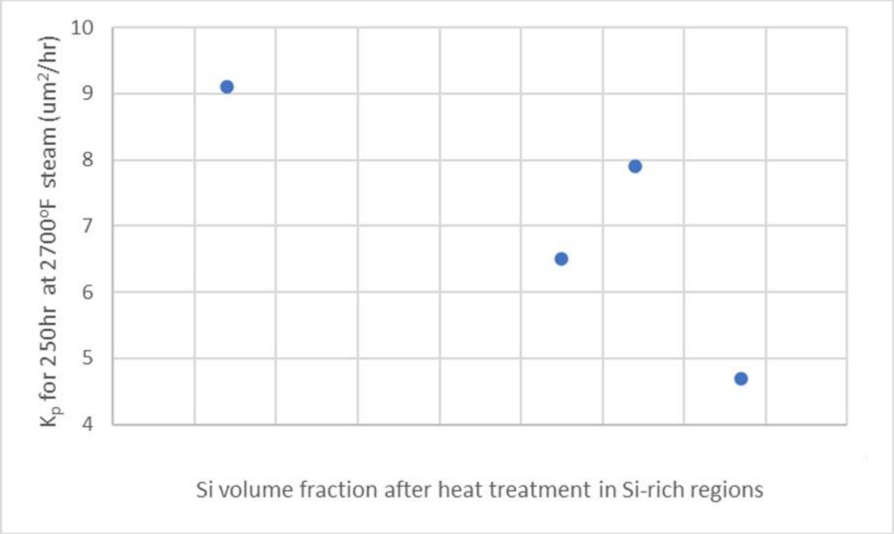

Figure 13: Plot of single-point Kp estimated for 2700F steam oxidation for 250 hrs versus initial Si content for mullite-Si layers with TS REDS intermediate layer. These Kp values are calculated assuming that the mullite barrier layer is completely permeable.

3.1.1.4 Oxidation response of mullite-Si bondcoats with matrix composition modifications

Prior to the HyTEC program, GEA screened several pseudo-binary mullite-oxide systems, primarily looking at the minimum eutectic temperature for refractory mullite matrix composition modifications whose T_{liq} was near or above 2700F. In the HyTEC program, GEA extended this screening study to nine other pseudo-binary mullite/metal-oxide systems. These additives were formulated into the feedstock formulation at concentrations defined relative to the mullite matrix content.

In general, there was significantly more rapid bondcoat consumption in our air environment oxidation studies for bondcoats with modified mullite matrix compositions versus the baseline composite bondcoat system. In accelerated oxidation tests in air at 2800F, this relationship appeared to translate into a parabolic rate constant of ~0.5 mil^2/hr.

In tests conducted at 2700F in 1atm-O_2 for cyclic oxidation using GEA typical oxidation testing furnaces, GEA derive two separate K_p values for the growth of the reaction product and the consumption of the bondcoat. These K_p values for 2700F-1atm O_2 are on the order of ~0.1 mil^2/hr and ~0.05 mil^2/hr for TGO / reaction product growth and bondcoat consumption, respectively. While this analysis uses a simple parabolic kinetic to describe reaction layer growth, the kinetics in these limited experiments could be somewhat slower than parabolic kinetics. There could be microstructural and compositional changes at 2700F that may alter the oxygen permeability.

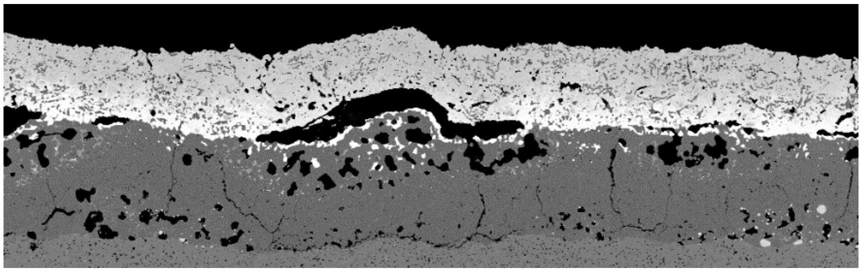

Figure 14: BSE-SEM micrograph of a high Si-modified mullite bondcoat with a TS REDS topcoat using a HT6 annealing heat treatment after 2700F/750cyc oxidation in 0.9 atm H_2O-0.1 atm O_2 showing the rapid oxidative consumption of the bondcoat and other microstructural defects.

GEA has measured oxidation rates for bondcoats with modified mullite matrix compositions versus oxygen partial pressure. The tests were conducted in a horizontal tube furnace with flowing gas with a 2700F-250hrs exposure. GEA notes of general risk of tube furnace contaminations in these high temperature oxidation experiments. The tests were conducted using two different oxygen concentrations, 1%O_2/Ar and 100% O_2, in the same tube furnace, so the oxygen pressure relationship can still be extracted, albeit with the concern of variable contamination altering the mechanism for oxygen permeability. The single-point parabolic rate constants for TGO formation at 2700F in 1%O_2/Ar versus 100% O_2 are on the order of ~0.04 mil^2/hr and ~0.052 mil^2/hr, respectively. These parabolic rate constants would give a value of ~0.054 for the exponent “n” for the $P(O_2)^n$ dependence.

The relatively rapid oxidation of bondcoat specimens with modified mullite matrix composition at 2700F and for 2800F/ dry air heat treatments suggest that oxygen permeability of the modified mullite matrix could be limiting the oxidation lifetime. Since the liquidus temperature and viscosity of pseudo-binary mullite-oxide systems are lower than fused silica [6], oxygen self-diffusion coefficients at 2700F could be much higher in these modified mullite due to propensity to formation of eutectic liquid-phases that may interact with other impurities or contaminants from raw materials, processing, or test furnace environments.

Similar experiments were conducted with architecture 1 (HfO_2/$HfSiO_4$) coating system, with $HfSiO_4$ intermediate layers. Apart from the microstructure after heat treatment, the high Si-modified mullite bondcoat with a $HfSiO_4$ topcoat has an oxidation life of <500hrs in 2700F 0.9atm H_2O-0.1 atm O_2, a significant performance debit for the program TRL-5 criteria.

3.1.1.5 Summary and next steps for bondcoat oxidation results

For the mullite-Si composite bondcoat, all bondcoats met the HyTEC TRL-4 metric of 250 cycles at 2700F/0.9 atm H_2O-0.1atm O_2 with additional retained oxidation life, GEA aimed to exceed the HyTEC TRL-5 steam oxidation requirements 1000 cycles at 2700F/0.9 atm H_2O-0.1atm O_2. Only one bondcoat composition met TRL-5 steam oxidation requirement. In initial screening that compared initial and optimized annealing heat treatment schedules, the optimized heat treatment yielded better Si retention after 1000 cycles at 2700F/0.9 atm H_2O-0.1atm O_2 (Figure 12). Therefore, the bondcoat composition with a HT3 heat treatment was promoted for coating architecture evaluations at TRL-5.

The initial assumption that the top/intermediate layers have no effect on bondcoat behavior is not always correct. For example, similar bondcoat compositions with modified mullite matrix composition have a much shorter oxidation life in architecture 2 with $HfSiO_4$ topcoat versus the REDS topcoats.

GEA has continued screening of other composition improvements of bondcoat composition modifications, specifically the SiO_2/Al_2O_3 ratio of the mullite matrix. Baseline coatings with excess SiO_2 do not seem to have statistically significant differences after HT3 the annealing heat treatment versus control samples. However, some of these coatings showed better oxidation life retention after 1000 cycles at 2700F/0.9 atm H_2O-0.1atm O_2 (Figure 15). Further validation of these potential improvements could be part of future work.

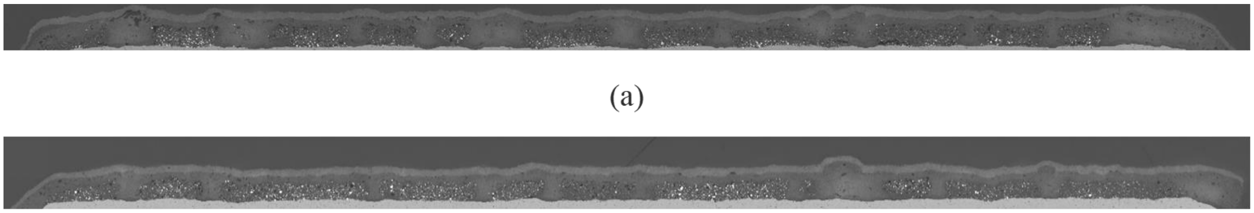

(a)

(b)

Figure 15: Optical mosaic micrographs comparing mullite- high Si /TS REDS coatings after 2700F/1000hrs oxidation in 0.9 atm H_2O-0.1 atm O_2 for (a) baseline system and (b) coating with alternative SiO_2-rich formulation.

GEA studied several bondcoat composition modifications, but these alternatives could not meet the more stringent TRL-5 requirements for oxidation life due to what appears to be contributions from eutectic liquid phases.

Finally, the discussion in this section has solely focused on bondcoat oxidation without consideration of other coating architecture requirements. The interactions between the composite bondcoat and the intermediate layer are a subject of further assessments under future architecture studies.

3.1.2 HTEBC outer layer compositions and architecture development

3.1.2.1 Preliminary evaluations of HTEBC architecture

The global architecture of GEA HTEBC system was introduced as a 3-layered system consisting of the composite bondcoat, intermediate layer and outer layer. Coating architecture refers to the design of a coating layer arrangement that satisfies the performance requirements of the intended mission. It is composed of the layer chemistry, microstructure, stacking sequence, thickness, and processing routes for a layered coating system. For the HyTEC program, a turbine engine operation with a CMC/EBC interface temperature of 2700F and maximum surface temperature of 3000F was set as the primary requirement. The assumed operating conditions are anticipated for an airfoil component such as a stage-1 nozzle. The total coating thickness was notionally set at 14mil to allow for the design the flexibility to utilize a substantial temperature drop for cooled components over a broader range of air-cooling budget.

The HTEBC architecture design followed the general philosophy that each layer protects the layer beneath it and the layers in contact remained thermo-chemically compatible at the required operating temperature ranges. The design roughly followed the GENII EBC architecture design, where the outer layer would serve as the primary recession barrier, the intermediate layer would serve as the barrier to water vapor diffusion, and the bondcoat would serve as a consumable oxygen barrier. Figure 16 shows the functional architecture of GEA HTEBC system with an additional barrier layer added between the composite bondcoat and the intermediate layer during the HyTEC program. This barrier layer is conceived to minimize reactions from the silicate TGO formed during oxidation of the composite bondcoat. The maximum coating life would nominally be set by the full consumption of the oxygen barrier function of the composite mullite-Si bondcoat as discussed and evaluated in detail in the previous sections.

Two GEA HTEBC Architectures 1, 2, and an early permutation of NASA Architecture 0 coating system are identified in section 2.2.1 (Figure *2*), and laid the foundation of the outer layer and architecture development efforts:

NASA Architecture 0: Mullite bondcoat / $HfSiO_4$ intermediate layer / HfO2 or TBD topcoat
GEA HTEBC Architecture 1: Mullite-Si bondcoat / $HfSiO_4$ intermediate layer / HfO_2 topcoat
GEA HTEBC Architecture 2: Mullite-Si bondcoat / REDS intermediate layer / REMS topcoat

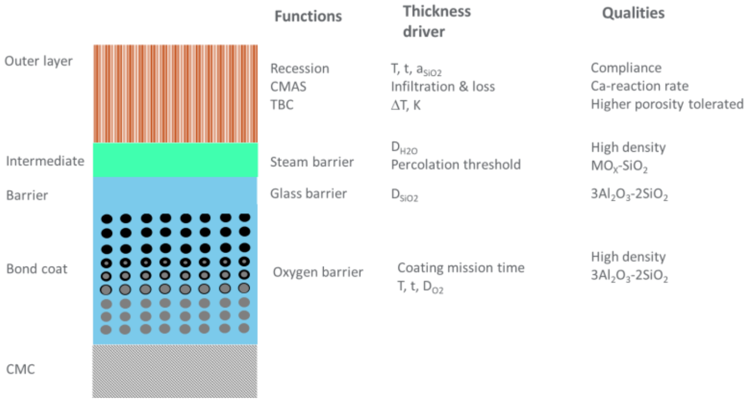

Figure 16: The GEA HTEBC concept is envisioned as three compatible layers working to perform specific functions.

Test coupons of these architectures were compared in a preliminary thermal gradient test (JETS). Architecture 0 performed well in the test but was thinner at only 6 mil. This prompted a series of evaluations of coatings within the Architecture 1 (hafnia-based) system to confirm the hypothesis that a thinner coating would naturally suffer less thermal strain-induced damage in the JETS test. However, the results did not clearly affirm the hypothesis. A study on Architectures 1 and 2 was thus commissioned to look at the interaction between the bondcoat and the upper layers with the annealing heat treat cycle to gage the thermo-chemical stability of the system. This study, referred to as “the architecture DoE” included cyclic steam test coupons as well to guide the architecture selection towards TRL-4 and TRL-5 objectives. The best candidates for Architectures 1 and 2 were chosen and coupons were fabricated to complete the technical program milestones of JETS and, subsequently, NASA QARE-rig testing of a subset of test architectures selected through the study. As discussed in the previous sections, because of higher temperature capability relative to the Architecture 2 system, Architecture 1 was chosen as the prime candidate for the TRL-5 airfoil test article fabrication for testing later in the program in the high-pressure combustor rig at NASA Glenn Research Center with Architecture 2 as a potential valuable second test candidate.

The first round JETS testing is summarized in Figure 17, which is a visual and flash IR comparison of the buttons. Architecture 0 did not spall, but the IR images show an increase in thermal conductivity consistent with pore elimination through sintering/densification of the porous mullite bondcoat layer. Architecture 1A showed coating spall at the bondcoat-hafnon interface between 500 and 600 cycles. Architecture 1B had the IR signature of a delamination at 500cycles but did not spall out to 1,000 test cycles. A cross-section sample prepared from this JETS button confirmed the delamination was between the bondcoat and intermediate layers. Architecture 2A with the TS-REDS upper layer spalled at the upper layer interface by 400cycles. Architecture 2B with the REDS non-spray upper layer also survived 1,000 cycles without coating spall but had a large delamination within the bondcoat. A coating layer delamination above the bondcoat-substrate interface passes the TPM requirement, but coating improvements would be needed and were implemented later in the program to address delamination in cyclic thermal gradient testing. Prior to these improvements a second JETS test campaign was designed to evaluate the effect of coating thickness as a potential reason to explain the difference between the architectures in the first-round testing.

While not part of the TRL exit criteria for HyTEC program, preliminary CMAS testing of HTEBC architecture was included in the program scope to collect some initial data on the responses of the material systems to CMAS threats. NASA Architecture 0 and early versions of GEA Architectures 1 and 2 were tested in the cyclical thermal gradient JETS test with CMAS dosing applied to the surface of the test buttons. These tests were conducted at 2800F surface temperature and resulted in early failures so a 2600F surface test was completed on Architectures 1 and 2 samples to bring the observations more in line with GENII EBC testing. Figure 18 summarizes the CMAS test results. At 2800F surface temperature, NASA Architecture 0 and GEA Architecture 2 with REDS non-spray layer lasted longest with 6 CMAS doses and 10 CMAS doses, respectively. The Architecture 1 samples failed in 4 doses at both the 2800F and 2600F surface temperatures. Cross-sectional analysis of the Architectures 1 and 2 samples revealed similar delamination behavior to the first JETS test, so the team decided not to pursue more CMAS testing at this stage of the development and focus on the cyclic thermal gradient and oxidation life requirements set in the program TPM.

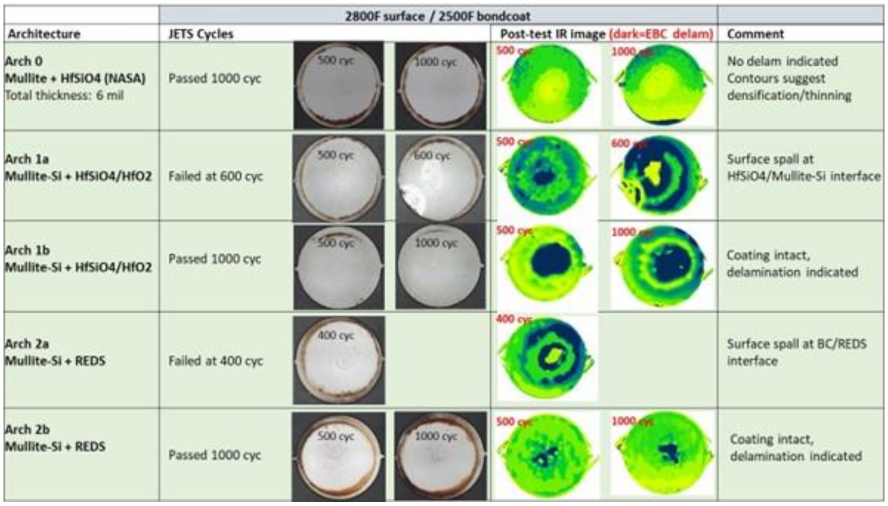

	2800F surface / 2500F bondcoat					
Architecture	JETS Cycles			Post-test IR image (dark=EBC delam)		Comment
Arch 0 **Mullite + HfSiO4 (NASA)** Total thickness: 6 mil	Passed 1000 cyc	500 cyc	1000 cyc	500 cyc	1000 cyc	No delam indicated Contours suggest densification/thinning
Arch 1a **Mullite-Si + HfSiO4/HfO2**	Failed at 600 cyc	500 cyc	600 cyc	500 cyc	600 cyc	Surface spall at HfSiO4/Mullite-Si interface
Arch 1b **Mullite-Si + HfSiO4/HfO2**	Passed 1000 cyc	500 cyc	1000 cyc	500 cyc	1000 cyc	Coating intact, delamination indicated
Arch 2a **Mullite-Si + REDS**	Failed at 400 cyc	400 cyc		400 cyc		Surface spall at BC/REDS interface
Arch 2b **Mullite-Si + REDS**	Passed 1000 cyc	500 cyc	1000 cyc	500 cyc	1000 cyc	Coating intact, delamination indicated

Figure 17: A summary of the JETS test for early Architectures 0, 1A, 1B, 2A, and 2B. The darker blue shades in the flash IR images are associated with a thermal interruption in the coating consistent with coating delamination.

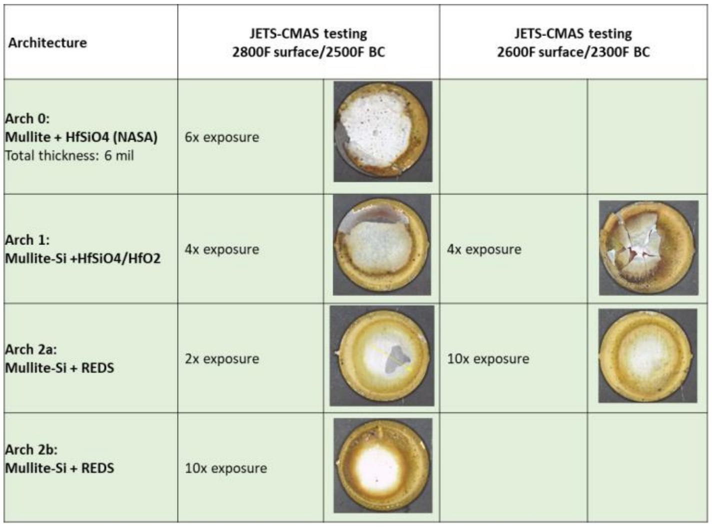

Architecture	JETS-CMAS testing 2800F surface/2500F BC		JETS-CMAS testing 2600F surface/2300F BC	
Arch 0: **Mullite + HfSiO4 (NASA)** Total thickness: 6 mil	6x exposure			
Arch 1: **Mullite-Si +HfSiO4/HfO2**	4x exposure		4x exposure	
Arch 2a: **Mullite-Si + REDS**	2x exposure		10x exposure	
Arch 2b: **Mullite-Si + REDS**	10x exposure			

Figure 18: A summary of the CMAS JETS performance for NASA Architecture 0 and GEA Architectures 1 and 2 at both 2600F and 2800F surface temperatures.

3.1.2.2 HTEBC Architecture refinement DoE

The Architecture DoE was a systematic exploration of interlayer compatibility in both the rare-earth silicate-based system, Architecture 2, and hafnium-oxide-based system, Architecture 1. At the outset it was decided to keep the two material systems distinct and separate for simple thermo-chemical compatibility reasons. For example, a hafnia outer layer on a REDS intermediate layer was not included in these investigations. The main factors considered in the Architecture DoE study are listed in Table 8 below.

Table 8: The factors and levels for the "Architecture DoE".

Factor	Levels
Bondcoat chemistry	(2) Baseline, ABC#4 (modified mullite matrix)
Intermediate layer chemistry	(4) TS REDS, REDS Non-spray, Spray $HfSiO_4$, Spray2 $HfSiO_4$
Outer layer	(4) No layer, REMS Non-spray, TS REMS, TS HfO_2
Annealing heat treatment	(7) None, 2700F/1hr, 2700F/10hrs, 2700F/100hrs, 2800F/1hr, 2800F/5hrs, 2800F/10hrs

Because the oxidation performance and the oxidation life of the composite mullite-Si bondcoat have significant impact on the durability of HTEBC architectures (as discussed in the previous sections) and because the thermo-chemical compatibility at the composite mullite-Si/intermediate layer drive long-term stability of the architecture, the main responses of the study were directed to:

- silicon content retained in the bondcoat,
- reaction (TGO) layer thickness, and
- derived figures of merit from the first two measures.

The architectures were then ranked based on their responses with the architectures showing signs of reduced oxidation ranked the highest. These measures were obtained from quantitative microstructural evaluations. Finally, a subset of test architectures was selected for cyclic steam to rank performance at 2700F and feasibility to meet both TRL-4 and TRL-5 exit criteria.

A total of 16 architectures were designed and each architecture was given an identification number 1 thru 16 for simplicity of tracking as listed in Table 9 below. The total thickness of HTEBC architecture was kept constant for this study.

A series of optical micrographs were obtained from the cross-section samples of the test coupons before and after the designated oxidation heat treatment exposure tests. The optical micrographs were converted into two basic quantitative metrics: the amount of reflective silicon (bright areas in the images) and the thickness of the layer formed by the mullite barrier layer plus the oxidized upper portion of the bondcoat, referred to as the TGO or the reaction layer thickness. The amount of retained silicon content was normalized to that of just the silicon containing area of the bondcoat thickness and the total bondcoat area.

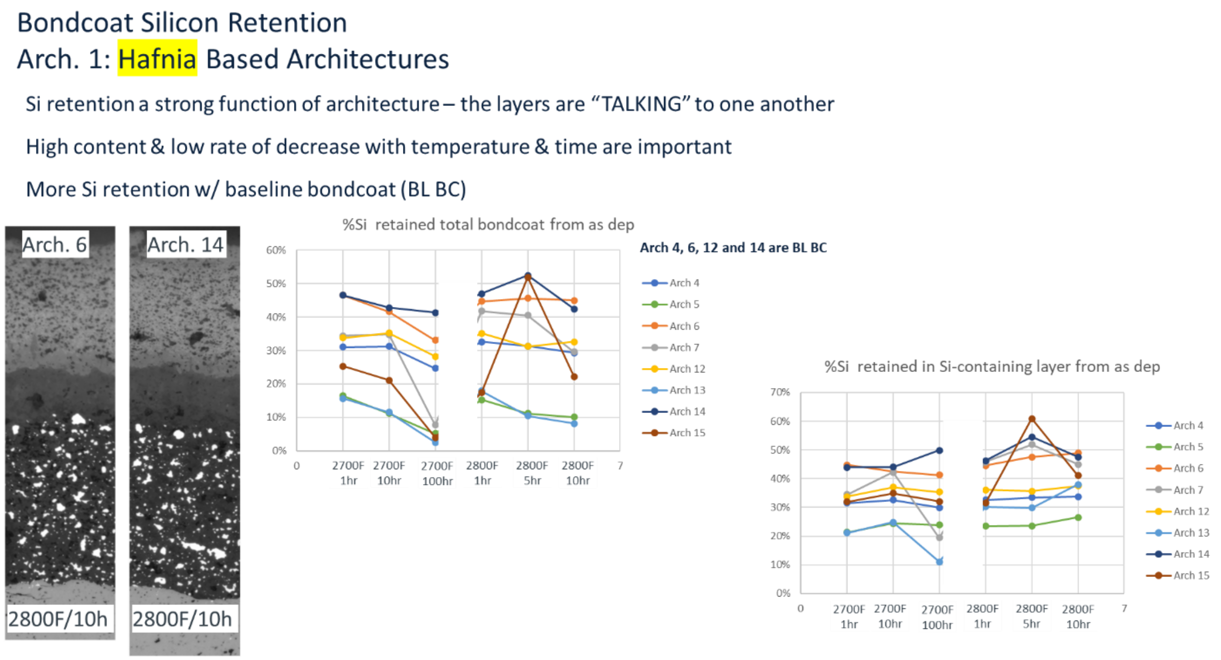

Bondcoat Silicon Retention

Arch. 1: Hafnia Based Architectures

Si retention a strong function of architecture – the layers are "TALKING" to one another

High content & low rate of decrease with temperature & time are important

More Si retention w/ baseline bondcoat (BL BC)

Figure 19: Silicon retention metrics for HTEBC Architecture-1 coatings.

Figure 19 shows example micrographs and the percentage of silicon retained normalized to the total deposited silicon content and normalized to the silicon content in the Si-containing layer. From these measures, GEA describes a figure of merit for the rate of silicon lost per unit time at both 2700F and 2800F. The initial silicon content should be identical for each of the bondcoat compositions, but these two metrics normalize the data against silicon content variation between samples. A clear trend emerges in both HTEBC Architecture-1 and HTEBC Architecture-2 derivative coatings, where the baseline composite mullite-Si bondcoat retains more silicon than the coupons with ABC#4 bondcoat. The primary difference between the two is that ABC#4 contains an oxide-doped mullite matrix formulation as used in the bondcoat oxidation studies that was discussed in the previous section. Clearly, and consistent with the results discussed in the previous section, the alteration of mullite matrix composition of the composite bondcoat had negative impacts on the oxidation performance at high temperatures.

A quantitative rating system was developed to analyze the Architecture DoE based on the silicon retention within the composite bondcoat layer. A figure-of-merit ranking was made for the 16 architecture variants (Labelled Arch 1 to 16) resulting an average ranking score as shown in Table 9. The right side of Table 9 arranges the variants by their average rank, where "1" is the best in category and "16" is the worst. Based on these evaluations and bondcoat oxidation kinetics discussed in the previous section, Arch 10, 14, 12 were selected for further considerations and evaluations.

Table 9: Calculated figure-of-merit scores and ranking of 16 test architectures.

	2700F slope (%Si retained per hour)	2700F1h Si retained	2800F slope (%Si retained per hour)	2800F1h Si retained
Arch 1	0.026%	53.235%	-1.803%	50.817%
Arch 2	-0.053%	41.794%	-0.960%	41.378%
Arch 3	-0.131%	31.828%	-2.190%	16.382%
Arch 4	-0.068%	31.068%	-0.359%	32.581%
Arch 5	-0.095%	16.443%	-0.562%	15.325%
Arch 6	-0.119%	46.531%	0.023%	44.739%
Arch 7	-0.282%	34.433%	-1.393%	41.781%
Arch 8	-0.039%	33.481%		28.273%
Arch 9	-0.142%	23.662%		25.582%
Arch 10	-0.029%	55.251%	-0.963%	48.250%
Arch 11	-0.072%	36.069%	7.534%	19.981%
Arch 12	-0.065%	33.751%	-0.252%	35.106%
Arch 13	-0.120%	15.635%	-1.055%	17.965%
Arch 14	-0.038%	46.525%	-0.570%	47.011%
Arch 15	-0.204%	25.277%	0.276%	17.384%
Arch 16	-0.107%	18.862%	-2.919%	32.548%

	Average Rank	ABC#4 (0) or Baseline (1)	RE or Hf
Arch 1	4.4	1	RE
Arch 10	4.6	1	RE
Arch 14	5.0	1	Hf
Arch 6	6.1	1	Hf
Arch 2	6.2	1	RE
Arch 12	6.3	1	Hf
Arch 8	6.3	1	RE
Arch 11	6.4	0	RE
Arch 4	7.3	1	Hf
Arch 5	10.0	0	Hf
Arch 13	10.1	0	Hf
Arch 7	10.5	0	Hf
Arch 15	10.8	0	Hf
Arch 16	11.6	0	RE
Arch 3	11.7	0	RE
Arch 9	12.0	0	RE

Cyclic steam testing of selected architectures followed the Architecture DoE to confirm the ability of the selected candidates to pass TRL-4 and ultimately TRL-5 exit criteria for oxidation life. Two versions of hafnon (Arch 12 and 14 from above) were tested to 1000 hours at 2700F in a 90%H_2O/10%O_2 atmosphere. The test results summarized graphically in Figure 20 and show that both coatings survived the test with remaining oxidation life in the composite mullite-Si bondcoat layer as indicated by retained silicon phase after the test (the bright phase in the optical cross-sections).

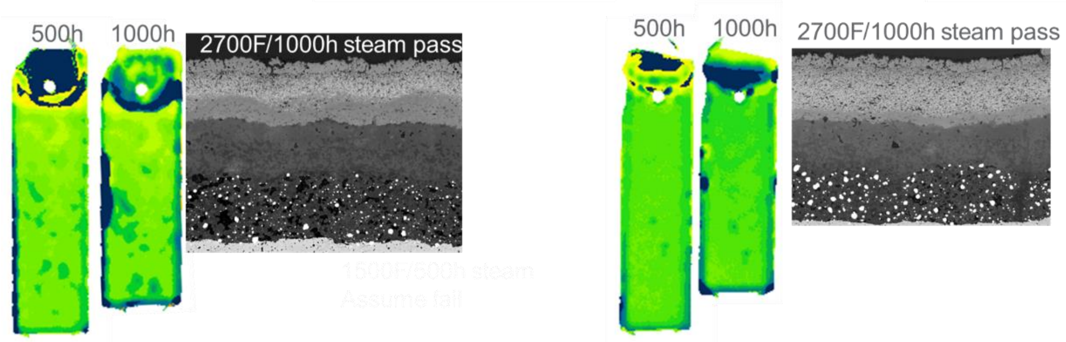

Figure 20: Cyclic steam test results of two HTEBC Architecture-1 variants at 2700F/1000hrs.

The coating on the left represents Arch 12 and the coating on the right represents Arch 14 selected based on the Architecture DoE results.

The HTEBC Architecture-2 based on rare-earth silicates also passed the TRL-4 and TRL-5 oxidation life criteria at 2700F/1000hrs 90%H2O/10%O2. The test results are summarized graphically in Figure 21. As can be seen, there is still retained silicon in the composite bondcoat layer after the test indicating residual bondcoat life although it is less than both HTEBC Architecture-1 coatings.

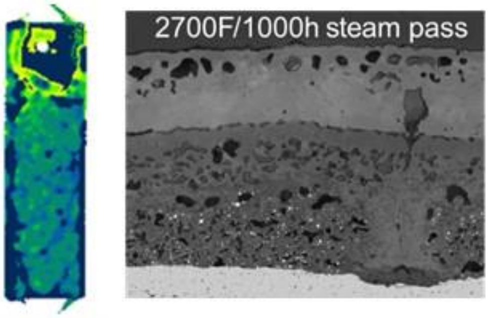

Figure 21: Cyclic steam test results and post-test appearance of HTEBC Architecture-2 after 2700F/1000hrs.

Upon successful completion of the steam tests, both Architectures 1A and 1B were ranked as candidates for potential application to airfoil test article for high-pressure combustor rig testing. To perform a final down selection between these two leading coating architecture options, another round of JETS test campaign at 3000F surface temperature / 2700F bondcoat was needed. While the main objective of this test campaign was to achieve TRL-5 exit of 1000 cycles of thermal gradient tests, it was decided that the test campaign should continue to specimen failure should any of the specimens pass the TRL-5 exit criteria. The intermittent inspections of the test buttons via flash IR and surface profile via Keyence microscope were used to monitor the conditions of the test specimens. Figure 22 shows the progression of the JETS test for two example buttons representing two different permutations of Architecture-1 system with the blended or graded transition between the mullite-Si composite and hafnon intermediate layer. The pictures shown are surface profile height maps collected from the two test buttons to discern surface uplift expressions at different cycle intervals throughout the test campaign.

As can be seen, both architectures passed the 1000 cycle thermal gradient TRL-5 exit criteria successfully and continued to 2000 cycles and beyond in the test campaign.

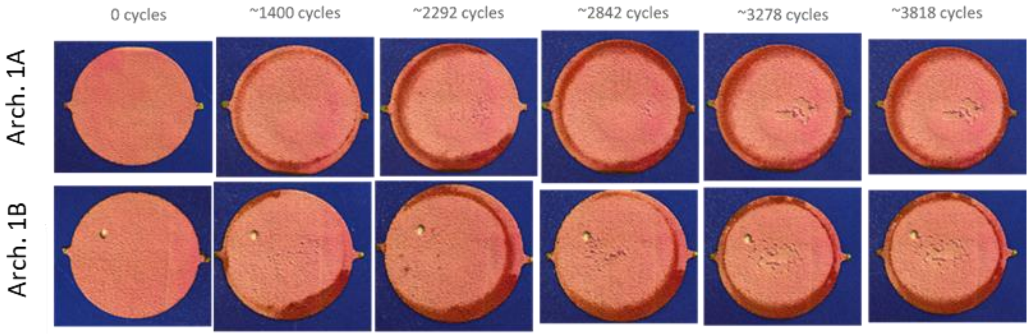

Figure 22: 3000F JETS test progression for architectures 1A and 1B. The images shown are surface height map profiles.

Based on this set of final test results, the team decided that Architecture 1A would best represent HTEBC Architecture-1 on the airfoil for the high-pressure combustor rig testing at NASA CE-5 rig test facility at the end of the program.

3.2 NASA HTEBC Architecture 0 Development

3.2.1 EBC Optimization

NASA Architecture 0 baseline EBC, a three-layer EBC comprising mullite bond coat (BC), $HfSiO_4$ intermediate coat (IC) and $Yb_2Si_2O_7$ topcoat (TC), was optimized to meet the HTEBC durability requirements. Steam cycling durability was the key metric used to assess the performance of EBC. The test condition was 2700F in 90% H_2O-10% O_2 with 1 hour hot and 1 hour cool cycling frequency.
The architecture 0 chemistry listed in Sections 3.2.1.1 through 3.2.1.4 of this report are based on work mentioned under [41], [42], [43], [44], [45] and [46].

3.2.1.1 Initial Optimization

The baseline Architecture 0 EBC system (mullite/$HfSiO_4$/$Yb_2Si_2O_7$) exhibited > 1000 hours life at 2600F (Figure 23a). It, however, generated excessive $Yb_2Si_2O_7$-mullite and $Yb_2Si_2O_7$-alumina eutectic products (eutectic point = 2732F or ~1500°C), leading to premature debonding at < 100 hours at the mullite/CMC interface (Figure 23b). Several rounds of modifications on sintering aid chemistry and concentration were conducted on the bond coat and intermediate coat (mullite and $HfSiO_4$) to mitigate the excessive eutectic reactions. The optimized mullite/$HfSiO_4$ EBC without $Yb_2Si_2O_7$ topcoat successfully completed 1000 hours testing with no spallation (Figure 24).

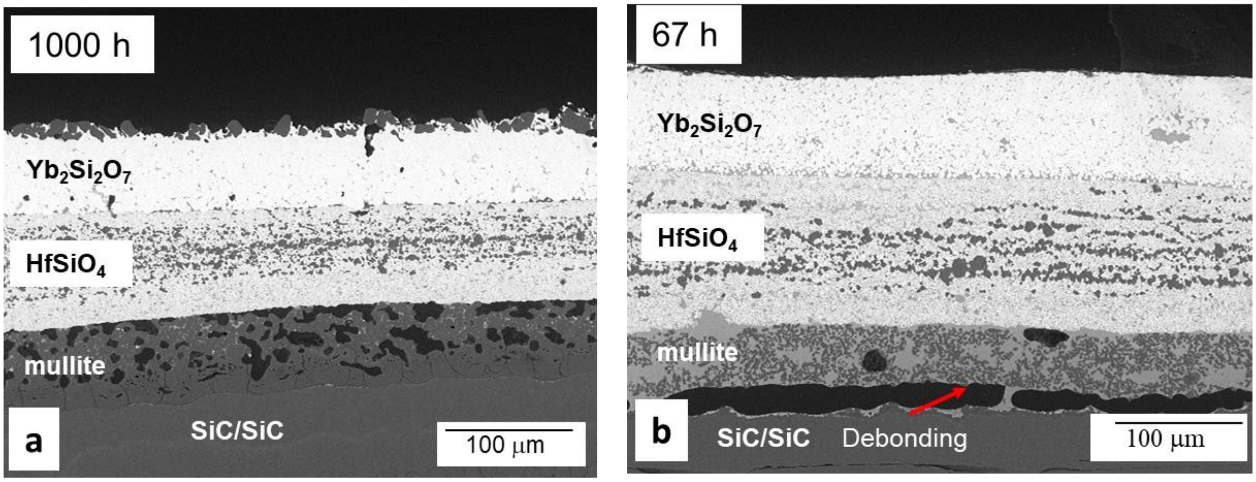

Figure 23: Baseline EBC exhibited >1000 hrs life at 2600F, while excessive Yb2Si2O7-mullite and $Yb_2Si_2O_7$-alumina eutectic reactions caused premature debonding at 2700F (a: 2600F; b: 2700F)

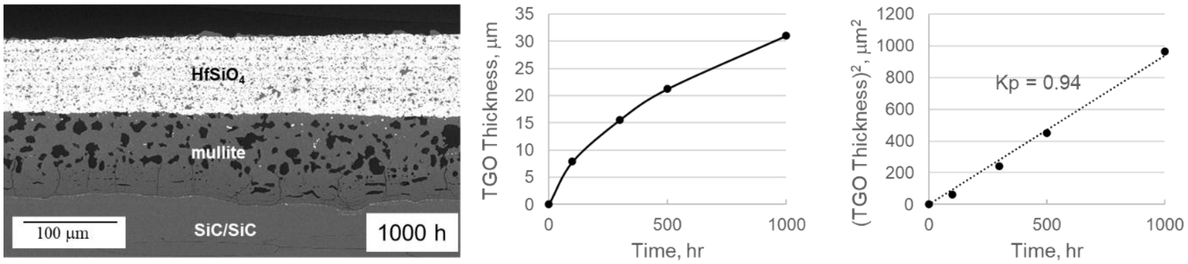

Figure 24: Modified mullite/ $HfSiO_4$ EBC without $Yb_2Si_2O_7$ topcoat exhibited >1000hrs life at 2700F with parabolic oxidation (rate constant (kp) = 0.94 mm2/h)

3.2.1.2 Alternative Topcoat Development

It was determined that the $Yb_2Si_2O_7$ topcoat is not viable at 2700F due to the low $Yb_2Si_2O_7$-(mullite, Al_2O_3) eutectic. $Sc_2Si_2O_7$ and HfO_2 were, therefore, chosen as alternative topcoat candidates (Figure 25).

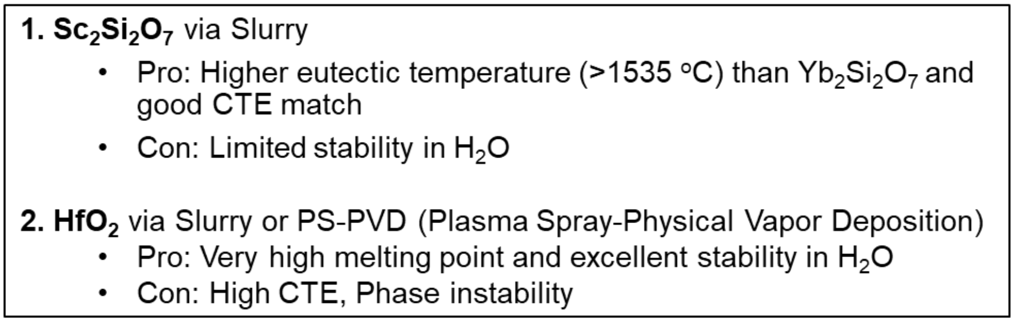
1. $Sc_2Si_2O_7$ via Slurry

- Pro: Higher eutectic temperature (>1535 °C) than $Yb_2Si_2O_7$ and good CTE match
- Con: Limited stability in H_2O

2. HfO_2 via Slurry or PS-PVD (Plasma Spray-Physical Vapor Deposition)

- Pro: Very high melting point and excellent stability in H_2O
- Con: High CTE, Phase instability

Figure 25: Alternative topcoat candidates and their pros and cons.

3.2.1.3 Slurry $Sc_2Si_2O_7$ Topcoat

$Sc_2Si_2O_7$ has a substantially higher eutectic temperature with mullite or alumina (> ~2800F or ~1535°C) compared to the $Yb_2Si_2O_7$ – (mullite or alumina) system (~2732F or ~1500°C). It also has a good match of CTE (coefficient of thermal expansion) with CMC, however, exhibits limited H_2O recession resistance at high temperatures. A slurry process was developed for $Sc_2Si_2O_7$ and an all slurry mullite/$HfSiO_4$/ $Sc_2Si_2O_7$ EBC successfully completed 1000 hours steam oxidation without spallation (Option 1 – Figure 26a). The $HfSiO_4$ layer was further optimized, and a transition layer was added at the $HfSiO_4$/ $Sc_2Si_2O_7$ interface to improve the durability under the HTEBC temperature gradient (2700F CMC-EBC interface / 3000F EBC surface) in QARE rig test described in the next section (Option 2 - Figure 26b).

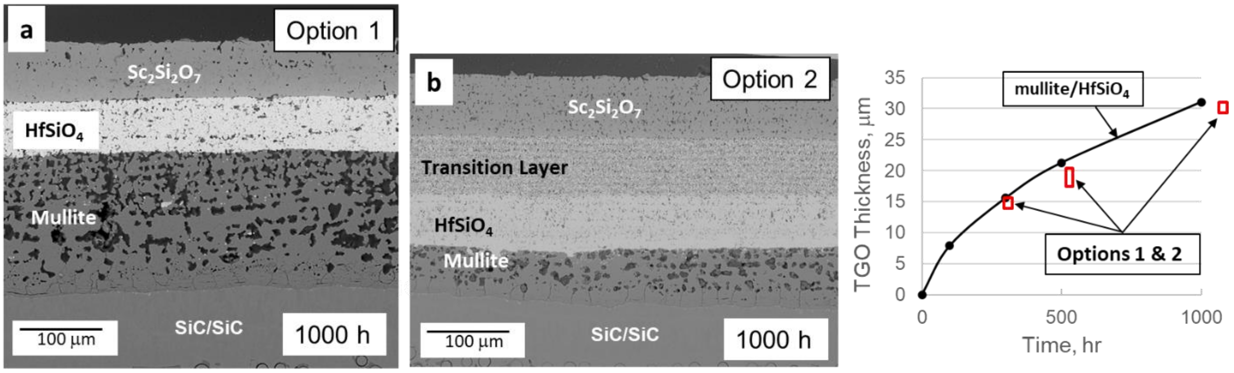

Figure 26: All slurry EBCs exhibited >1000 hrs life at 2700F with parabolic oxidation. *(a: mullite/$HfSiO_4$/$Sc_2Si_2O_7$ b: mullite/$HfSiO_4$/Transition Layer/$Sc_2Si_2O_7$)*

3.2.1.4 Slurry and PS-PVD HfO_2 topcoat

HfO2 has a very high melting point (~4997F or ~2758°C) and excellent recession resistance. The major drawback is the large CTE mismatch with CMC. Plasma Spray-Physical Vapor Deposition (PS-PVD) is a promising process because its pseudo columnar microstructure imparts high compliance to the coating, which mitigates the CTE mismatch stress. Slurry and PS-PVD processes were developed to deposit HfO2 topcoat. Undoped monoclinic HfO_2 was used to prevent low melting eutectic reactions between the dopants in stabilized HfO_2 and the other EBC layers.

For the slurry HfO_2 topcoat, $HfSiO_4$ + HfO_2 compositionally graded layers were deposited between $HfSiO_4$ and HfO_2 to mitigate the CTE mismatch. The all slurry mullite/$HfSiO_4$/HfO_2 EBC successfully completed 500 hours steam oxidation (Figure 27a). The slurry mullite/$HfSiO_4$ + PS-PVD HfO_2 EBC began to exhibit partial topcoat spallation at about 500 hours (Figure 27b). The PS-PVD HfO_2 topcoat spallation is attributed to the large CTE mismatch. Both slurry and PS-PVD HfO_2 topcoats gradually convert to $HfSiO_4$ over time due to the HfO_2-SiO_2 reaction. Further optimization is in progress to improve the chemical stability and EBC life.

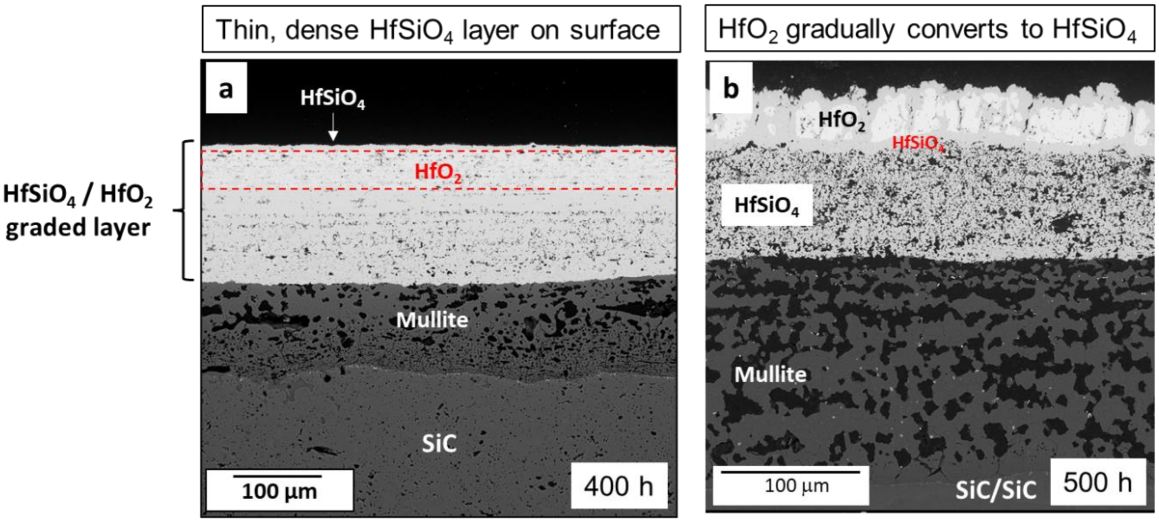

Figure 27: Mullite/$HfSiO_4$/HfO_2 EBCs exhibited ~500hrs life at 2700F *(a: Slurry HfO_2; b: PS-PVD HfO_2)*

3.2.2 JETS Test

The temperature profile for the JETS test was the same as the QARE rig test (2700F mullite/CMC interface and 3000F topcoat surface). The cycling frequency was 5 minute hot and 5 minute cool.

Two CMC samples coated with the same Architecture 0 EBC as the final QARE rig test EBC (mullite 2 / mod $HfSiO_4$ / Transition Layer / Sc_2Si_2O7) completed 1245 cycle JETS test with no spallation (Figure 28a and b). The coating maintained good bonding at all interfaces, except for a small (~2 mm long) debonding at the CMC/EBC interface in one sample (Figure 28b2). Some vertical cracks developed in the hot zone (Figure 28a and b), which are attributed to thermal stresses due to temperature gradient coupled with the high frequency cycling. Most cracks are arrested in the transition layer (Figure 28a), while some propagated to the mod $HfSiO_4$ or mullite 2 (Figure 28b). No cracks propagated into the CMC. Vertical cracks disappeared away from the hot zone. Recession at the topcoat surface in the form of a porous Sc2O3 layer, similar to the QARE rig test, was observed.

The architecture 0 chemistry listed in section 3.2.2 of this report are based on work mentioned under [41], [42], [43], [44], [45] and [46].

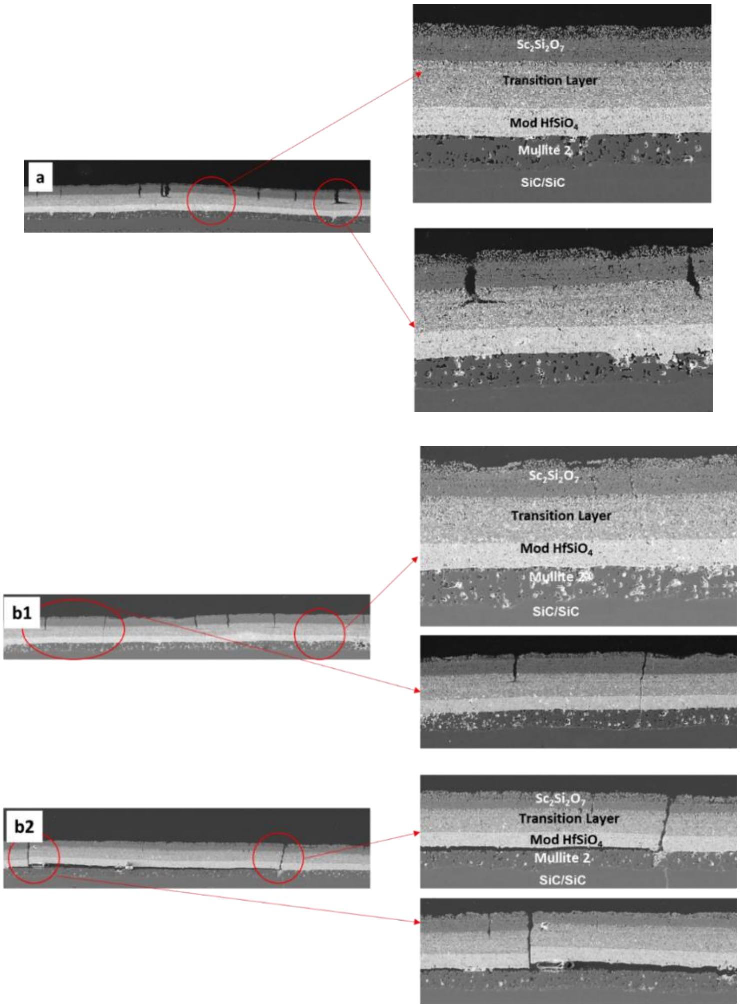

Figure 28: Mullite 2 / mod $HfSiO_4$ / Transition Layer / $Sc_2Si_2O_7$ EBC maintained good bonding at all interfaces after 1245 cycles, except for a small (~2 mm long) debonding at the CMC/EBC interface in Sample B. (a: Sample A; b1 & b2: Sample B)

3.2.3 Preliminary CE-5 Test

Mullite 2 / mod $HfSiO_4$ / Transition Layer / $Sc_2Si_2O_7$ EBC was fabricated on a NASA CVI-PIP Hybrid CMC airfoil and a GEA CVI Airfoil. The coated NASA CVI-PIP Hybrid CMC airfoil was tested for 9 hours in CE-5 to check the functionality of the newly designed test fixture prior to the HyTEC HTEBC EBC-coated GEA CVI airfoil testing. The target EBC surface temperature was 2800F, however, the actual temperature could not be confirmed. The EBC was intact visually after 9 hours with no signs of distress except for two small (~2 mm x 2 mm) spalls on the leading edge (Figure 29). Destructive post-test analysis will be performed to determine the cause of the spallation.

The architecture 0 chemistry listed in section 3.2.3 of this report are based on work mentioned under [41], [42], [43], [44], [45] and [46].

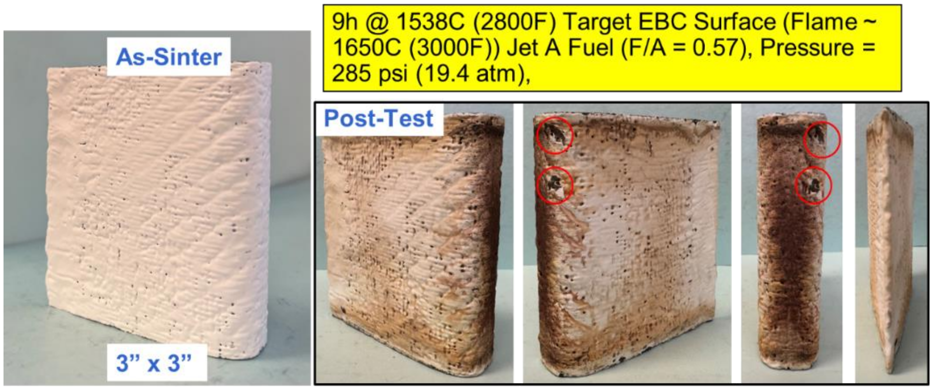
9h @ 1538C (2800F) Target EBC Surface (Flame ~ 1650C (3000F)) Jet A Fuel (F/A = 0.57), Pressure = 285 psi (19.4 atm),

Figure 29: Mullite 2 / mod $HfSiO_4$ / Transition Layer / $Sc_2Si_2O_7$ EBC showed no signs of distress except for two small (~2 mm x 2 mm) spalls on the leading edge after 9hrs CE-5 test

3.2.4 Summary

Table 10 summarizes the evolution of NASA Architecture 0 EBC and the highlights of test results throughout the project. All layers were processed via slurry except for the PS-PVD HfO2.

The architecture 0 chemistry listed in section 3.2.4 of this report are based on work mentioned under [41], [42], [43], [44], [45] and [46].

Table 10: Progression of NASA HTEBC Architecture 0 throughout the HyTEC program.

EBC	Highlights of Test Results
Baseline EBC (mullite/$HfSiO_4$/$Yb_2Si_2O_7$)	>1000hrs steam oxidation life at 2600F
Two-layer EBC (Mod mullite/$HfSiO_4$)	>1000hrs steam oxidation life at 2700F
Mod Mullite/$HfSiO_4$/$HfSiO_4$+HfO_2 Graded Layers/HfO_2	~500hrs steam oxidation life at 2700F
Mod Mullite/$HfSiO_4$/PS-PVD HfO_2	~500hrs steam oxidation life at 2700F; $HfSiO_4$/HfO_2 partial spall at ~100hrs QARE; Mullite remains at 250hrs QARE
Mullite 2/$HfSiO_4$/PS-PVD HfO_2	$HfSiO_4$/HfO_2 partial spall at ~100hrs QARE; Mullite remains at 250hrs QARE
Mullite 2/Mullite 3/$HfSiO_4$/PS-PVD HfO_2	$HfSiO_4$/HfO_2 partial spall at ~100hrs QARE; Mullite 2 and Mullite 3 remain at 250hrs QARE
Mullite 2/Mullite 3/$HfSiO_4$/$Sc_2Si_2O_7$/PS-PVD HfO_2	$HfSiO_4$/$Sc_2Si_2O_7$/HfO_2 partial spall after 100hrs; Mullite 2 and Mullite 3 remain at 250hrs QARE
Mullite 2/$HfSiO_4$/$Sc_2Si_2O_7$	>1000hrs steam oxidation life at 2700F
Mullite 2/Mod $HfSiO_4$/Transition Layer/ $Sc_2Si_2O_7$	>1000hrs steam oxidation life at 2700F No spall at 250hrs QARE; No spall at 1245 cycle JETS; Applied on CMC airfoils for CE-5

3.3 HTEBC fabrication on CMC airfoil test article

3.3.1 Process translation from flat coupon to shape

Coating deposition process adaptations, scaleup and validation trials are required to ensure quality translation of each coating process from a flat coupon to a shaped part. In the absence of the actual CVI CMC parts during the development phase, several surrogate test airfoil articles were fabricated using MI CMC with matching geometry to the CVI CMC test article. The translation and adaptation of the deposition processes from test coupons were performed in three parts: robot programming, coating thickness control, and microstructure evaluation.

A fixture was designed and fabricated to hold the dummy and test articles, Figure 30, and to be compatible with all the coating processes used in the translation to shape. Thermal spray modality coating layers are deposited using a torch mounted on a programmable robot arm. A robot program for each thermal spray coating layer is developed to produce a sufficiently uniform coating thickness and to reduce overspray over the shaped part.

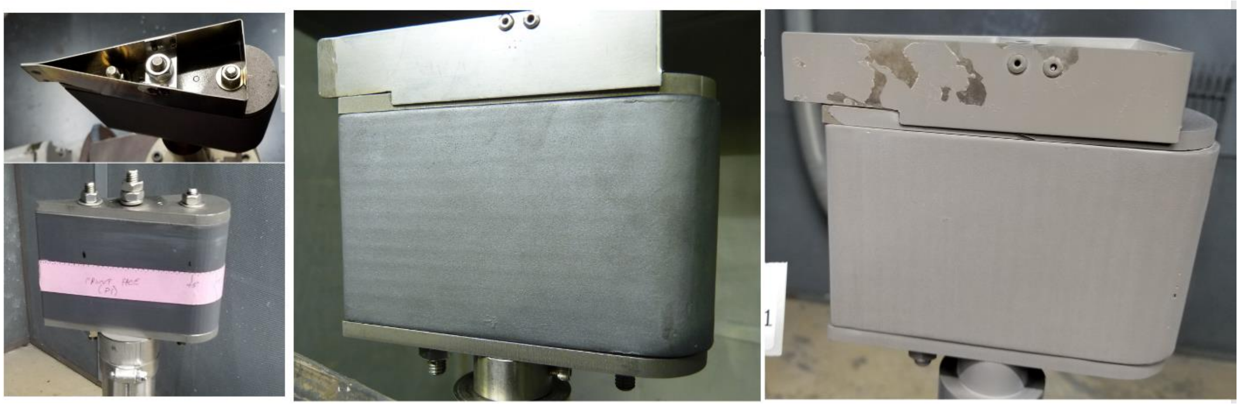

Figure 30: Airfoil coating fixturing and dummy airfoil before and after first coating run mounted in thermal spray fixturing.

The coating process and parameters associated with each coating layer of the two HTEBC systems, Architectur-1 and Architecture-2, were adapted successively to the part geometry. The coating layers were deposited onto the dummy articles at a thickness sufficient to be measured by a comparative analysis of the part. An ATOS Scanner with a 560 lens bluelight inspection system, Figure 31, was used to evaluate coating thickness. Part alignment utilized a fixture and same orientation for each scan. A standard scan was developed during the dummy article spray campaign to capture the largest area of the part without significant overlap. Significant overlap can result in data quality reduction due to averaging.

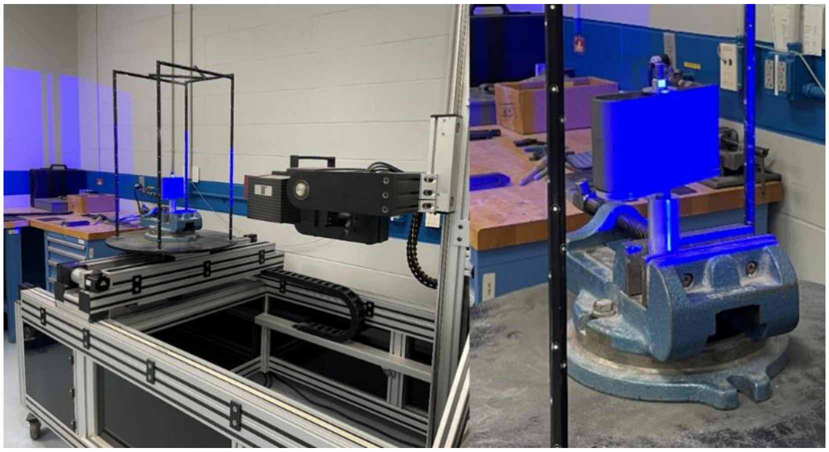

(a) (b)

Figure 31: Blue light setup for scanning airfoil parts. (a) Bluelight scanner and robot setup. The part is on a robotically controlled rotating turn table and the scanner is on robotically controlled arm that is able to move vertically and angle the camera. (b) Fixturing for airfoil bluelight scan to hold the airfoil in the same location securely and allow for uncoated regions of the part to be exposed for alignment to measure coating thickness in post processing.

Inspection software was used to inspect and report thickness measurement. Automated inspection and report template allowed more accurate analysis and rapid robot program iterations to adjust/adapt the robot program and indexing of the part to achieve uniform coating layer thickness around the part. Alignment of pre- and post-layer deposition was the key to enabling the method accuracy. Manual alignment was employed to reduce tilt between the two objects for comparison. The symmetry of the airfoil contributed to alignment challenges, a locator notch was thus added to the inside surface of the airfoil as a fiduciary marker to improve the alignments of subsequent scans after each coating layer or deposition iteration.

Coating thickness was measured by the difference in the pre-coating and post-coating blue light scans. Three analysis plane profiles were used to evaluate overall thickness with inspection points placed at 2 mm intervals, Figure 32. The first plane was 6 mm from top airfoil surface, the second plane was at the airfoil midplane and used as the most representative value, the third plane was 6 mm from the bottom of the airfoil. In addition to the three inspection planes, the entire mesh body was compared to identify major defects, Figure 33.

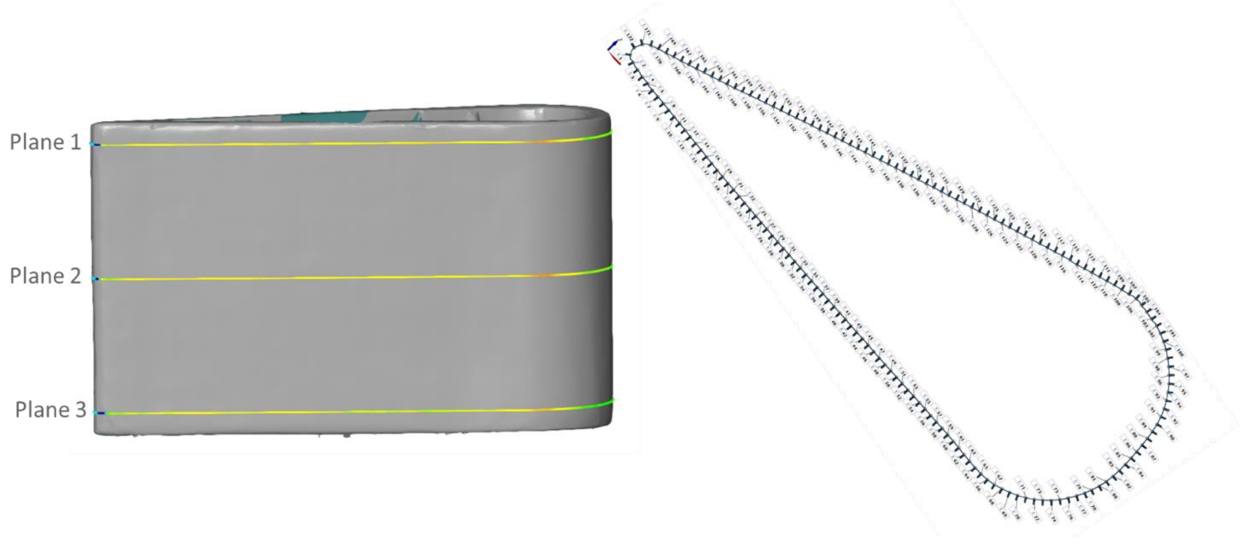

Figure 32: Bluelight inspection planes and inspection points for airfoil coating thickness evaluation.

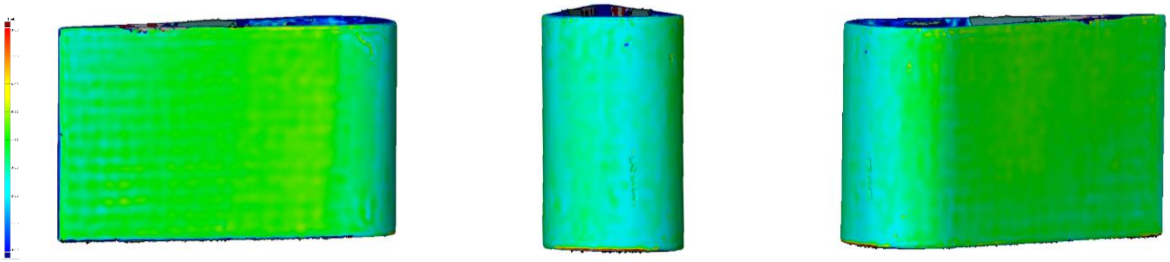

Figure 33: Example of bluelight mesh body inspection output.

The adaptation process of coating process for each of the different coating layers developed started from a similar base-coating robot program. The final version of these programs differed as different materials and deposition processes associated with a particular layer interacted with part shape differently.

Finally, a dummy airfoil article with CVI SiC skin, the optimized process for coating architecture and robot programming was produced to validate the process adaptation to shape using metallographic analysis. The key process translation metrics were coating thickness, thickness uniformity and microstructure quality attributes relative to the flat test coupons from the material and coating architecture development efforts.

3.3.1.1 Architecture 1 coating process adaptations to test article

Architecture 1 bondcoat was the first coating layer to be translated to shape. The robot program went through five revisions (designated R1 through R5) before meeting the desired coating thickness profile, shown in Figure *34*.

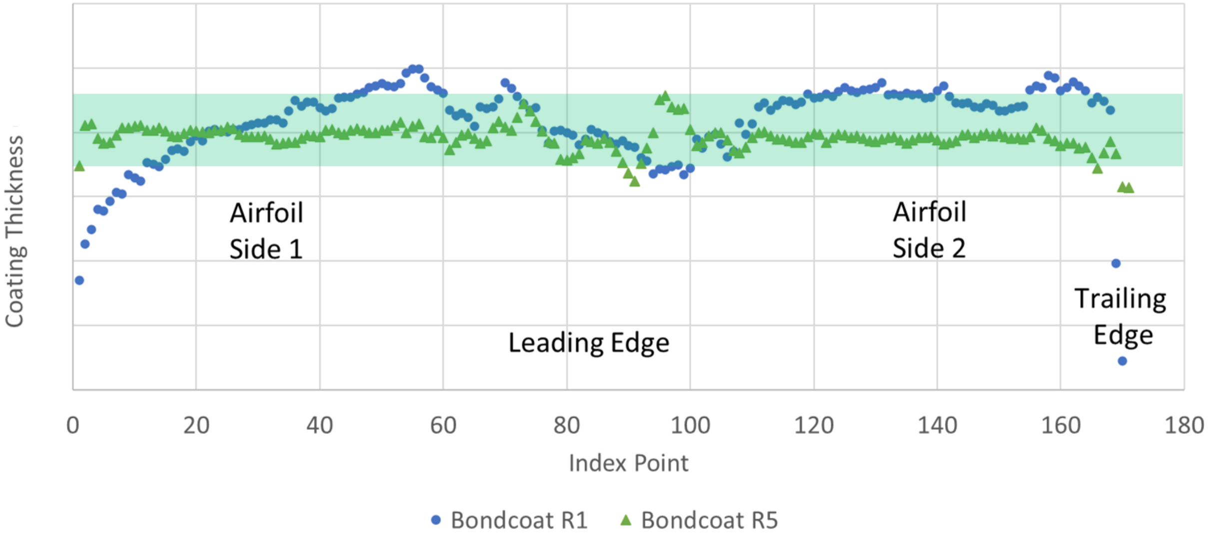

Figure 34: Coating thickness profile report for first and final bondcoat robot program development trials. Green region shows preliminary thickness control target. Note the improvement of coating uniformity over time.

The first Architecture-1 intermediate layer coating trial gave an unexpected result, where the deposition rate was found to be significantly lower along the curved leading edge, as shown in Figure 35. Iterative adjustments of the robot program produced a more uniform coating in three spray runs. Figure 35 compares the thickness profiles from the first and the third iterations of the deposition process.

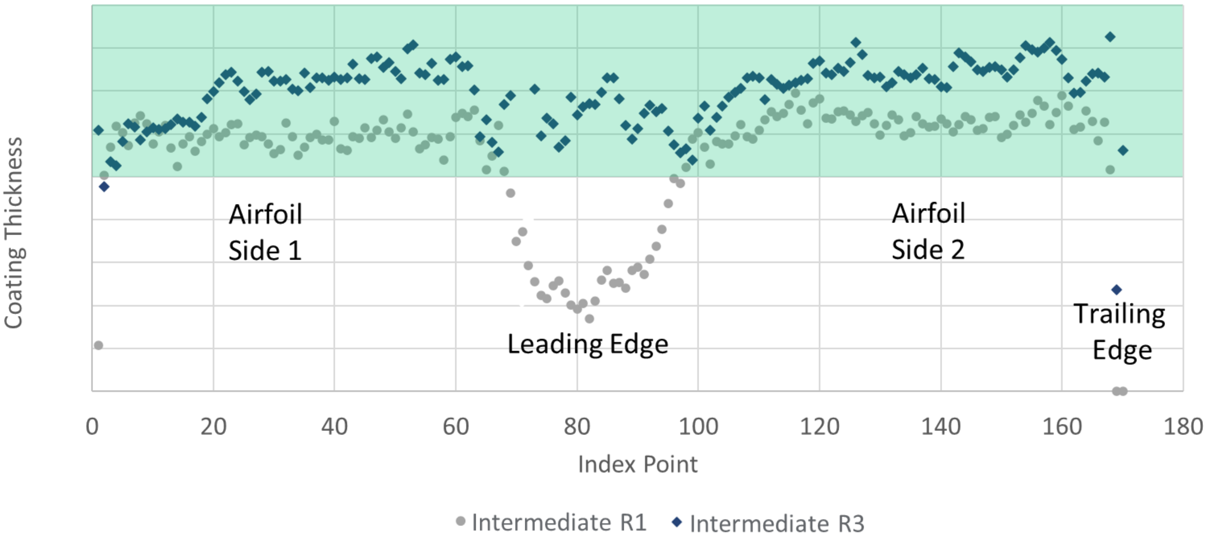

Figure 35: Intermediate layer coating trials to achieve uniform thickness initial (R1) and final (R3) Green region shows preliminary thickness control target.

The initial topcoat trial demonstrated ability to meet specifications, Figure 36. Subsequent topcoat layers were deposited with more coating passes to shift the average toward the upper specification limits.

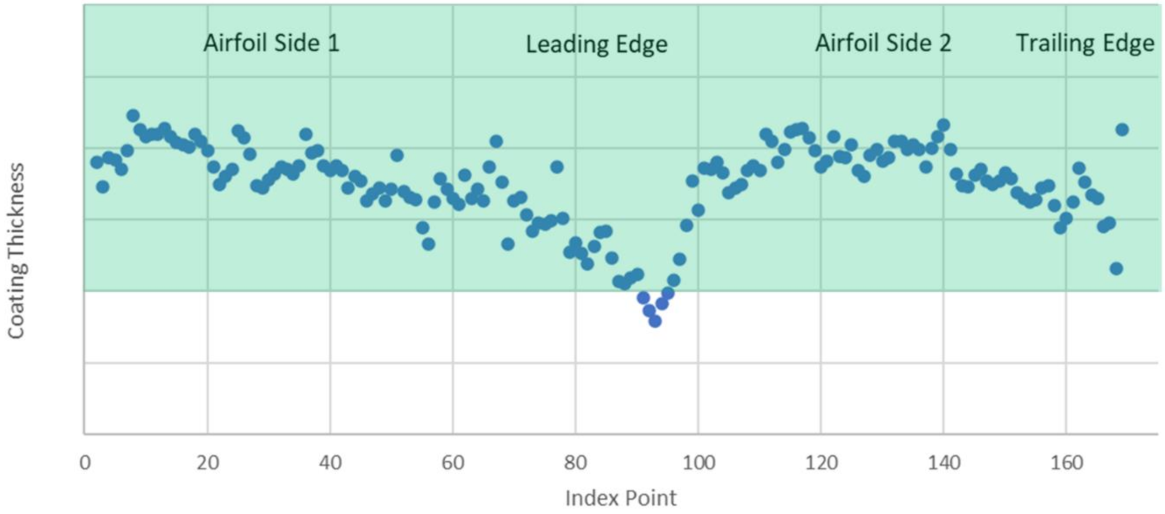

Figure 36: First topcoat layer coating trial on dummy airfoil Green region shows preliminary thickness control target.

3.3.2 Architecture 2 coating process translation to test article

The Architecture 2 coating process translation to part was performed after the completion of Architecture 1 test articles. The learnings from those deposition trials, including the composite mullite-Si bondcoat layer as a common layer between Architecture 1 and Architecture 2 systems, were similarly applicable and translated to these different layers in a more direct way due to increased experience with the component and thickness control strategies exercised with Architecture 1 test articles. The resulting coating architecture thickness control outcomes are shown in Figure 37.

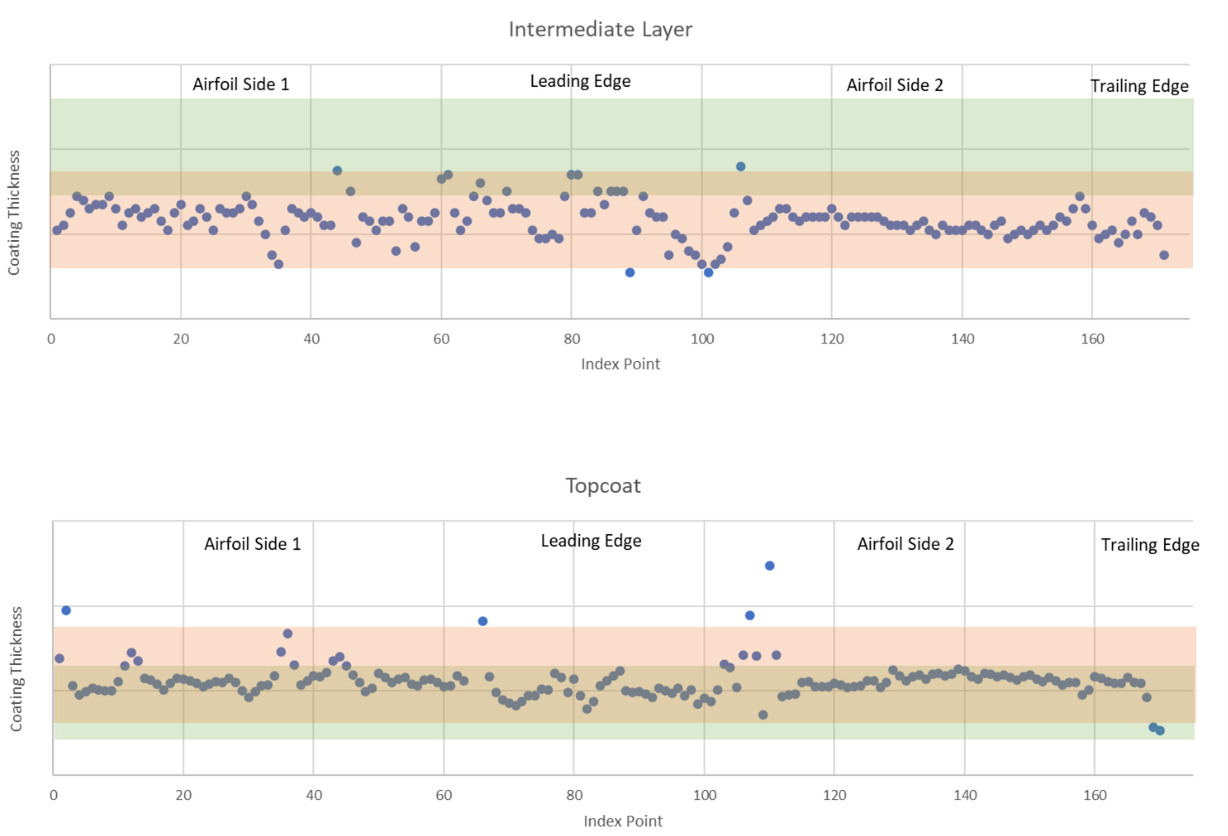

Figure 37: Architecture 2 intermediate layer and topcoat thickness evolution. The green region is the target thickness. The peach region is the shifted target region to account for changes in pass count.

3.3.3 HTEBC architecture applications to CVI CMC airfoil rig test articles

A total number of six CVI CMC airfoil test articles were delivered to the coating process. Based on program team discussions and plans for rig tests, two airfoil articles were designated per each of the three coating systems, Architecture 0 (NASA), GEA Architecture 1 and GEA Architecture 2. The test article fabrication plans called for a primary and a back-up test article for each HTEBC architecture. GEA team's primary focus was on HTEBC Architecture 1 as the primary candidate for TRL-5 rig testing and Architecture 2 as a runner up (rig test schedule and test resources permitting).

3.3.3.1 Part acceptance criteria

Using the experience from the dummy test articles GEA program team set the following acceptance criteria for the airfoil test articles with GEA HTEBC architectures:

- All coating layer thickness measurements and verifications by bluelight.
- EBC chipping and surface spalls during layer deposition and after the annealing heat treatment to be less than 0.5 inches in diameter or lateral dimensions. Identified by visual inspection.

3.3.3.2 Architecture 1 test article coating

CVI CMC airfoils 16282 and 16284 were selected as the primary and backup Architecture 1 test articles. The test articles were designated Architecture 1A (16282) and 1B (16284) for tracking purposes. Photographs for the Architecture 1 test articles are shown in Figure 38 and Figure 39.

Figure 38: Optical images of AF16282 pre-test, the primary Architecture 1 test article, Architecture 1A.

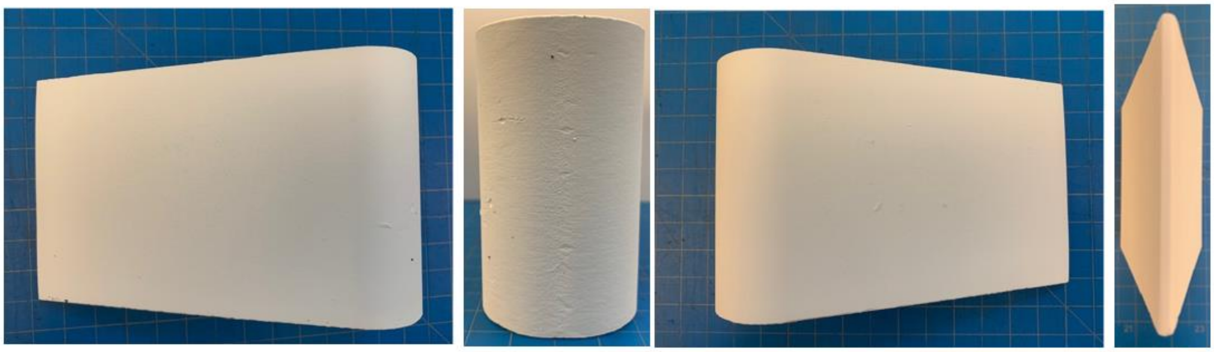

Figure 39: Optical images of AF16284. This is the backup Architecture 1 test article, Architecture 1B.

3.3.3.3 Architecture 2 test article coating

CVI CMC airfoils 16287 and 16285 were selected as the primary and backup Architecture 2 articles. The first application trial of Architecture 2 on airfoil 16285 ran into unexpected processing issues during the deposition of the bondcoat layer. The coating process was placed on hold, due to timing and spray cell resource availability, to resume at a later date and starting with airfoil article 16287, which was then designated as primary test article or Architecture 2A.

On resuming the coating production campaign, an improvement was made to surface preparation to the airfoil article 16287 based on experience and observations on airfoil 16285. The modified surface preparation process successfully yielded the coating Architecture 2A and was subsequently extended to airfoil 16285. Because of surface quality issues after striping the coating, the test article 16287 became the primary test article Architecture 2A and the article 16285 became the backup article Architecture 2B. Architecture 2 test articles photographs are shown in Figure 40 and Figure 41.

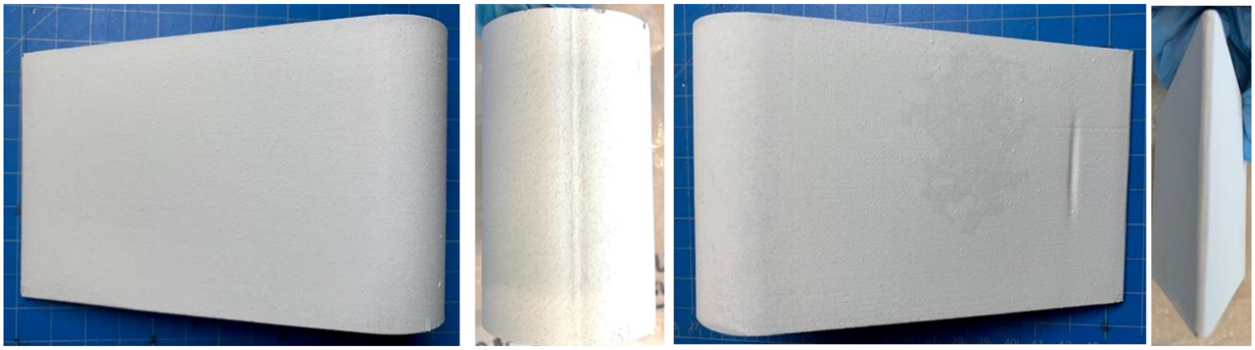

Figure 40: Architecture 2A primary test article, AF16827 pictures of final coating.

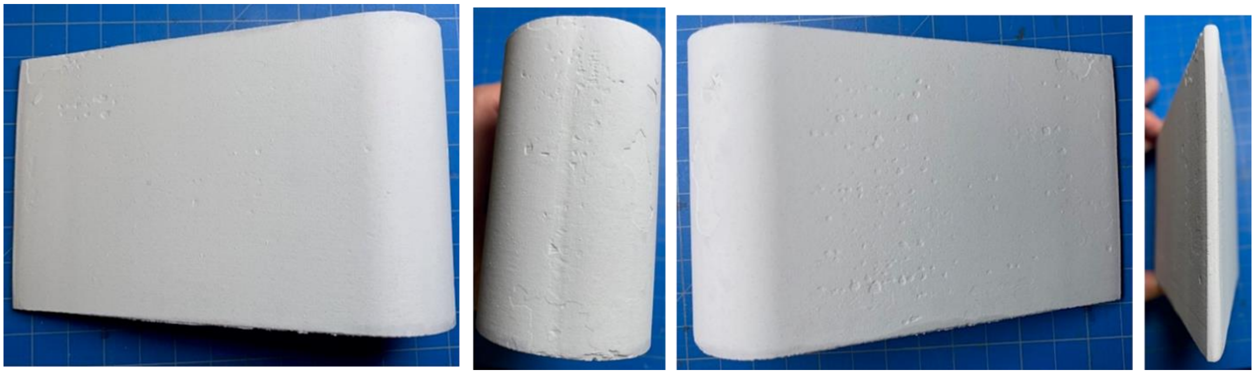

Figure 41: Architecture 2B backup test article AF16825 pictures of final coating.

4. HTEBC Demonstration

4.1 QARE Rig Testing for TRL 4

QARE rig test is a required test in the HyTEC program to qualify high temperature EBCs for TRL 4. It is also a tool that has been used to down select coatings for further development TRL-5. A total of 8 coatings have completed the test, the result helped to qualify both GEA's Architecture 1 and Architecture 2 coatings for TRL-5 tests. This report summarizes the test results from this campaign, emphasizing on the cut-up microstructure that gives information on the performance of the coatings. The test results only represent one aspect of the performance of the high temperature EBCs in question, for comprehensive understanding, reference to other reports, such as the reports on steam test performance and JETS thermal cyclic tests is recommended.

4.1.1 Introduction

QARE rig is a natural gas/oxygen (NG/O_2) burner rig that has been described in detail elsewhere [1], but a brief overview will be provided for this report. The burner can consume up to 700 SCFH (standard cubic feet per hour) of natural gas, and up to 1,500 SCFH of oxygen. A picture of the burner is displayed in Figure 42. An interchangeable selection of burner nozzles (3/4 inch, 1 inch and 1 ½ inches in diameter) can be used to produce flames with different diameters. The ¾'' diameter nozzle was chosen and used throughout this work. The hoses, solenoid valves, gas regulators, mass flow controllers, controls, check valves, and E-stops are integrated into the burner platform.

Figure 42: Natural gas/oxygen burner rig platform [1]

The rig has a pilot light to ignite and sense the flame. The natural gas and oxygen flow is closed off and the operator is alerted if no flame is detected. A programmable logic controller (PLC) (Allen-Bradley ®) is used to operate the burner and provides ignition, flame-out alarm, safety shutdown, and gas flow control. A Human Machine Interface (HMI) to enable additional operator control and monitoring of functions during both attended and unattended operation was developed. Wonderware Historian is used for data acquisition which includes recording of the rig operating conditions, alerts/alarms, and test specific data such as sample temperature from pyrometers.

The rig is integrated into the building natural gas supply for a continuous flow of fuel while the oxygen is supplied using an on-site oxygen generator system. The oxygen generating system supplies ~93% purity oxygen to the rig. The process of generating oxygen enriched air (~93% O_2 and ~7% N_2) begins by passing filtered, 110-psig shop air from the building supply through a refrigerated air dryer to remove water vapor. The dried air is transferred into a service air holding tank prior to being fed into the oxygen generators. Three OG-500 oxygen generators are then used to separate oxygen from the dried shop air. The oxygen enriched air is then stored in two holding tanks that are piped directly to the rig. The oxygen generator system provides an uninterrupted supply of oxygen that enables continuous (24/7) operation for long-term durability studies.

4.1.2 Experimental Procedure

The EBC/CMC samples tested in the NG/O_2 burner rig were 3 inches by 1 inch (length by width). The target samples were fixtured in a 3 inch by 3 inch holder with one CMC spacer on each side of the target sample. The target and CMC spacers were then held in place with a CMC clamp as shown in Figure 43. The EBC sample temperature was monitored using a long wavelength infrared (LWIR) pyrometer with a spectral range of 10.1 to 11 µm, and a LWIR thermal imaging camera with a spectral range of 9.7 to 11.2 µm. The backside, CMC surface, temperature was monitored using a two-color pyrometer with spectral bands of 0.7 to 1.1 µm and 1.0 to 1.1. µm. The target test duration for each sample was 250 hours. While testing was generally continuous, there were periodic shutdowns to clean the nozzle of carbon buildup.

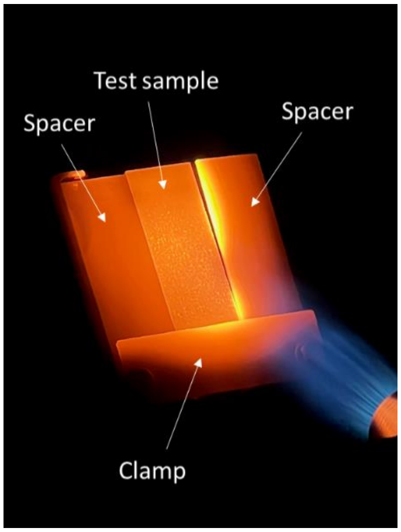

Figure 43: Sample fixturing for burner rig testing.

As an interim tool between conventional lab tests (steam and JETS) and the high-pressure burner rig test, NASA GRC QARE rig test plan is structured into the program TPM exit for TRL-4 to validate the performance capabilities of HTEBC architectures prior to down selection. The approach intended to gain additional maturity for selected HTEBC architectures toward TRL-5 testing to reduce both the performance and the program risks associated with coating performance on CMC airfoil test article evaluations in the high-pressure burner rig test at NASA CE-5. As an atmospheric burner rig, QARE rig test offers the capability to evaluate the candidate HTEBC architectures at relatively high gas flow rate compared to steam test yet combine both the thermal and the chemical gradient attributes associated with the high flow, high velocity of combustion gases to have a closer resemblance to the high-pressure combustor rig environment. Therefore, the test was deemed a valuable evaluation tool for down selected architectures and qualification path for TRL 4. The TPM set for TRLs is surviving 250 hours at surface temperature of 3000F and substrate temperature of 2700F. The criterion of survival was set to be less than 25% area exposure of the CMC substrate.

The QARE rig is adapted for burning pre-mixed natural gas as fuel oxygen, using a ¾ inch shower-head type nozzle. The size of a typical sample is 1 inch x 3 inch, fixed into a 3 inch x 3 inch picture frame with two pieces of 1 inch x 3 inch CVI-CMC as spacers. From front side of the sample, the temperature is monitored by an IR thermal imaging camera with long wavelength (10-11microns). Emissivity used is 0.97. On the back (CMC side), a dual wavelength (0.8 and 0.9micron wavelength) was used to monitor the CMC temperature Prescribed temperature and thermal gradient is achieved by adjusting torch flow and cooling flow (Figure 44).

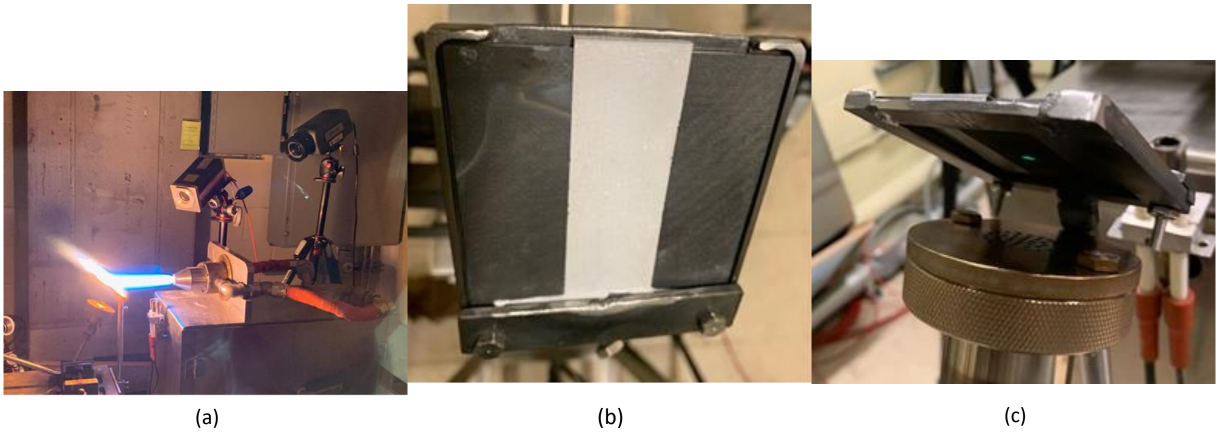

Figure 44: QARE rig test setup and burner configuration.
(a), and details of the specimen positioning using a metallic frame with CVI CMC spacers (b and c).

The flow conditions in QARE rig are not exactly measured or simulated in this program. From NASA Glenn's previous data, the maximum gas speed the samples are exposed to is about 0.3 Mach or ~100m/s. Averaged over a ¾ inch "hot zone" the gas speed is about 75m/s. The water vapor partial pressure is about 0.3 atm averaged over the "hot zone" (Figure 45).

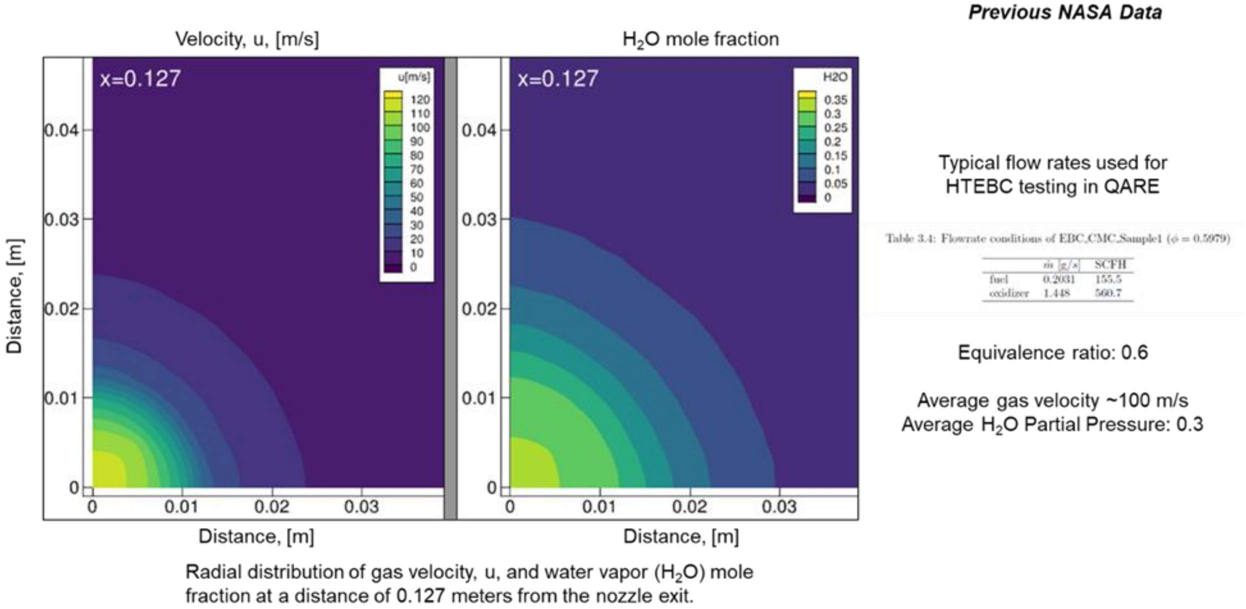

Previous NASA Data

Typical flow rates used for HTEBC testing in QARE

Table 3.4: Flowrate conditions of EBC_CMC_Sample1 ($\phi = 0.5979$)

	$\dot{m}$ [g/s]	SCFH
fuel	0.2031	155.5
oxidizer	1.448	560.7

Equivalence ratio: 0.6

Average gas velocity ~100 m/s
Average H_2O Partial Pressure: 0.3

Radial distribution of gas velocity, u, and water vapor (H_2O) mole fraction at a distance of 0.127 meters from the nozzle exit.

Figure 45: Gas flow rate and water vapor content for a typical QARE rig test condition from prior NASA internal program evaluations.

With NASA Glenn EBC and Facility team support, QARE rig test facility modifications to support 24/7 operation enhanced the availability and utilization of the test substantially. The updated QARE rig test facility enabled both GEA and NASA teams to run 250 hours test campaigns on a large number of test specimens under the HyTEC development efforts. A pool of GEA HTEBC architecture test specimens completed the QARE rig test. Only surface temperature of the EBC and the back side temperature of the CMC were prescribed and measured. All the internal interface temperatures were calculated with a 1D thermal conduction model.

The same nominal test temperature conditions were defined for QARE rig tests as for JETS, with HTEBC target surface temperature of 3000F and bondcoat/CMC interface temperature 2700F.

24 hr

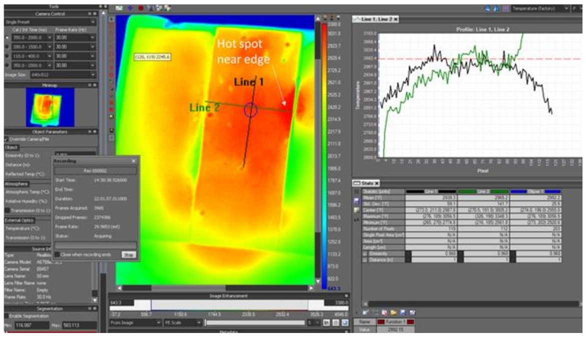

49 hr

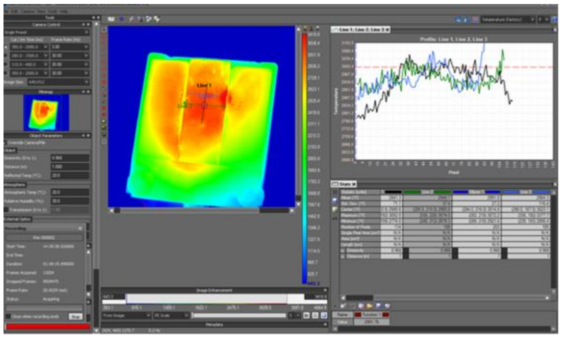

74 hr

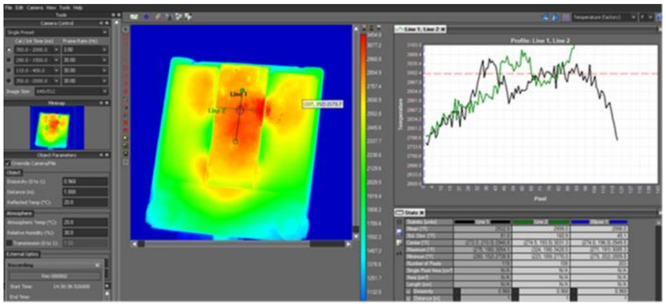

96 hr

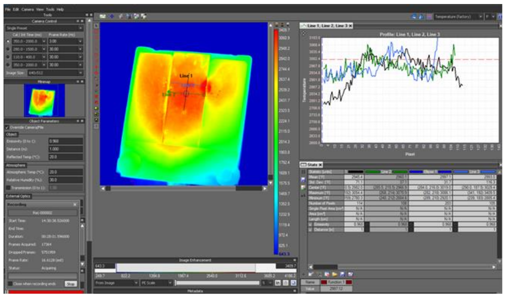

250hr

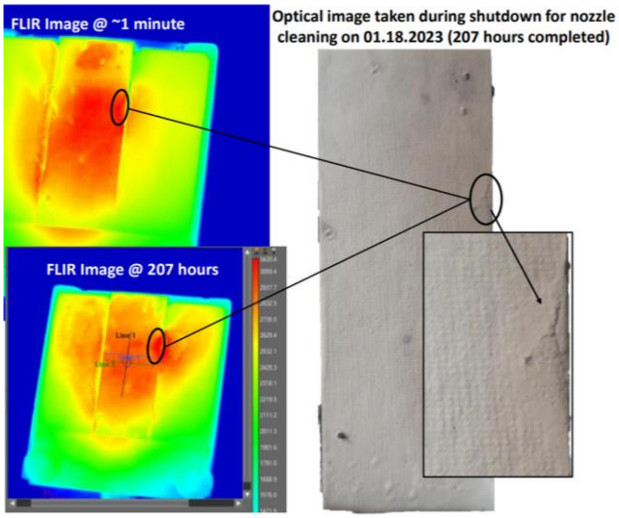

Example of concurrent thermal map capturing in QARE rig test

Figure 46: Example of QARE rig test campaign at nominal surface temperature of 3000F and IR camera monitoring of the test coupon front surface temperature profile.

4.1.3 Results from Architecture 1 and 2

A tabulated summary of the test results and final appearance of the test coupons from QARE rig test campaigns are shown in Figure 47 (HTEBC architectures test coupons described in Figure 47), after completion of 250 hours tests.

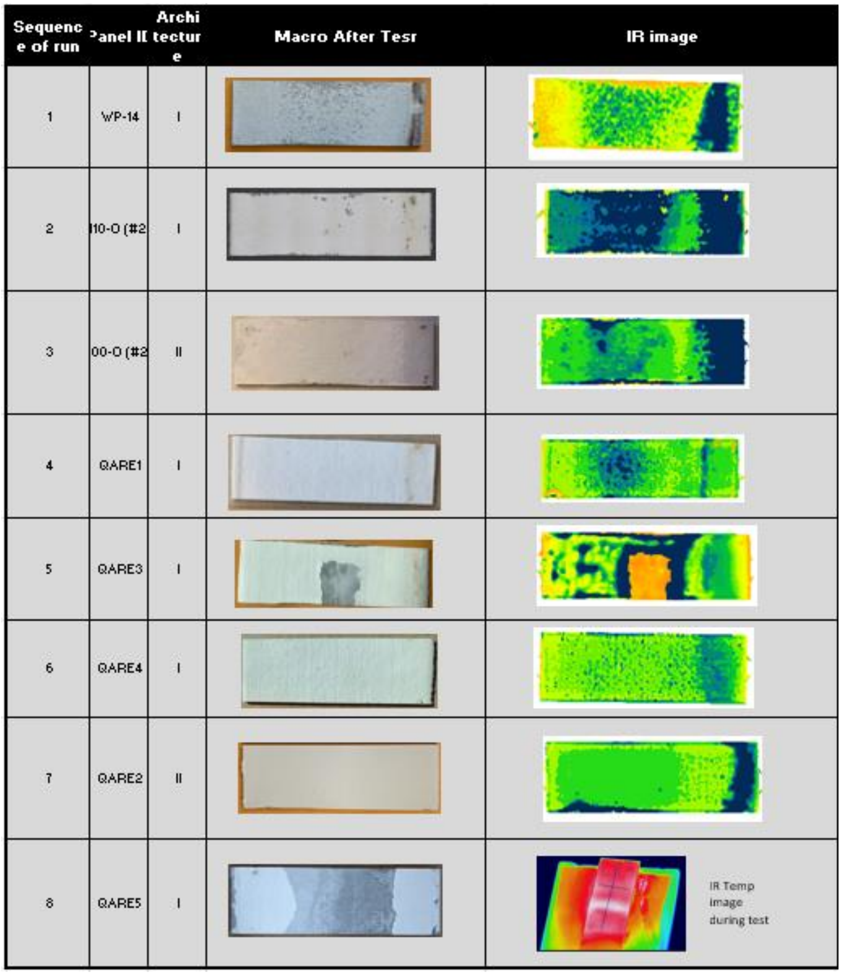

Sequence of run	Panel II	Architecture	Macro After Test	IR image
1	WP-14	I		
2	10-0 (#2	I		
3	00-0 (#2	II		
4	QARE1	I		
5	QARE3	I		
6	QARE4	I		
7	QARE2	II		
8	QARE5	I		IR Temp image during test

Figure 47: Summary of QARE rig test results and post-test appearance of the HTEBC test coupons.

Applying the criterion set forth by program TPM, namely less than 25% of exposure of CMC substrate, all of the samples are considered passed the test. There are two samples, however, that show macroscopic spallations, QARE 3 and QARE 5. Both of these are from Architecture 1 (Hf-oxide material system) based architectures. QARE 3 shows sign of distress (hot spot in IR image indicates delamination) at about 160-170 hours into the test, while QARE 5 developed a crack across the coating at a re-start event 237 hours into the test. The spallation occurs at the interface between the bondcoat and the upper layers, consistent with prior observation in JETS tests, with no direct exposure of CMC substrate. Due to the apparent stability issues of the upper layers, these samples need further development. It should be noted that IR images do point to sub-surface indications as interpreted from darker color map (higher thermal resistance), although the rest of the samples maintained their overall integrity. Most of the samples appear to experience different degrees of subsurface distress as a result of the 250hrs-3000F test campaign. The nature of the distresses appears to vary with coatings of different architectural features.

4.1.3.1 Baseline coating

Specimen WP-14 is a baseline coating representative of HTEBC architecture. This coating serves as the baseline architecture, from which HyTEC development of Architecture 1 coating systems proceed.

A cross section of the sample was made along the middle sample longitudinally, and the low magnification image is shown Figure 48, along with the zoom-in of the hot section. Consistent with the macroscopic observation, some of the HfO2 top layer flakes off along the interface with the bondcoat. Periodically vertical cracks run through the thickness of the coating, this is expected considering the CTE mismatch of the coating with the CMC substrate.

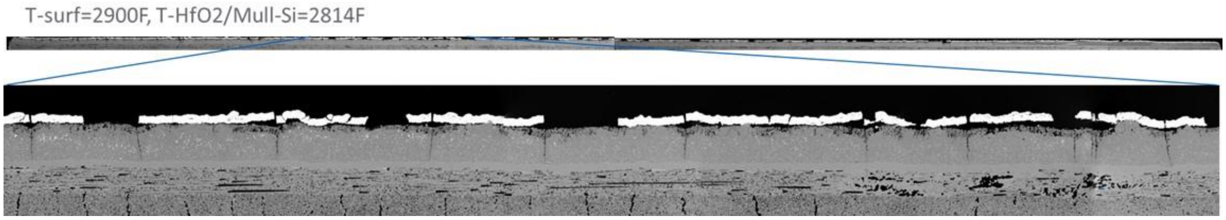

Figure 48: Low magnification SEM montage of the cross-section of test specimen WP-14

4.1.3.2 Architecture I (Bondcoat/$HfSiO_4$/HfO_2) specimens

SPECIMEN 110-O

This test specimen is a coating featuring GEA's baseline bondcoat system with a mullite barrier layer, with GEA's thermally sprayed hafnon intermediate layer, and NASA's PS-PVD hafnia top layer. This top layer, as compared to GEA's thermal sprayed hafnia top layer of similar thickness, shows a higher tendency to locally spall off during the test, as shown Figure 49. The depth of the spallation indicated local removal of both the PSPVD hafnia top layer along with the hafnon intermediate layer. The reason for this is not entirely clear, but due to this tendency of aggravated spallation, this coating architecture was given a lower rank compared to the rest of the GEA Architecture 1 coatings.

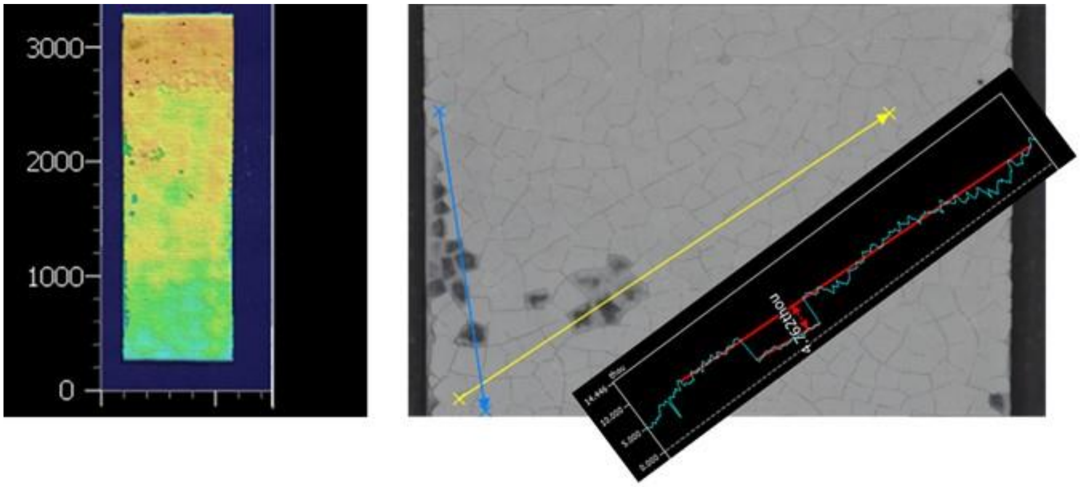

Figure 49: Keyence profilometry of locally spalled PS-PVD hafnia top layer along with hafnia intermediate layer after QARE rig test in sample 110-O

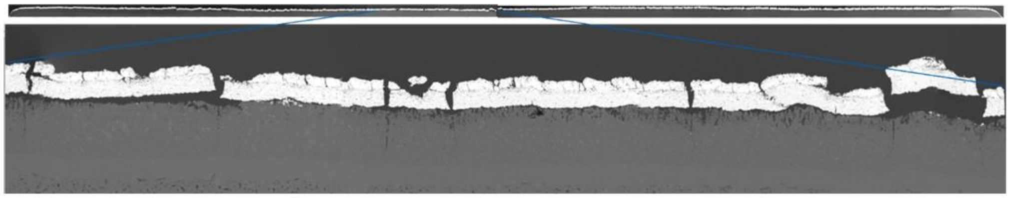

Figure 50: Cross section of 110-O Overall microstructure of hot zone,

The cross-section of the hot zone (Figure 50) confirms the tendency of this coating to delaminate along the interface between the bondcoat (the barrier layer included) and the intermediate layer, in agreement with the Keyence measurements. The TGO (including the barrier layer), is about 2-3 mils thick.

QARE 1

QARE 1 is in many attributes similar to 110-O, the only apparent difference between these two is that the top layer is GEA “columnar” hafnia instead of NASA PS-PVD hafnia. QARE 1 survived QARE rig test without local spallation. It is the comparison between QARE 1 and 110-O that led to the selection of hafnia as the go-to top layer. Aside from that the basic features of these two samples are quite similar. In this section more emphasis will be given to the details of the microstructure.

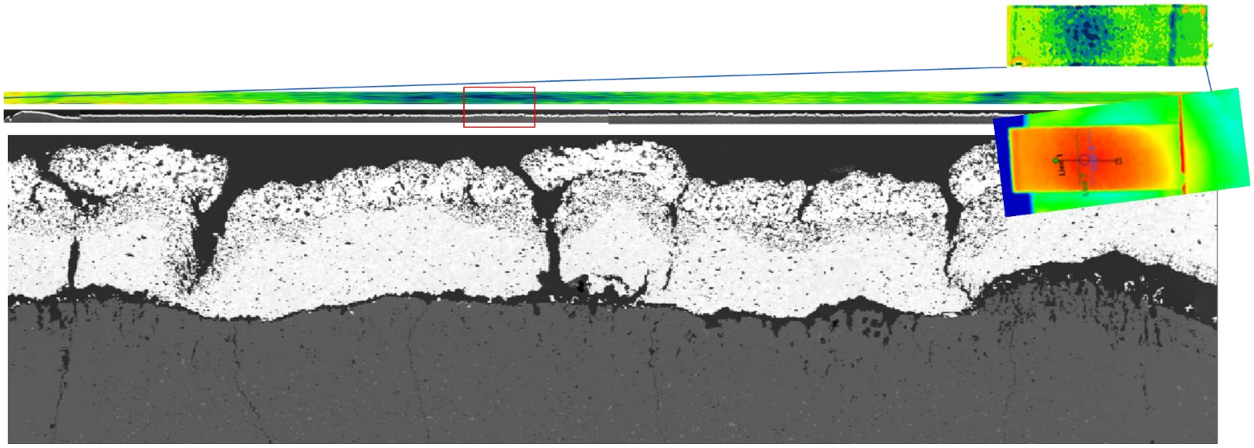

Figure 51: Cross section of QARE 1 showing its overall integrity after test and hot zone microstructure.

The cross section shown in Figure 51, again, reveals that the interface between the hafnon intermediate layer and the bondcoat is the primary location for delamination.

QARE 3 AND QARE 4

QARE 3 and QARE 4 are two Architecture 1 samples designed for side-by-side comparisons between two varieties of GEA proprietary hafnon compositions (denoted at Hafnon A and Hafnon B) to determine which type possessed higher resistance to microvoiding. Thus, the coatings were designed to have no deposited HfO_2 top layer and formed HfO_2 in-situ by volatilization of silica from hafnon. Furthermore, the temperature gradient was controlled in a way that there is identical gradient across the hafnon layers.

Due to an unexpected spallation event in one of the coatings (QARE 3), the goal of comparing microvoiding resistance between QARE 3 and QARE 4 was not reached. However, the remaining coating still provided a qualitative comparison between the two hafnon compositions. QARE 3 with Hafnon A, microvoids to a thickness about twice of that of QARE 4 with Hafnon B. Therefore, purely from microvoiding point of view, Hafnon-B is superior.

QARE 5

QARE 5 features the bondcoat with modified mullite matrix composition, ABC#4. The oxidation behavior of this bondcoat is still under development. The JETS test results had shown interfacial delamination with this modified bondcoat composition. A similar behavior was anticipated for this specimen hence no surprise to observe spallation of the upper layers during QARE rig test.

The hot zone microstructure is shown in Figure 52. The interface between the bondcoat and the hafnon intermediate layer is very porous, which is one of the reasons this interface has much stronger tendency to delaminate. Therefore, in order for this coating architecture to better survive the test condition, the quality of the interface has to be improved.

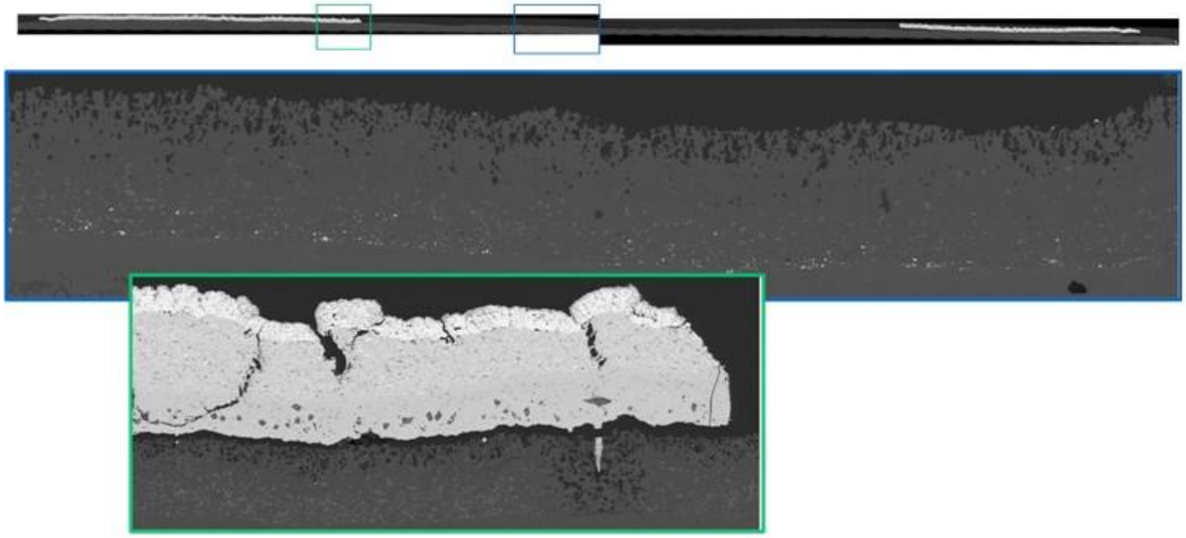

Figure 52: Hot zone microstructure of QARE 5. The porous structure at the top of the bondcoat is not oxyhydroxide dendrites, it is porous mullite.

4.1.3.3 Architecture 2 coatings (Bondcoat/REDS/REMS) specimens

Two coating samples from the Architecture 2 family were subjected to QARE rig test, 100-O and QARE 2. Both coatings feature the GEA standard HyTEC bondcoat with a barrier layer. The only difference is that 100-O has only a REDS upper layer, while QARE 2 has an additional REMS layer on top of the REDS layer to boost its resistance to water vapor attack. From previous studies, it is known that REDS volatilization in water-vapor atmosphere yields a highly porous layer of RE oxide instead of REMS, in contrast to other REDS systems.

100-O

Representative microstructure at lower mag, of areas experienced temperature in the 2700-3000F, is shown in Figure 53. At the hottest spot (Point A), the microstructure is dominated by two features: (1) Significant microvoiding of REDS to create a rather porous surface; (2) larger voids form in the REDS layer, very close to, but not exactly at, its interface with the bondcoat. The larger voids connect with each other, threatening to form a delamination slightly above the bondcoat/REDS interface. When surface temperature drops to about 2900F (Point B), the formation of large voids stopped. At 2700F location (Point C), the voided TGO layer thickness is actually thicker than that at point A.

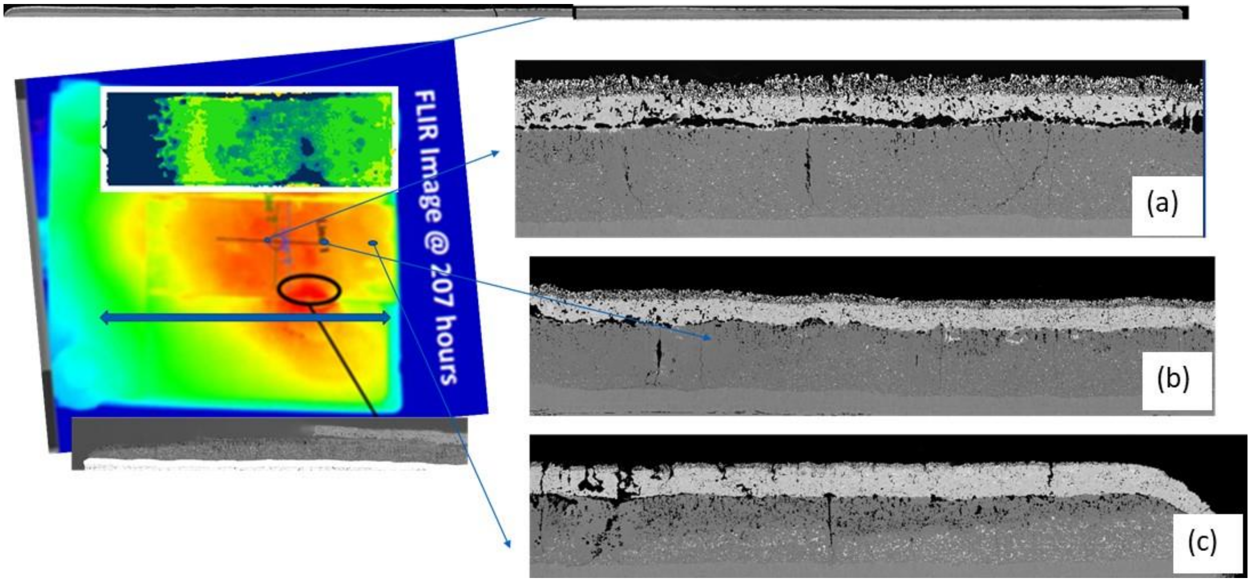

Figure 53:Condition of QARE 3 coating in the temperature range 2700-3000F (surface temperature) (a)~3000F; (b)~2900F; (c) ~2700F.

QARE 2

A lower mag image of the overall microstructure of QARE 2 after the 250 hours QARE rig test is shown in Figure 54. As compared to 100-O (Figure 53), the coating is in much better condition, there is no voiding or delamination at the REDS/bondcoat interface, and the REDS layer is well-protected from microvoiding because of the REMS top layer.

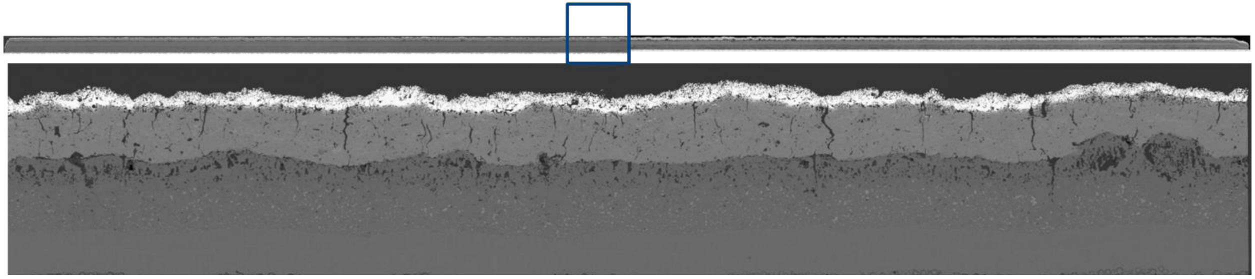

Figure 54: Microstructure of hot zone on QARE 2

4.1.3.4 Summary

The QARE rig test campaign generated valuable results and information that helped the program to select and mature the HTEBC candidate architectures for TRL-4 selections, and to perform down selection of coating architectures for high pressure combustor rig test. Due to the program's time limit, there are still aspects of the test and the underlying data that need to be considered if further work is conducted in continuation of what is described in this report. These are captured in section 6.3.2.1.

4.1.4 Results from Architecture 0

QARE rig test was conducted at 2700F mullite/CMC interface and 3000F topcoat surface. It was cooled to room temperature occasionally for inspections. The mullite/$HfSiO_4$/PS-PVD HfO_2 EBC was fabricated on a 3" x 1" CMC panel. The mullite and HfSiO4 were fabricated via slurry process. About 30% of the surface layer spalled after 76 hours (3 cycles) (Figure 55a). The test was terminated to investigate the root cause of the spallation. The EBC was spalled at the mullite/ $HfSiO_4$ interface (Figure 55c). The root cause was an excessive amount of eutectic at the mullite/ $HfSiO_4$ interface, weakening the interface. The same spallation mode was observed previously in steam cycling tests when an excessive amount of eutectic was generated in the bond coat. The excessive eutectic in the QARE rig test was attributed to the exposure of the bond coat to >2700F due to the temperature gradient, which was above temperature at which the bond coat chemistry was optimized.

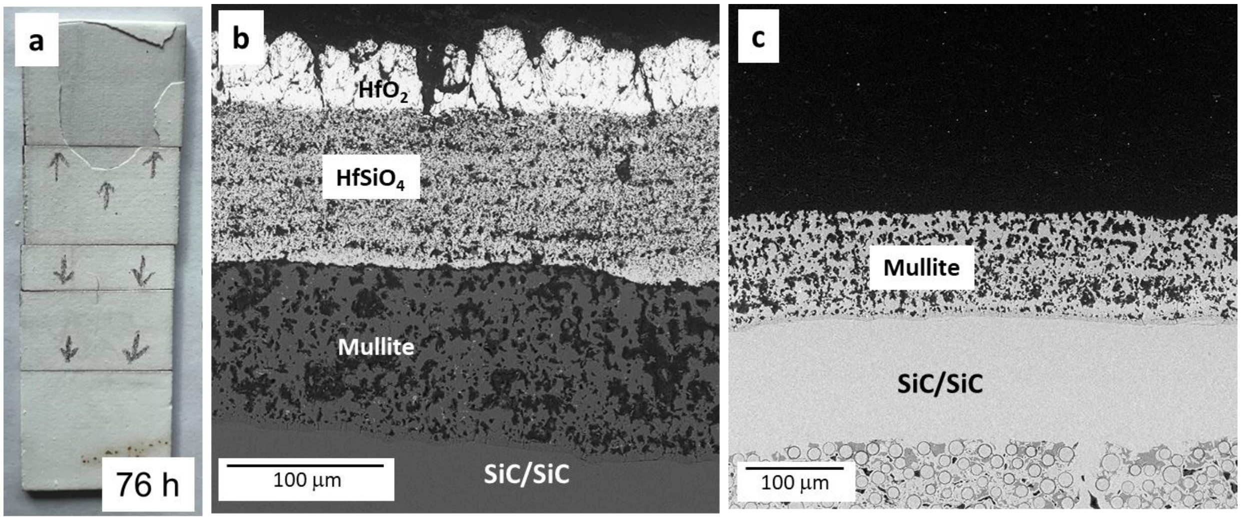

Figure 55: Mullite/$HfSiO_4$/PS-PVD HfO_2 EBC lost ~30% of the $HfSiO_4$/HfO_2 layers at 76 hrs (3 cycles)

The second QARE rig test, a modified mullite/$HfSiO_4$/PS-PVD HfO_2, also resulted in partial spallation of the $HfSiO_4$/HfO_2 layers at 117 hours (2 cycles). The test was continued to the target duration (250 hours). The mullite still stayed on while ~70% of the $HfSiO_4$/HfO_2 layers spalled at 250 hours (4 cycles) (Figure 56a, b and c). The root cause for the spallation was the same as the first QARE rig test, i.e., an excessive amount of eutectic at the mullite/$HfSiO_4$ interface.

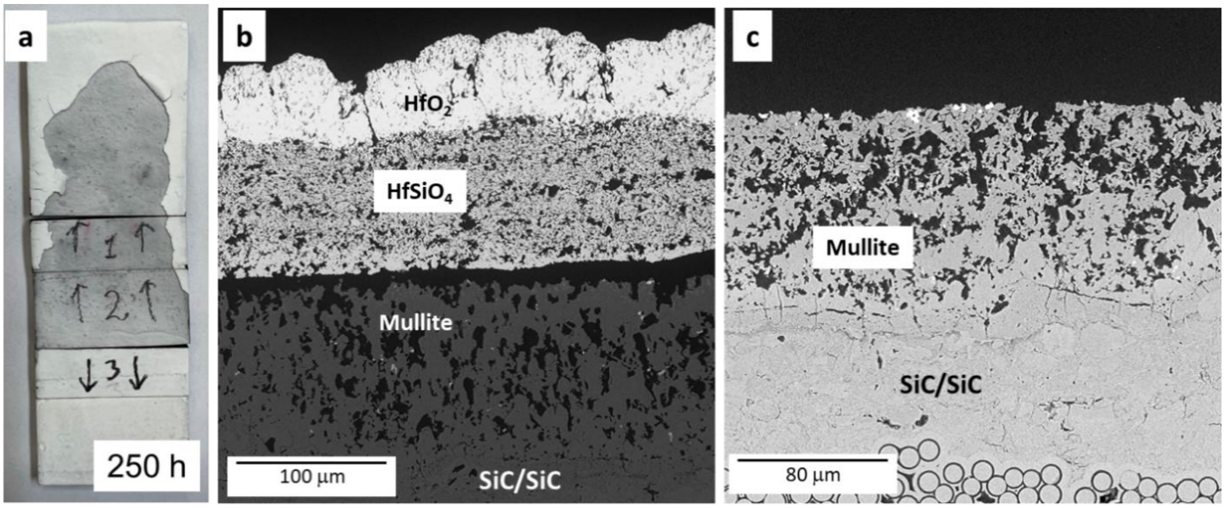

Figure 56: Modified mullite/$HfSiO_4$/PS-PVD HfO_2 EBC showed the first spallation at 117hrs (2 cycles) and lost ~70% of the $HfSiO_4$/HfO_2 layers at 250hrs (4 cycles)

Three additional modifications were tried in the next round of tests: 1) Modified bond coat (mullite 2)/$HfSiO_4$/PS-PVD HfO_2; 2) Mullite 2/Second mullite bond coat (mullite 3)/$HfSiO_4$/PS-PVD HfO_2; 3) Mullite 2/mullite 3/$HfSiO_4$/Second intermediate coat ($Sc_2Si_2O_7$)/HfO_2. The first two modifications showed no improvements, suffering partial surface layer spalling at ~100 hours. The third modified EBC (mullite 2/mullite 3/ $HfSiO_4$/ $Sc_2Si_2O_7$/PS-PVD HfO2) lost most of the HfO_2 topcoat at 112 hours (1 cycle), while most of the $HfSiO_4$/ $Sc_2Si_2O_7$ layers spalled during the subsequent exposures to 250 hours (3 cycles) (Figure 57).

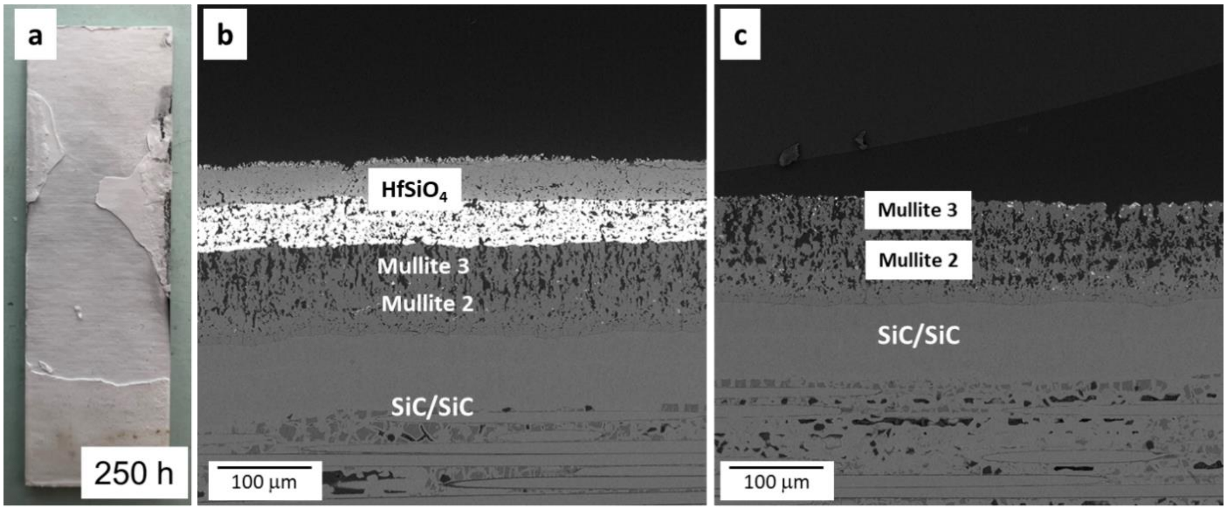

Figure 57: Mullite 2/mullite 3/$HfSiO_4$/$Sc_2Si_2O_7$/HfO_2 EBC lost most of the HfO_2 topcoat at 112hrs (1 cycle), while most of the $HfSiO_4$/$Sc_2Si_2O_7$ layers spalled during the subsequent exposure to 250hrs (3 cycles)

In the next round optimization, $Sc_2Si_2O_7$ was used as the topcoat considering the early spallation of the HfO_2 topcoat in all previous QARE rig tests. The $HfSiO_4$ intermediate coat was further modified, and a transition layer was added between $HfSiO_4$ and $Sc_2Si_2O_7$ to strengthen the bonding between all coating layers (mullite 2 / mod $HfSiO_4$ / Transition Layer / $Sc_2Si_2O_7$) (Figure 26b and Figure 58b). The EBC completed 250 hours / 10 cycles without spallation. Post-test SEM analysis showed that the coating maintained good bonding at the mullite/CMC interface as well as between all coating layers (Figure 58b and c).

The topcoat surface showed ~10-micron thick, porous scandium oxide (Sc_2O_3) surface layer, indicating that the surface of the $Sc_2Si_2O_7$ topcoat transformed to scandium oxide due to the selective volatilization of silica (SiO_2) by the high-speed flame (Figure 59).

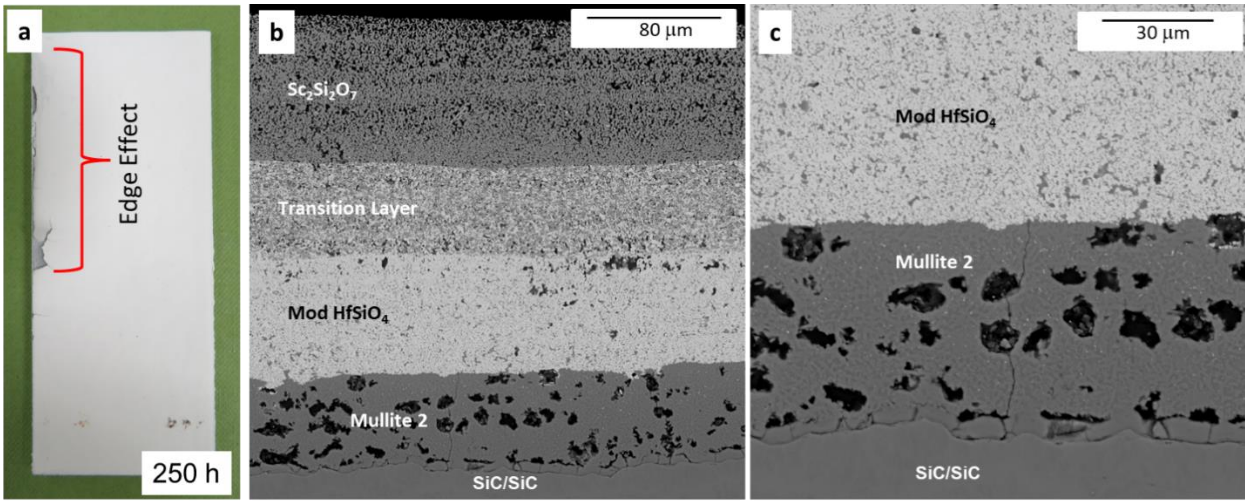

Figure 58: All slurry (mullite 2 / mod $HfSiO_4$ / Transition Layer / $Sc_2Si_2O_7$) EBC completed 250 hours / 10 cycles without spallation. All layers maintained good bonding.

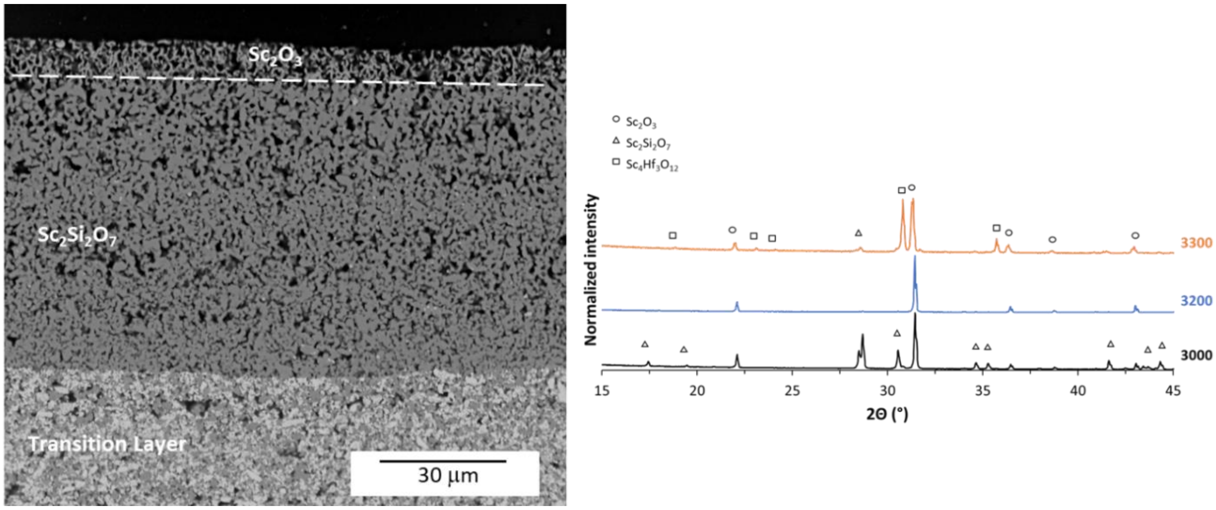

Figure 59: The $Sc_2Si_2O_7$ topcoat showed ~10-micron thick, porous scandium oxide (Sc_2O_3) surface layer after 250 hours / 10 cycles due to the selective volatilization of SiO_2.

4.2 CE-5 Rig Testing for TRL 5

4.2.1 NASA Rig Readiness

4.2.1.1 Introduction

Turbine engine materials and coatings are tested in the laboratory using a number of methods including furnace cycling, high heat flux lasers as well as atmospheric burner rig exposure. These methods are low-cost and accessible for material screening and technology maturation. However, there is a significant gap in available testing facilities that generate environments that are comparable to the hot section of the turbine engine. These facilities can be considered beyond laboratory capabilities but not to the fidelity or cost of a full-scale engine demonstration. This testing is critical for reducing risk by evaluating materials and components in relevant thermal and environmental conditions prior to moving to scaled engine demonstrations. The use of flame tube facilities offers a capability to test effects such as recession, oxidation, and material durability at conditions similar to those found in engine environments. NASA's advanced aeronautics programs such as the Advanced Air Vehicle Program (AAVP) have indicated there is a need for combustion environment testing for advanced materials to mature the technology readiness level (TRL) of components and coatings. Under the Hybrid Thermally Efficient Core (HyTEC) project and the partnership with General Electric Aerospace (GEA) on the HTEBC NRA, combustion facility testing was identified as the final tollgate to qualification of advanced environmental barrier coatings (EBCs) to a TRL-5. This document identifies the rig that is used for this test and the readiness to provide the required testing capability.

At NASA GRC a pre-existing sector combustor test facility known as CE-5 was identified as an ideal location to incorporate this new materials test capability. This facility has two flame tube combustor legs for testing sector arrangements of injector elements. Both sector legs have an inlet air supply pressure of 450 psig that can be preheated from 350-1350F (177-732°C). The facility has the capability of fuel flexibility, but for this work Jet-A was used. The maximum fuel flow rate for both legs is 7 gal/min at 400-900 psig. The larger of the two legs, referred to as "Stand I", has an inlet airflow range from 0.5-12.0 lb/s and a maximum rig pressure of 275 psig. "Stand II", which is used throughout this work, has an inlet air flow rate of 0.5-5.0 lb/s and a maximum rig pressure of 400 psig. Prior work with the CE-5 Stand 2 facility has focused on utilizing non-intrusive optical and laser-based techniques to observe fluid and chemical processes during combustion. The 9-point lean direct injector (LDI) hardware for this work has a 3 x 3 array that has been characterized in previous publications. This geometry was chosen for consistency with prior work as well as its reliability. The previous configuration of the hardware and the modified section is shown in Figure 60.

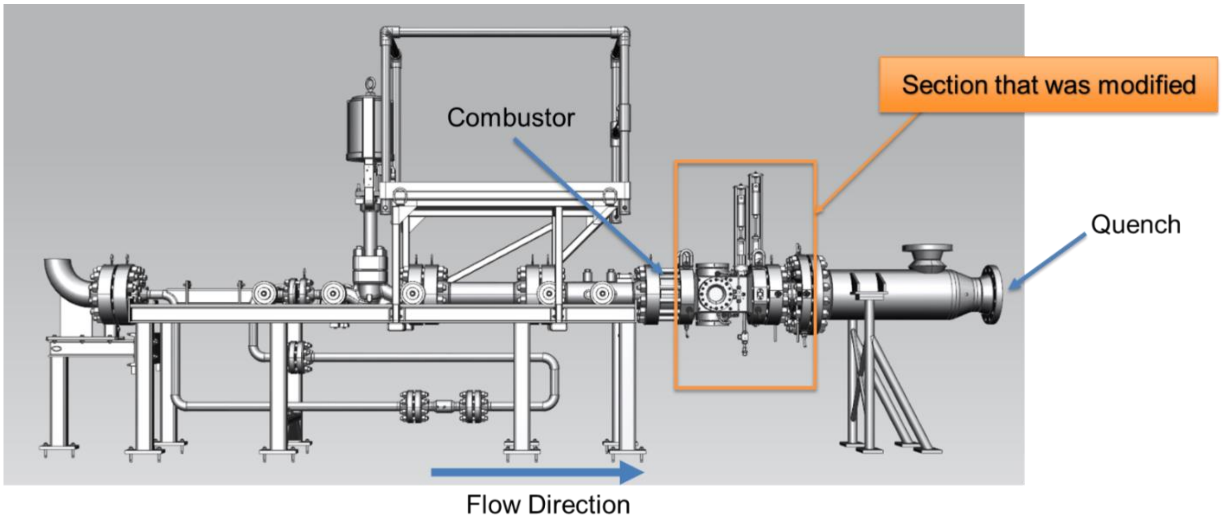

Figure 60: Previous hardware configuration of the CE-5 Stand II combustion facility.

To take advantage of the CE-5 facility and the combustion environment for materials testing, three new sections needed to be designed and fabricated. The sections are referred to as the "Transition Spool", "Test Section," and "Exhaust Adaptor," all of which are placed downstream of the injector, which is shown in Figure 61. In this system diagram, combustion gas flows from left to right. The maximum working combustion gas pressure of the new additions to the CE-5 facility has initially been limited to 300 psi although future analysis could increase this capability.

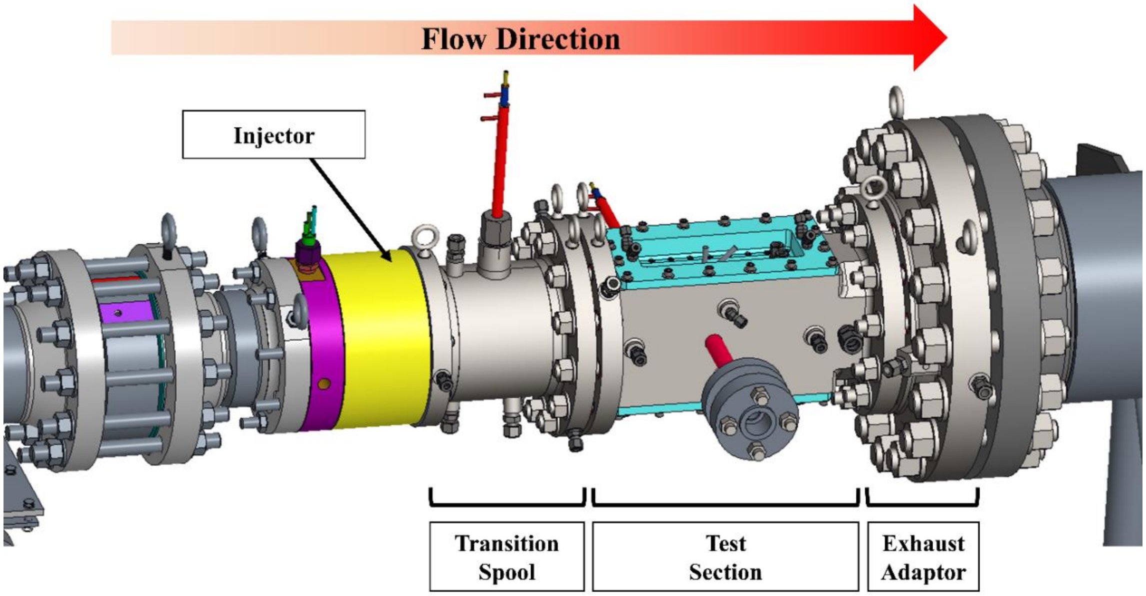

Figure 61: New CE-5 Stand II materials test sections.

The planned tests in the CE-5 Stand II facility were for a symmetric 'teardrop' shaped airfoil suspended in the combustion environment. As part of this effort, two sizes of airfoils were tested. The first airfoil tested was a symmetric 3" x 3" 3D woven ceramic matrix composite (CMC) airfoil developed and coated under NASA's Transformational Tools and Technologies (TTT) project. The CMC utilized Super Sylramic fibers with a CVI/PIP matrix and the EBC was denoted as NASA Architecture 0. While the design of the Test Section was initially sized to test this symmetric airfoil, a modular design for the hardware was used to incorporate various article geometries (such as the larger HyTEC airfoil) for future testing. The TTT airfoil was used to check-out the hardware and reduce risk for the larger (~5.8") symmetric CVI airfoils developed by GEA for the HyTEC project. The HyTEC airfoils were coated by both GEA and NASA GRC with high temperature environmental barrier coatings (HTEBC) architectures that were tested to TRL-4 in the laboratory. Examples of the TTT airfoil and the HyTEC airfoil are shown in Figure 62.

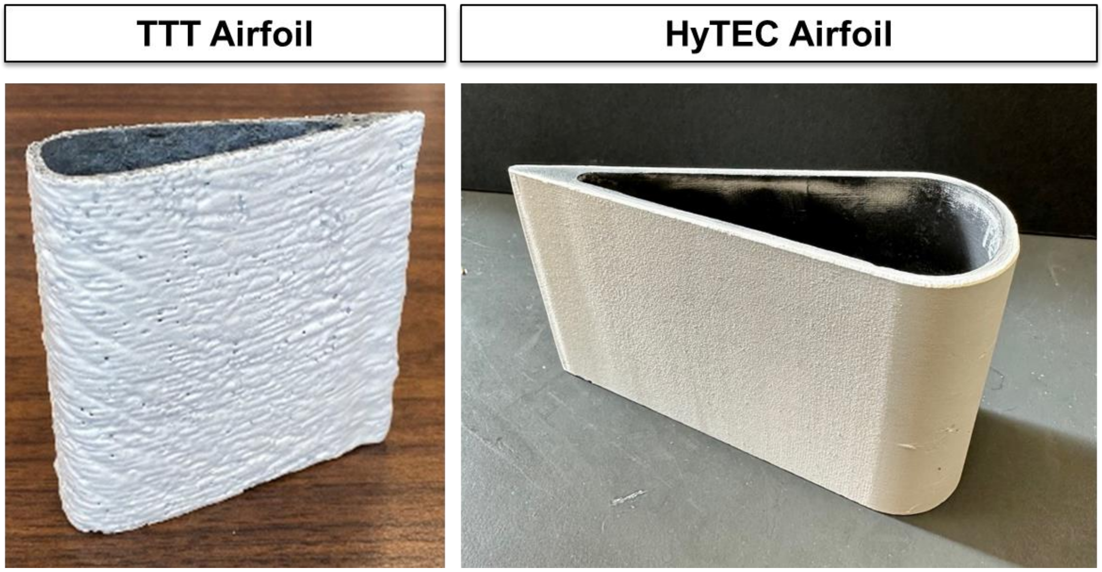

Figure 62: Images of the airfoils for the TTT and HyTEC tests.

A minimum of 72 hours was required for completion of testing for each of the HyTEC airfoils. Test Section and mounting hardware needed to be durable to endure the test conditions and duration. Test conditions required combustion gas temperatures >3000F (1650°C) at 300 psi working pressure and >30 m/s velocity. In addition, 900F cooling air was routed to the back side of the airfoil, which was achieved by diverting a portion of the inlet air temperature to the hardware. A more detailed view of the hardware is discussed in the following sections.

4.2.1.2 Transition Spool

The transition spool shown in Figure 63 is the furthest upstream spool piece, following the injector and directly before the test section. This section was designed to assist in lighting the fuel from the injector and allowing the gas to come to a uniform flow condition. The spool was milled from a 304/304L stainless steel (per ASTM A276) billet and includes externally milled water-cooling traces closed by a welded cover plate. The transition spool contains three ports or penetrations: one holds the flame ignition source, one has a thermocouple to check the temperature of the flame, and a third on top is for an emissions probe that is used to inform on the combustion conditions. In the inner portion of the transition spool section, a castable refractory cement known as Greencast®-94 Plus (HarbisonWalker International) was used to line the walls of the stainless-steel spool. This refractory is ~94 wt% Al_2O_3, ~5 wt% CaO, and 0.1-0.2 wt% each of SiO_2, Fe2O3, TiO_2, MgO, and $Na_2O + K_2O$. The wall thickness of the ceramic was approximately 0.844” (21.4 mm). This castable ceramic insulation was used to prevent quenching the combustion gas prior to reaching the test section. There is a long history of using this material as a ceramic liner in previous emissions studies to keep the combustion gas at temperature while also maintaining the integrity of the stainless-steel spool. If a water-cooled liner was in contact with the combustion gas as was done in the test and exhaust sections, there was concern that the combustion gas would be much cooler than the target temperature of 3000F (1650°C).

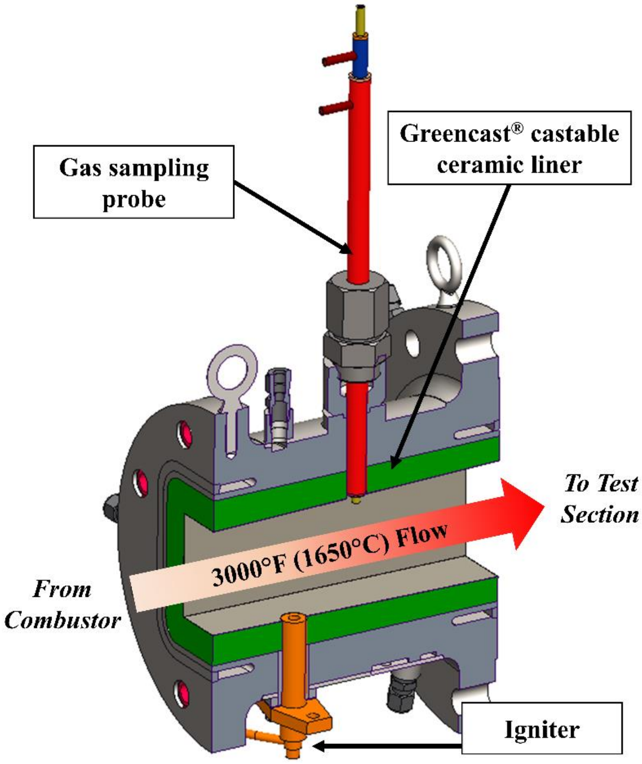

Figure 63: Transition Spool.

4.2.1.3 Test Section

The Test Section sub-assembly shown in Figure 64 features a dual-material construction consisting of a 304/304L stainless steel (per ASTM A276) pressure wall encapsulating a water-cooled copper liner which directly contacts the hot combustion gas flow. The design intent is to isolate the stainless-steel spool(s) from thermal loads without the use of thick, and possibly fragile insulation. The Test Section is meant to be reconfigured frequently and therefore the ceramic insulation would also present additional challenges for hardware buildup and instrumentation.

The Test Section was fabricated in two separate sections. The design concept for this hardware is analogous to rocket engine manufacturing with additively made and brazed 2-layer components, and therefore the fabrication followed a similar process. The external jacket was made from a single billet of 304/304L stainless steel. The inner liner was additively manufactured using selective laser melting (SLM) by Additive Manufacturing Engineering (AME, Huntsville, AL) from a copper alloy known as GRCop-84 that was initially developed for use in high-heat flux applications such as rocket engine components and combustion liners. The stainless-steel jacket is expected to manage the mechanical loads of the test while the internal copper liner is designed to handle the thermal load of the 3000F (1650°C) combustion gas. The copper inner liner was designed to be oversized for the opening in the stainless-steel housing, with an interference of 0.001-0.002” (0.025-0.051 mm) across cross section. The opening and the copper section were match machined to have a 1° taper along the length for ease of fitting and alignment. The interference fit was desired to maximize the contact between the surfaces when they were brazed together. CuSil-ABA alloy that was 0.002” (0.051 mm) thick was tack welded to the inside wall of the stainless-steel outer jacket and the inner copper liner was chilled with liquid nitrogen to a temperature of approximately -200°C to overcome the interference with the outer housing. The copper liner was fit into the stainless-steel jacket and allowed to return to room temperature, then brazed to a temperature of 1531F (833°C) for 30 minutes by Thermal-Vac (Orange, CA). Once the brazing was complete, 3.25” x 9.50” (82.55 mm x 241.3 mm) openings were machined on opposing sides for sample fixturing plates that will be discussed later.

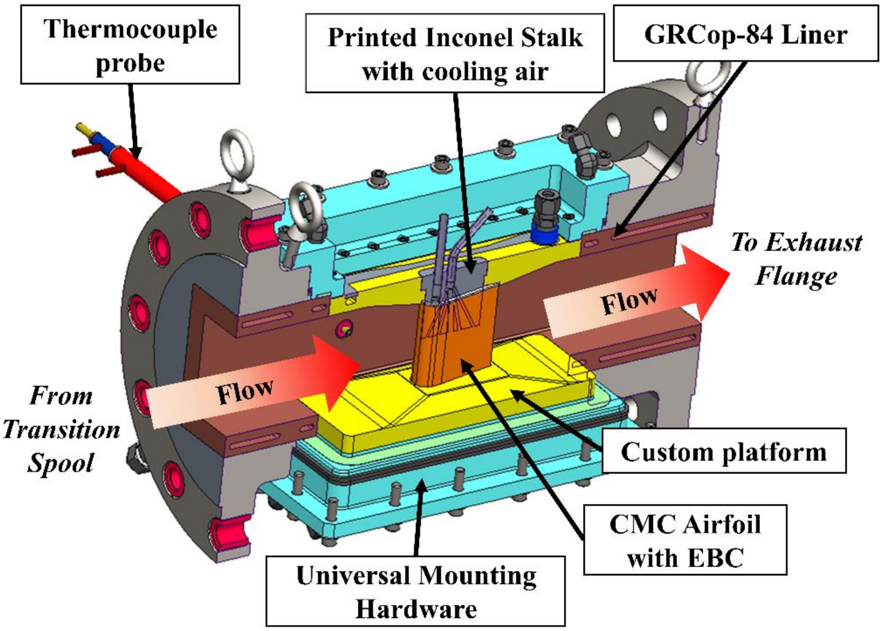

Figure 64: Sample Test Section

4.2.1.4 Exhaust Adaptor

The Exhaust Adaptor shown in Figure 65 follows the Test Section and was also constructed of a stainless-steel outer shell with a GRCop-84 liner made additively by SLM (AME, Huntsville, AL). This hardware was constructed using SLM processing due to the complex embedded cooling channels within the copper layer. The GRCop-84 liner was brazed into the steel using 0.002” (0.051 mm) thick AMS 4777 braze alloy at a temperature of 1900F (1038°C) for 0.5 hour by Paulo Heat Treating (Willoughby, OH). The Exhaust Adaptor is used to increase the diameter of the flow path from 3.5” x 3.5” (89 mm x 89 mm) to the quench section, which is a 12-inch ANSI B16.5 flange with a round diameter of 12.875” (327 mm).

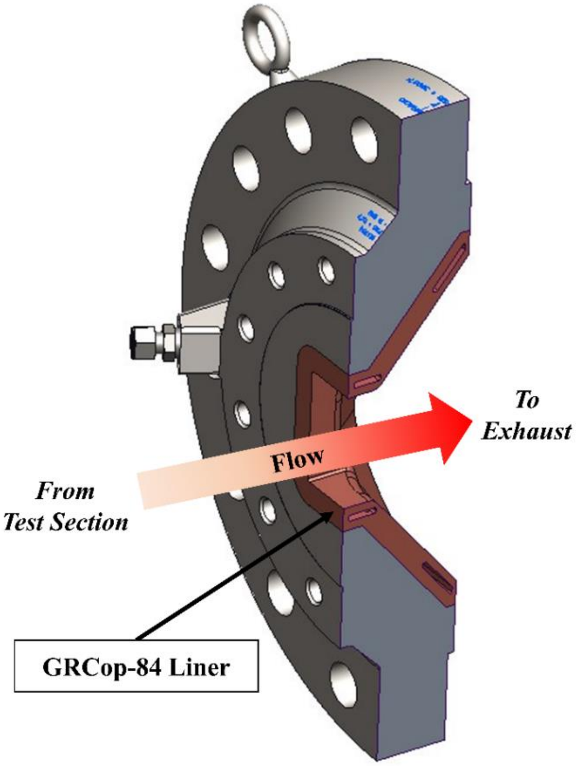

Figure 65: Exhaust Adaptor

4.2.1.5 Airfoil Support Stalk

For the airfoils, the customized platform inserts were built in two sections. The top section of the platform was a GRCop-84 alloy manufactured via additive (SLM) methods by AME (Huntsville, AL) and brazed to a 304 stainless backing plate. Water flows between the plates and through the copper platform to provide sufficient cooling. Two symmetric platforms from opposing sides of the Test Section were used to lock the airfoil test hardware in place. An additively manufactured Inconel-718 (Cumberland Additive, Austin TX) airfoil supporting structure (shown in Figure 66) goes through each of the platforms and into the open body of the CMC airfoil. Two different sizes were made for the TTT and HyTEC tests. These platforms deliver and direct cooling air to the backside of the airfoil, and Inconel was selected due to significant thermally driven and bolted interface stresses that exceeded the capabilities of either stainless-steel or copper. The cooling air is routed from the 1000F inlet air upstream of the injector. The air enters the backside of the Inconel fixture and flows through the open channels, impinging on the inner wall of the CMC airfoil. There is a 0.25” (6.35 mm) gap between the opposing airfoil support structures where the air returns through a central exhaust on either side. The exhausted air is directed out of the rig and back into the flow downstream away from the airfoil. Exhausting into the Test Section downstream of the airfoil avoided the cost and complexity of venting high temperature air into room or laboratory exhaust system. Computational fluid dynamics (CFD) analysis showed that the exhausting backside cooling air would not impinge on the trailing edge of the test article. The nominal cooling air rate of 1-10% of the bulk combustion gas flow (0.02-0.2 lb/s [0.0045-0.045 kg/s]) was used to evaluate component temperatures and stresses. A range of 1-3% of the bulk combustion gas flow (0.02-0.06 lb/s [0.0045-0.0135 kg/s]) was determined to be sufficient to achieve the desired cooling of both the airfoil support stalk and the symmetric CMC vane.

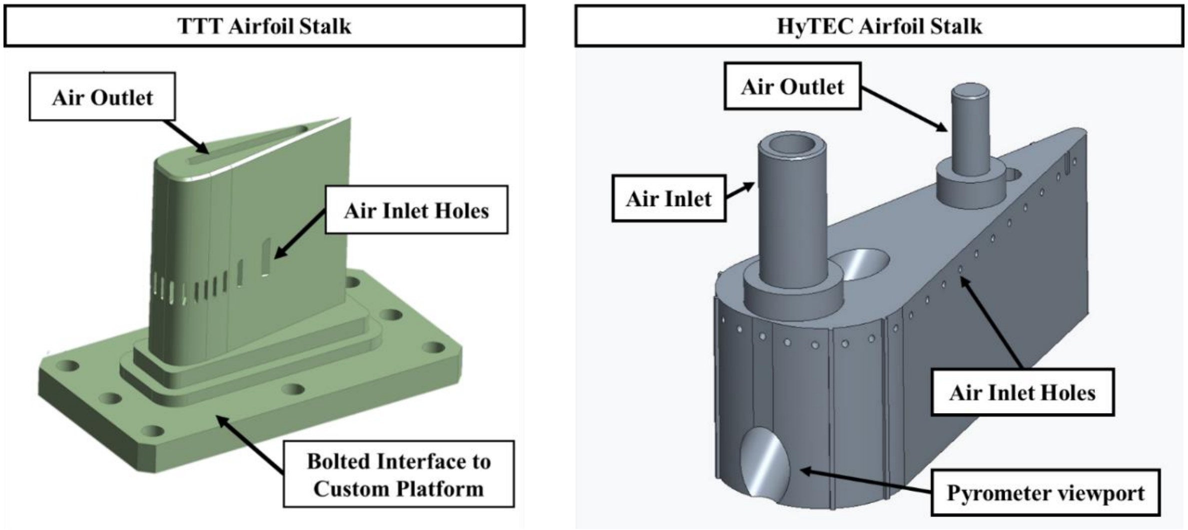

Figure 66: Inconel airfoil support stalks for TTT and HyTEC hardware.

4.2.1.6 Test Configuration and Hardware Changeover

The setup for the Test Section for each of the tests is shown in Figure 67. The top and bottom of the hardware as well as the platforms are identical, making the rig symmetric. The only differences between the two configurations are the custom platform, the 3D printed Inconel stalk, and of course, the airfoil. The two custom platforms mount onto the same universal mounting hardware, shown in blue. The additional pyrometer ports in the HyTEC configuration are supported by the custom platform. Water and air inlets and outlets are swappable between the two configurations and monitored by ESCORT data acquisition. To minimize the installation time of the airfoils, changing the configuration of the hardware only requires the removal of the top and bottom flanges, which are colored in teal in Figure 67, by removing the attachment bolts shown in Figure 68.

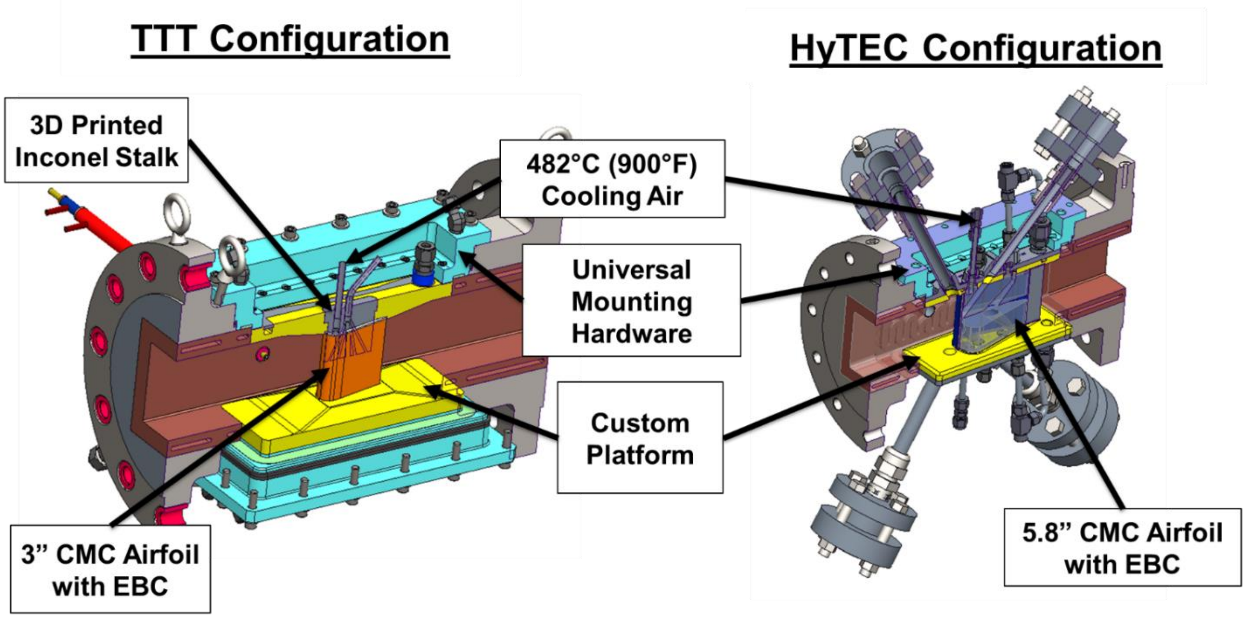

Figure 67: Test Section configurations for the two airfoil tests.

The procedure to change from the TTT configuration to the HyTEC configuration is as follows:

- Disconnect water lines and instrumentation
- Unbolt top flange (universal mounting hardware) and remove
- Remove test article
- Unbolt custom platform (flat configuration shown here)
- Remove bottom flange and custom platform
- Bolt new custom platforms on to flanges
- Perform pressure test on benchtop hardware
- Bolt bottom flange with platform onto test section
- Insert test article
- Bolt top flange onto test section and reconnect water lines and instrumentation

If the airfoil geometry remains the same from the removed article to the newly installed article, only the top flange needs to be removed to swap the hardware. In practice, changing from the TTT hardware to the HyTEC hardware took ~1 week and changing from one HyTEC airfoil to another took ~1 day.

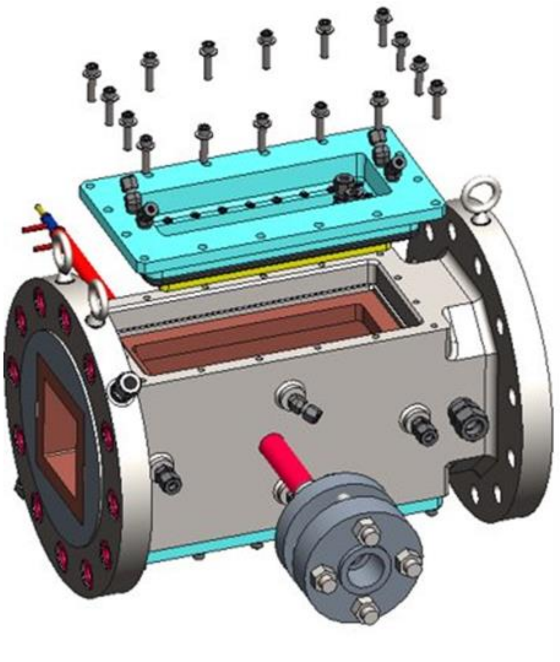

Figure 68: Test section images showing the bolting of the top flange (left) and a photo of the hardware (right).

4.2.1.7 Test Conditions

Although the rig can run at a variety of conditions as mentioned in the introduction, the conditions for the initial testing are shown in Table 11. Run conditions were determined with a 'blank' plate configuration prior to the TTT test.

Table 11: CE-5 Test Conditions.

CE-5 Run Parameters	
Parameter	Operating Value
Inlet air supply pressure	450 psig
Inlet air temperature (T3)	1030F
Inlet airflow	~2 lb/s
Exhaust	Atmosphere
Rig Pressure (P3)	270 psig
Equivalence Ratio	0.515
Combustor Pressure (P4)	~259 psig (4% under P3)
Gas Temperature (T4)	3000-3100F
Velocity	~44 m/s
Rig Fuel (Jet-A) flow	35 gal/hr
Backside cooling airflow	0.125-0.170 lb/s
Backside cooling air temperature	1000F
Backside cooling air pressure	15 psig over P3

Regarding the fuel consumption, as shown in Table 11, the run conditions utilize ~35 gallons per hour. A single fuel delivery provides 800-1000 usable gallons of fuel, which provided 23-28 hours of burn time. This resulted in approximately 3 days of run time before more fuel was needed.

For silicon-based ceramics such as SiC, the degradation is measured by the volatility of the SiO_2 scale. This rate has been calculated and measured for a variety of laboratory and combustion facilities at NASA GRC. Given the conditions shown in Table 11, the expected linear volatilization rate for a bulk SiC substrate can be calculated and compared to previous facilities. The flux of a volatile species (Si(OH)4 in this case) is expressed by the following relationship:

$$k_l \propto e^{-Q/RT} \frac{v^{1/2} P(H_2O)^2}{P_t^{1/2}} \tag{1}$$

where k_l is the linear volatilization rate, Q is the activation energy assumed to be 108 kJ/mol, R is the universal gas constant, T is the sample temperature, v is the velocity, and P_t is the total pressure. For the conditions shown in Table 11, the estimated $P(H_2O)$ content was calculated using the NASA Glenn chemical equilibrium program CEA to be 6.7%. The normalized expected recession conditions in the CE- 5 Stand 2 test environment are plotted in Figure 69 to determine how this facility compares to other laboratory recession tests shown in Table 12. Based on these preliminary calculations, it can be expected that an uncoated SiC component would experience weight loss significantly faster than other previously used test methods, which is ideal for the best simulation of turbine engine conditions.

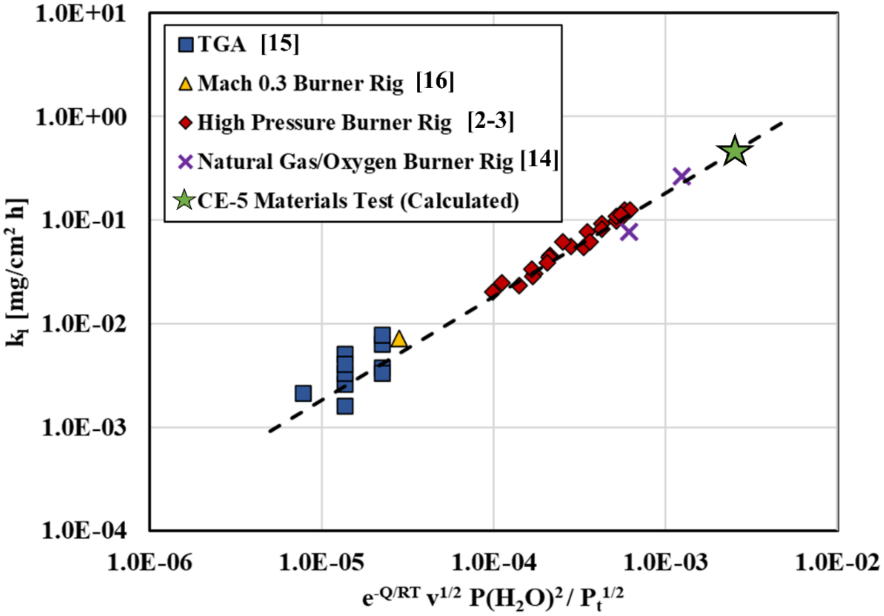

Figure 69: Expected linear recession rate for SiO_2 in various NASA Glenn combustion facilities. Note: Combustion simulations were utilized to predict gas velocity, v and partial pressure of water vapor, $P(H_2O)$ for the Natural Gas/Oxygen Burner Rig data.

Table 12: Comparison of Laboratory Testing Conditions.

Rig	P_{total} (atm)	$P(H_2O)$ (atm)	V (m/s)
TGA	1	0.5	0.044
Mach 0.3 Burner Rig	1	0.1	100
High Pressure Burner Rig	6-15	0.6 - 1.5	10-20
Natural Gas/Oxygen Burner Rig	1	0.3 - 0.35	110-115
CE-5 Materials Test	17.6	1.18	44

4.2.1.8 Instrumentation

The general configuration of the material instrumentation is shown for the TTT test in Figure 70 and for the HyTEC test in Figure 71. In the TTT test, the combustion conditions are monitored using an emissions probe in the transition spool. This probe is capable of measuring NO, O_2, CO_2, CO, as well as additional hydrocarbons within the combustion gas. The real time data is logged and used to maintain consistent combustion conditions. Due to the leading-edge pyrometers for the HyTEC test, the gas sampling probe needed to be removed. There is a water-cooled Type B thermocouple probe within the sample Test Section to measure the combustion gas temperature (T4). A ¾" (19.05 mm) tube is set at the midpoint of the Test Section with a 'bullseye' flange (PresSure Products, Charleston, WV) that contains a ZnSe lens. A N2 purge is used to maintain integrity in the ZnSe lens. This tube is centered on the side of the airfoil described above for the measurement of the surface temperature with a pyrometer or a thermal imaging camera. The EBC materials are partially transmissive at low wavelengths, and therefore a higher wavelength (10-11 μm) is used.

The HyTEC hardware has all the same instrumentation as the TTT airfoil hardware with the addition of a leading edge and backside flanges for viewing with thermal cameras or pyrometers. The top and bottom plates are symmetric, which provide dual access to the airfoil. The complexity of the hardware limited the use of multiple pyrometers/cameras, but there was sufficient space around the rig to mount two leading edge pyrometers, one backside pyrometer on the top and the thermal imaging camera on the side tube. As in the TTT test, the emissivity of the coated surface requires long wavelength (10-11μm) pyrometry. For these wavelengths, the 'bullseye' flanges require ZnSe lenses. The emissivity for the single-color pyrometer was dictated by the EBC topcoat. However, the backside surface of the SiC was evaluated using shorter (2-color) 1μm pyrometers, which can utilize quartz lenses. Both types of bullseye flanges use a N2 purge that is set just over the rig pressure. The pyrometer tubes and cooling air were monitored by surface and in-line thermocouples, respectively. The data from the thermocouples, pressure transducers, and flowmeters were all monitored and collected into ESCORT. The pyrometer voltage signals were collected into ESCORT and converted to temperatures based on manufacturer's requirements. The thermal imaging camera video signal from the side viewing port was collected on a separate laptop.

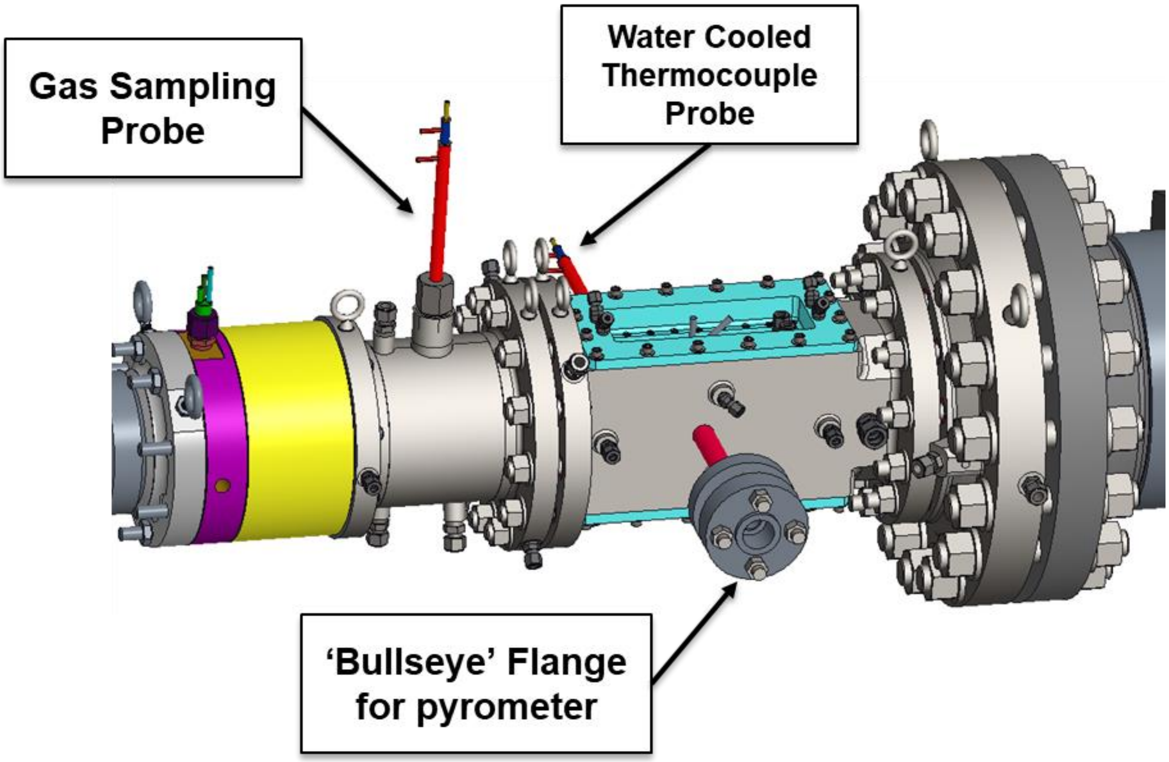

Figure 70: Instrumentation configuration for the TTT test.

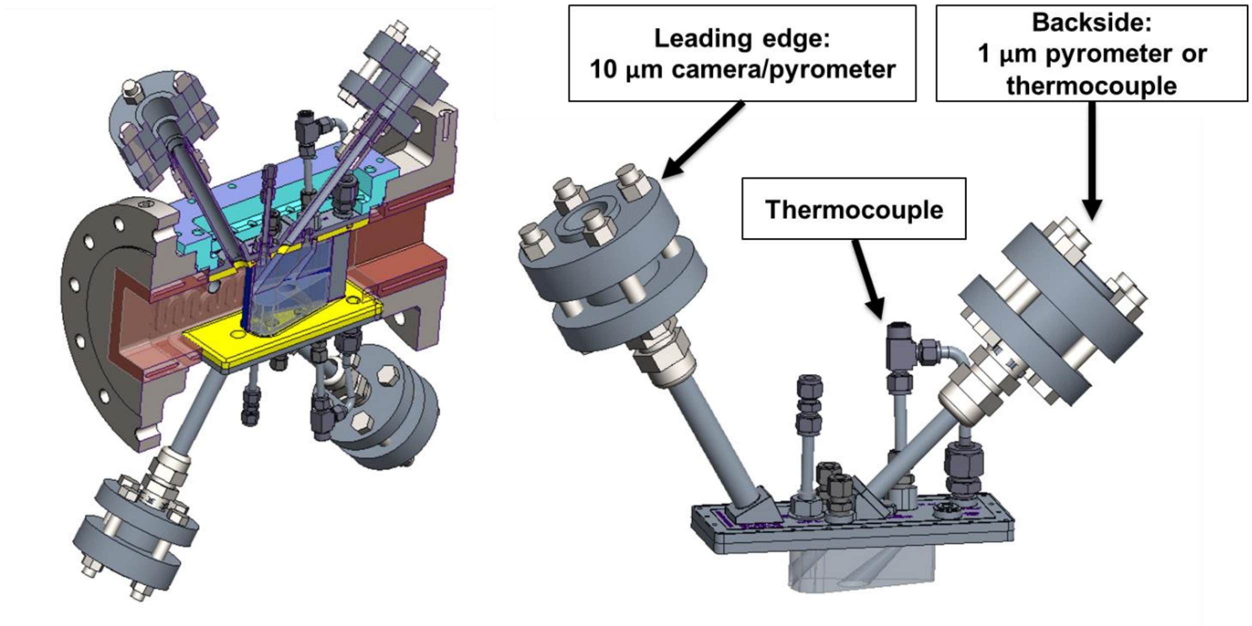

Figure 71: HyTEC mounting plate instrumentation.

The cooling water loop temperatures were monitored via data acquisition in ESCORT. Thermocouples are present on all return loops and flowmeters are in-line to maintain flow rates determined by thermal modeling using ANSYS Workbench. Low flow and high temperature alerts and shutdowns were incorporated into ESCORT to avoid damage to the facility.

4.2.1.9 Preliminary Checkout (NASA TTT Airfoil)

The NASA TTT airfoil was installed in CE-5 in the beginning of January for testing. This test was used to determine the rig capability and provide a degree of risk reduction for the GEA airfoil testing. The TTT airfoil was a high temperature 3D CMC that was roughly 3” tall and 3” long. The combustion conditions for the test were as follows:

Test Conditions for TTT airfoil

- Pressure: 275 psi
- Combustion gas temperature: 3000F
- Mass Flow: ~2.0 lb/s
- Velocity: 44 m/s
- Time: 9hrs

The side single wavelength 10-11 micron pyrometer was used to measure the EBC surface temperature. However, the observed temperature through this side lens was significantly lower than expected, and it was determined later that the lens was not ZnSe, which resulted in an incorrect temperature measurement. A new, correct lens was installed but testing was stopped after the first day when air leaks were observed on some of the bolts holding the mounting plates in place. The issue may have been related to bottoming out of the bolts as well as unloading due to the thermal cycle. Increasing the torque load did not completely fix the issue and for the sake of schedule the test was ended, and airfoil removed (shown in Figure 72) so that there would be additional time for the HyTEC hardware installation. Belleville washers were recommended for the HyTEC hardware to avoid the issue of unloading via the thermal cycle.

Figure 72: TTT airfoil before and after testing. Red circled areas are locations of spallation.

The architecture 0 chemistry listed in section 4.2.1.9 of this report are based on work mentioned under [41], [42], [43], [44], [45] and [46].

4.2.1.10 Summary

A new material test capability was incorporated into the pre-existing sector of the CE-5 combustor test facility at NASA GRC. Three separate spool pieces and supporting hardware were manufactured to expose both the NASA TTT airfoil as well as the larger HyTEC airfoil geometries to 3100F combustion gas. The TTT test provided initial results that validated the rig capability for testing under the HyTEC program.

4.2.2 NASA Rig Testing

4.2.2.1 Introduction

As mentioned in the CE-5 Airfoil Rig Readiness Review, the test facility was validated using the smaller TTT airfoil geometry. Once this testing was completed, the facility was prepared for the HyTEC airfoil test. Six airfoils were produced in preparation for testing in CE-5. The outer dimensions were nominal to the design, but the interior dimensions varied, with 3 airfoils slightly smaller in cavity size. Two of the airfoils were coated with GEA Architecture 1, two were coated with GEA Architecture 2, and one was sent to NASA GRC for coating with Architecture 0. The GEA coating architectures were named ‘A’ and ‘B’ based on the order preference. The sizes are noted in Table 13.

Table 13: Airfoil numbers and coating identification.

Airfoil	Architecture ID	Cavity Size
16282	1A	Nominal
16283	0A	Nominal
16284	1B	Nominal
16285	2A	5-10 mils smaller cavity
16286	Not assigned	5-10 mils smaller cavity
16287	2B	5-10 mils smaller cavity

The initial testing plan in CE-5 was to test Architecture 1A, then 1B, then Architecture 0A. The 1B and 2B architectures were prepared as backups or alternates if needed.

4.2.2.2 HyTEC Architecture 1A

Architecture 1A (Figure 73) was installed during the week of February 5th and began testing on February 14th, 2024. There was a misfit with the airfoil initially because the drawings did not account for the coating thickness. The copper platform was machined wider to allow for fit and installation after a short delay.

Architecture 1A As-Received

Figure 73: As-received airfoil with GEA Architecture 1A EBC.

The test conditions for Architecture 1A were as follows:

Test Conditions for Architecture 1A

- Pressure: 275 psi
- Combustion gas temperature: 3000-3100F
- Mass Flow: ~2.0 lb/s
- Velocity: 44 m/s
- T3: 1025-1050F

The pyrometer configuration is shown in Figure 74. The setup initially started on 2/22/24 with the FLIR camera on the side port and the single wavelength 10-11 μm pyrometers on the top and bottom leading edge. During the testing, it was difficult to get consistent measurements with the single wavelength (10-11 micron) pyrometers on the leading edge or on the side view. This was attributed to challenges with alignment and that the single wavelength pyrometer reads an average measurement over the spot size which would consistently result in low temperature values. The FLIR camera and the single wavelength pyrometers were switched for 2/26 and 2/27, as noted in Table 14. A 2-color pyrometer was installed on the lower leading-edge tube since deposits on the surface lowered the emissivity and provided a second data point to compare the single wavelength pyrometer number. The 2-color pyrometer should not be utilized as a high-fidelity measurement due to transmission effects through the coating but should be noted nonetheless as a likely upper bound. Run conditions were varied to maximize the temperature in the rig and on the airfoil, and the backside cooling air was minimized with only the pyrometer nitrogen flows from February 28th onward. The nominal temperatures during the test days are shown in Table 14.

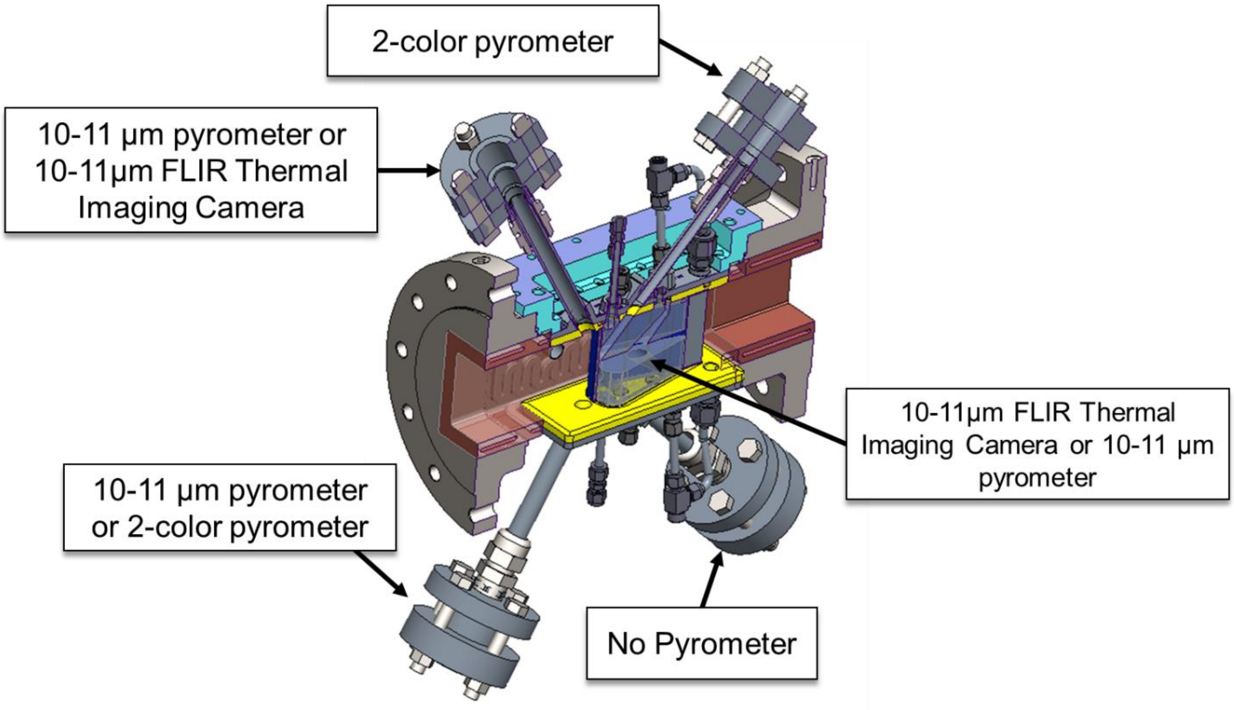

Figure 74: Pyrometer configuration for Architecture 1A.

In addition to the pyrometer measurements of the airfoil, an open-ball thermocouple was placed into the flow to validate the combustion gas temperature. This temperature was taken ~1” in front of the airfoil and ~1.5” away from the cold wall. As shown in Figure 75, the measured temperature was >96% of the calculated adiabatic flame temperature, which provided confidence in the calculated combustion gas temperature.

Table 14: Nominal temperatures and run times for Architecture 1A test days.

Architecture 1A					
Date	**Single Wavelength Leading Edge (°F)**	**2-color Leading Edge (°F)**	**Side Temperature (°F)**	**Backside Leading Edge (°F)**	**Hours at Condition**
2/22/2024	1900	N/A	2450	1700	4
2/26/2024	1675	2250	2250	1675	5
2/27/2024	1700	2300	2200	1630	6.7
2/28/2024	1650	2325	1900	1650	6.1
2/29/2024	1650	2325	1800	1650	5.5
3/6/2024	1575	2270	2365	1450	8.2
				Total Hours:	**35.5**
****2/26 & 2/27 had thermal camera on the leading edge and the pyrometer on the side.***					
All other days had the camera on the side and the pyrometer on the leading edge					

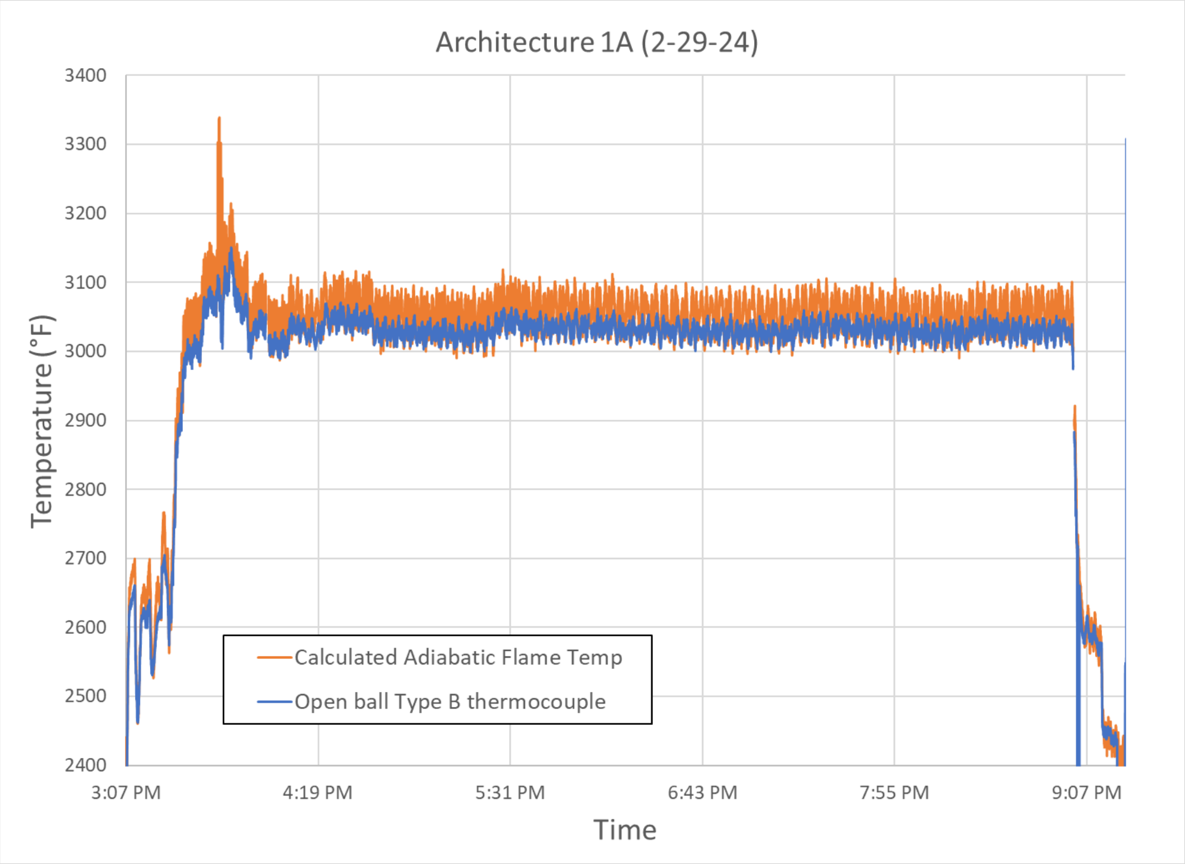

Figure 75: Plot of temperature of the calculated adiabatic flame temperature and the open ball Type B thermocouple in the combustion environment at the airfoil.

The temperatures on the leading edge of the airfoil measured by the single wavelength pyrometer dropped over time with exposure. This was attributed to deposits forming on the surface that likely lowered the emissivity. A 2-color pyrometer was also integrated as an additional data point. An example of the temperatures and pressures during a test are shown in Figure 76. Once the conditions were set, the rig was very stable until shutdown at approximately 9:00pm.

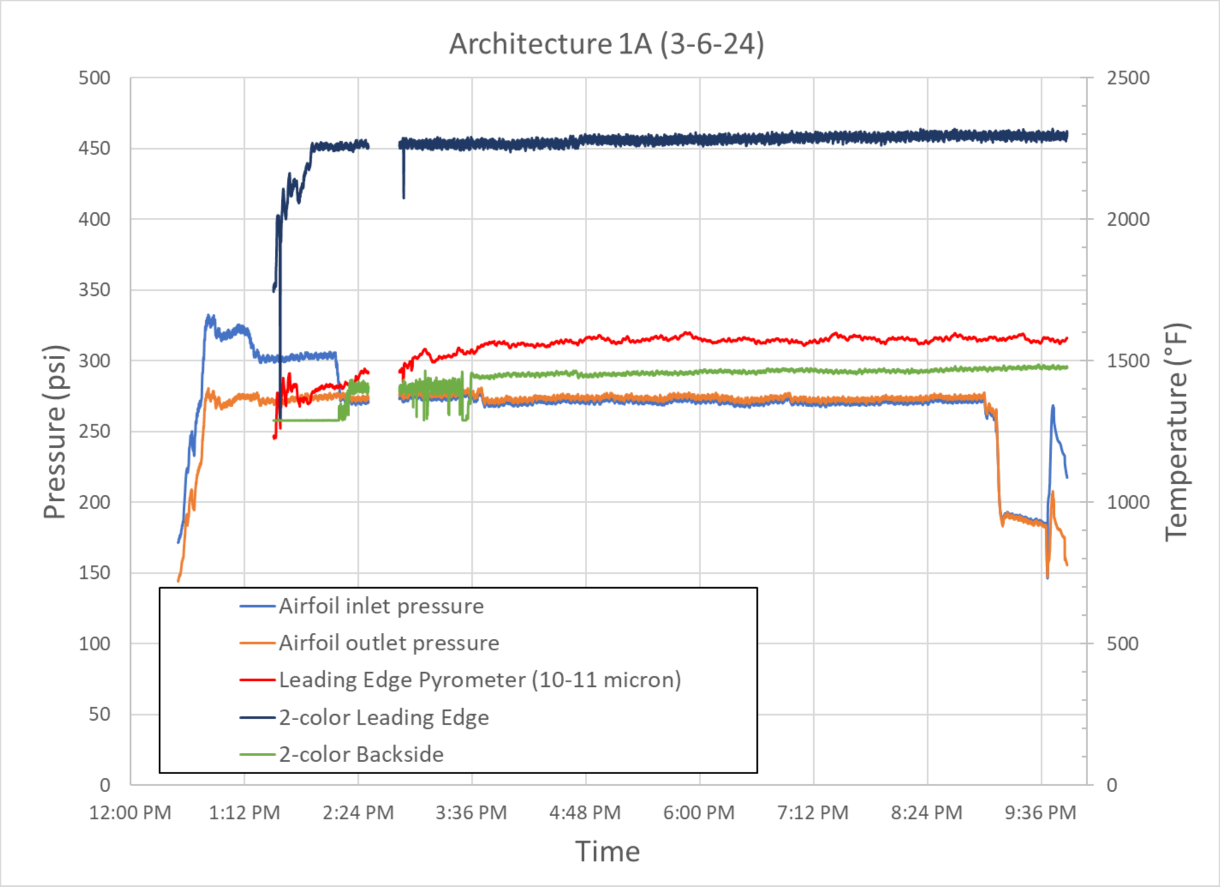

Figure 76: Example data of pressures and temperatures for Architecture 1A airfoil test.

After ~27 hours of exposure, borescope inspection on March 5th determined the epoxy join on the stainless-steel sleeve on the side pyrometer port had become compromised and the sleeve slid out close to the airfoil, as shown in the top left image in Figure 77. Examination of previous borescope images indicated that this took place during the previous run day on 2/29/24. The test section was opened, and the airfoil was removed to make the repair. A copper liner and high thermal conductivity epoxy was used to re-sleeve the pyrometer tube and the hardware was reassembled. Architecture 1A was photographed and images are shown in Figure 77. The discoloration on the centerline near the leading edge (noted with an arrow) on the top right image is the location of the side pyrometer viewport.

Figure 77: (Top left) Borescope image showing the stainless-steel sleeve slid into the combustion path and images of the Architecture 1A airfoil after ~27hrs of testing. The top right image is the side pyrometer side, and the bottom right image is the opposite side without the pyrometer viewport.

During the hardware startup on March 8th, there was an issue with the backpressure valve and the inlet air reached a temperature at which point the autoignition of the fuel took place, which resulted in a stoppage of work for inspection. There was evidence of some water making its way back into the downstream section due to this valve issue. Upon inspection of the rig after the autoignition event, a break down the trailing edge of the airfoil was found. It is unknown whether the breakage occurred during the autoignition or if it took place earlier in the testing. The valve was repaired, and future testing would take place with ignition below 800F to avoid future autoignition events. The GEA and NASA teams agreed to remove Architecture 1A and install the next architecture on the list. The airfoil was very dark in color after removal (shown in Figure 78), which was attributed to the autoignition events and incomplete combustion. In total, the Architecture 1A airfoil was tested at a variety of conditions and configurations for a total of ~35.5 hours before removal. Minimal spallation was observed in the coating. There was minimal spall of the topcoat on the leading edge, and only 1-2 small spalls on the trailing edge that went to the substrate. The airfoil was shipped back to GEA during the week of March 11th.

Figure 78: Images of Architecture 1A after 35.5hrs of testing. The bottom right image is side that was in view of the thermal imaging camera.

Throughout the testing of Architecture 1A, there were concerns that the nitrogen purge from the leading-edge pyrometer ports was cooling the combustion gas and subsequently the airfoil. Experimental testing did not indicate a significant change in measured temperatures when the nitrogen pressure was increased or decreased substantially. Preliminary model results (shown in Figure 79) indicated that any amount of nitrogen has a significant effect on the gas temperature, especially on the trailing edge. To increase the airfoil temperature as much as possible, the pyrometer tubes were removed and plugged.

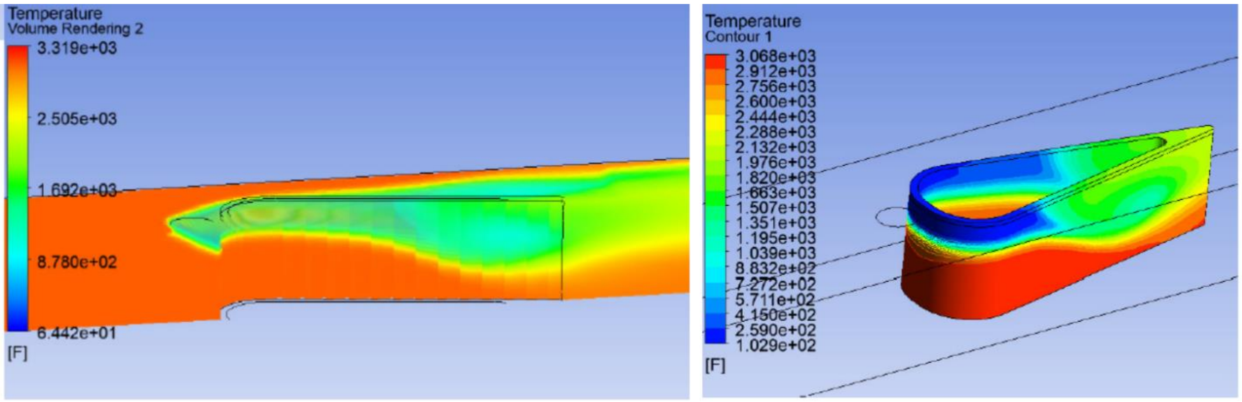

Figure 79: Initial modeling results showing the gas temperature contours with the influence of the cold nitrogen purge of the leading-edge pyrometer tubes.

4.2.2.3 Down selected Testing Procedure (Architectures 2B, 1B, and 0A)

Given the lessons learned from testing the TTT Airfoil, Architecture 1A, and the combustion flow modeling results, the decision was made to remove the upstream pyrometers for the future testing as noted in Figure 80. The threaded ports were sealed with stainless steel plugs and Type K thermocouples were tack welded to the caps to monitor the temperature. These temperatures were recorded in the ESCORT data acquisition system and logged as the pyrometer tube temperatures.

In all the airfoil testing from this point onward (Airfoils 2B, 1B, and 0A), the run conditions and test progression were kept consistent. Prior to testing, the water systems were flushed, and fuel was transferred to the main CE-5 tank. Air was available at approximately 9AM and the rig was pressurized to ~100 psi to complete a leak check. While at leak check pressure, cameras were set up and water valves to the test hardware were opened. Next, the preheater was lit, and the rig began to heat while the fuel system was readied. At 780F the injector was lit. The temperature and pressure of the rig were raised to get to the testing condition of 275 psi and 1030F while fuel was adjusted to obtain a calculated adiabatic flame temperature (T4) in the range of 3000-3100F.

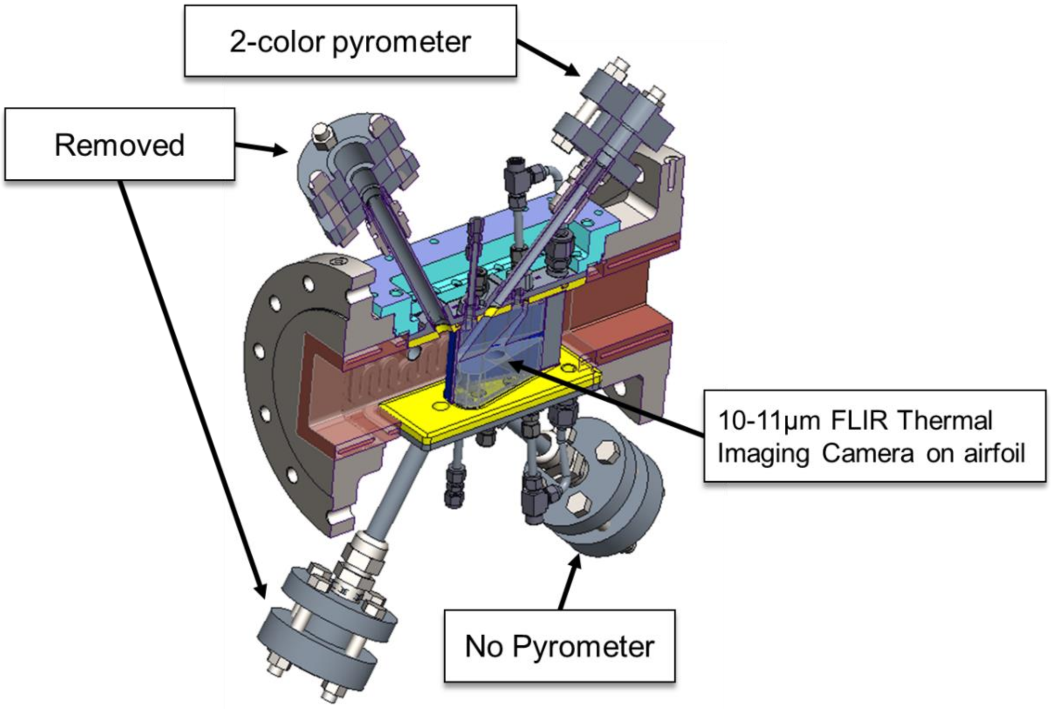

Figure 80: Test configuration for Architectures 2B, 1B, and 0A.

During the ramp up and light off conditions, a ‘maximum’ cooling flow was maintained on the backside of the airfoil through the Inconel support. Maximum cooling is defined by the inlet valve opening to the piping that goes to the backside of the hardware through the Inconel stalk. For the tests that will be discussed, a value of ~0.150-0.170 pounds/second of T3 air was delivered. The valve was sized to provide a higher flow rate, but the orifice size in the Inconel stalk limited this flow of air through the hardware. At these maximum flow conditions, the inlet temperature was ~850F and the outlet (back into the rig) was ~900F, although these values varied between the airfoils and throughout the test. After reaching the maximum flow conditions and holding for 5-10 minutes, the valve was closed to a nominal value of ~30% open which lowered the backside flow rate to ~0.125 pounds/second. This condition was also held for 5-

10 minutes to collect additional data. At the reduced conditions, the inlet and outlet temperatures were both approximately 800-820F. Finally, the backside T3 air supply was closed off completely and the only flow on the backside of the airfoil was the nitrogen purge through the backside pyrometer tubes. The nitrogen inlet pressure was reduced until the temperature of the pyrometer tubes began to rise. Ultimately, the inlet nitrogen pressure was held between 252 and 265 psig (close to the P5 value to minimize flow), which maintained a steady state temperature of 200-250F on the inlet nitrogen tubes. The pyrometer tube nitrogen flow rate was not measured since it was pressure controlled. The inlet temperature was assumed to be ~75F and the outlet temperature was 700-900F, although this value is difficult to measure since the flow rate was so low.

By stepping down the cooling air under the described manner above, three run points were collected during each run day to check consistency and for future modeling efforts. The test parameter with nearly no cooling air (solely nitrogen flow) was chosen as the optimal condition since it provided the highest surface and backside temperatures of the EBC and CMC, respectively.

Test Conditions for Architectures 2B, 1B, and 0A

- Pressure: 275 psi
- Combustion gas temperature: 3000-3100F
- Mass Flow: ~2.0 lb/s
- Velocity: 44 m/s
- T3: 1025-1050F

For shutdown, the preheater setpoint is lowered to start bringing the T3 down to 700F. Fuel conditions are set to a lower value for the 30-40 minutes required to drop T3. At ~700F, the fuel is turned off and pressure and air flow are adjusted to maintain around a 4-5% ΔP across the rig while cooling down to 200F. At ~200F, water cooling is turned off, air is shut down and the remaining systems are secured.

4.2.2.4 HyTEC Architecture 2B

Architecture 2B was installed on March 11, 2024, for testing to begin on Tuesday, March 12th. 2B was chosen instead of 2A given the challenges and questions from the Architecture 1A test. As mentioned above, the leading edge (upstream) pyrometer tubes were removed and plugged during the install to eliminate any upstream nitrogen airflow that would cool the airfoil. Table 15 shows the nominal ranges for the temperatures measured during the test with minimal cooling (pyrometer nitrogen only).

There was minimal change in the airfoil temperatures or rig during the testing, as shown in Figure 81. Borescope inspection of the test section after the first day revealed that Architecture 2B had cracked along the trailing edge in a nearly identical manner to Architecture 1A. However, the GEA and NASA teams discussed this issue, and it was decided that since there was no danger to the facility, the airfoil would continue to be tested. The team considered that the break in the CMC did not significantly affect the test since the focus for the effort was to test the EBC, not the CMC. Testing on Architecture 2B concluded during the week of April 1. A total of ~76.25 hours of time at condition was accumulated on the airfoil and images of the airfoil are shown in Figure 82-Figure 83.

Table 15: Nominal temperatures and run times for Architecture 2B test days.

Architecture 2B				
Date	**Side Temperature (°F)**	**Backside Leading Edge (°F)**	**Hours at Condition**	**Notes**
3/12/2024	2550-2600	N/A	8	
3/13/2024	2500-2550	N/A	7.5	
3/18/2024	2500-2525	1170	9	Changed to 2.1/2.4 micron pyro
3/19/2024	2550-2575	1620	8.5	Lowered pyro tube pressure
3/20/2024	2550-2575	1650	9	
3/21/2024	2550-2600	1650	8.5	
3/27/2024	2250-2300	1635	8	Alignment or obstruction?
4/1/2024	2350-2400	1590	9	
4/3/2024	2350-2500	1600	8.75	Lens showing deposit
		Total Hours:	**76.25**	

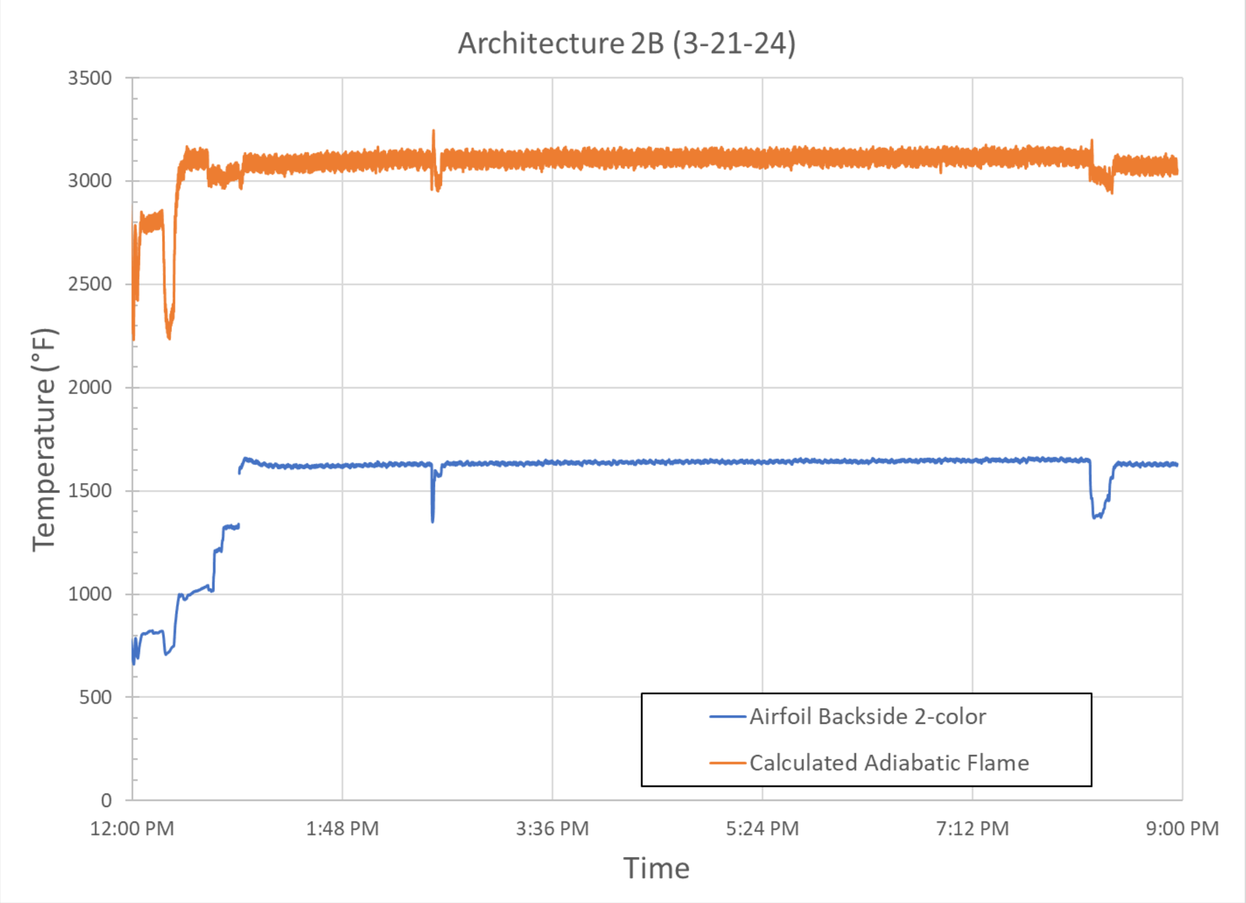

Figure 81: Temperature plots for the leading-edge backside and adiabatic flame temperatures for Architecture 2B on 3-21-24.

Architecture 2B As-Received

Architecture 2B After Testing (76.5h)

Figure 82: Leading Edge of Architecture 2B before and after testing.

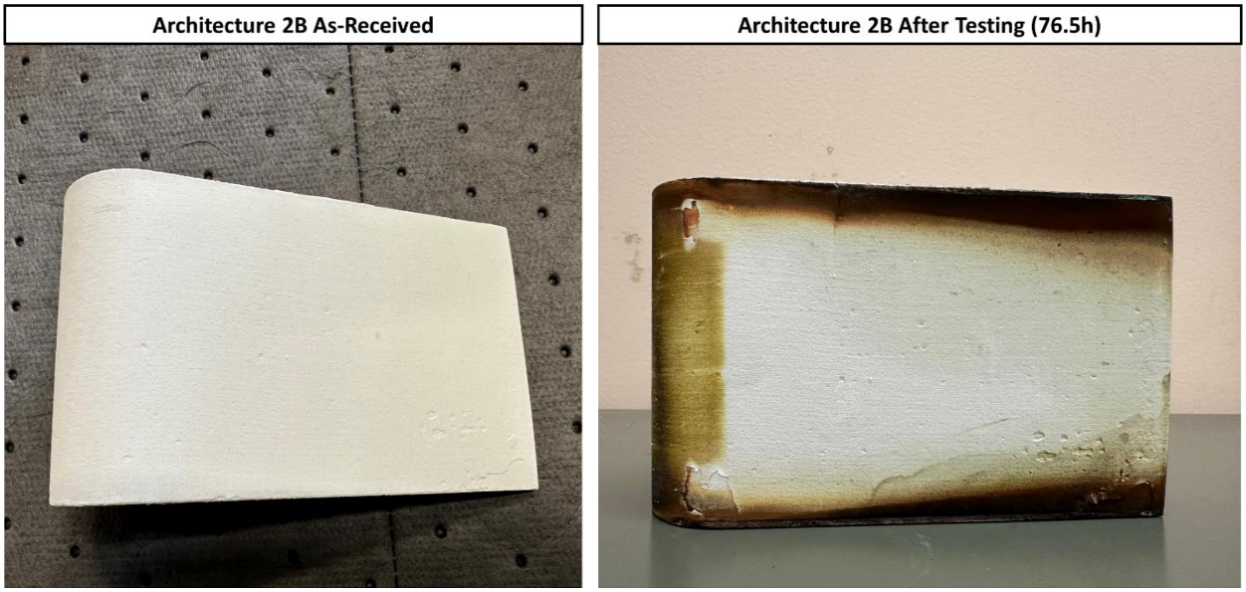

Architecture 2B As-Received

Architecture 2B After Testing (76.5h)

Figure 83: Thermal imaging camera side view of Architecture 2B before and after testing.

There was more spallation of the topcoat observed in Architecture 2B than Architecture 1A. It is unknown currently whether the spallation can be attributed to coating processing defects, additional testing time, a more aggressive testing environment, or some combination thereof. However, after a similar amount of time to the 1A airfoil (33 hours), borescope images from March 20th show that the airfoil was already showing significant spall on the leading edge. However, the spallation that was observed was generally on the leading edge and did not extend through the bond coat to the substrate. The trailing edge was well adhered with limited spallation. After testing, the airfoil was photographed and shipped back to GEA during the week of March 11th.

4.2.2.5 HyTEC Architecture 1B

Architecture 1B was installed on April 8th, 2024 for testing to begin on Tuesday, April 9th. The test conditions were maintained as mentioned in the Procedure section. Prior to the installation, a Type B thermocouple was mounted by GEA to the inside of the leading edge between the gap of the two Inconel stalks to provide a temperature comparison to the 2-color pyrometer. The leads for the Type B thermocouple were determined to be too short and problematic to support and the research team at NASA opted to remove the Type B and mount a longer insulated Type K thermocouple at the same location. The thermocouple wire exited the airfoil via a fitting in front of the bottom backside pyrometer viewing flange. The intent of this thermocouple was to help validate the 2-color pyrometer data. Table 16 shows the nominal ranges for the temperatures measured during the test with minimal cooling (pyrometer nitrogen only).

Table 16: Nominal temperatures and run times for Architecture 1B test days.

Architecture 1B					
Date	**Side Temperature (°F)**	**Backside Leading Edge (°F)**	**Hours at Condition**	**Backside mounted T/C (°F)**	**Notes**
4/9/2024	2175	1750	6.75	1240	
4/10/2024	2275-2300	1755	9.25	1375	Cleaned side lens
4/11/2024	2425-2450	1775	0.58	1300	Replaced side lens
4/16/2024	2375-2400	1800	5.5	1275	
4/18/2024	2375-2400	1825	8.75	1300	
4/22/2024	2400	1800	9.5	85	
4/23/2024	2375	1775	9.5	88	
4/24/2024	2375-2400	1750	10	78	
4/25/2024	2375-2400	1725	9	82	
4/29/2024	2400	1600	7.5	83	
		Total Hours:	**76.33**		

The backside mounted Type K thermocouple survived for ~30 hours at testing conditions. It was confirmed to be broken during the disassembly of the rig on April 30th, but relevant data was not collected since April 18th. The backside temperature of the mounted thermocouple was shown to be in the range of 1200-1400F while working at conditions, which was consistently ~400F lower than the pyrometer temperature. A plot of the temperature of the mounted thermocouple and the backside pyrometer during an entire day’s testing is shown in Figure 84. Both measurements are very consistent during the testing window and trends typically follow each other. The likely difference in temperature is likely related to the ceramic adhesive that was used to affix the thermocouple to the backside of the airfoil. Two other considerations are that the 2-color pyrometer data reports the maximum temperature in the viewport, and that the two temperature measurements are not likely in the same location. This information indicates that the two measurements likely bound the average temperature in the region, although the 2-color pyrometer data may be more reliable because of the uncertainty of configuration of the ceramic adhesive.

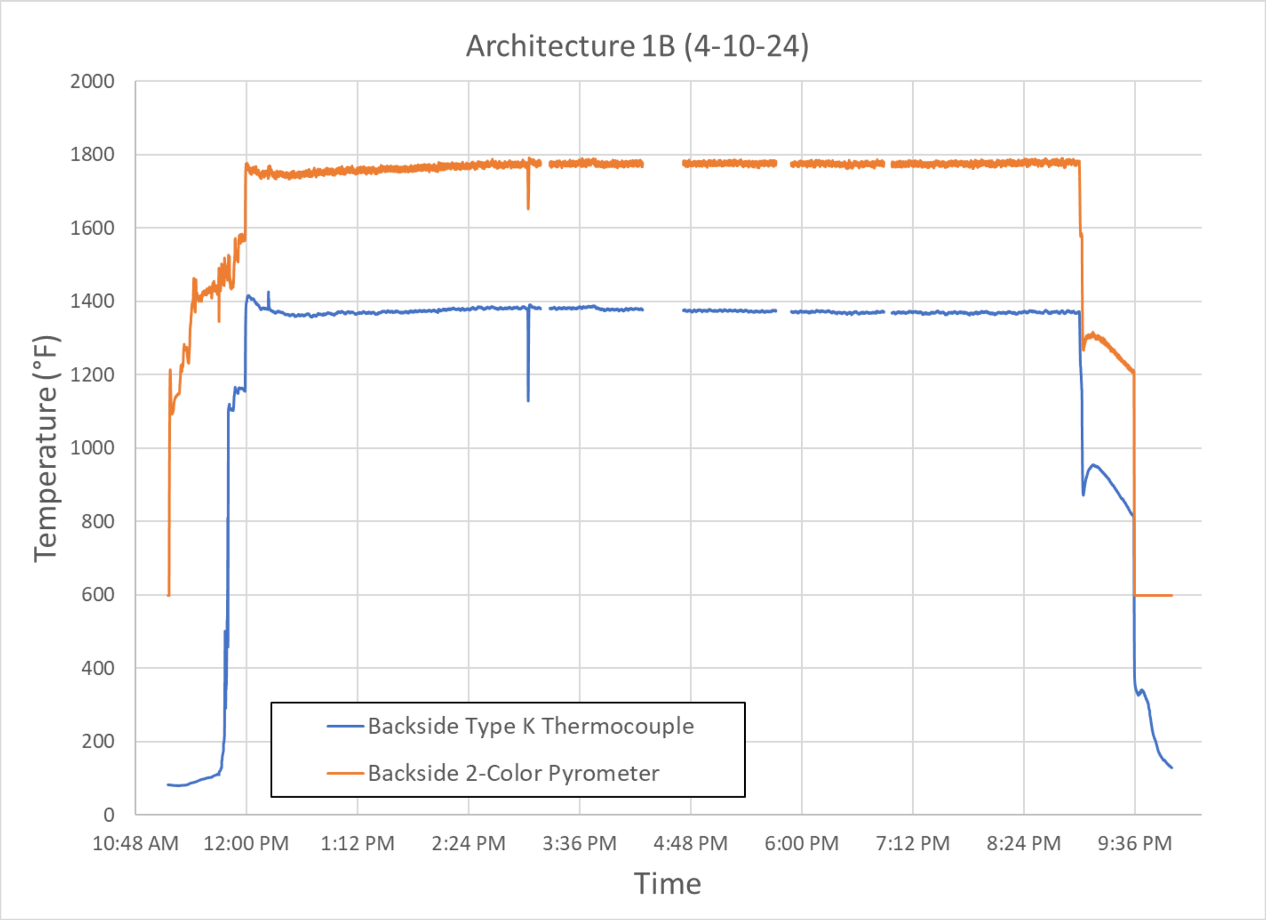

Figure 84: Pyrometer and mounted thermocouple data for Architecture 1B for the entire day of testing on 4-10-24.

Images of the Architecture 1B airfoil after testing are shown in Figure 85 and Figure 86. As in the Architecture 2B airfoil, the coating delamination was generally located on the leading edge. The airfoil split in the same location as both previous airfoils after the first day of testing (4/9/24). As in Architecture 2B, testing continued to a final exposure time of 76.3 hours. Any observed spallation was generally the topcoat and did not extend through the bond coat to the substrate. The trailing edge was well adhered with limited spallation despite the split. After testing, the airfoil was photographed and shipped back to GEA during the week of May 6th.

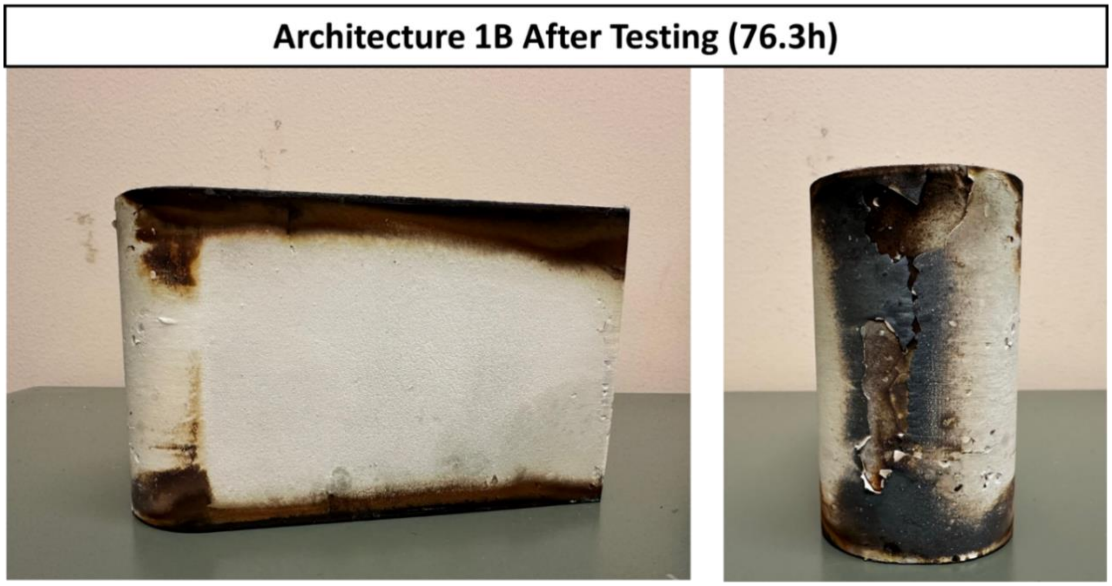

Figure 85: Photos of the airfoil with coating Architecture 1B after 76.3hrs of testing. The left image is the thermal imaging camera side of the hardware,

Figure 86: Photos of the airfoil with coating Architecture 1B after 76.3hrs of testing. The topmost image is the top surface of the airfoil, and the top image has the thermal imaging camera side up. The bottom images are the opposing sides.

4.2.2.6 HyTEC Architecture 0A

The architecture 0 chemistry listed in section 4.2.2.6 of this report are based on work mentioned under [41], [42], [43], [44], [45] and [46].

Architecture 0A was installed on May 1, 2024 to begin testing on Thursday, May 2nd. Architecture 0A was the NASA-developed EBC chemistry evaluated under the HTEBC project, but the CMC substrate was manufactured by GEA in the same manner as the previously discussed airfoils. The test conditions were maintained as mentioned in the Procedure section. Prior to the installation, a Type K thermocouple was mounted by NASA to Inconel airfoil stalk behind the outlet opening, as shown in Figure 87. As in the Architecture 1B test, the thermocouple wire exited the airfoil via a fitting in front of the bottom backside pyrometer viewing flange. The intent of this thermocouple was to provide input for the model and to better understand the backside condition of the airfoil.

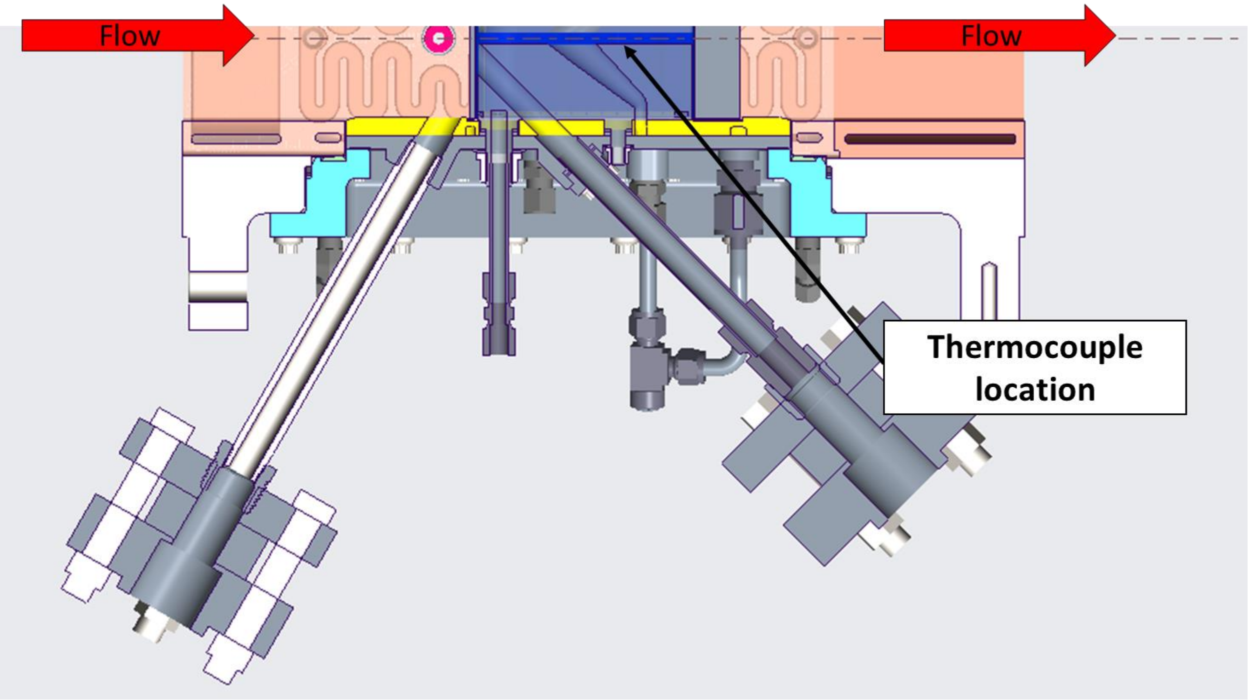

Figure 87: Cross section of the hardware indicating the location of the Type K thermocouple on the airfoil stalk. Note that the leading-edge pyrometer was removed for Architecture 0A.

On the first day (5/2/24), the rig was run with maximum cooling of ~0.165 lb/s air to determine if this could avoid the airfoil splitting down the trailing edge. Unfortunately, borescope results indicated that the airfoil was split after the first day and subsequent run days would be executed in an identical manner to Architectures 2B and 1B with only pyrometer tube nitrogen cooling flow. Table 17 shows the nominal ranges for the temperatures measured during the test. As mentioned above, a thermocouple was mounted on the Inconel airfoil stalk to monitor the temperature and correlate it to the thermal model. The thermocouple survived the entire test and was still intact when the hardware was removed. A trace of the backside 2-color pyrometer and the Inconel airfoil stalk thermocouple is shown in Figure 88. There was some variation in both temperatures for the first 90 minutes, but after that point the two temperatures were very consistent. The difference in the two temperatures was consistently ~175F.

Table 17: Nominal temperatures and run times for Architecture 0A test days.

Architecture 0A					
Date	**Side Temperature (°F)**	**Backside Leading Edge (°F)**	**Hours at Condition**	**Airfoil T/C (°F)**	**Notes**
5/2/2024	2450-2475	1350	8.5	1097	Ran max cooling conditions
5/6/2024	2600-2650	1590	9.5	1408	
5/8/2024	2680	1575	8.32	1460	
5/14/2024	2600-2625	1600	10	1490	
5/16/2024	2600-2625	1585	10.75	1557	
5/20/2024	2450-2475	1500	5.5	1500	
5/21/2024	2425-2450	1500	11	1512	
5/22/2024	2425-2450	1615	10	1550	
5/23/2024	2650-2675	1585	5	1490	Cleaned lens prior to run
		Total Hours:	**78.57**		

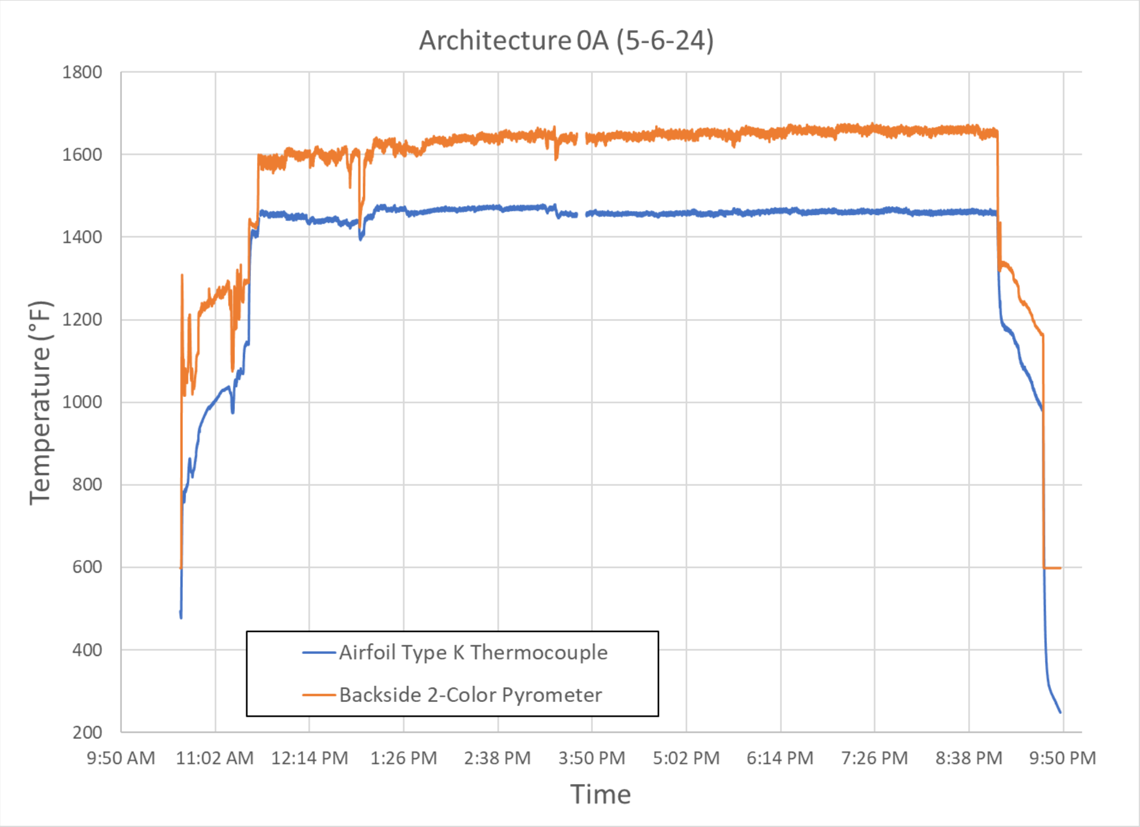

Figure 88: Pyrometer and airfoil mounted thermocouple data for Architecture 0A for the entire day of testing on 5-6-24.

Images of the Architecture 0A airfoil after testing are shown in Figure 89 through Figure 92. As in the Architecture 2B and 1B airfoils, the coating delamination was generally located on the leading edge. The airfoil split in the same location as both previous airfoils after the first day of testing (5/2/24). In the

Architecture 0A sample, there was observed spots of failure that occurred down below the bond coat. There was also a single (uncoated) ply that delaminated completely from the internal surface of the airfoil, seen in Figure 90. The internal surface also showed significant matrix spallation, noted by the small missing circles on the inner body in Figure 92. The CMC also showed significant interlaminar failure on the leading edge. The main airfoil surfaces were well adhered, but cracks were present and parallel to the direction of the combustion flow. After testing, the airfoil was photographed and shipped back to GEA during the week of May 27th.

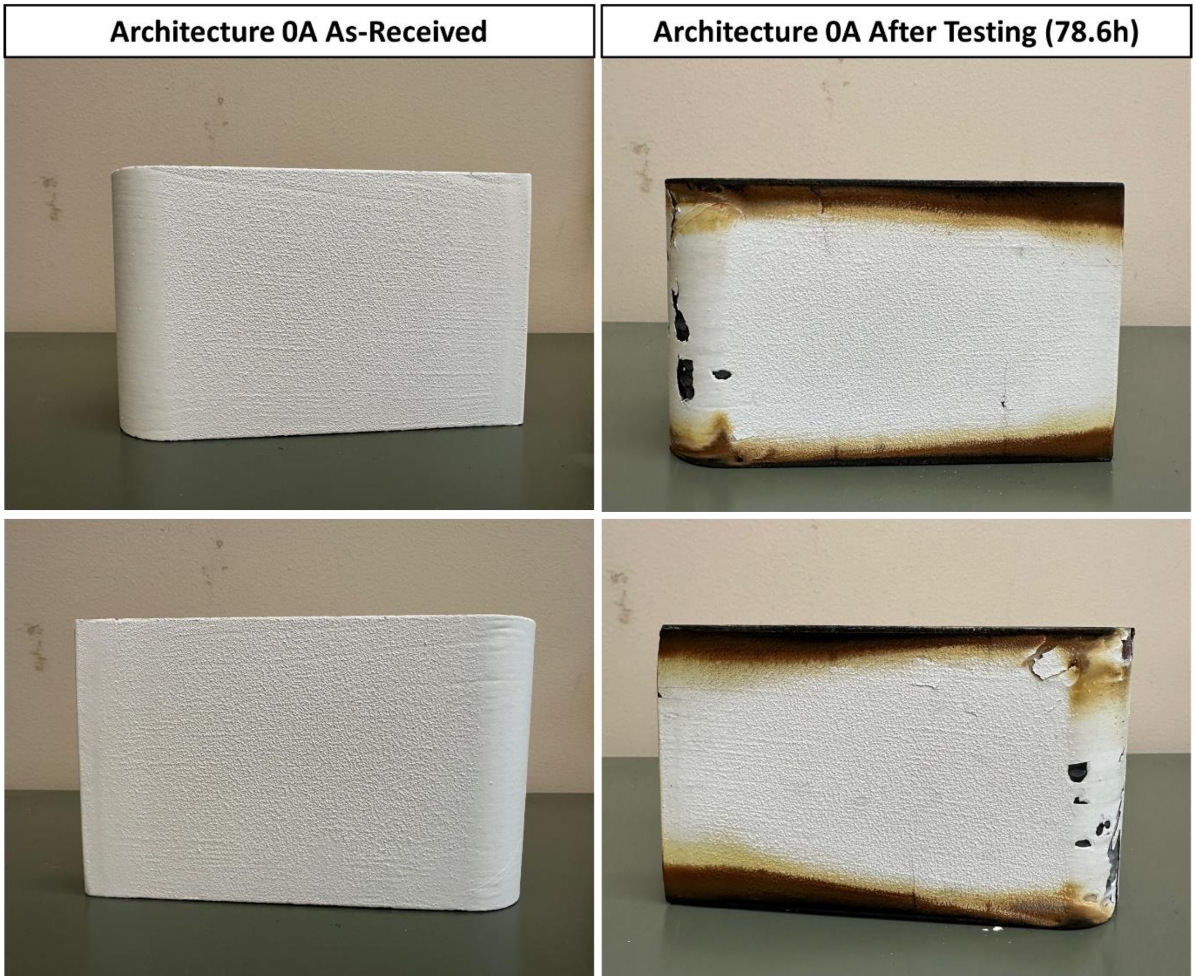
Architecture 0A As-Received

Architecture 0A After Testing (78.6h)

Figure 89: Airfoil with coating Architecture 0A before and after testing for the thermal camera side (top) and thermocouple side (bottom).

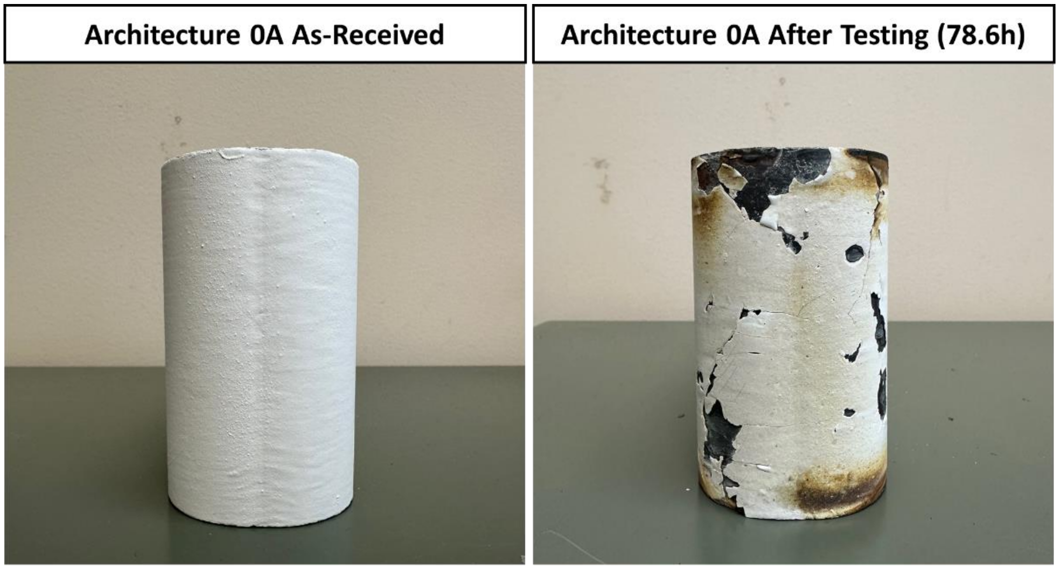

Figure 90: Airfoil with coating Architecture 0A before and after testing.

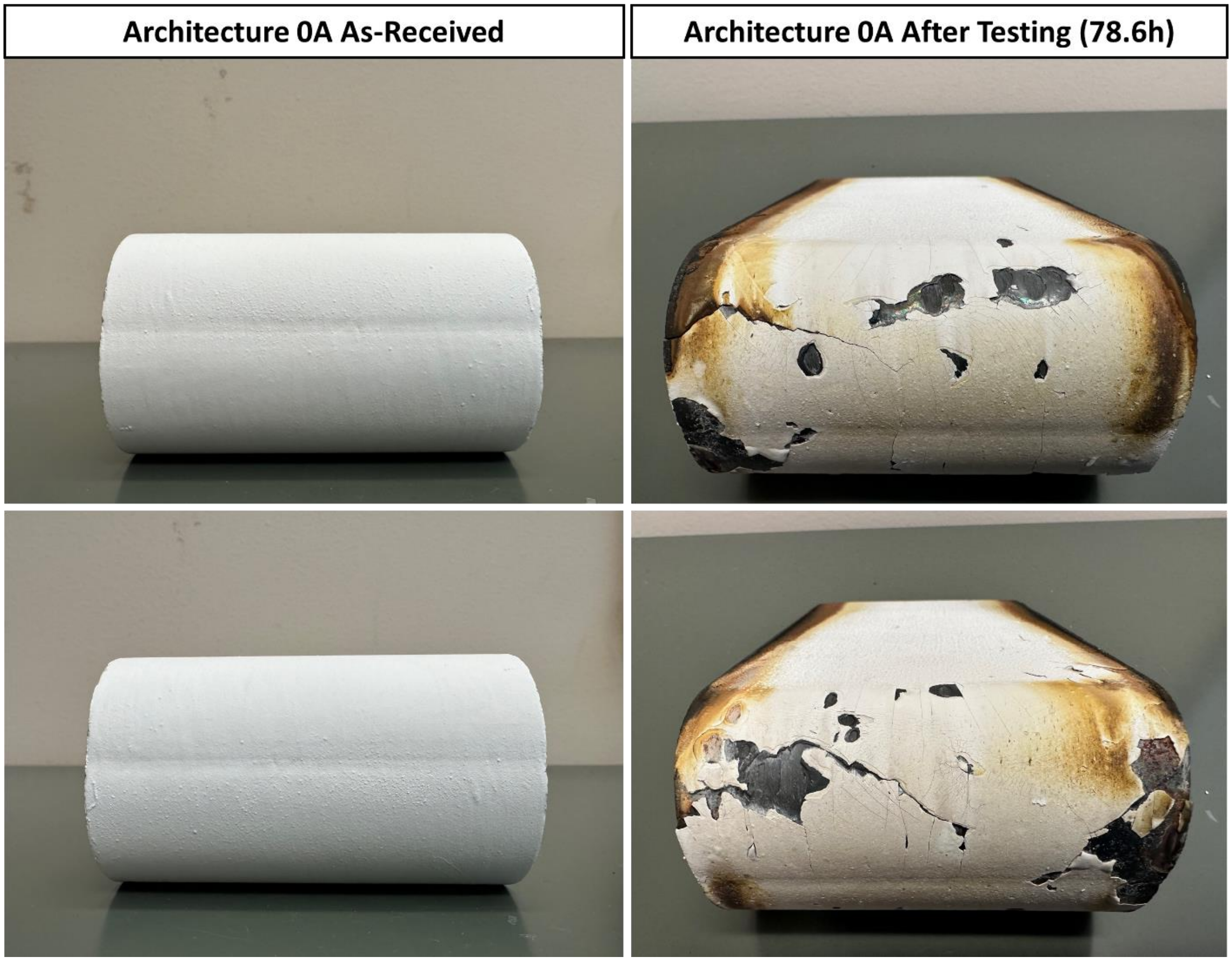

Figure 91: Airfoil with coating Architecture 0A before and after testing.

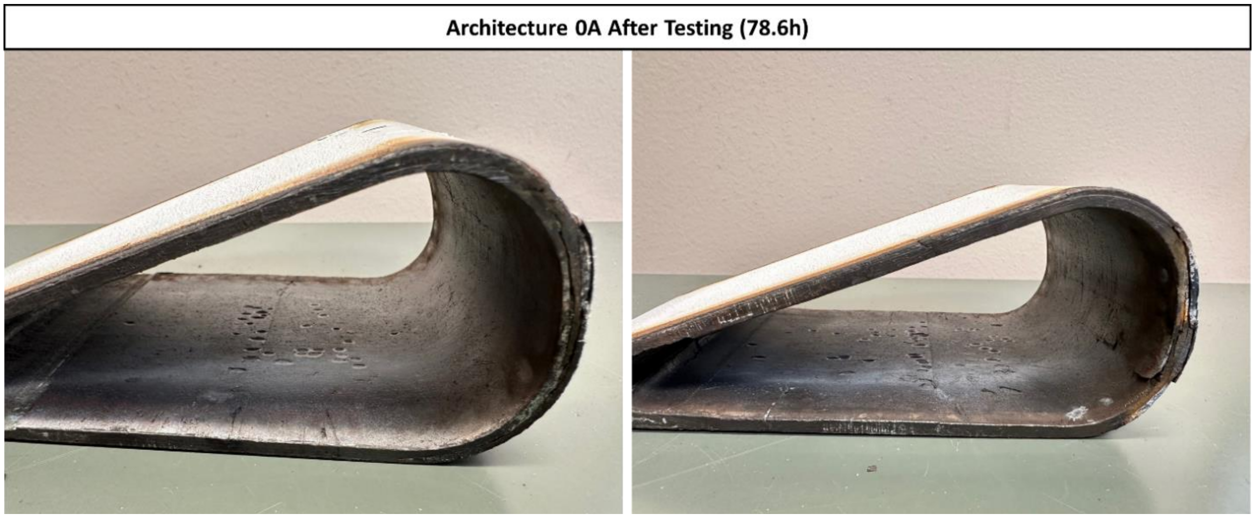

Figure 92: Airfoil internal surface for the thermal camera side (left) and the thermocouple side (right) showing matrix spallation.

4.2.2.7 Comments for CE-5 Test Rig

The testing of the hardware under similar conditions above yielded a range of temperatures on the airfoils. The test temperatures mentioned above are shown here for ease of comparison:

Table 18: Representative temperature readings for Architecture 1A during CE-5 rig test run.

Architecture 1A					
Date	**Single Wavelength Leading Edge (°F)**	**2-color Leading Edge (°F)**	**Side Temperature (°F)**	**Backside Leading Edge (°F)**	**Hours at Condition**
2/22/2024	1900	N/A	2450	1700	4
2/26/2024	1675	2250	2250	1675	5
2/27/2024	1700	2300	2200	1630	6.7
2/28/2024	1650	2325	1900	1650	6.1
2/29/2024	1650	2325	1800	1650	5.5
3/6/2024	1575	2270	2365	1450	8.2
				Total Hours:	**35.5**
2/26 & 2/27 had thermal camera on the leading edge and the pyrometer on the side.					
All other days had the camera on the side and the pyrometer on the leading edge					

Table 19: Representative temperature readings for Architecture 2B during CE-5 rig test run.

Architecture 2B				
Date	**Side Temperature (°F)**	**Backside Leading Edge (°F)**	**Hours at Condition**	**Notes**
3/12/2024	2550-2600	N/A	8	
3/13/2024	2500-2550	N/A	7.5	
3/18/2024	2500-2525	1170	9	Changed to 2.1/2.4 micron pyro
3/19/2024	2550-2575	1620	8.5	Lowered pyro tube pressure
3/20/2024	2550-2575	1650	9	
3/21/2024	2550-2600	1650	8.5	
3/27/2024	2250-2300	1635	8	Alignment or obstruction?
4/1/2024	2350-2400	1590	9	
4/3/2024	2350-2500	1600	8.75	Lens showing deposit
		Total Hours:	**76.25**	

Table 27: Representative temperature readings for Architecture 1B during CE-5 rig test run.

Architecture 1B					
Date	**Side Temperature (°F)**	**Backside Leading Edge (°F)**	**Hours at Condition**	**Backside mounted T/C (°F)**	**Notes**
4/9/2024	2175	1750	6.75	1240	
4/10/2024	2275-2300	1755	9.25	1375	Cleaned side lens
4/11/2024	2425-2450	1775	0.58	1300	Replaced side lens
4/16/2024	2375-2400	1800	5.5	1275	
4/18/2024	2375-2400	1825	8.75	1300	
4/22/2024	2400	1800	9.5	85	
4/23/2024	2375	1775	9.5	88	
4/24/2024	2375-2400	1750	10	78	
4/25/2024	2375-2400	1725	9	82	
4/29/2024	2400	1600	7.5	83	
		Total Hours:	**76.33**		

Table 20: Representative temperature readings for Architecture 0A during CE-5 rig test run

Architecture 0A					
Date	**Side Temperature (°F)**	**Backside Leading Edge (°F)**	**Hours at Condition**	**Airfoil T/C (°F)**	**Notes**
5/2/2024	2450-2475	1350	8.5	1097	Ran max cooling conditions
5/6/2024	2600-2650	1590	9.5	1408	
5/8/2024	2680	1575	8.32	1460	
5/14/2024	2600-2625	1600	10	1490	
5/16/2024	2600-2625	1585	10.75	1557	
5/20/2024	2450-2475	1500	5.5	1500	
5/21/2024	2425-2450	1500	11	1512	
5/22/2024	2425-2450	1615	10	1550	
5/23/2024	2650-2675	1585	5	1490	Cleaned lens prior to run
		Total Hours:	**78.57**		

The general trend of these data is that Architecture 0A exhibited the highest temperatures on the surface and lowest on the backside, Architecture 1B had the lowest temperatures on the surface but the highest on the backside, and Architecture 2B was somewhere between the two. This suggests that the effective thermal conductivity of the three would rank 0A < 2B < 1B. However, this is a relatively simplistic view to this complex test and there may be many other factors that impact the performance.

It is also worth noting that all 3 coatings tested to >76 hours exhibited some amount of coating delamination on the leading edge or just outside the leading edge. While this is likely due to a variety of factors such as processing defects as well as pressure and/or thermal gradients, it is worth considering that the trailing edge split could be inducing a compressive stress on the leading edge that could assist in buckling the coating on the leading edge. The trailing edge in all 3 airfoils were split with a ~0.125” gap. This gap opened to ~0.25” upon removal from the hardware. The copper platform restricted the airfoil from opening further during testing.

4.2.2.8 Comments on Airfoil Splitting

All 4 tested airfoils split along the trailing edge early in the testing effort. While the outcome was consistent between the tests, the cause for this has not been explicitly determined. One consideration was that the gap between the airfoil and the Inconel airfoil stalk was too small. The minimum nominal expected gap at room temperature was determined between the hardware to be ~0.0202”, as shown in Figure 93. If the Inconel 718 was assumed to have an approximate CTE of ~12 x 10-6 K-1 and the airfoil stalk reached a temperature of 1500F (~1090K), there is over 75% of the remaining minimum distance remaining. Airfoil 2B had a 5-10 mil smaller cavity size but this is not expected to make a difference given the margins. Although there is theoretically enough space, if the airfoil is offset from center and shifted forward, the gap at the trailing edge will be much smaller than the nominal gap. Shims were used with Airfoils 1B and 0A to avoid the airfoil shifting but did not avoid the airfoil splitting during the first day. The airfoils could have shifted during installation after the shims were removed or when the top was bolted into place.

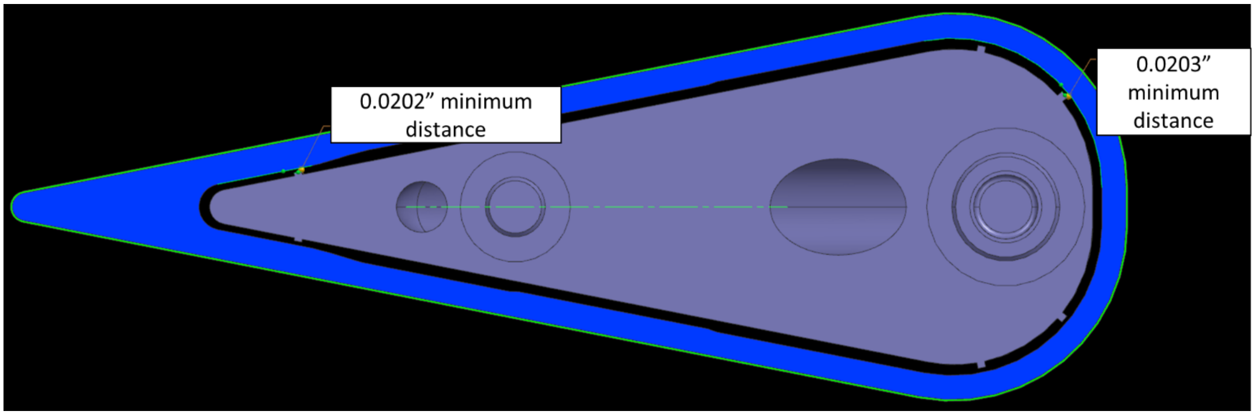

Figure 93: Overhead view of airfoil (blue) and Inconel (purple) with minimum gap assuming the airfoil is centered.

In addition to the lack of sufficient gap with the airfoil stalk, the pressure and airflow temperatures within the airfoil could have resulted in fracture along the trailing edge. If the airfoil broke during testing, there should be an observed pressure drop in the inlet/outlet pressures across the hardware. The data for the day prior to the crack observation was analyzed for these pressure drops and shown in Figure 94. In airfoils 2B, 1B, and 0A there is a noted drop in pressure of ~25psi at various points during the run. These have been noted as ‘possible’ points of failure since this is being inferred, but the noted drops in pressure are significantly larger than other fluctuations. Other runs had similar occasional pressure drops like those shown here after the airfoil was confirmed to have split. However, those pressure drops could be due to further cracking or flow fluctuations in and around the airfoil. Airfoil 1A did not have any noted drops in pressure during the test on March 6th, and borescope results afterwards did not indicate any failures. Testing on March 7th had issues with backpressure and autoignition, and the trailing edge was shown to have split which resulted in the removal.

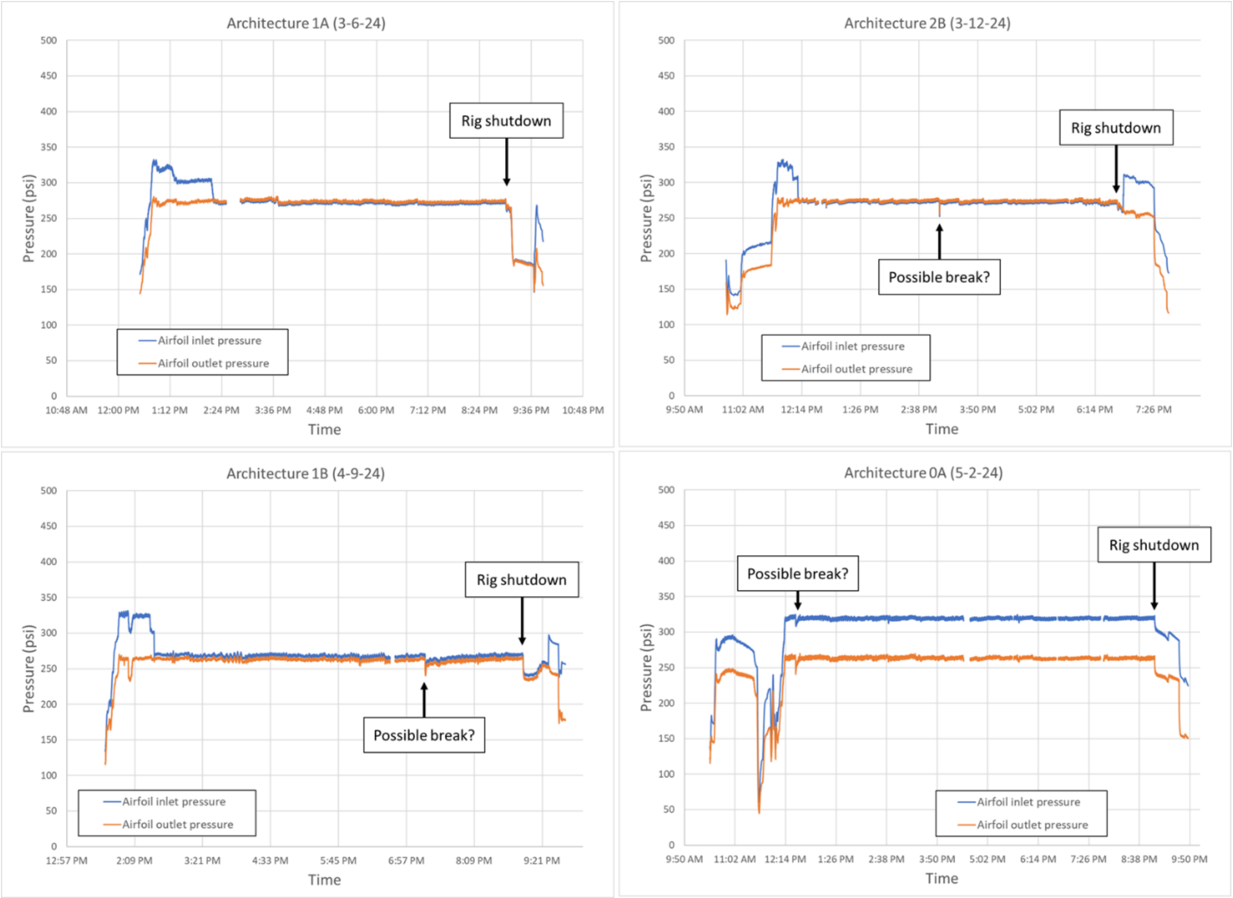

Figure 94: Pressure plots of the inlet and outlet air for the four tested airfoils on selected days.

One final consideration for the airfoil failure could be related to the shutdown sequence. The backside cooling air was usually brought back up at the end of the run during shutdown, clearly shown in Architectures 2B and 1B shown in Figure 94. Pushing colder (~600F) air onto the backside could cause a thermal condition that could exacerbate the stress at the small radius. However, this does not entirely explain why Architecture 0A fractured after the first day of testing on May 2nd when cooling air was flowing during the entire test and no pulse was observed during shutdown. An over pressurization of the airfoil was also considered, but the maximum pressure difference of the internal cavity with the combustion environment was only ~100psi. This differential was expected to be below to pressure needed to cause fracture of the airfoil. Ultimately the fracture of the airfoil is likely due to a combination of the above considerations. Future work should strongly consider larger gaps by reducing or eliminating any airfoil support structures as well as significant modeling under various conditions.

4.2.3 Rig Modeling

4.2.3.1 Introduction

Under the Hybrid Thermally Efficient Core (HyTEC) project, four ceramic matrix composite (CMC) airfoils were tested with advanced high temperature environmental barrier coatings (HTEBC). This testing was part of a larger joint effort with General Electric Aerospace (GEA). GEA provided the CMC airfoils and coatings were developed by both NASA and GEA and tested in the laboratory up to surface temperatures of 3000F. Three coating candidates were selected for testing in a relevant TRL-5 environment in the NASA CE-5 combustion test stand facility. There was no modeling initially planned under this task but to better understand the observed temperatures and the rig conditions, some basic modeling was performed and is detailed below. The models described below should still be considered preliminary, although they should provide a semi quantitative view of the complex test environment.

4.2.3.2 Model Construction

The thermal model for the GEA Airfoil is assembled in ANSYS Workbench, analyzed with the CFX module, and is a symmetrical split of the CE-5 Materials Test Fixture airfoil configuration. This configuration in the CE-5 test rig consists of an identical Test Plate (to fixture the airfoil sample) in the two modular positions (12 o'clock and 6 o'clock) in the Test Section Spool. Each test plate has its own identical Airfoil Stalk (fixtures and seals airfoil end as well and providing input and output ports for backside cooling) and an angled viewing tube for a pyrometer. With this vertical symmetry in mind, the model utilizes one test plate, one stalk, and half the airfoil model (split at the vertical center line). The combustion air flow area is also split at the vertical center line. The Test Spool was omitted from this simulation as it does not contribute significantly to the thermal condition of the airfoil sample.

The model was constructed using the CAD data for the Test Plate, Airfoil Stalk, and Airfoil. The air-solid for the cooling air flow path was created using the negative space between the airfoil, stalk, and test plate, with the entry and exit flow areas extended for modeling stability. The combustion air-solid is simple rectangular extrusion with dimensions corresponding to half of the flow area of the Test Spool (based on the 3D model). The volume of the combustion flow area occupied by the Airfoil sample was Boolean subtracted from the combustion flow volume. The coating on the outside of the Airfoil is a solid extrusion extending a uniform .014" from the airfoil surface.

4.2.3.3 Material Property Definition

The test plate is assigned CFX default copper and steel materials for the two layers of the test plate. Note: steel is an approximation for the 304 stainless steel used in the actual cool-side layer of the test and minor property difference are inconsequential for the overall thermal analysis. Both the combustion air flow and cooling air flow are modeled as CFX default ideal gas air. The Airfoil Stalk is a custom material, with the material properties assembled from the MMPDS handbook and data provided by the High Temperature Materials branch. The Airfoil CMC material and coating material are custom materials with properties assembled from data provided by GEA and NASA. Selected material properties are shown in Table 21.

Table 21: Constituent properties used for the thermal model.

	Molar Mass (g/mol)	Density (g/cm^3)	Specific Heat Capacity (J kg^{-1}K^{-1})	Thermal Conductivity (W m^{-1} K^{-1})
EBC	514	5.58	526	2.35 or 1.50
Inconel	58.10	8.19	435	11.2
Copper	63.55	8.933	385	401
Stainless Steel	55.85	7.854	434	60.5

Properties for each of the constituents were assumed to be isotropic. The EBC systems on the airfoils were multilayer, but for simplicity here they were assumed to be a single material. $Yb_2Si_2O_7$ properties were used for the molar mass, density, and heat capacity. Thermal conductivity was provided from GEA and/or measured via laser flash diffusivity. The thickness of the CMC airfoil wall was assumed to be 0.130" and the thickness of the EBC was assumed to be 12 mil (~300 μm). Two different thermal conductivities were used for the EBC and shown in two model results. Architecture 1 and Architecture 2 are expected to have a thermal conductivity of ~2.35 W/m-K while Architecture 0 is expected to have a thermal conductivity of ~1.50 W/m-K. The results that will be shown used the lower thermal conductivity value of 1.50 W/m-K, but the use of 2.35 W/m-K did not change the results significantly.

4.2.3.4 Meshing

The model was meshed with the ANSYS Mechanical using CFD PrePost options. The element shape was left to program control – with all parts except for the coating defaulting to tetrahedrons. Mesh sizing varied between parts with the finest mesh being .010” and .011” target size on the coating and cooling flow areas respectively (smallest features). Inflation layers were added to all fluid-to-solid contact surfaces. An example of the meshed surface is shown in Figure 95.

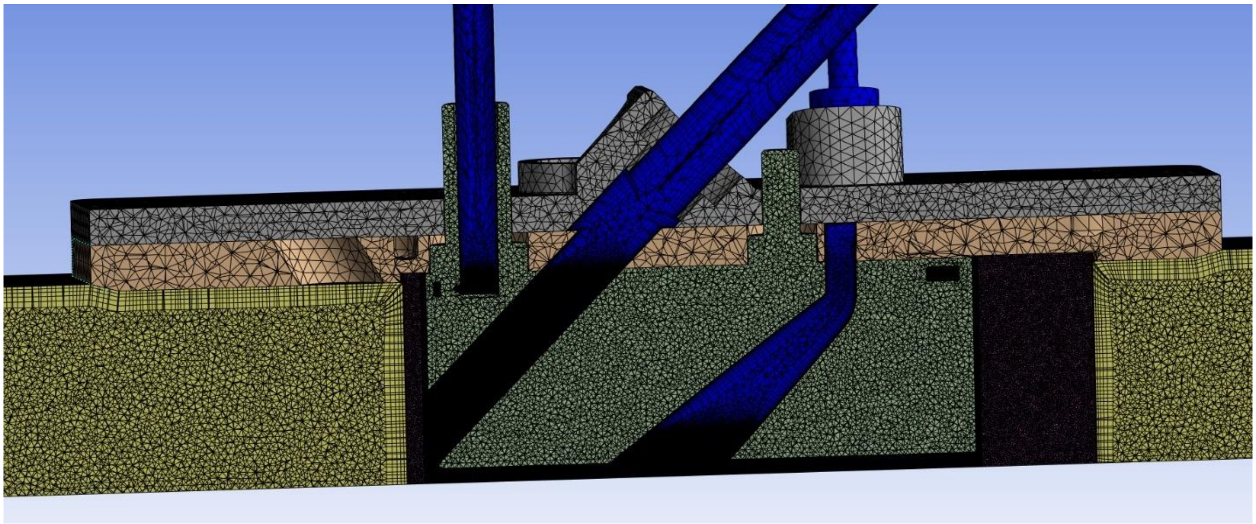

Figure 95: Meshed surface of the cross section of the airfoil and combustion path.

4.2.3.5 Boundary Conditions and Thermal Modeling Properties

The combustion flow area, airfoil, and cooling air area all use symmetrical boundary conditions at the system centerline. The copper test plate uses a temperature set point of 55°C in the water-cooling channel surfaces to simulate heat pulled from the system by water cooling. Thermal analysis for the flat plate water cooling came from previous test plate analysis. Exterior test plate surfaces used a heat transfer coefficient of 5 W/m2-K (80F outside temperature) applied to add minor convective cooling to the room facing surfaces. All solid-to-solid contacts utilized the default conservative interface flux method. Fluid to solid contact surface also utilize conservative interface flux method.

Radiative heat transfer is accomplished by setting both working fluids (combustion air and cooling air) and the solids of interest (CMC, coating, and Inconel stalk) to Monte Carlo thermal radiation method, with the gray spectral model and participating model options selected. All fluid to solid boundaries had the thermal radiation option set to conservative interface flux.

4.2.3.6 Combustion Assumptions and Cooling Configuration

Combustion conditions were designed based on the rig conditions, but pressures were changed to evaluate various configurations. A solid model of the hardware is shown in Figure 96. The inlet airflow was assumed to be 1 lb/s (half of the combustion stand flow) with a pressure of 270psi and a velocity of 44 m/s. The combustion flow was considered fully mixed and at a temperature of 3100F. In the CE-5 rig testing, a variety of cooling configurations were used. The details of these varied conditions are found in the CE-5 Rig Readiness Report as well as the Airfoil Rig Testing Report. Backside cooling air supplied into the airfoil via the Inconel Airfoil Stalk, at a T3 temperature of ~900F. This backside cooling mass flow was 0.0625-0.085 lb/s depending on the conditions. Pyrometer nitrogen cooling flow was primarily in place to keep the windows cool. In the CE-5 test, the nitrogen flow was controlled via pressure and was assumed to be ~70F. During the testing, the backside flow was eliminated in order to increase the airfoil temperatures as much as possible. This was considered the ‘minimum cooling’ configuration. The only cooling fluid for the airfoil was the nitrogen flow through the pyrometer windows, which was minimized to be as low as possible. There was still some flow measured, but it was very low and assumed to be ~0.01 lb/s for the model. In this report, from a simplicity standpoint NASA will only be evaluating the ‘minimum cooling’ configuration so the backside cooling flow noted in Figure 2 can be assumed to be zero. Models were performed with other cooling conditions but since the focus of the testing was on the case with minimum cooling, that will be the subject of this report.

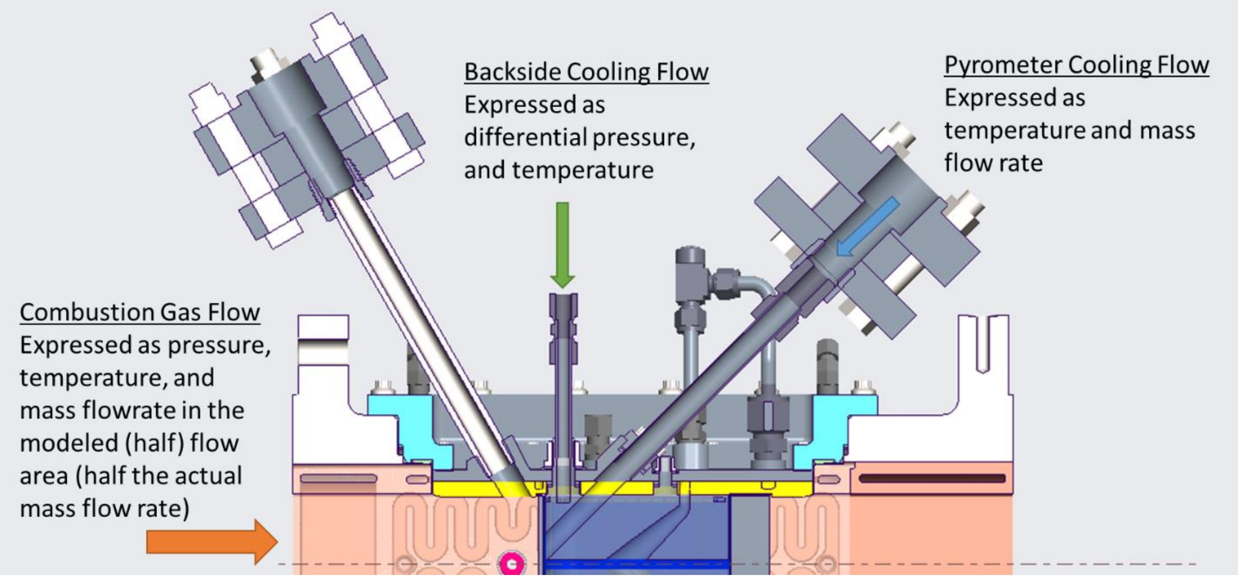

Figure 96: Cross section of the CAD drawing of the Test Section.

4.2.3.7 Temperature Measurement Locations

Thermal models were generated for the entire airfoil and EBC, but there were selected areas of interest that were selected to compare to the measured data from the rig testing in CE-5. A schematic of the hardware is shown in

Figure *97*. Data were collected for all airfoils from the 2-color pyrometer on the backside of the airfoil, and the exact dimensions of this location are shown in Figure 98. The thermal imaging camera spot location is shown in Figure 99. For Architecture 1B, a Type K thermocouple was mounted on the backside of the leading edge, just below the spot location for the backside 2-color pyrometer. For Architecture 0A, a Type

K thermocouple was mounted on the Inconel airfoil stalk. The model reports shown in later sections will identify temperatures at all these locations to compare to combustion test results.

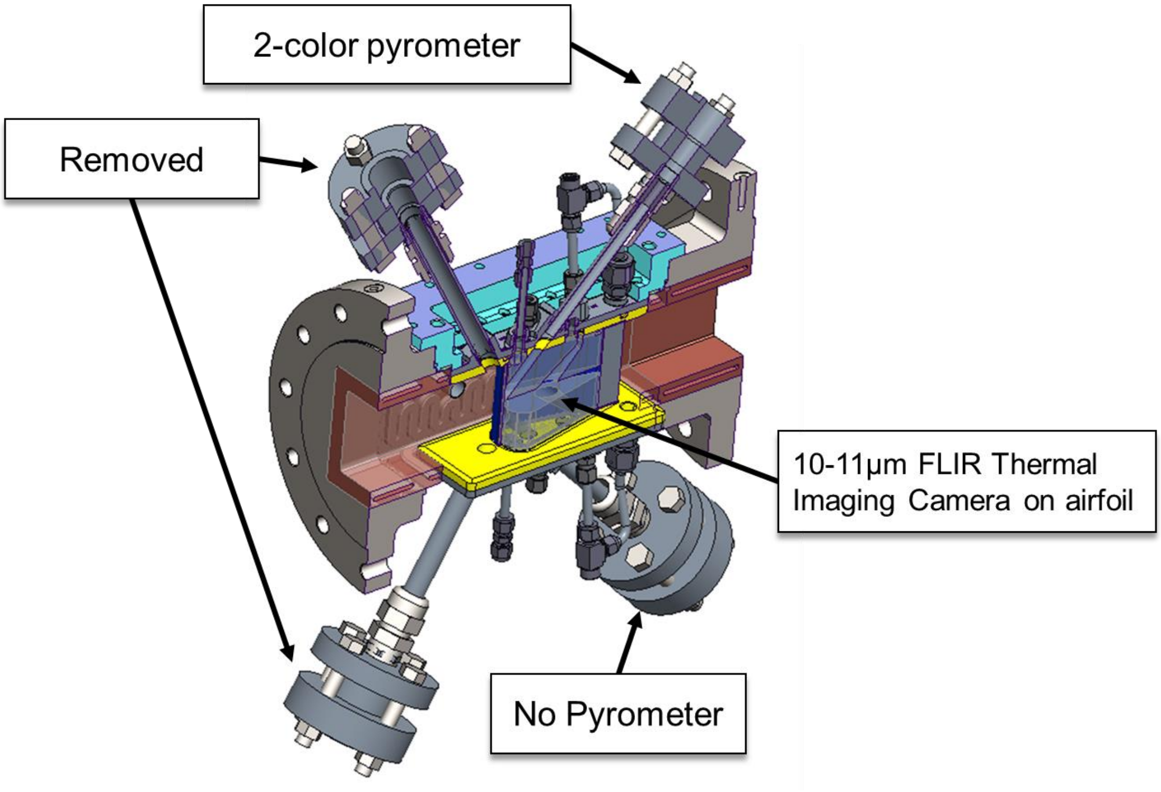

Figure 97: Schematic of the CE-5 HyTEC testing hardware indicating the location of pyrometer and thermal camera.

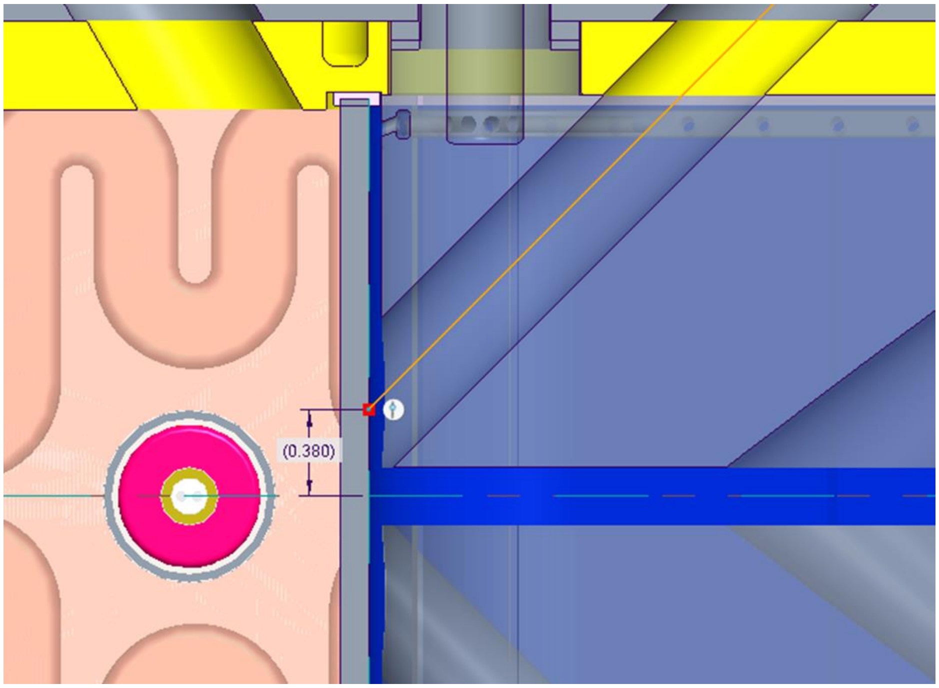

Figure 98: Side view of backside pyrometer spot location.

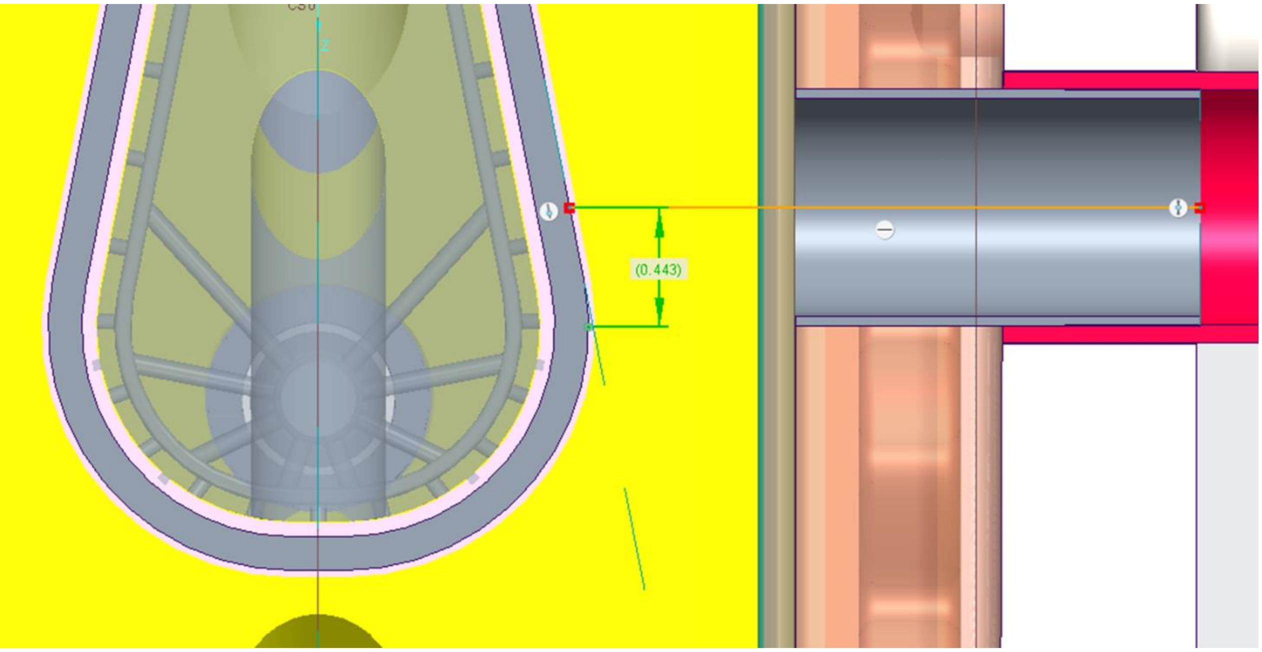

Figure 99: Overhead view of side view of thermal imaging camera on airfoil.

4.2.3.8 Model Results

The temperatures at the locations of interest are shown in Figure 100-Figure 104.

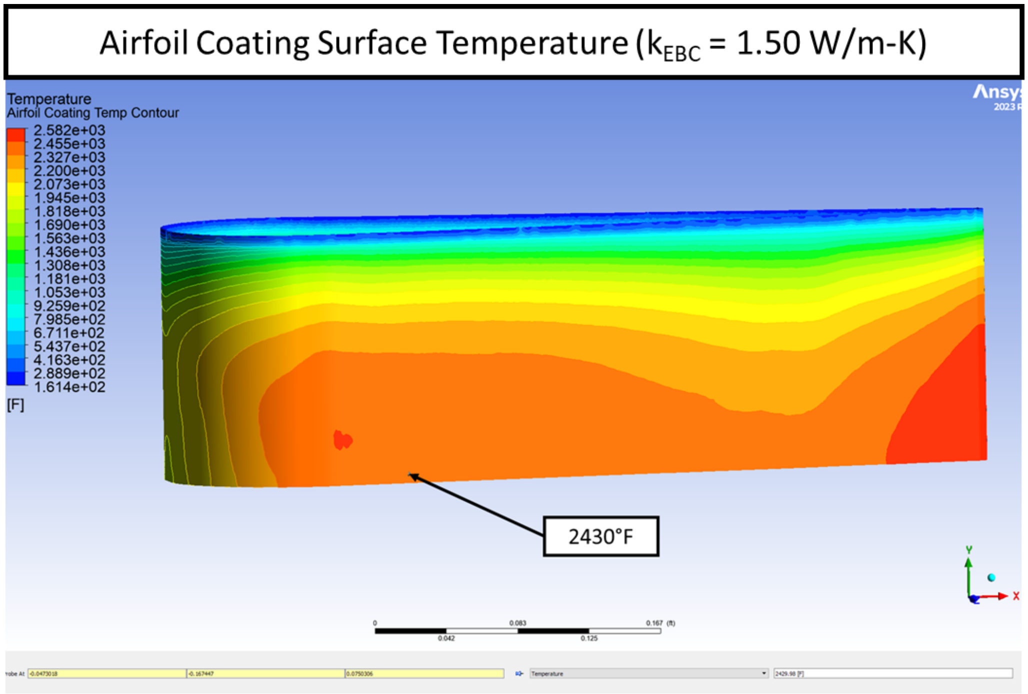

Figure 100: Airfoil EBC surface temperature surfaces with the temperature noted at the location of the thermal imaging camera.

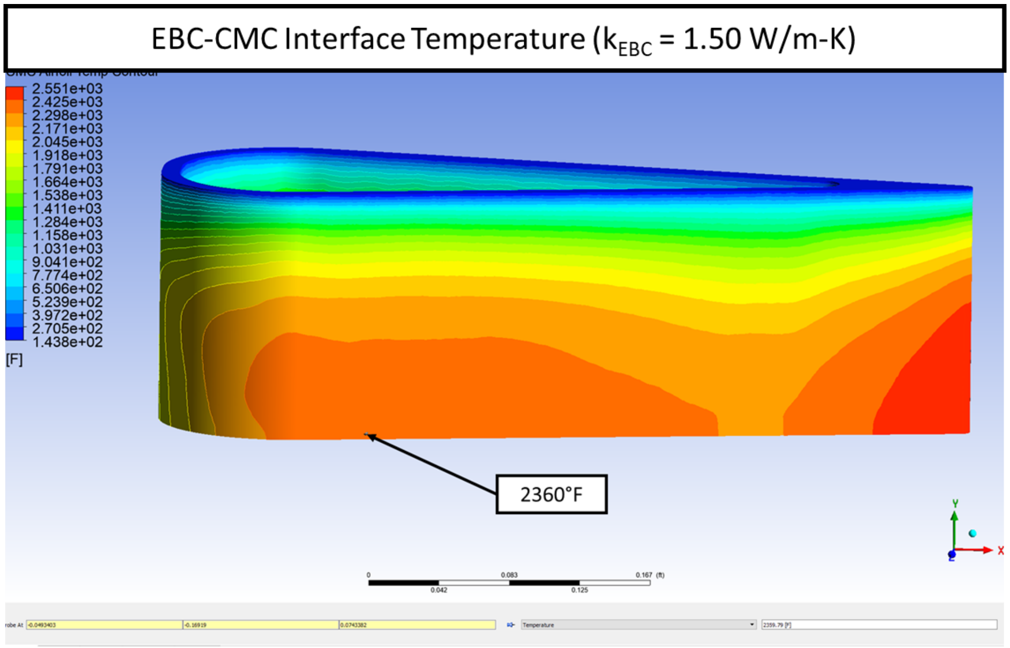

Figure 101: Airfoil EBC/CMC interface temperature surfaces with the temperature noted at the location of the thermal imaging camera.

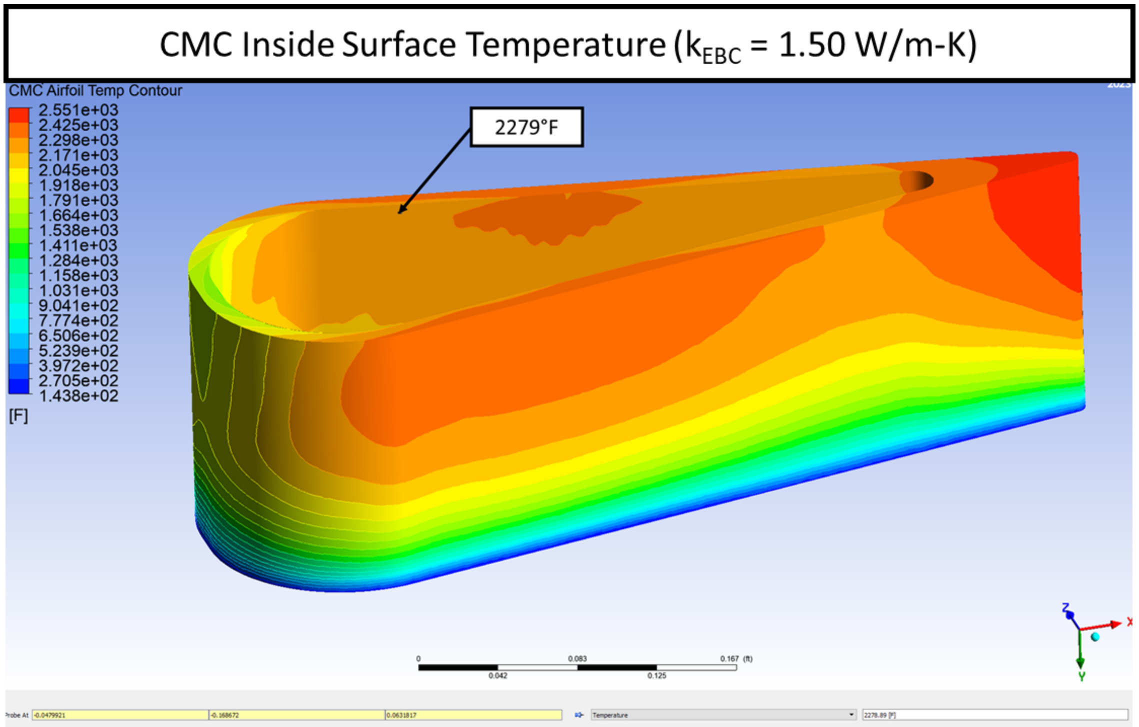

Figure 102: Airfoil CMC temperature surfaces with the CMC backside temperature noted at the location of the thermal imaging camera.

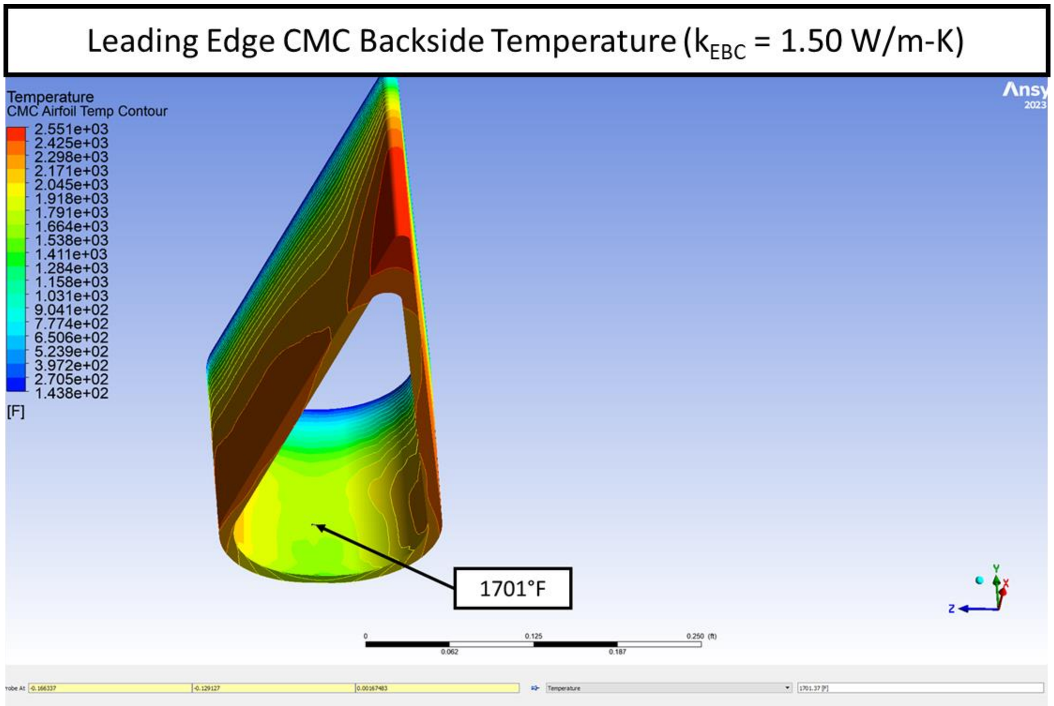

Figure 103: Airfoil CMC temperature surfaces with the CMC backside temperature noted at the location of the 2-color pyrometer.

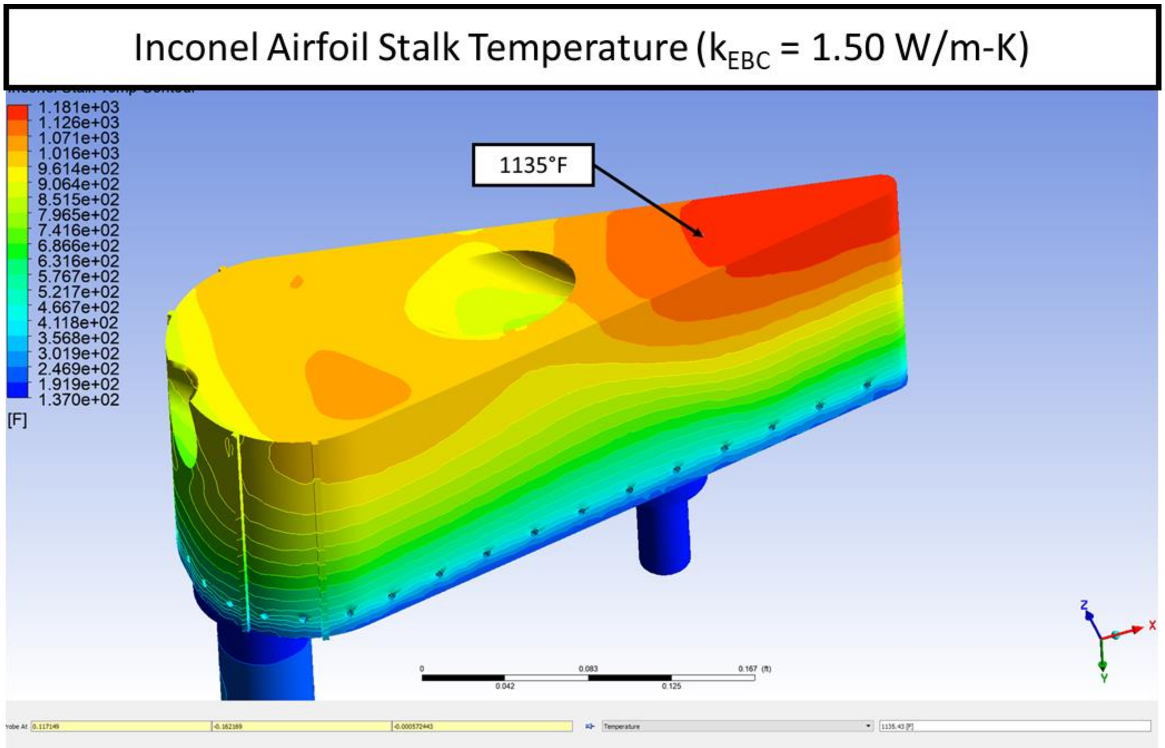

Figure 104: Inconel airfoil stalk temperature surfaces with the temperature noted at the location of the Type K thermocouple in Architecture 0A testing.

4.2.3.9 Discussion

A summary of the model results as well as measurements from three airfoils tested in the CE-5 combustion facility are shown in Table 22.

Table 22: Summary of measured and modeled values at locations on the airfoil.

	EBC Side Temperature (°F)	CMC Leading Edge Backside Temperature (°F)	Inconel Airfoil Temperature (°F)
Architecture 1B	2425	1800	---
Architecture 2B	2575	1625	---
Architecture 0A	2675	1600	1525
Thermal Model (k_{EBC} = 1.50 W/m-K)	2430	1701	1135
****Note Architecture 1B also had a leading-edge backside thermocouple that read ~1400F***			

Overall, the modeled parameters seem to provide an approximation of the Architecture 1B temperatures. One would expect that lower thermal conductivity values would cause the backside temperature to drop, as it did in Architecture 0A (compared to 1B). The measured side temperature values in Table 22 are discussed extensively in the Airfoil Rig Testing Final Report. Based on observations, the temperatures for each architecture should be considered a lower bound for the EBC temperature. Likewise, the backside temperature is heavily influenced by the pyrometer pressure although the reported values for the 2-color pyrometer are reasonable. The model results are in line with Architecture 1B but are significantly lower than Architecture 2B and 0A despite all airfoils experiencing the same combustion conditions. Therefore, it is likely that this thermal model is likely underestimating the airfoil temperatures in the CE-5 materials test facility.

As mentioned in the introduction, the results shown here are by no means a perfect representation of the CE-5 combustion test, which is very complex. For example, all the airfoils had split on the trailing edge and this model assumed a completely intact airfoil. The pursuit of this model was also very late in the testing process and should be evaluated further to improve the fidelity. However, if NASA uses these results as a lower bound and the temperature gradient distribution as a guide, the model can provide at least a semi-quantitative examination of the airfoil conditions.

The highest temperature determined on the airfoil by the model was noted as 2552F at the trailing edge and shown in Figure 105. As mentioned in the Airfoil Rig Testing Report, the likely limitation for temperature in this test was the size of the airfoil. A smaller airfoil such as the 3” x 3” TTT test article would likely reach higher temperatures with a much smaller surface area. Future work should utilize this thermal model to evaluate the TTT airfoil and compare the temperatures to what was achieved under the HyTEC effort.

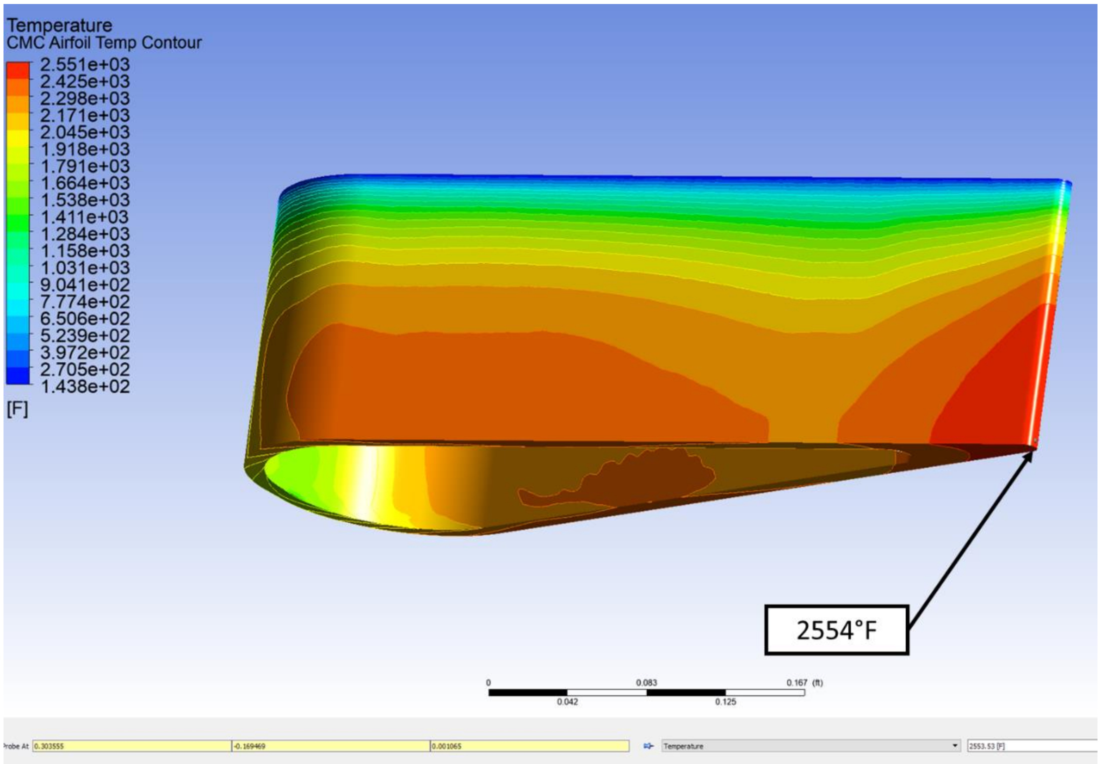

robe At 0.303555 -0.169469 0.001065 Temperature 2553.53 [F]

Figure 105: Airfoil EBC/CMC interface temperature with the highest temperature on the airfoil noted on the trailing edge.

4.2.3.10 Summary

The thermal model shown here provides a projection of what the expected combustion conditions should provide on the large, coated CMC airfoils for the HyTEC project. While preliminary, the temperatures shown here match reasonably well with the Architecture 1B airfoil. The temperatures measured for Architectures 2B and 0A were higher than 1B under the same combustion conditions, which suggests that these model results are underestimating the material temperatures. The thermal conductivities of these coatings and substrates likely play a significant role that is not captured, but these results provide a lower bound on the test conditions for the hardware. Future testing should perform this kind of modeling much earlier in the process to better understand the potential environmental conditions.

4.2.4 Post Rig Test Coating Assessments

The CE-5 rig, the rig test campaigns, and the test observations associated with HTEBC coated CMC test articles were described in the previous section. The test campaigns included four articles, which ran in sequence starting with test article Architecture 1A, Architecture 2B, Architecture 1B and Architecture 0A between February 5, 2024 and May 24, 2024. To avoid any confusions with several occasions in this report, where letters A and B were used in a generic manner to describe several Architecture 1 and Architecture 2 coating variants, GEA will re-introduce the Architecture nomenclature definitions applied to the rig test airfoil articles:

GEA HTEBC Architecture 1: Mullite-Si bondcoat / $HfSiO_4$ intermediate layer / HfO_2 topcoat.
GEA HTEBC Architecture 2: Mullite-Si bondcoat / REDSREDS intermediate layer / REMS topcoat.
Letter A: designates test articles selected as the primary candidate for rig test.
Letter B: designates test articles selected as the backup candidate for rig test.

The test conditions and nominal surface temperatures recorded on each test article via the pyrometers installed on the rig test sections were summarized in Table 14 through Table 17. The testing of the airfoil articles under similar conditions were discussed and noted in the previous section to have yielded broad ranges of temperatures on the airfoils.

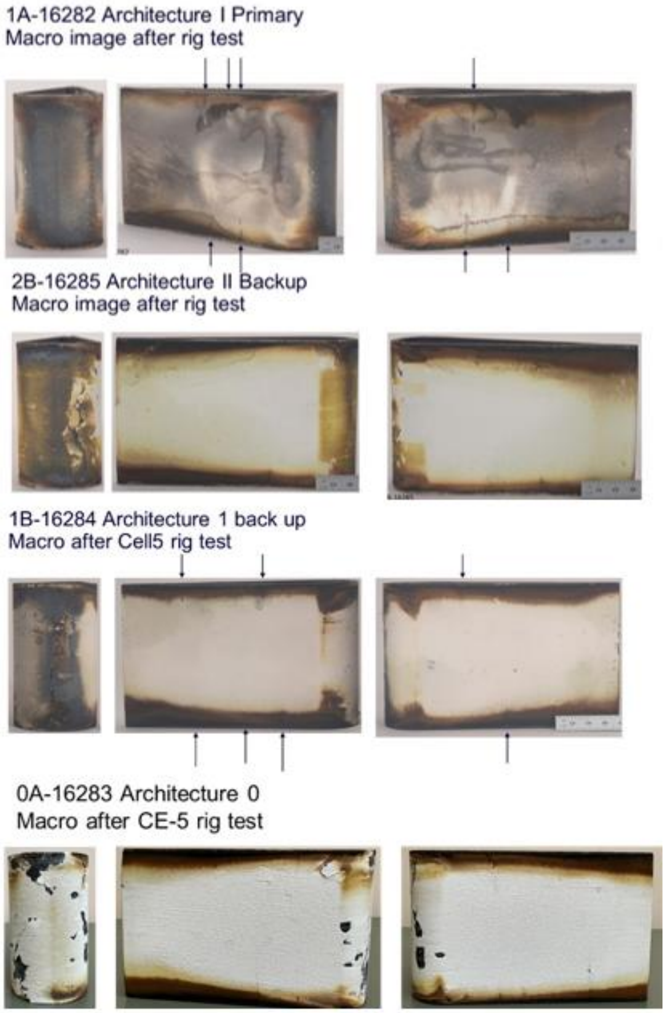

Figure 106: Macroscopic appearance of airfoil test articles after the completion of their rig test runs at CE-5 high-pressure combustor rig test facility at NASA GRC.

On completion of the rig tests, all test articles were returned to GEA Research Center for post-test evaluations. Figure 106 shows the appearance of the four test articles after their removal from the rig. The brown and black discolorations visible on the surface of the parts and within the colder areas at the leading edge and along the side edges of the test articles are identified as Fe2O3 by XRF and XRD analyses. Because of the limited time remaining in the program, the scope of the post-test evaluations had to be curtailed and narrowly focused on two main questions:

a) condition of the coating: overall assessment of the coating after the test relative to pre-test recorded NDE (flash IR data), and

b) assessment of exposure temperature: based on microstructural observation of the coating cross-section samples, estimate the exposure temperature using TGO or other microstructural attributes by comparison with lab test coupons.

Any other evaluations, including the observed cracking of CMC article, were deferred to a future evaluation, and considered as complementary outcome relative to the scope of the program but not a priority at the time of preparing this report.

A three-step evaluation process sequence was defined and applied to each test article examined:

1- Macroscopic photographic documentation,
2- NDE, flash IR, imaging of the article, and
3- Microscopic observation of cross-section samples extracted from the leading edge, trailing edge and middle of the article.

For step three, the team organized a sectioning plan as shown and marked on one of the example airfoil articles in Figure 107. This sectioning plan was applied to all test articles.

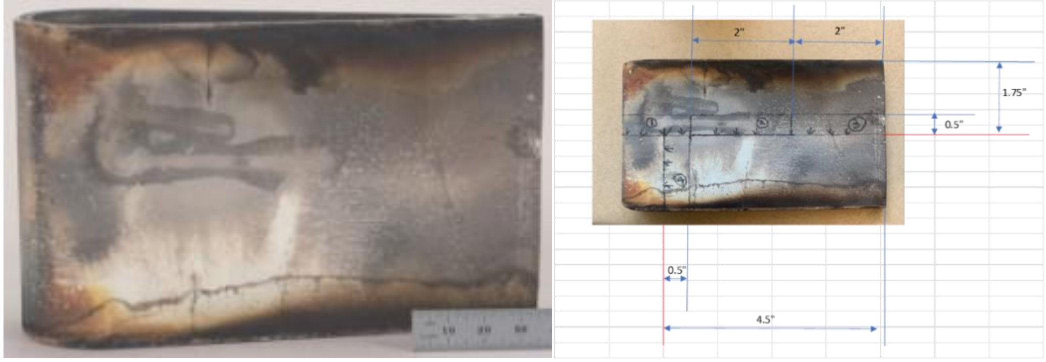

Figure 107: Sequence of post-rig test observations & sample preparation. Left) photographic documentation Right) Cut plan to extract four cross-section samples #1 through #4.

Four cross-section specimens were prepared from one of the two symmetric halves of each airfoil for microstructural evaluations. The other half of each test article was preserved for future evaluations. The cross-section samples were numbered 1 through 4 (as shown in Figure 107, right). All four cross-section samples were observed and catalogued using SEM but because of time limitations, cross section specimens #1, #3 (centerline at trailing edge) and #4 (location corresponding to side body pyrometer) are the primary focus of the quick evaluations documented here.

4.2.4.1 Test article Architecture 1A (CMC airfoil #16282)

Figure 111 and Figure 109 show the local microstructural observations at different positions of the cross-section #4 of test article Architecture 1A. The microstructural features of the coating layers, along the cold edge of the specimen are shown through Figure 109. This and similar colder edge areas of the test articles are assumed to represent the condition of the coating layers after the annealing heat treatment. In Figure 108, the location imaged corresponds to the area viewed by the side-body pyrometer as discussed in the previous section. Particular attention is given to the differences in the thicknesses of the TGO layer on mullite-Si bondcoat layer between the two regions identified. The TGO thickness change can be used to interpret the temperature using the TGO growth data and oxidation kinetic model organized based on lab tests.

. Other microstructural features worthy of note are those corresponding to the condition of all coating layers along the cold edge and the delamination of HfO_2 layer observed in the hot areas of the part. The delamination of HfO_2 layer in this area, the incidence of relatively wide vertical cracks and reduced porosity of this layer are viewed as self-consistent indications of densification and are directionally consistent with higher temperatures on the surface of the EBC in this area.

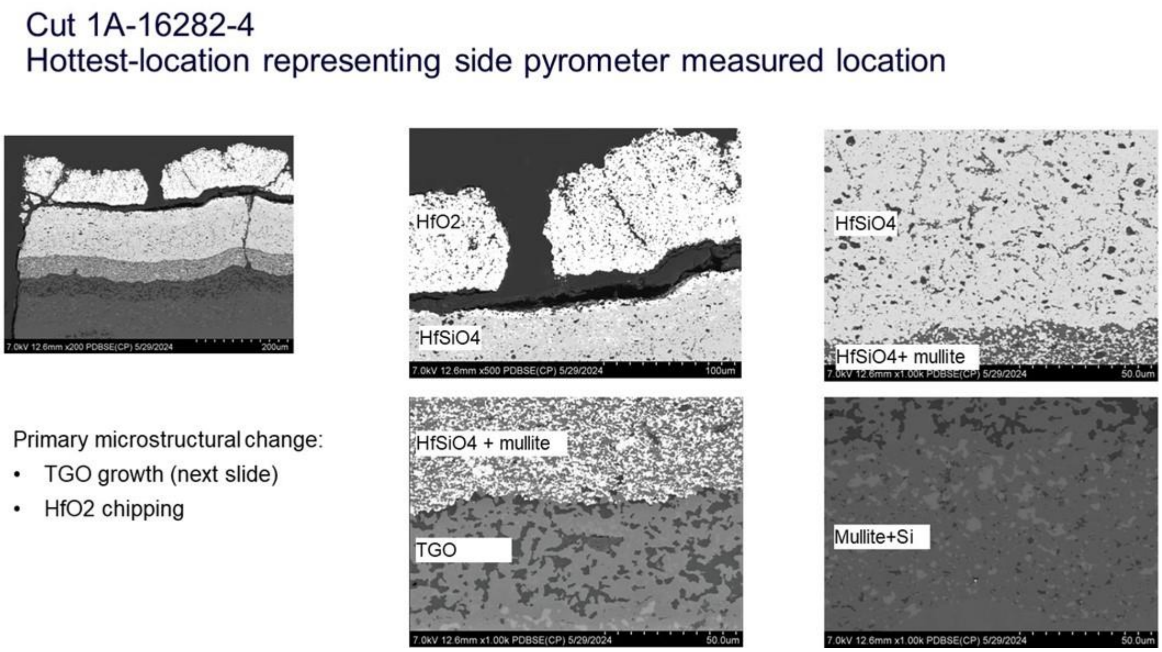

Cut 1A-16282-4
Hottest-location representing side pyrometer measured location

Primary microstructural change:
- TGO growth (next slide)
- HfO2 chipping

Figure 108: Architecture 1A-16282, cross section #4. Location shown representative of side body pyrometer view area, hottest region of the test article. Microstructural features including TGO represent the condition of coating layers and changes in the local microstructure due to high temperature dwell.

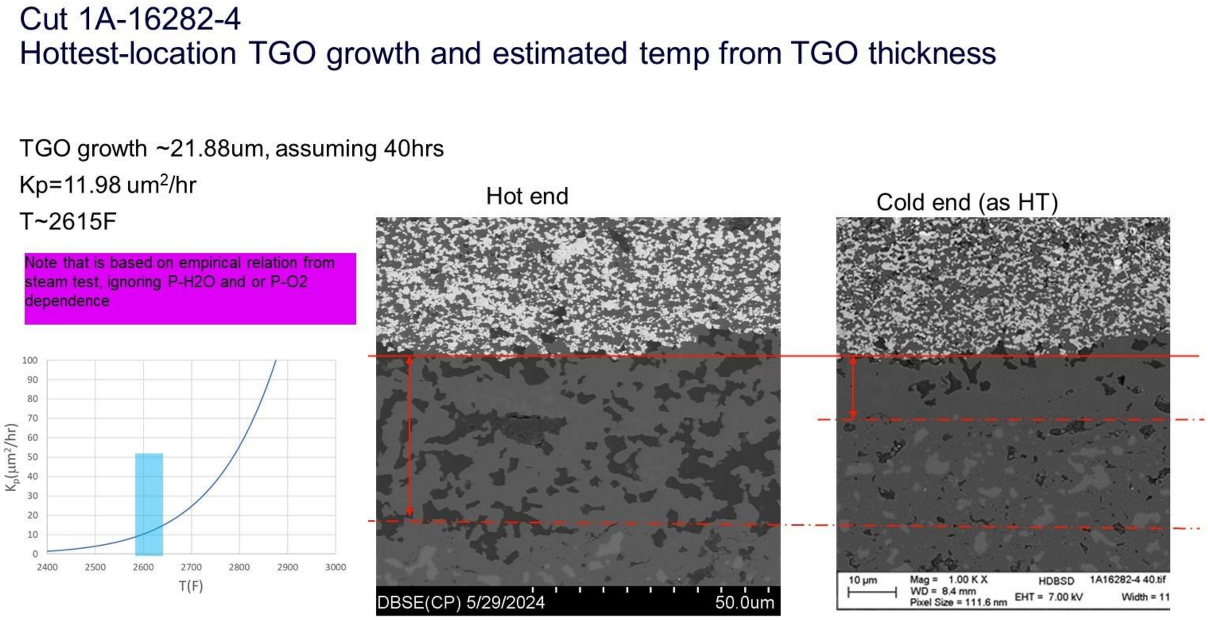

Cut 1A-16282-4
Hottest-location TGO growth and estimated temp from TGO thickness

TGO growth ~21.88um, assuming 40hrs
Kp=11.98 um^2/hr
T~2615F

Note that is based on empirical relation from steam test, ignoring P-H2O and or P-O2 dependence

Figure 109: Estimation of temperature based on TGO thickness change between the cold and hot areas and oxidation kinetic model from lab tests.

Overall, and based on the limited microstructural observations reported here, GEA interpretation of the microstructural observations from this article is that Architecture 1A coating performed as intended.

4.2.4.2 Test article Architecture 2B (CMC airfoil #16285)

The letter B designation in this article signifies it as a backup test article as discussed in section 3.3. However, because of timing concerns and the sequence of test campaign, a decision was made by GEA and NASA Glenn team to take this article into the rig test campaign prior to the primary article Architecture 2A (which could not ultimately enter the test campaign due to program schedule). This article had experienced some processing issues during the coating deposition process leading to localized coating delamination and spall along its leading and trailing edges. The area with spalled coating layers seemed to have grown during the test but no further delamination or coating spall appeared to have propagated down to the CMC-EBC interface.

Overall, the microstructural observations indicate that this example of Architecture 2 coating system behaved well during the rig test campaign except for the areas with the pre-existing coating delamination damage from the coating production phase.

4.2.4.3 Test article Architecture 1B (CMC airfoil #16284)

This was the last GEA HTEBC architecture test article that entered the rig test campaign. The letter B designation in this article signifies it as a backup test article. The test campaign was planned for this article after improvement to the rig test protocol following the Architecture 1A rig run and the changes to the operating conditions of CE-5 rig by NASA team in a more consistent manner with the conditions applied to the test article Architecture 2B.

For additional verifications, two separate locations were selected for TGO-based temperature analysis. One additional area was selected on the longitudinal section #1, which is along the article center line and perpendicular to the cross-section sample #4. This position also coincides with the side body pyrometer area. The TGO measurement in this area yielded a K_p value that results in an estimated local temperature was ~2560F. Another area was selected on section #3 and in close proximity of the trailing edge. The TGO analysis of this section gave a K_p value with a corresponding temperature of 2575F. These values are within a temperature spread of <75F. GEA treats this data consistent given the uncertainties of the analysis approach.

4.2.4.4 Summary of post-test observations

Post-test evaluations of the GEA HTEBC Architecture 1 and Architecture 2 test articles combined visual appearance, flash IR and microstructural evaluations to determine the condition of the coatings. The brown and black discolorations observed at the leading edge and along the colder edge sections of the test articles were determined to be Fe_2O_3. Four cross-section test specimens were prepared from each test articles examined to assess the condition of the coating layers after the test and to assess the temperature history of the coating layers through changes in the local microstructures of the layers including the TGO thickness. Based on limited post-rig test microstructural observations comparing Architecture 1A and 1B test articles, GEA concluded that the two test articles experienced similar test temperature conditions. GEA also concludes that in both cases the HTEBC Architecture 1 system behaved similarly and consistent with the design intents for this high-temperature, highly refractory EBC system. In addition, GEA used the observations of the TGO on the composite mullite-Si bondcoat layers of these articles to obtain a point estimate of the local maximum temperatures to which the bondcoat layer was exposed. These estimated values were in the range of ~2575F-2725F and were treated as a lower-bound estimate for the temperature. The test article with Architecture 2B similarly showed good performance and surprisingly a similar TGO thickness between the cold and hot areas. Therefore, a similar estimation of bondcoat layer temperature could not be applied to this test article. The observed TGO behavior in Architecture 2B test article was unexpected and could not be explained with the limited evaluations made at this time.

5. HTEBC Modeling

5.1 NASA Durability Modeling

5.1.1 Introduction

EBC systems have many failure modes as shown in Figure 110 ([6] and [7]). Key contributors to EBC failure include oxygen-induced oxidation, water-vapor-induced oxidation, water-vapor-induced recession, degradation by calcium-magnesium-aluminum-silicate (CMAS) deposits, thermomechanical strains, particle erosion, and foreign object damage (FOD). Synergies between extrinsic failure modes determine EBC lifetime and design requirements (Reference 6). Finally, all these mechanisms coalesce into thermomechanical durability. However, in this work NASA is only focusing on steam oxidation that leads to growth of a silica layer, sometimes referred to as thermally grown oxide (TGO). TGO grows out of a silicon (Si) bond coat (if present) or from a SiC substrate. With time, the oxide layer grows in thickness, and it has been observed that under thermal cycling conditions the EBC spalls from CMC substrate once the TGO layer reaches a critical thickness usually between 20 to 30 μm [8].

The stresses or the driving forces in the EBC systems are generated primarily due to coefficient of thermal expansion (CTE) mismatch between various EBC layers and substrate. EBC intrinsic requirements are CTE match, phase stability and no EBC/CMC interaction. In other words, minimizing the CTE mismatch between various layers along with the thermochemical stability is a key design consideration for EBC systems. The objective of the present work is to describe a pragmatic engineering (phenomenological model) approach to estimate the in-situ residual stress state (which is a function of constituent properties and geometry) and thus the critical TGO layer thickness (i.e., lifetime) that induces spallation and failure of the EBC system when subjected to thermal loads only. Results, based on the analysis of a particular EBC system, indicate that a single allowable interfacial strength value can be used to predict damage failure/spallation of the EBC system. If the EBC system is also subjected to mechanical loads, then failure will occur prior to reaching the critical (thermal cycling alone) oxide layer thickness depending upon the magnitude of the applied mechanical load.

Sections 5.1.1 through 5.1.6 of this report were taken from Subodh K. Mital and Steven Arnold, A Phenomenological Durability Model for Environmental Barrier Coating Systems Subjected to Steam Oxidation, NASA TM/M-20240000936 [39]

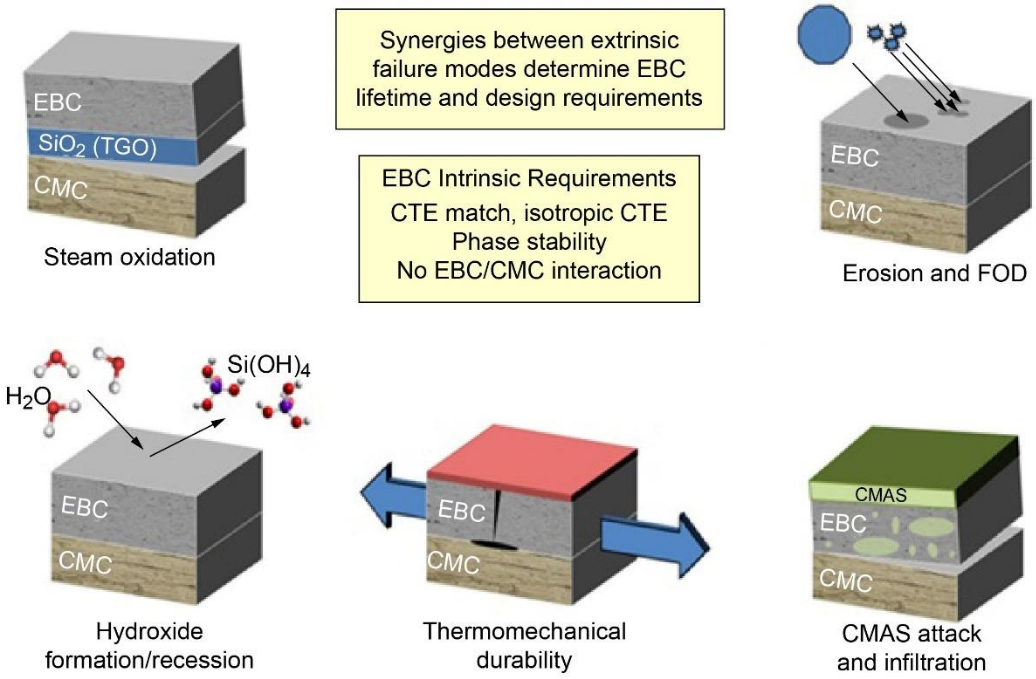

Figure 110: Failure modes of EBC systems.

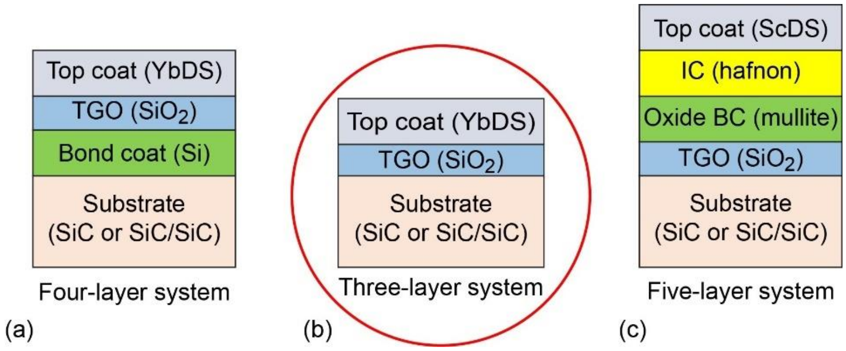

Figure 111: EBC systems nomenclature (a) Gen 2 (2,400F) system. (b) Early (2,700F) system. (c) Gen-3 NASA EBC base architecture (3,000F).

(YDS – ytterbium disilicate; Si – silicon; REDS – Scandium disilicate; IC – intermediate coat; BC – bond coat; SiC – monolithic silicon carbide (Hexoloy); SiC/SiC – CMC composite with silicon carbide fiber and silicon carbide matrix.)

5.1.2 Nomenclature of EBC Systems

EBC development has been underway for many years. First generation of EBCs were developed in the 1990s under NASA's High Speed Civil Transport—Enabling Propulsion Materials (HSCT-EPM) program. These EBC systems consisted of mullite and BSAS materials. Second generation EBCs were developed under NASA's Ultra Efficient Engine Technology (UEET) program in the early 2000s ([6]). Most of the current EBCs are variations of the second generation EBC systems. Figure 111 shows the currently accepted EBC systems nomenclature. The Gen-2 system has a silicon bond coat and an ytterbium di-silicate

(YbDS) topcoat. Its use temperature is limited to 1315°C (2400F) due to the presence of the silicon bond coat which has a melting temperature of 1410°C. Within NASA GRC it is referred to as a four-layer (substrate/bond coat/TGO/topcoat) system. There have been some modifications of these systems by modifying the chemistry of the topcoat wherein slower TGO growth has been demonstrated and thus longer life as compared to the original system ([9]). The EBC system referred to as the early 2700F system removed the silicon bond coat as it was limiting the use temperature of the EBC system. As the name suggests, this system has a use temperature up to 1482°C (2700F) when applied to a 1315°C (2400F) capable CMC substrate. This system has also been referred to as a three-layer system (substrate/TGO/topcoat). Some of the newest EBC systems under development are so-called Gen-3 EBC systems that have a potential use temperature up to 3000F (1650°C) if applied on a 2700F (1482°C) capable CMC substrate. These Gen-3 systems, in the base architecture, typically have five layers (substrate/TGO/bond coat/intermediate coat/topcoat). The bond coat in these systems is an oxide-based material (mullite) and intermediate coat is Hafnon ($HfSiO_4$; Hafnium silicate), while the topcoat is Scandium disilicate (REDS). In another variation of this system, the topcoat is Hafnia (HfO_2) and in yet another variation, the topcoat consists of a hafnia layer over a scandia layer.

The architecture 0 chemistry listed in section 5.1.2 of this report are based on work mentioned under [41], [42], [43], [44], [45] and [46].

5.1.3 Observations From Analyses of Early EBC Systems

Analyses were performed previously on 2400F Gen-2 EBC systems (four-layer systems) as well as early 2700F systems (three-layer systems) subjected to an isothermal cooldown from a high temperature to room-temperature ([10] and [11]). The TGO grows when the bond coat or the substrate is oxidized at very high temperatures in the presence of oxygen and/or water vapor. Further, it was observed that when these systems are subjected to realistic thermal cycling, the oxide (TGO) layer is in compression in the in- plane direction during the heat up portion of the cycle. Chemical reactions at high temperature cause the oxide layer thickness to increase during the time the EBC is at high temperature and there is a volumetric change associated with this conversion of bond coat/substrate to TGO. However, the associated thermal chemical induced stresses are quickly relaxed out as these materials, particularly the TGO material, exhibit very high creep rates ([12] and [13]) at temperature as well.

However, during cooldown, tensile stresses develop in the oxide layer, which in conjunction with coating interface roughness and prior damage will induce further initiation/propagation of damage within the TGO and interface surfaces. The damage in the form of vertical cracks in the oxide layer is modeled explicitly in these analyses. However, there are other types of damage in the system such as horizontal cracks, porosity etc., which is not modeled explicitly, but their effects are accounted for lowering the layer stiffness. The resulting stress-state in the oxide layer from these analyses can be summarized as follows:

1. Out of plane peel (that cause delamination/cracking) and shear stresses (that drive the delamination) are minimal for uniform layers with no damage. Only in-plane tensile stresses are present which cause self-similar vertical cracks to develop as the TGO grows.
2. In-plane stresses (that cause vertical cracks) are high and are primarily driven by CTE mismatch. They are independent of the oxide layer thickness and only increase slightly in the presence of nonuniformity/damage.
3. In real systems, damage, in the form of vertical cracks in the oxide layer, are always present. TGO layers are also highly nonuniform in thickness.
4. Shear stresses are high in the presence of damage (e.g., vertical cracks) and increase only slightly with increase in oxide layer thickness or with increasing nonuniformity.

5. Peel stress is present in the presence of damage and increases rapidly with the introduction of even a slight nonuniformity (or roughness) of TGO. Peel stress also increases with increasing oxide layer thickness.
6. As these systems are cooled from a high temperature to room temperature, the stresses that develop quickly relax out due to the assumed high creep rate of these materials as mentioned before. To perform an actual creep/relaxation analysis, the creep rates of all constituent materials as a function of stress and temperature are required. Similarly, one must know the time temperature profile of the cooling applied to the EBC system. Usually, such information is not readily available. Further, such calculations are extremely computationally expensive as the finite element meshes of these systems are relatively large and the time increments very small. Consequently, one can use a lower "stress-free" temperature (much lower than the temperature at which the coating is applied) and perform a simple elastic time-independent analysis to obtain reasonably accurate residual stress states. The value of this "stress-free" temperature is chosen in a way that will result in the stress state at room- temperature being similar to that if a full-scale creep/relaxation analysis would have been performed [14].

Figure 112 shows maximum in-plane, peel, and shear stresses for an early 2700F system under isothermal cooldown from a stress-free temperature of 500°C to room temperature based on 2-D plane stress finite element analyses. The stresses are plotted as a function of nonuniformity as defined by the parameter R, which is the ratio of minimum oxide layer thickness to the nominal thickness. Thus, R = 1 implies uniform oxide layer thickness and R = 0 implies very severe nonuniformity with islands of oxide layer. The location of these maximum not always being the same. In these analyses, a monolithic, isotropic, silicon carbide material, Hexoloy®[1][23], has been used as the substrate material. The resulting driving forces, specifically peel and shear stresses, depend upon not only on material properties and damage (vertical crack spacing), but most importantly on EBC architecture, i.e., layer thickness and roughness (nonuniformity) of the oxide layer. In-plane stresses (the cause of vertical cracking) in the oxide layer are relatively constant and independent of TGO thickness and nonuniformity (roughness).

Given these results, the tensile strength of the oxide (TGO) material appears to be approximately 80 MPa, given this stress-free temperature.

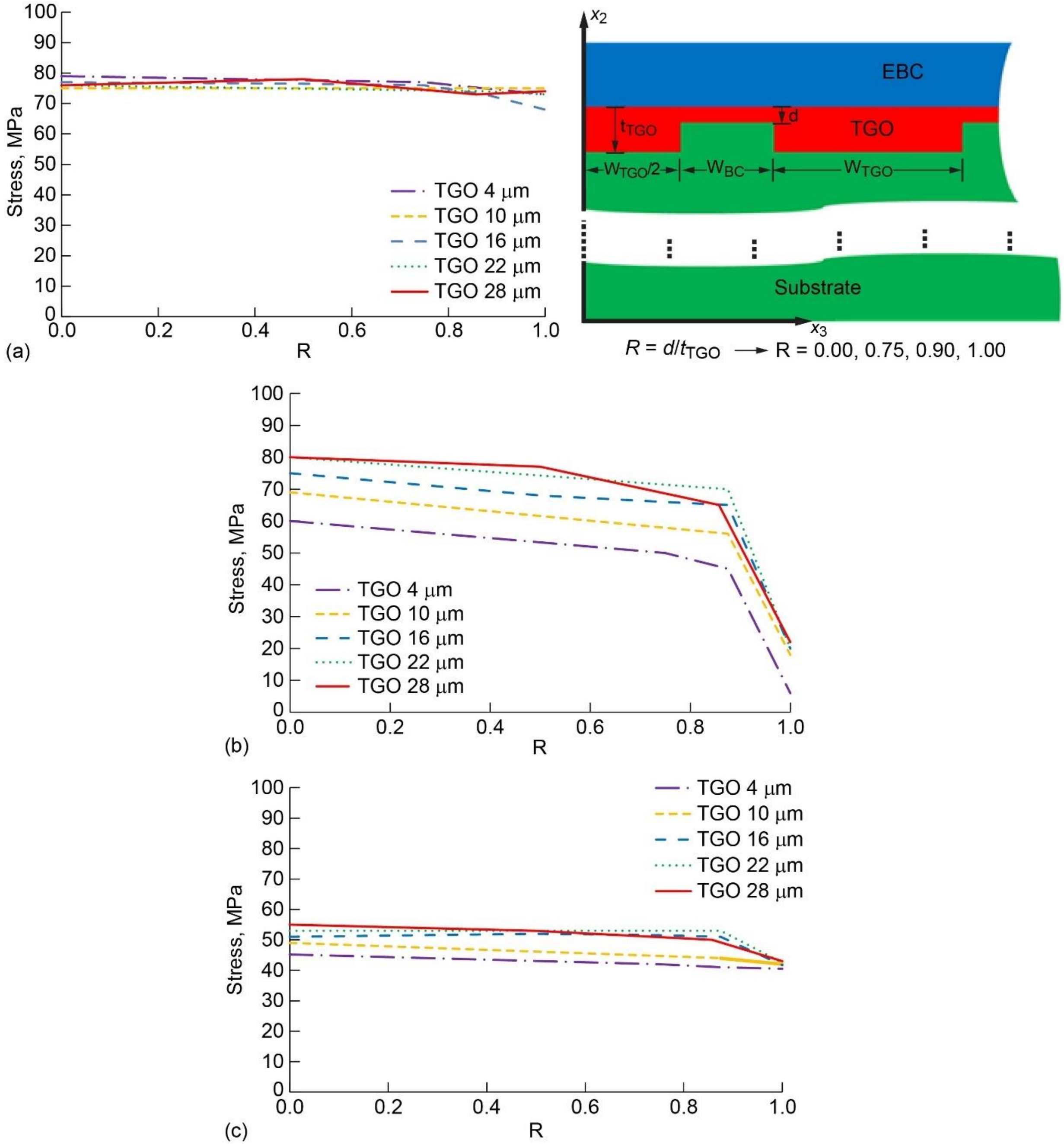

Figure 112: Driving forces (stress) as a function of TGO roughness and thickness for early 2700F system; (a) in- plane (severity of nonuniformity considered by adjusted R factor), (b) peel stress (maximum peel stress in TGO layer cracks at 10 µm spacing, ∆T = 500 °C), (c) shear stresses (maximum shear stress in TGO layer cracks at 10 µm spacing, ∆T = 500 °C) (Refs. 10 and 11).

Figure 113 and Figure 114 show the stress contours (J2, σ11, σ22, σ12, I1) for two cases—one with an oxide layer thickness of 16 µm and R = 0.5 (see Figure 113) and the other one with an oxide layer thickness of 22 µm and R = 0 (see Figure 114). Both cases have vertical cracks, 10 µm apart, in the oxide layer. Note that the material layers above (topcoat) and below (substrate) the TGO are not shown in the figures but were present in the calculations. Results show that stresses are generally maximum at the crack tips and at the corners (idealized by zeroing out the stiffness of a column of elements every 10 µm) and usually at the TGO/substrate interface located along the bottom edge of the contour plots.

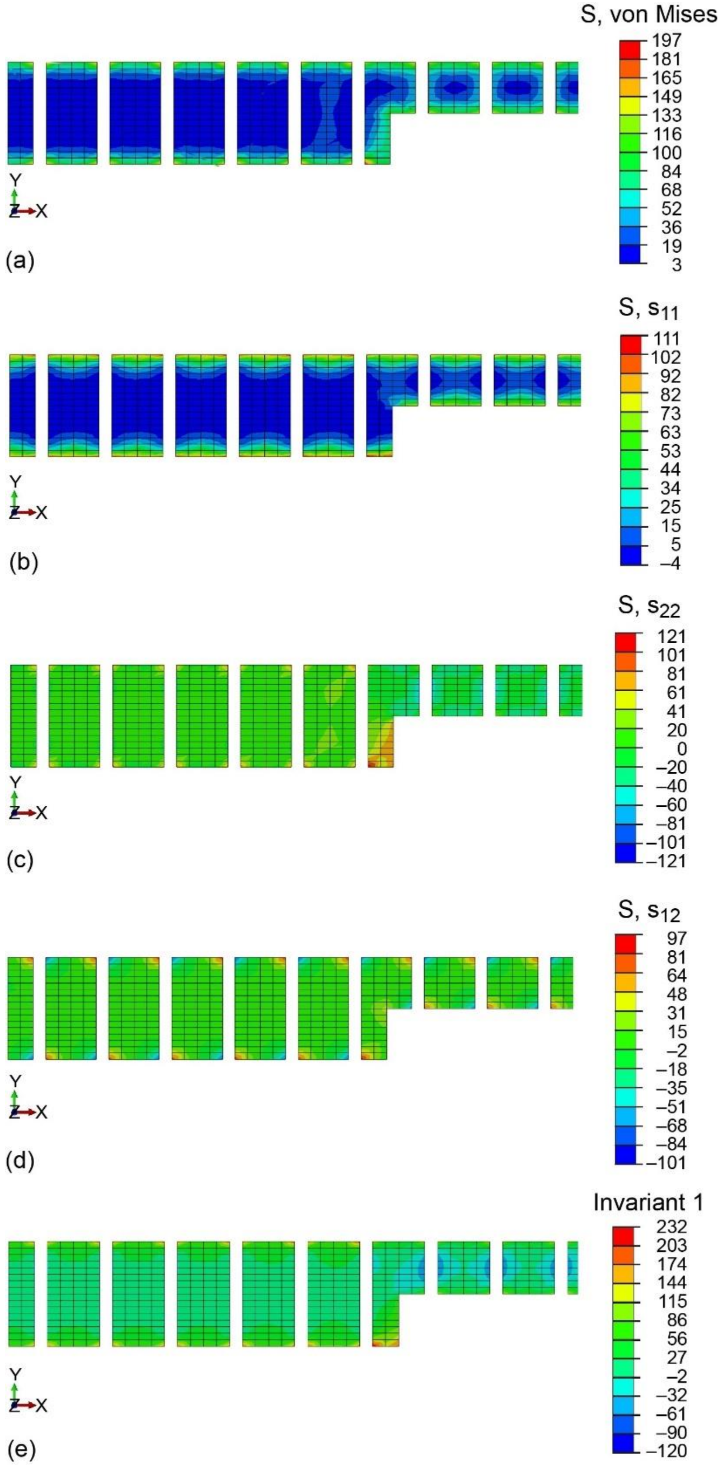

Figure 113: Stress contours (MPa) in the oxide layer in a EBC system with 16 µm thick oxide layer and R = 0.5, left edge of the image is centerline. (a) J2, (b) σ11, (c) σ22, (d) σ12, and (e) I1.

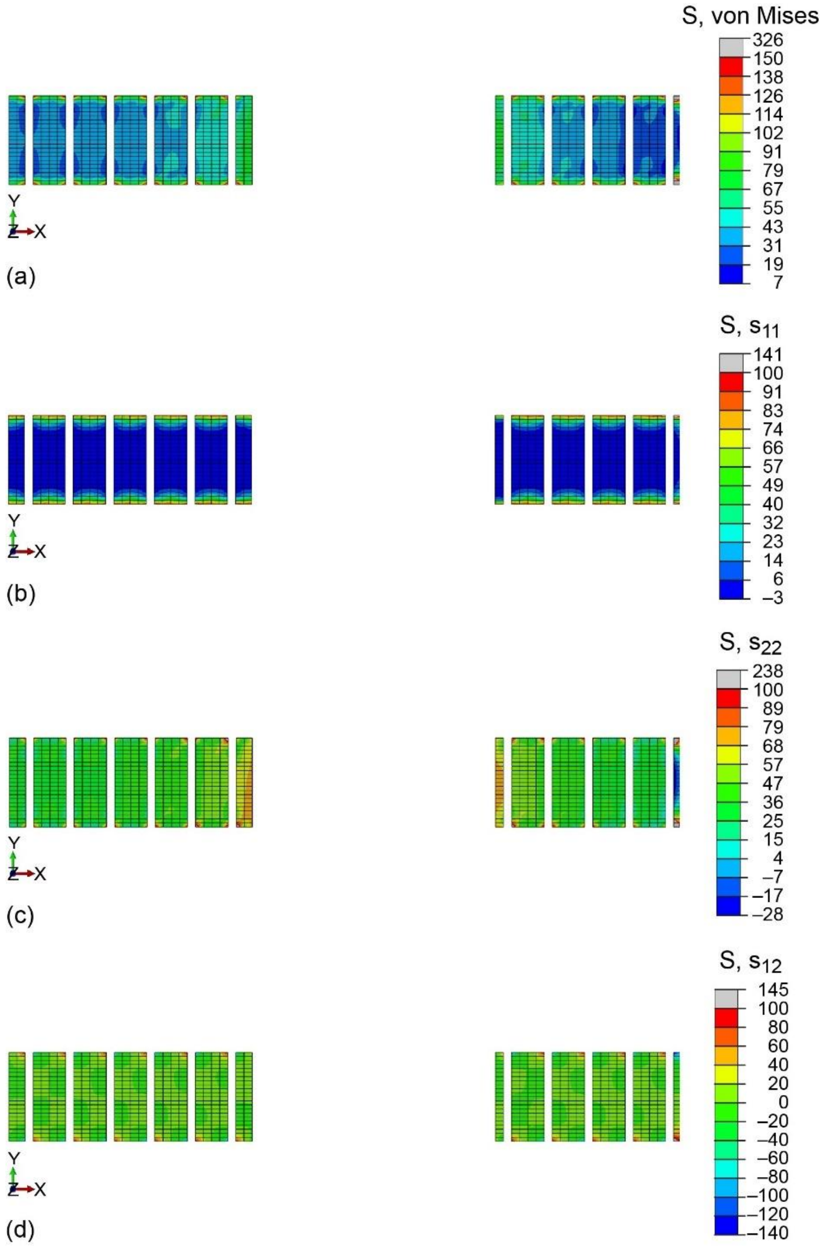

Figure 114: Stress contours (MPa) in the oxide layer in a EBC system with 22 μm thick oxide layer and R = 0.0, left edge of the image is centerline. (a) J2, (b) σ11, (c) σ22, and (d) σ12.

5.1.4 Phenomenological Modeling Approach

Here a phenomenological modeling approach is outlined to provide an estimate of the in-situ residual stress state (which is a function of constituent properties and geometry) and thus critical thickness of the oxide layer that will cause spallation of a given EBC system when subjected to thermal loads only. This approach, which consists of seven steps is outlined here, and will be explained in the next section by using the example of an early 2700F system.

1. Define the system to be modeled - First the architecture (constituent materials and geometry) of the system that is being modeled must be identified and defined. For example, it could be Gen-2 EBC system or a modified Gen-2 EBC system, etc.
2. Obtain a consistent set of material properties - One must obtain a set of material properties for each material in the system e.g., Young's modulus, Poisson's ratio, and coefficient of thermal expansion (CTE), each as a function of temperature. If possible and available, time-dependent properties or creep rates for each material as a function of temperature and stress level are also useful, although they are not always easily available. If unavailable, one can perform an elastic analysis using the concept of stress-free temperature. This assumes that above the stress-free temperature, stresses do not build up because they relax out as fast as they are generated (clearly this is dependent upon the rate of cooling).
3. Characterize the roughness and damage in the oxide layer - since the local stresses depend upon the damage (vertical cracks, porosity, etc.) and the roughness of the TGO layer, it is critical to characterize these for a given EBC system and for a given exposure time. Exposure time is also crucial as the TGO layer thickness is a function of exposure time, i.e., time at temperature. To characterize the damage (generally in the form of vertical cracks in the oxide layer) as well as the roughness or the nonuniformity of the oxide layer, one needs a set of micrographs from a test sample. Information such as average oxide layer thickness and roughness and the related statistics need to be extracted from those micrographs. One way to achieve that is to use a convolutional neural network and extract relevant features from the micrographs as shown in Figure 115. A set of python instructions are provided in [15] to perform such analyses and results have been documented in [16]. Usually, hundreds of images are required across a test specimen to obtain a statistical distribution of those required features.
4. Knowing the nonuniformity and average crack spacing in the TGO layer, one can compute the peel and shear stresses from "design curves" such as those shown in Figure 112 which are established by running numerous computations utilizing this microstructural information. These curves provide "residual stresses" as a function of microstructure and cooldown from a stress-free temperature to room-temperature.
5. In-situ interface failure allowables are inferred from pull tests or flatwise tension tests on a given EBC system- given the applied load/stress at failure for the given oxide layer thickness. Since this is the applied global load/stress, it must be converted to in-situ stress at failure or in-situ strength by multiplying the applied global stress by a magnification factor (MF). The value of this magnification factor depends upon the TGO microstructure for the EBC system under consideration, i.e., layer thickness, level of nonuniformity, etc.
6. Repeat the above step for a different exposure time and thus a different TGO thickness and compute the in-situ interfacial strength. Often, a single value of interfacial in-situ strength can be used to estimate the critical oxide layer thickness. Note this strength has associated with it a given volume of material in which both initiation and propagation of damage are assumed to have occurred within - thus the phenomenological nature of the method.
7. This value will help to determine critical TGO thickness where cracks join, driven by local shear stresses, to ultimately cause spallation of the coating.

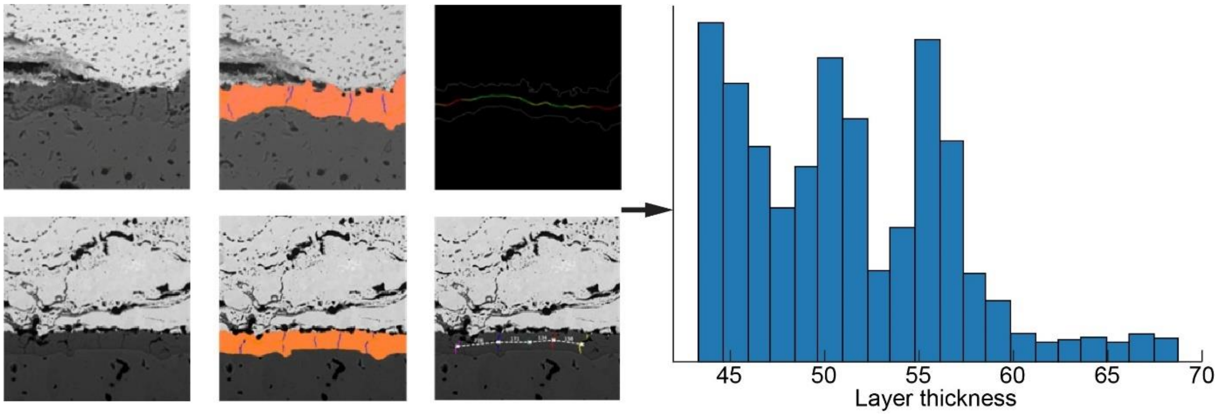

Figure 115: Extraction of oxide layer features from micrographs of specimens.

Du et al. [17] have also performed a comprehensive study and modeled the effects of the TGO and interfacial roughness on the stress distribution in EBCs. However, they have not accounted for the damage in the oxide layer in the form of vertical cracks that are always present as well as stress relaxation that occurs due to creep in EBC layers. The damage in the oxide layer and creep/relaxation totally changes the nature of the stress distribution in EBCs and thus their results cannot be compared with the results from the present study.

Furthermore, it is imperative that modelers strive to understand exactly how a given experiment was conducted to ensure proper interpretation of the results and idealization consistency. Many interdependent factors are comprised within the concept of idealization consistency and can be classified into three main categories: theoretical, mechanistic, and numerical consistencies. Theoretical consistency requires preserving the mathematical aspects (e.g., theory, model dimensionality, functional form, etc.) used throughout characterization to prediction. Mechanistic consistency would be associated with assumed measures and definitions of damage and modes of failure and their interactions which should be accounted for not only in the final prediction but also during characterization. Length scale (e.g., material volume element) and mesh accuracy are both examples that would fall within the numerical consistency category and thus the preservation of these accuracies from characterization to prediction is important. It is important to remember that these categories are typically not mutually exclusive and thus the influence of one on another is often difficult to explicitly determine. This is particularly true in the case of multiscale analysis wherein all factors can interact aggressively as one traverses various length scales ([18]).

In the next section, the above steps will be explained with the help of an example.

5.1.5 Example of Early 2700F EBC System

These steps will be demonstrated here using an early 2700F system with a SiC (Hexoloy®) substrate. A stress-free temperature of 500°C has been assumed (based off the temperature dependent creep rates of the constituents) and the specimens are cooled in an isothermal manner from this stress-free temperature to room temperature. The non temperature dependent thermomechanical properties used for various materials in this EBC system are shown in Table 23. Temperature dependent properties within this range make only slight changes in the resulting stress calculations, i.e., <5 percent.

EBC coated samples were exposed to 1426°C in 90 percent H_2O in a continuous exposure with no cycling. Specimens were imaged from one end to the other (~140 images for a 1-in. diameter specimen). For each image, multiple measurements were taken of oxide layer thickness, roughness etc. and the following statistics were obtained for two exposure times 49 and 100 hours. These statistics are shown in Table 24.

Table 23: Material Properties (RT–500°C)

Material	Young's modulus GPa	Poisson's ratio	Coefficient of thermal expansion 10^{-6}/°C
Topcoat	200	0.27	4.5
TGO	35	0.17	10
Substrate	400	0.17	5.25

Table 24: Oxide Layer Measurements and Statistics

Property	49 hrs exposure	100 hrs exposure
Average thickness, µm	4.3	9.8
Standard deviation, µm	142	2.96
Coefficient of variation	0.3	0.3
Minimum thickness, µm	1.64	2.6
Maximum thickness, µm	13.8	23.5
Average roughness-top, µm	2.15	2.23
Average roughness-bottom, µm	1.99	1.94
Total roughness, µm	4.14	4.17

Table 25: Maximum Interfacial Stresses

	R=0.40		R = 0.27	
TGO average thickness	Peel stress	Shear stress	Peel stress	Shear stress
µm	MPa	MPa	MPa	MPa
4.3	55	44	--	--
9.8	--	--	67	46

As one can see from Table 24, there is tremendous variation in the oxide layer thickness and roughness profile. The roughness in the model is defined as the ratio of minimum oxide layer thickness to the nominal (average) thickness. Based on this definition, the R for 49 hours of exposure is computed as 1.64/4.3 = 0.4 as the worst-case scenario, while for the 100 hours exposure time, it is 2.6/9.8 = 0.27. Based on these R values and oxide layer thickness, one can "read" the peel and shear stresses from the design curves shown in Figure 112. Those extracted are shown in Table *25*.

These stresses are compared to the strengths that are obtained by performing a flatwise tension test on these specimens. For this early 2700F system, Figure 116: EBC strength as a function of oxide layer thickness. shows the strength of the TGO interface as a function of oxide layer thickness. These tests are done at room-temperature, so the layers in the specimen have residual stresses due to the cooldown from a high temperature to room-temperature.

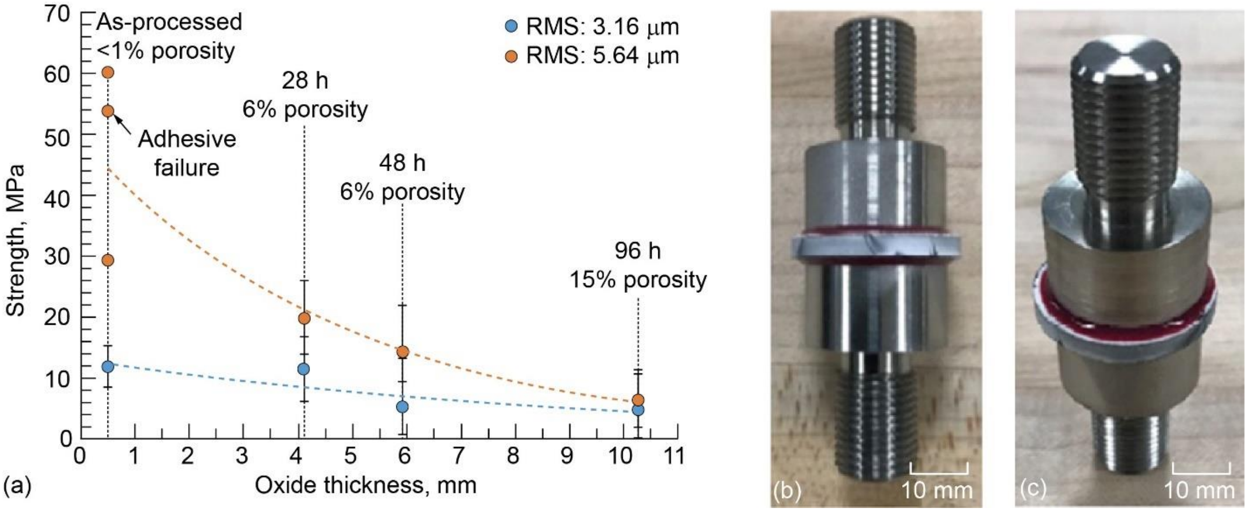

Figure 116: EBC strength as a function of oxide layer thickness.

Details on how these strength tests are performed are provided in [19] and [20]. The specimen geometry is also shown in the upper right corner of Figure 116. Strength values show a fair amount of scatter. It also appears that the effect of initial roughness is not important after the oxide layer thickness is greater than 10 µm for the average strength value. This scatter in measured strength can possibly be due to large scatter in oxide layer thickness and nonuniformity. However, the strength shown in Figure 116 is merely the magnitude of the applied global stress (applied load at failure/tab cross-sectional area) at which the specimen failed (residual strength). It is not the in-situ stress at failure near the oxide layer interfaces. Analyses have shown that in-situ peel and shear stresses are anywhere from 3 to 5 times (magnification factor) of the applied global stresses depending upon the oxide layer thickness and the level of nonuniformity (roughness) with a given damage in the form of vertical cracks in the oxide layer at an average distance of 10 µm apart. Note as stated before this strength inherently also assumes a given volume of material over which failure has initiated and propagated (or in other words full separation of specimen occurred). The area is 0.75 in^2.

It appears, from Figure 116, that for a 4 µm thick oxide layer, the average value of measured strength is approximately 15 MPa. Residual peel stresses are 55 MPa as shown in Table *25*. Therefore, the actual interfacial strength is approximately 15 × 3.5 (magnification factor given R = 0.4) + 55 = 107.5 MPa with a lower bound value of 97 MPa and upper bound value of 132 MPa given the scatter in measured strength. If one performs a similar calculation for the specimen with average oxide layer thickness of 10 µm, the average measured strength is approximately 10 MPa. Therefore, the actual interfacial strength is approximately 10 × 4 (magnification factor for a R value of 0.27+67 (residual peel stress due to cooldown) = 107 MPa with a lower bound value of 75 MPa and an upper bound value of 115 MPa. Based on the average values, these results show that a single allowable in-situ interfacial strength value of approximately 107 MPa (with a range of 75 to 132 MPa) can be used to predict critical TGO thickness (one that is due to thermal loading only) that will cause failure initiation/spallation of approximately 0.75 in2 of EBC from the substrate. Alternatively, one can also apply an in-plane global load in combination with thermal cooldown to obtain critical thicknesses associated with a given applied mechanical loading.

Figure 117 shows a typical TGO growth curve in steam environment ([21] and [22]). This curve is shown for schematic purposes only and is not necessarily for the EBC system under consideration here. It should be noted that such a curve is specific to an EBC system and environment (e.g., temperature, moisture, architecture etc.). Once the value of the critical TGO thickness that will cause initial failure/spallation over a given area is known, it can be converted to the time in hours using a TGO growth curve like the one shown above in Figure 117.

The following example demonstrates how the failure of EBC/TGO can be predicted using an average strength value of 107 MPa computed above and a stress-free temperature. It must be emphasized again that the stresses and strength values being used here are very specific to an EBC system as well as environment (in particular, temperature and moisture). Let’s say the average thickness of oxide layer is 16 µm after a certain time of thermal exposure. Let’s say that nonuniformity or roughness as indicated by the parameter R is equal to 0.15. The peel stress for these values is 75 MPa as shown by design curves in Figure 114. That means the remaining interfacial strength is equal to 107 – 75 = 32 MPa. Assuming a magnification factor of 4 between in-situ interfacial stress versus applied global stress, the remaining external load/pressure is 32/4 = 8 MPa. Consequently, if one were to conduct a flatwise tension test of this EBC system like the one shown in Figure 116, it would fail at an applied global stress of 8 MPa on average. Thus, once the in-situ stress in the oxide layer reaches the strength value (80 MPa in this system), the oxide layer itself can fail even though the interface may be intact. On the other hand, if the interfacial peel stress reaches the interfacial strength, delamination/failure initiates and the high shear stress can cause that failure to propagate, leading to spallation of the EBC from substrate.

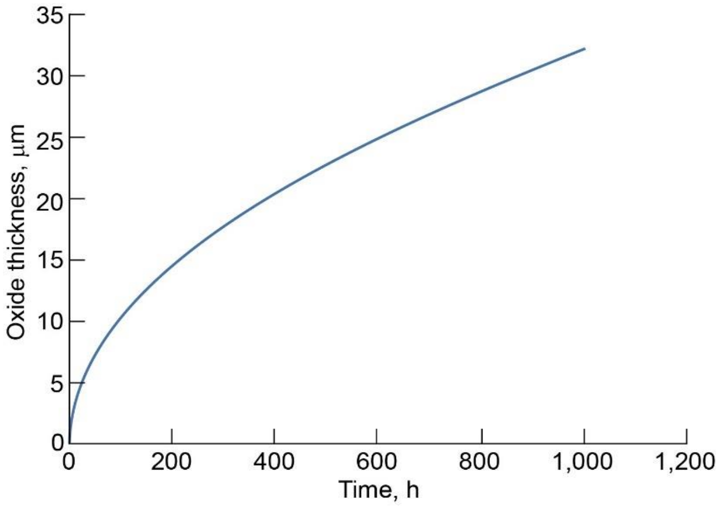

Figure 117: Typical TGO growth curve in steam environment.

5.1.6 Summary

In this paper, a phenomenological, pragmatic modeling approach to estimate the failure strength of EBC systems, subjected to thermal loads only, ΔT, given the thickness, roughness, and damage state of the oxide layer, architecture of the system, and constituent properties was outlined. It was shown that for a given system, one needs to generate the driving forces (stress) curves as a function of oxide layer thickness and nonuniformity for both thermal only and thermomechanical loadings. It was found that damage (vertical cracking) in the oxide layer always occurs during cooldown from a high temperature to room temperature. In lieu of performing a full creep/relaxation analysis, one can perform a linear elastic analysis assuming a lower stress-free temperature. Out of plane strength curves of the EBC as a function of oxide layer thickness and roughness are also needed. Data from two or more exposure times are needed to calibrate a value of interfacial strength that can be used to obtain an estimate of critical thickness of oxide layer that will initial failure and cause spallation. Given a TGO growth curve for a given system, one can convert a critical oxide layer thickness to get an estimate of the lifetime of the EBC system in hours. Additionally, these types of materials might exhibit a volume or area effect as many ceramics do. Consequently, the interfacial strength numbers shown here pertain to a 1-in. diameter disc specimen loaded with a 0.85 in. diameter pull tab. For specimens with a bigger area/volume, the strength values may be different. Lastly, the approach also estimates the remaining strength of the EBC systems at any given point. Consequently, if the coating is also subjected to the mechanical stresses, then the EBC system will fail whenever the applied load exceeds the remaining strength.

5.2 Bond Coat Model Development - Oxidation of Silicon Particles Suspended in Mullite Matrix with Dual-Mode Vacancy Diffusion of Oxygen

5.2.1 Summary

GEA's novel HTEBC design approach utilizes a composite bond coat consisting of silicon particles suspended in a mullite matrix. The sacrificial oxidation of the silicon particles in the mullite bond coat consumes the oxidant molecules, thereby protecting the underlying substrate from oxidation. To investigate the efficacy of the novel bond coat design approach, a mathematical formulation and resulting numerical method have been developed for simulating the oxidation of silicon particles embedded in a mullite matrix. The focus is on the oxidation of the silicon in a dry oxygen environment where the oxidant is presumably oxygen. Oxygen transport from the exterior environment through the mullite is assumed to occur via two lattice defect diffusion mechanisms. As a result, the rate of oxygen transport is dictated by the self-diffusivity of the lattice defects. The numerical method is implemented using the COMSOL Multiphysics® Program. The method is applied to simulate the oxidation of silicon particles in a mullite pellet in recent oxidation experiments. Numerical results compare favorably with the oxidation behavior observed in the oxidation experiments. The method is also utilized to perform the oxidation analysis of a SiC substrate coated with a generic environmental barrier system containing the novel mullite + silicon bond coat approach.

5.2.2 Introduction

GEA’s approach of adding silicon particles to the mullite bond coat [28 and 29] should help to limit the rate of TGO substrate growth. Oxidation of the silicon particles will limit the amount of oxidant available for substrate oxidation. The various features of the bond coat such as the average particle diameter and silicon volume fraction can affect the oxidation behavior within the bond coat and affect the protection efficiency of this novel EBC approach. Consequently, a model that accurately simulates the physics associated with the oxidant diffusion and oxidation of the silicon particles would serve as a useful design tool.

The objective of this section of the report is to show the development and implementation of a model that calculates the spatial and temporal distributions of the silicon particle oxidation within the mullite bond coat. The focus here is on the oxidation of the silicon particles in the mullite within a dry oxygen environment. Oxygen diffusion from the exterior through the mullite matrix to the location of the silicon particles is assumed to occur by two lattice defect diffusion mechanisms [27]. The rate of oxygen transport depends on the diffusivity of the lattice defects. At the silica/mullite interface, it is assumed that oxygen ions combine to form molecular oxygen. Diffusion of molecular oxygen through the silica layer to the silicon surface and the subsequent oxidation of the silicon occurs in a manner similar to that described in Deal and Grove [21]. Herein, the mathematics describing the diffusion of oxygen and the oxidation of the silicon particles is presented. The mathematical formulation is implemented numerically using the COMSOL Multiphysics® simulation software [24]. The resulting numerical model is applied to simulate the oxidation of silicon particles in a mullite pellet during oxidation experiments conducted in an oxygen environment at high temperatures. It is also applied to model the oxidation of a SiC substrate coated with an environmental barrier coating system containing a mullite + silicon bond coat. Sections 5.2.3 through 5.2.6 of this report were taken from Sullivan Roy M., Oxidation of silicon particles suspended in mullite matrix with dual-mode vacancy diffusion of oxygen, NASA/TM-20230010839 [38].

5.2.3 Mathematical Model

5.2.3.1 Conservation of Oxygen Mass in Mullite Matrix

The local rate of silicon particle oxidation is tied directly to the local concentration of oxygen in the mullite surrounding the silicon particle. Thus, to calculate the spatial and temporal silicon oxidation distributions, one must calculate the spatial and temporal variations of the oxygen concentration in the mullite. The local one-dimensional form of the oxygen mass conservation equation is

$$\frac{\partial C_O}{\partial t} + \frac{\partial J_O}{\partial x} = \left(\frac{dC_O}{dt}\right)_{ox} \tag{1}$$

where C_O is the local concentration of oxygen in the mullite matrix per unit volume, J_O is the oxygen flux in the mullite, and $\left(\frac{dC_O}{dt}\right)_{ox}$ is the local rate of change of oxygen concentration in the mullite per unit volume due to the consumption of oxygen by the silicon oxidation reaction.

It is assumed that the silicon particles are spherical with an initial radius R_0 and are arranged in a hexagonal pattern with a spacing b, as shown in Figure 118(a). The initial volume fraction of the silicon particles in the mullite is then

$$\phi_{Si}^{0} = 2\frac{4\pi}{3}\frac{R_0^3}{b^3} \tag{2}$$

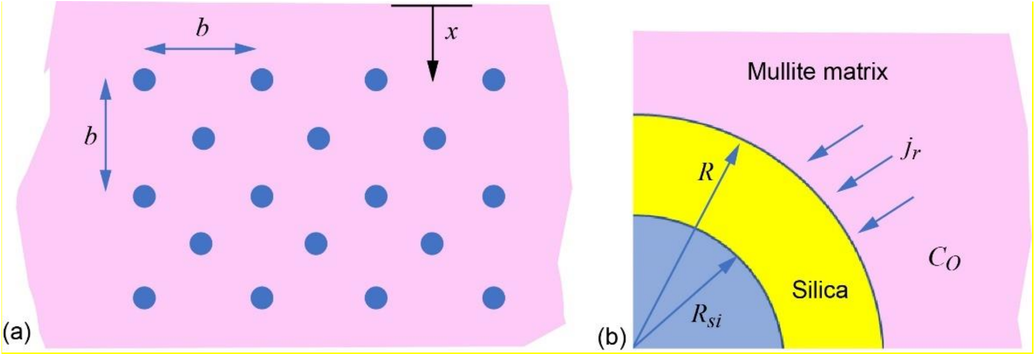

Figure 118: Spherical silicon particles dispersed in mullite matrix. (a) Arrangement of particles in mullite. (b) Growth of silica layer on silicon particle.

As time progresses, a layer of silica forms on the outer radius of each silicon particle (see Figure 118(b)). The outer radius of the silica layer is denoted by R, and the radius of the receding silicon particle surface is denoted by R_{Si}. The local flux of oxygen from the mullite matrix into the silica layer is denoted by j_r. Thus, the local rate of change of oxygen concentration in the mullite per unit volume due to growth of the silica layer is

$$\left(\frac{dC_O}{dt}\right)_{ox} = -2j_r \frac{4\pi R^2}{b^3} \tag{3}$$

Using Equations (2) and (3), Equation (1) may be written as

$$\frac{\partial C_O}{\partial t} + \frac{\partial J_O}{\partial x} = -3j_r \frac{\phi_{Si}^0}{R_0^3} R^2 \tag{4}$$

5.2.3.2 Expressions for Oxygen Flux in Mullite

Oxygen is transported through fully dense and undamaged mullite at high temperatures via the movement of lattice defects. To calculate the flux of oxygen through the mullite, one must calculate the flux of the defects. Consider the diffusion of oxygen across a mullite layer with an oxygen partial pressure differential across the layer thickness as shown in Figure 119. Here, it is assumed that $P_{O_2}^A > P_{O_2}^B$. (Kitaoka et al[27]) suggests the transport of oxygen through a mullite layer at high temperatures occurs by the following two defect reactions, which are shown using Kroger-Vink notation:

$$\frac{1}{2}O_2 \rightarrow O_O^x + 2h^{\cdot} + \frac{2}{3}V_{Al}''' \tag{5a}$$

and

$$\frac{1}{2}O_2 + \left(V_O^{\cdot\cdot} \cdot Al_{Si}'\right)^{\cdot} + e' \rightarrow O_O^x + Al_{Al}^x \tag{5b}$$

The defect reactions in Equations (5a) and (5b) occur at the higher pressure surface, and the reverse reactions occur at the lower pressure surface, as shown in Figure 119. In the transport mechanism illustrated by Equation (5a) and Figure 119(a), oxygen transport through the lattice is the result of the simultaneous diffusion of aluminum vacancies $V_{Al}^{'''}$ and electron holes $h^{\cdot}$; and in the mechanism illustrated by Equation (5b) and Figure 119(b), oxygen transport through the lattice is the result of the simultaneous diffusion of electrons e′ and the lattice defect $(V_O^{\cdot\cdot} \cdot Al_{Si}')^{\cdot}$.

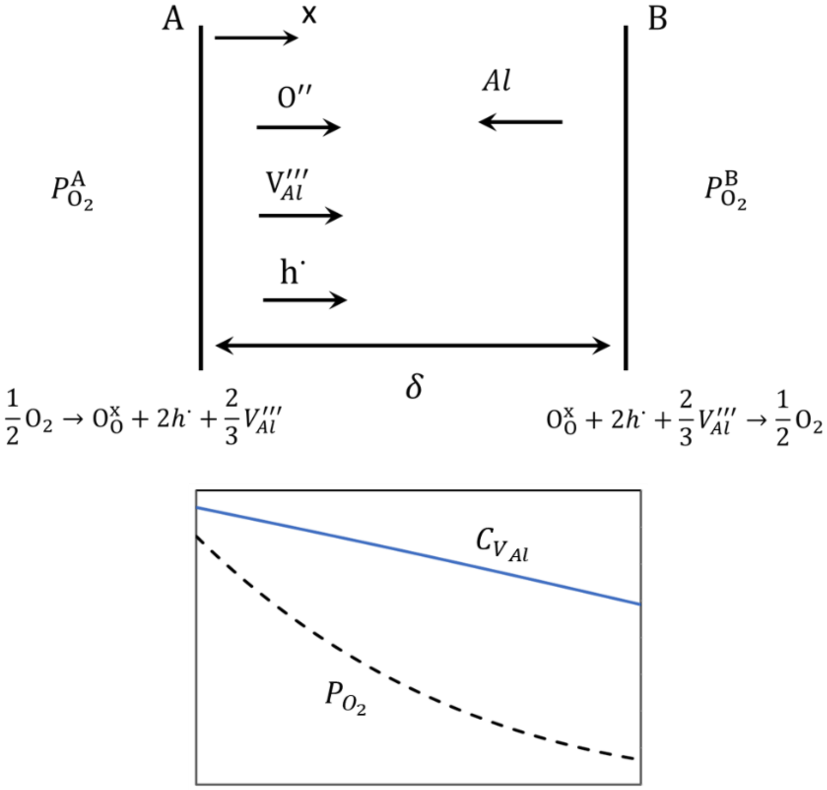

(a)

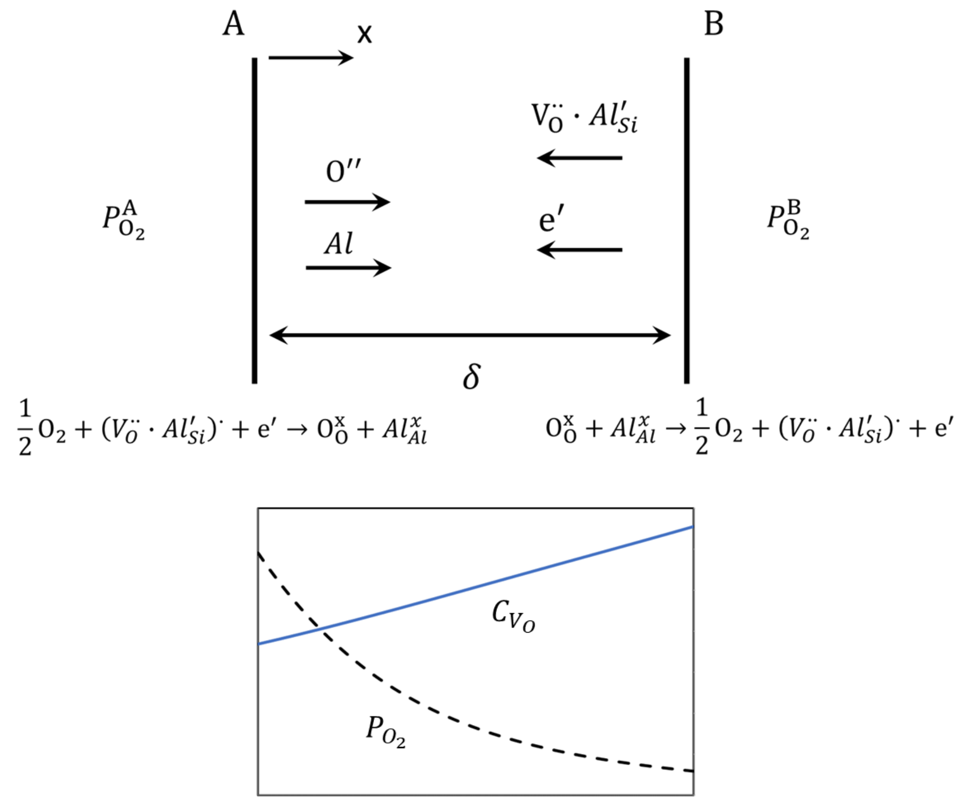

(b)

Figure 119: Layer of mullite, illustrating oxygen transport mechanisms. Included are notional sketches of oxygen partial pressure and defect concentration distributions under steady-state conditions. (a) Transport by aluminum vacancy diffusion. (b) Transport by $(V_O^{\cdot\cdot} \cdot Al_{Si}')^{\cdot}$ defect diffusion.

The equilibrium constants for the reactions shown in Equations (5a) and (5b) are written, respectively, as

$$K_{V_{Al}} = \frac{[h^{\cdot}]^2[V_{Al}''']^{2/3}}{P_{O_2}^{1/2}} \tag{6a}$$

and

$$K_{V_O} = \frac{P_{O_2}^{-1/2}}{[V_O^{\cdot\cdot} \cdot Al_{Si}'][e']} \tag{6b}$$

Denoting the aluminum vacancy V_{Al}''' and the $(V_O^{\cdot\cdot} \cdot Al_{Si}')^{\cdot}$ defect concentrations as $C_{V_{Al}}$ and C_{V_O}, respectively, Equations (6a) and (6b) may be rearranged as

$$C_{V_{Al}} = \widetilde{K}_{V_{Al}} P_{O_2}^{\frac{3}{16}} \tag{7a}$$

and

$$C_{V_O} = \widetilde{K}_{V_O} P_{O_2}^{-\frac{1}{4}} \tag{7b}$$

where $\widetilde{K}_{V_O} = \left(\frac{1}{K_{V_O}}\right)^{\frac{1}{2}}$ and $\widetilde{K}_{V_{Al}} = \left(\frac{K_{V_{Al}}}{9}\right)^{\frac{3}{8}}$. Herein, the units for the defect concentrations are m^{-3}. Using pascals as the units for the partial pressure, $\widetilde{K}_{V_{Al}}$ and $\widetilde{K}_{V_O}$ are in units of $\mathrm{m}^{-3}\mathrm{Pa}^{-3/16}$ and $\mathrm{m}^{-3}\mathrm{Pa}^{1/4}$, respectively. Notional sketches of the oxygen partial pressure and defect concentration distributions under steady-state diffusion are also included in Figure 119.

The flux of oxygen that occurs by the defect reaction in Equation (5a) will be denoted as J_p, and the flux of oxygen that occurs by the reaction in Equation (5b) will be denoted as J_n. Both mechanisms can occur simultaneously, so the total flux of oxygen is $J_O = J_p + J_n$. Furthermore, $J_p = J_{V_{Al}}$, where $J_{V_{Al}}$ is the flux of aluminum vacancies in Figure 119(a), and $J_n = -J_{V_O}$ where J_{V_O} is the flux of the $(V_O^{\cdot\cdot} \cdot Al'_{Si})^{\cdot}$ defects in Figure 119(b). All oxygen fluxes are in units of m–2s–1.

The expression for the flux of the defects $J_{V_{Al}}$ and J_{V_O} can be derived in a manner similar to that described in [26]. For both diffusion mechanisms shown in Figure 119, one assumes that the simultaneous diffusion of the charged particles occurs under the condition of electroneutrality. The derivations for the flux $J_{V_{Al}}$ are presented in the following paragraphs. Derivations for the flux J_{V_O} may be performed in a similar manner.

For the first oxygen transport mechanism shown in Figure 119, the simultaneous diffusion of aluminum vacancies and electron holes ($V_{Al}^{'''}$ and $h^{\cdot}$), the electroneutrality condition may be expressed as $Z_{V_{Al}} J_{V_{Al}} + Z_h J_h = 0$. The flux for each charged particle is given by $J_i = -D_i \frac{dC_i}{dx} + u_i E C_i$, where D_i is the self-diffusion coefficient, C_i is the concentration, u_i is the mobility, and E is the electric field. The mobility of each particle is given by the Einstein relation $u_i = \frac{Z_i e D_i}{k_B T}$, where Z_i is the charge number of the particle, e is the electron charge, k_B is the Boltzmann constant, and T is the absolute temperature. The partial conductivity of each of the charged particles is given by $\sigma_i = Z_i e u_i C_i$, and the total conductivity is the sum of the two partial conductivities $\sigma_T = \sigma_{V_{Al}} + \sigma_h$. The transport number is the ratio of the partial conductivity to the total, $t_i = \frac{\sigma_i}{\sigma_T}$.

Substituting the expressions for the charged particle fluxes into the electroneutrality condition yields an expression for the electric field:

$$E = \frac{Z_{V_{Al}} e D_{V_{Al}} \left(\frac{dC_{V_{Al}}}{dx}\right) + Z_h e D_h \left(\frac{dC_h}{dx}\right)}{Z_{V_{Al}} e u_{V_{Al}} C_{V_{Al}} + Z_h e u_h C_h} \tag{8}$$

Substituting this expression for the electric field back into the equation for aluminum vacancy flux $J_{V_{Al}}$ and using Einstein's relation, the equations for the partial conductivities and the transport numbers leads to

$$J_{V_{Al}} = -\frac{t_{V_{Al}} t_h \sigma_T}{\left(Z_{V_{Al}} e\right)^2} \left[\left(\frac{k_B T}{C_{V_{Al}}}\right)\left(\frac{d\,C_{V_{Al}}}{d\,x}\right) - \left(\frac{Z_{V_{Al}}}{Z_h}\right)\left(\frac{k_B T}{C_h}\right)\left(\frac{dC_h}{dx}\right)\right] \tag{9}$$

The equilibrium equation for the reaction in Equation (5a) is $\mu_O = 2\mu_h + \frac{2}{3}\mu_{V_{Al}}$, where μ_O, μ_h, and $\mu_{V_{Al}}$ represent the chemical potentials of the oxygen, electron hole, and aluminum vacancy, respectively. Since $Z_{V_{Al}} = -3$ and $Z_h = +1$, and recognizing that $\left(\frac{k_B T}{C_i}\right)\left(\frac{dC_i}{dx}\right) = \frac{d\mu_i}{dx}$, the terms in square brackets in Equation (9) simplify to $\frac{d\mu_{V_{Al}}}{dx} + 3\frac{d\mu_h}{dx}$. Using the equilibrium equation, Equation (9) becomes

$$J_{V_{Al}} = -\frac{3}{2}\left[\frac{t_{V_{Al}} t_h \sigma_T}{\left(Z_{V_{Al}} e\right)^2}\right]\left(\frac{d\mu_O}{dx}\right) \tag{10}$$

Recognizing that $t_h \approx 1$ and that $\sigma_{V_{Al}} = t_{V_{Al}}\sigma_T = \frac{\left(Z_{V_{Al}} e\right)^2 C_{V_{Al}} D_{V_{Al}}}{(k_B T)}$, Equation (10) becomes

$$J_{V_{Al}} = -\frac{3}{2}\left(\frac{C_{V_{Al}} D_{V_{Al}}}{k_B T}\right)\left(\frac{d\mu_O}{dx}\right) \tag{11}$$

Substituting Equation (7a) into (11) and using the expression for the chemical potential $\mu_O = \frac{1}{2}\mu_{O_2} = \frac{1}{2}\left(\mu^*_{O_2} + k_B T \ln P_{O_2}\right)$, Equation (11) becomes

$$J_{V_{Al}} = -\frac{3}{4} D_{V_{Al}} \widetilde{K}_{V_{Al}} P_{O_2}^{-\frac{13}{16}} \frac{dP_{O_2}}{dx} \tag{12}$$

The second oxygen transport mechanism shown in Figure 119 involves the simultaneous diffusion of the charged particles $(V_O^{\cdot\cdot} \cdot Al'_{Si})^{\cdot}$ and e' diffusing under the condition of electroneutrality (i.e., $Z_{V_O} J_{V_O} + Z_e J_e = 0$). The derivation of the lattice defect flux J_{V_O} follows in a similar manner as described above for the aluminum vacancy flux $J_{V_{Al}}$. The following relations are obtained at the intermediate steps:

$$J_{V_O} = \left(\frac{t_{V_O} t_e \sigma_T}{\left(Z_{V_O} e\right)^2}\right)\left(\frac{d\mu_O}{dx}\right) \tag{13a}$$

$$J_{V_O} = \left(\frac{C_{V_O} D_{V_O}}{k_B T}\right)\left(\frac{d\mu_O}{dx}\right) \tag{13b}$$

$$J_{V_O} = \frac{1}{2} D_{V_O} \widetilde{K}_{V_O} P_{O_2}^{-\frac{5}{4}} \frac{dP_{O_2}}{dx} \tag{13c}$$

where Z_{V_O}, D_{V_O}, and t_{V_O} are the charge number, self-diffusion coefficient, and transport number for the $(V_O^{\cdot\cdot} \cdot Al'_{Si})^{\cdot}$ defect, respectively.

Thus, the total flux of oxygen by both n- and p-type diffusion is

$$J_O = J_p + J_n = -\frac{3}{4} D_{V_{Al}} \widetilde{K}_{V_{Al}} P_{O_2}^{-\frac{13}{16}}\left(\frac{dP_{O_2}}{dx}\right) - \frac{1}{2} D_{V_O} \widetilde{K}_{V_O} P_{O_2}^{-\frac{5}{4}}\left(\frac{dP_{O_2}}{dx}\right) \tag{14}$$

The term in Equation (14) (and the associated oxygen diffusion mechanism) that is dominant depends on the magnitude of the oxygen partial pressure. The plots of $P_{O_2}^{-\frac{13}{16}}$ and $P_{O_2}^{-\frac{5}{4}}$ versus P_{O_2} in Figure 120 show that the former function is 2 orders of magnitude greater than the latter when $P_{O_2} \rightarrow 1$ atm. However, $P_{O_2}^{-\frac{5}{4}}$ is more than 2 orders of magnitude greater than $P_{O_2}^{-\frac{13}{16}}$ when the partial pressure is on the order of 10^{-6} Pa.

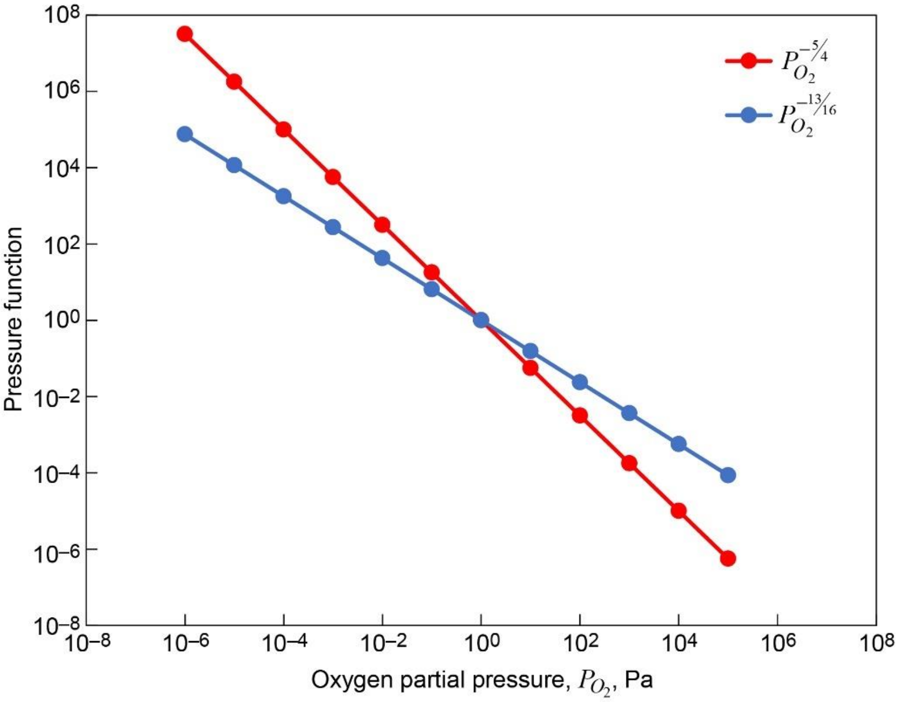

Figure 120: Pressure functions $P_{O_2}^{-\frac{5}{4}}$ and $P_{O_2}^{-\frac{13}{16}}$ versus oxygen partial pressure P_{O_2}.

5.2.3.3 First Term of Equation (4)

The significance of the oxygen partial pressure and oxygen partial pressure gradients in the oxygen transport is illustrated by Equation (14). Indeed, the oxygen partial pressure is the essential variable for the diffusion and oxidation simulation. Consequently, one may expand the first term in Equation (4) as $\frac{\partial C_O}{\partial t} = \left(\frac{\partial C_O}{\partial P_{O_2}}\right)\left(\frac{\partial P_{O_2}}{\partial t}\right)$. From Figure 119 and Equations (5a) and (5b), one can see that within the control volume at each material point, the incremental change in oxygen concentration is $\Delta C_O = \Delta C_{V_{Al}} - \Delta C_{V_O}$. As a result, one may write

$$\frac{\partial C_O}{\partial t} = \left(\frac{\partial C_{V_{Al}}}{\partial P_{O_2}} - \frac{\partial C_{V_O}}{\partial P_{O_2}}\right)\frac{\partial P_{O_2}}{\partial t} \tag{15}$$

Using Equations (7a) and (7b), Equation (15) becomes

$$\frac{\partial C_O}{\partial t} = \left(\frac{3}{16}\widetilde{K}_{V_{Al}} P_{O_2}^{-\frac{13}{16}} + \frac{1}{4}\widetilde{K}_{V_O} P_{O_2}^{-\frac{5}{4}}\right)\frac{\partial P_{O_2}}{\partial t} \tag{16}$$

Substituting Equations (14) and (16) into Equation (4) yields

$$\left(\frac{3}{16}\widetilde{K}_{V_{Al}} P_{O_2}^{-\frac{13}{16}} + \frac{1}{4}\widetilde{K}_{V_O} P_{O_2}^{-\frac{5}{4}}\right)\frac{\partial P_{O_2}}{\partial t} + \frac{\partial}{\partial x}\left(-\frac{3}{4}D_{V_{Al}}\widetilde{K}_{V_{Al}} P_{O_2}^{-\frac{13}{16}}\frac{\partial P_{O_2}}{\partial x} - \frac{1}{2}D_{V_O}\widetilde{K}_{V_O} P_{O_2}^{-\frac{5}{4}}\frac{\partial P_{O_2}}{\partial x}\right) = -3j_r\frac{\phi_{Si}^0}{R_0^3}R^2 \tag{17}$$

5.2.3.4 Equations for Oxide Growth on Spherical Substrate

In this section, equations are derived to simulate the silicon particle oxidation and silica layer growth around each particle. Here, the formulation from Deal and Grove [21] is modified to simulate oxide growth on a spherical substrate. An essential element of the Deal and Grove formulation is the assumption that oxidation of the silicon surface is facilitated by permeation of molecular oxygen through the silica layer. Thus, it is assumed here that the oxygen ions that diffused via lattice defects through the mullite to each silicon particle combine to form molecular oxygen at each silica/mullite interface. Molecular oxygen then permeates through the silica layer to the silicon/silica interface. A similar scenario was assumed in Sullivan [31]. It is also assumed that the local oxygen partial pressure in the mullite surrounding each silicon particle plays the same role as the oxygen partial pressure in the external gaseous environment in the Deal and Grove formulation.

To distinguish between the oxygen flux and oxygen concentrations in the mullite with those in the silica, a superscript s is used to denote these two quantities in the silica layer. The steady-state, one-dimensional form of the oxygen mass conservation equation in the silica layer written in polar coordinates is $\frac{\partial}{\partial r}\left(r^2\frac{\partial C_O^s}{\partial r}\right) = 0$. Upon integration, the general expression for the oxygen concentration in the silica scale is $C_O^s = -\left(\frac{\lambda_1}{r}\right) + \lambda_2$, where λ_1 and λ_2 are constants. If one assigns the oxygen concentrations at the interfaces (see Figure 121) as $C_O^s = C_{O\ a}^s$ at $r = R$ and $C_O^s = C_{O\ b}^s$ at $r = R_{Si}$, then

$$C_O^s(r) = \frac{(C_{O\ b}^s - C_{O\ a}^s)}{(R - R_{Si})}\frac{RR_{Si}}{r} + \frac{(C_{O\ a}^s R - C_{O\ b}^s R_{Si})}{(R - R_{Si})} \tag{18}$$

and

$$\frac{dC_O^s}{dr} = -\frac{(C_{O\ b}^s - C_{O\ a}^s)}{(R - R_{Si})}\frac{RR_{Si}}{r^2} \tag{19}$$

The oxygen fluxes at the two interfaces are then

$$J_O^s(r = R) = J_{O\ a}^s = D_{ox}\frac{(C_{O\ b}^s - C_{O\ a}^s)}{(R - R_{Si})}\frac{R_{Si}}{R} = j_r \tag{20a}$$

$$J_O^s(r = R_{Si}) = J_{O\ b}^s = D_{ox}\frac{(C_{O\ b}^s - C_{O\ a}^s)}{(R - R_{Si})}\frac{R}{R_{Si}} \tag{20b}$$

where D_{ox} is the diffusivity of oxygen in the silica layer.

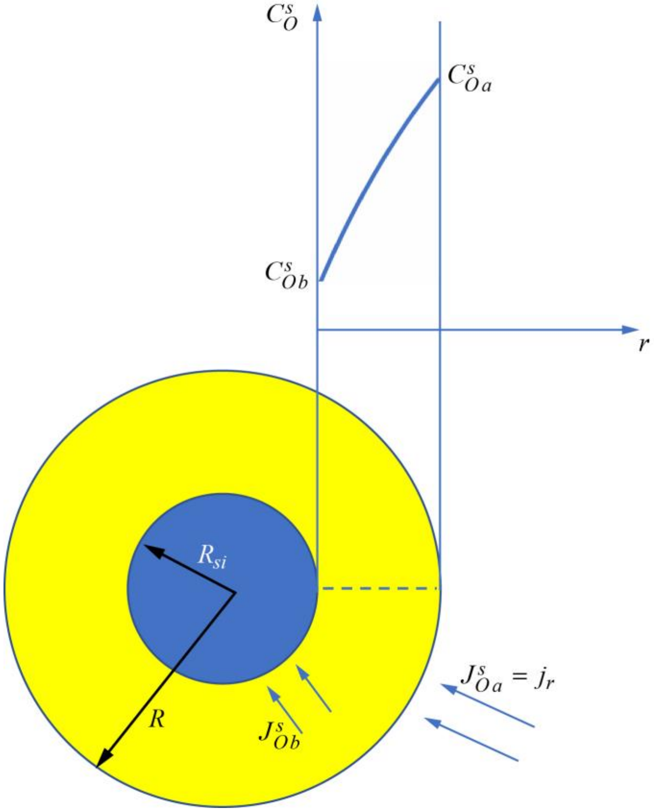

Figure 121: Spherical silicon particle with growing silica layer illustrating oxygen fluxes J^s_{Oa} and J^s_{Ob} and oxygen concentration distribution in silica layer.

The flux of oxygen at the silica/silicon interface is assumed to be consumed by a first-order oxidation reaction. Conservation of oxygen mass at this interface yields

$$J^s_{O\ b} = kC^s_{O\ b} = -D_{ox}\frac{(C^s_{O\ b} - C^s_{O\ a})}{(R - R_{Si})}\frac{R}{R_{Si}} \tag{21}$$

where k is the reaction rate constant. Rearranging Equation (21) leads to

$$C^s_{O\ b} = \frac{D_{ox}R}{kR_{Si}(R - R_{Si}) + D_{ox}R}C^s_{O\ a} \tag{22a}$$

and

$$C^s_{O\ b} - C^s_{O\ a} = \frac{-kR_{Si}(R - R_{Si})}{kR_{Si}(R - R_{Si}) + D_{ox}R}C^s_{O\ a} \tag{22b}$$

During oxidation of the silicon particles, the relation between the change in volume of silicon and silica is

$$\frac{dV_{SiO_2}}{dt} = -\Omega \frac{dV_{Si}}{dt} \tag{23}$$

where Ω is the ratio of the molar volume of silica to silicon (~2.2). Furthermore, the relation between the volume changes of silicon and silica and the changes in the radii *R* and R_{Si} is

$$\frac{dV_{Si}}{dt} = 4\pi R_{Si}^2 \frac{dR_{Si}}{dt} \tag{24}$$

$$\frac{dV_{SiO_2}}{dt} = 4\pi \left(R^2 \frac{dR}{dt} - R_{Si}^2 \frac{dR_{Si}}{dt} \right) \tag{25}$$

Substituting Equations (24) and (25) into (23) yields

$$R^2 \frac{dR}{dt} = (1-\Omega) R_{Si}^2 \frac{dR_{Si}}{dt} \tag{26}$$

Conservation of oxygen mass at the mullite/silica interface (r = R) yields

$$-4\pi R^2 j_r = N_1 \frac{dV_{SiO_2}}{dt} \tag{27}$$

where N_1 is the number of oxidant molecules incorporated into a unit volume of oxide. Using Equations (20a), (23), and (24), Equation (27) becomes

$$D_{ox} R \frac{\left(C_{O\ b}^{S} - C_{O\ a}^{S} \right)}{R - R_{Si}} = \Omega N_1 R_{Si} \frac{dR_{Si}}{dt} \tag{28}$$

Substituting Equation (22b) into (28) and then rearranging the resulting equation, one obtains

$$\frac{dR_{Si}}{dt} = -\frac{1}{\Omega} \frac{\frac{2D_{ox}}{N_1} C_{O\ a}^{S}}{\left[2(R - R_{Si}) + \frac{2D_{ox}}{k} \frac{R}{R_{Si}} \right]} \left(\frac{R}{R_{Si}} \right) \tag{29}$$

Recognizing the terms $\frac{2D_{ox} C_{O\ a}^{S}}{N_1}$ and $\frac{2D_{ox}}{k}$ in Equation (29) as the expression for the parabolic rate constant *B* and the expression for the rate constant *A* from Deal and Grove (1965) [21], respectively, one can rewrite Equation (29) as

$$\frac{dR_{Si}}{dt} = -\frac{1}{\Omega} \frac{B}{\left[2(R - R_{Si}) + \frac{R}{R_{Si}} A \right]} \left(\frac{R}{R_{Si}} \right) \tag{30}$$

Using Equations (26) and (30), one obtains the expression for the rate of change of the radius *R*:

$$\frac{dR}{dt} = \frac{(\Omega - 1)}{\Omega} \frac{B}{\left[2(R - R_{Si}) + \frac{R}{R_{Si}} A \right]} \left(\frac{R_{Si}}{R} \right) \tag{31}$$

Note the similarity in the form of the equations for dR/dt and dR_{Si}/dt and the form of the equation given by Deal and Grove [21] for the rate of oxide growth on a flat surface dx_o/dt (i.e., $\frac{dx_o}{dt} = \frac{B}{2x_o + A}$).

Finally, using Equations (23), (24), (27), and (30), one obtains the expression for the local flux of oxygen from the mullite to the silica:

$$j_r = \frac{R_{Si}}{R} \frac{BN_1}{\left[2(R - R_{Si}) + \frac{R}{R_{Si}} A\right]} \tag{32}$$

The values of dR/dt, dR_{Si}/dt, and j_r will all vary with time and spatial location because they are all dependent on the parabolic rate constant B. The value of B varies with time and position as it is linearly dependent on the oxygen partial pressure (Deal and Grove, 1965). The parabolic rate constant may be calculated at each position using the equation $B = \left(\frac{B_o}{P_{O_2}^{ref}}\right) P_{O_2}$, where B_o is the value of B at a reference oxygen partial pressure $P_{O_2}^{ref}$. The value of B_o is a function of temperature, $B_o = f(T)$. In the following oxidation analysis, it will be convenient to use the values of B reported by Deal and Grove [21] for oxidation in dry oxygen at the reference pressure $P_{O_2}^{ref} = 1$atm to define the temperature dependence of B_o.

The ratio B/A is known as the linear rate constant [21]. The value of A is only a function of temperature. Its value was reported by Deal and Grove for oxidation of silicon in dry oxygen from 800 to 1200 °C.

5.2.4 Values for the Products of oxygen fluxes

One can see from Equation (14) that the material parameters that determine the magnitude of the oxygen fluxes J_p and J_n are the products $D_{V_{Al}}\widetilde{K}_{V_{Al}}$ and $D_{V_O}\widetilde{K}_{V_O}$, respectively. The experimental results from Kitaoka et al. [27] may be used to obtain an estimate of the values of these products. Kitaoka et al. measured the flux of oxygen through mullite wafers under steady-state conditions. In those experiments, oxygen diffusion was caused by an oxygen partial pressure differential applied across the thickness (denoted L) of a mullite wafer. The higher partial pressure, denoted $P_{O_2}(hi)$, was applied at $x = 0$; and the lower pressure, denoted $P_{O_2}(lo)$, was applied at $x = L$. Integrating the equation for the total oxygen flux (Eq. (14)) over the wafer thickness leads to

$$\int_0^L J_O dx = -\frac{3}{4} D_{V_{Al}}\widetilde{K}_{V_{Al}} \int_{P_{O_2}(hi)}^{P_{O_2}(lo)} P_{O_2}^{-\frac{13}{16}} dP_{O_2} - \frac{1}{2} D_{V_O}\widetilde{K}_{V_O} \int_{P_{O_2}(hi)}^{P_{O_2}(lo)} P_{O_2}^{-\frac{5}{4}} dP_{O_2} \tag{33}$$

Under steady-state conditions, the total flux of oxygen is uniform across the mullite layer, so $\int_0^L J_O dx = LJ_O$. Upon performing the integrations in Equation (33), one obtains

$$LJ_O = 4D_{V_{Al}}\widetilde{K}_{V_{Al}} \left[P_{O_2}(hi)^{\frac{3}{16}} - P_{O_2}(lo)^{\frac{3}{16}}\right] + 2D_{V_O}\widetilde{K}_{V_O} \left[P_{O_2}(lo)^{-\frac{1}{4}} - P_{O_2}(hi)^{-\frac{1}{4}}\right] \tag{34}$$

Kitaoka et al. [27] found that a plot of the product of the wafer thickness and measured oxygen flux versus the oxygen partial pressure conditions fit an equation with the same form as Equation (34). Comparing

Equation (34) to the expression in Kitaoka et al. for the product of the specimen thickness and the oxygen flux ($J_O = N_A P$), one finds that

$$D_{V_{Al}}\widetilde{K}_{V_{Al}} = N_A \frac{A_{Al}}{16} = N_A \frac{A_{Al}}{S_{gb}} \frac{S_{gb}}{16} \tag{35a}$$

$$D_{V_O}\widetilde{K}_{V_O} = N_A \frac{A_O}{8} = N_A \frac{A_O}{S_{gb}} \frac{S_{gb}}{8} \tag{35b}$$

where A_{Al} and A_O are diffusion coefficients introduced by Kitaoka et al., N_A is Avogadro's number, and S_{gb} is the length of the grain boundary per unit total area.

Kitaoka et al [27] gives the equations for the temperature dependence of of A_{Al}/S_{gb} and A_O/S_{gb} as

$$\frac{|A_{Al}|}{S_{gb}} = 1.139 \times 10^{-10}\, exp\left(\frac{-235{,}000}{RT}\right) \quad \frac{\text{mole}}{s \cdot \text{Pa}^{\frac{3}{16}}} \tag{36a}$$

and

$$\frac{|A_O|}{S_{gb}} = 3.612 \times 10^{-3}\, exp\left(\frac{-518{,}000}{RT}\right) \quad \frac{\text{mole} \cdot \text{Pa}^{\frac{1}{4}}}{s} \tag{36b}$$

and suggests an approximate value for the grain boundary length per unit area as $S_{gb} \approx 10^6$ m^{-1}. Thus, the temperature dependence of the products $D_{V_{Al}}\widetilde{K}_{V_{Al}}$ and $D_{V_O}\widetilde{K}_{V_O}$ may be determined from Equations (35) and (36).

5.2.5 Revised Formulation Using Dimensionless Variable ψ

Equation (17) can be rewritten as

$$\begin{aligned}\left[\widetilde{K}_{V_{Al}} \frac{\partial}{\partial t}\left(P_{O_2}^{\frac{3}{16}}\right) - \widetilde{K}_{V_O} \frac{\partial}{\partial t}\left(P_{O_2}^{-\frac{1}{4}}\right)\right] + \frac{\partial}{\partial x}\left[-4D_{V_{Al}}\widetilde{K}_{V_{Al}} \frac{\partial}{\partial x}\left(P_{O_2}^{\frac{3}{16}}\right) + 2D_{V_O}\widetilde{K}_{V_O} \frac{\partial}{\partial x}\left(P_{O_2}^{-\frac{1}{4}}\right)\right] \\ = -3j_r \frac{\phi_{Si}^0}{R_0^3} R^2\end{aligned} \tag{37}$$

If one defines the dimensionless variable $\psi = \left(\frac{P_{O_2}}{P_{O_2}^*}\right)^{\frac{3}{16}}$, where $P_{O_2}^* = 1$ Pa, then $P_{O_2}^{-\frac{1}{4}} = \psi^{-\frac{4}{3}}$ Pa$^{-1/4}$. Substituting these identities into Equation (37) leads to

$$\left(\widehat{K}_{V_{Al}} + \frac{4}{3}\widehat{K}_{V_O}\psi^{-\frac{7}{3}}\right)\frac{\partial \psi}{\partial t} + \frac{\partial}{\partial x}\left[\left(-4D_{V_{Al}}\widehat{K}_{V_{Al}} - \frac{8}{3}D_{V_O}\widehat{K}_{V_O}\psi^{-\frac{7}{3}}\right)\frac{\partial \psi}{\partial x}\right] = -3j_r \frac{\phi_{Si}^0}{R_0^3} R^2 \tag{38}$$

where $\widehat{K}_{V_{Al}} = \widetilde{K}_{V_{Al}}$ Pa$^{\frac{3}{16}}$ and $\widehat{K}_{V_O} = \widetilde{K}_{V_O}$ Pa$^{-\frac{1}{4}}$. Notice that both $\widehat{K}_{V_{Al}}$ and $\widehat{K}_{V_O}$ are in units of m^{-3}. The modified equilibrium constants $\widehat{K}_{V_{Al}}$ and $\widetilde{K}_{V_{Al}}$ will have the same numerical value. They only differ by their units. The same is true for the constants $\widehat{K}_{V_O}$ and $\widetilde{K}_{V_O}$.

Equation (38) will be used as the governing differential equation for the oxygen transport and silicon particle oxidation simulations. The dimensionless variable ψ will be the primary solution variable.

5.2.6 Application

5.2.6.1 Approach

Oxidation experiments have recently been performed by General Electric Aerospace (GEA) on thin pellets of mullite embedded with silicon particles (J, Wan, [33]). The mullite pellets had a thickness of 2 mm and a silicon particle volume fraction of approximately 15 percent. The average initial radius of the silicon particles was approximately 1 μm. The mullite pellets were exposed to an environment of P_{O_2} = 1 atm at a temperature of 1482°C. The pellets were examined under a microscope after various oxidation exposure durations to characterize the evolution of the oxidation over time.

In this section, the mathematical model will be applied to simulate the oxygen diffusion and silicon particle oxidation in the mullite pellets. The COMSOL Multiphysics® program is used to implement the mathematical theory and perform the oxidation simulations. It is assumed that at the interior sections of the pellet (Figure 122), the oxygen diffusion and the oxidation are purely one dimensional. The two-dimensional diffusion and oxidation at the ends of the pellet will be ignored. A one-dimensional finite element mesh (Figure 122) is used for the numerical simulation.

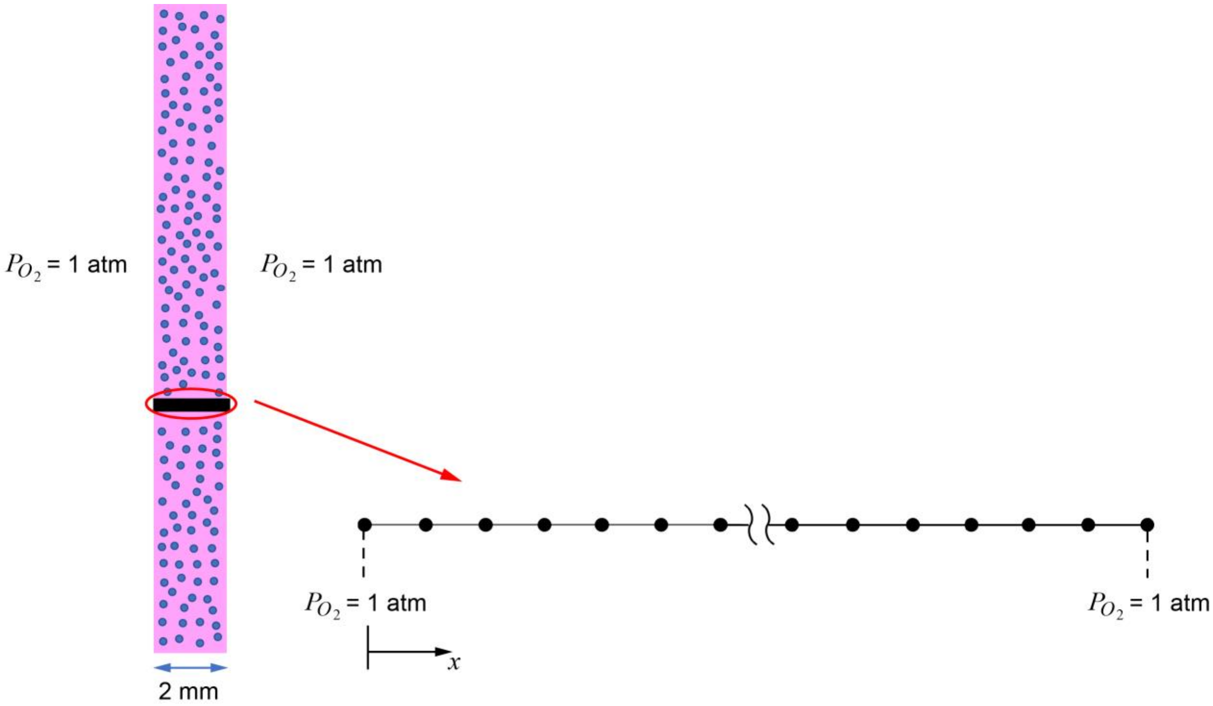

Figure 122: Flat pellet of mullite with embedded silicon particles and nodes and elements of one-dimensional finite element mesh used for numerical simulation. Numerical solution simulates one-dimensional diffusion and oxidation at interior section of pellet.

The oxidation simulations consist of the time-incremental solution of Equation (38) to obtain the spatial and temporal distributions of the solution variable $\psi = f(x,t)$. Equation (38) is solved in COMSOL using the General Form PDE interface. Initial and boundary conditions are applied on the variable ψ as

Boundary conditions: $\psi(0,t) = \psi(L,t) = (101{,}326)^{\frac{3}{16}} = 8.681$

Initial condition: $\psi(x,0) = (101{,}326)^{\frac{3}{16}} = 8.681$

where L is the thickness of the pellet.

The parabolic rate constant is calculated at each spatial location and time step using $B = B_O \frac{P_{O_2}^*}{P_{O_2}^{ref}} \psi^{\frac{16}{3}}$ where $P_{O_2}^{ref}$ = 101,325 Pa and $P_{O_2}^*$ = 1 Pa. The silicon particle radius R_{Si}, the silica outer radius R, and the local oxygen flux j_r are treated as variables in the COMSOL model. The flux j_r is calculated at each spatial location and time step using Equation (32). The values of R_{Si} and R are updated at each location and each time step with Domain ODE Interfaces. The rate of change of R_{Si} and R are calculated using Equations (30) and (31), respectively.

To quantify the degree to which a silicon particle at each material point has been oxidized, the extent of oxidation is defined here as $\omega = 1 - \left(\frac{R_{Si}}{R_0}\right)$. A fully oxidized material point (R_{Si} = 0) has an extent of oxidation ω = 1, whereas a completely unoxidized point ($R_{Si} = R_0$) has ω = 0.

The values of the input parameters for the baseline numerical solution are listed in Table 26. The parabolic rate constant B_o and the linear rate constant B_o/A have an Arrhenius temperature dependence. The pre-exponential coefficients and activation energies for B_o and B_o/A were obtained from the values for these rate constants listed in Deal and Grove [21] at temperatures from 800 to 1200°C for a dry oxygen environment. The values of B_o and B_o/A at 1482 °C were then calculated using the Arrhenius law. This provides the values of A and B_o used in the simulation.

Table 26: Input Parameters for Numerical Solution of Mullite+Silicon Pellet Oxidation Simulation

Temperature independent	L, μm	2000
	ϕ_{Si}^0	0.15
	R_0, μm	1
	Ω	2.2
Temperature dependent, evaluated at T = 1482 °C	A, μm	0.021
	B_o, $\mu m^2/h$	0.263
	$D_{V_{Al}}\widehat{K}_{V_{Al}}$, $m^{-1}s^{-1}$	4.34×10^{11}
	$D_{V_O}\widehat{K}_{V_O}$, $m^{-1}s^{-1}$	1.04×10^{11}
	$\widehat{K}_{V_{Al}}$, m^{-3}	4.34×10^{25}
	$\widehat{K}_{V_O}$, m^{-3}	1.04×10^{25}

The values of the products $D_{V_{Al}}\widetilde{K}_{V_{Al}}$ and $D_{V_O}\widetilde{K}_{V_O}$ at 1482°C were calculated using Equations (35) and (36). In addition, it is necessary to distinguish between the values of the defect diffusivities ($D_{V_{Al}}$ and D_{V_O}) and the values of the modified equilibrium constants ($\widehat{K}_{V_{Al}}$ and $\widehat{K}_{V_O}$), as the first term in Equation (38) contains only the modified equilibrium constants. One may estimate the values of $\widetilde{K}_{V_{Al}}$ and $\widetilde{K}_{V_O}$ with Equations (7a) and (7b) and by permitting only reasonable values for the defect concentrations. For example, at an oxygen partial pressure of 101,326 Pa, a modified equilibrium constant of $\widehat{K}_{V_{Al}} = 10^{27}$ m^{-3} would yield a defect concentration of 14,400 mole/m^3. This is a rather high concentration of aluminum vacancies, given that the concentration of aluminum in mullite is 45,200 mole/m^3 [27]. As a result, reasonable values for the modified equilibrium constants will be restricted to values $\leq 10^{26}$ m^{-3}. It is also noted that numerical solutions using modified equilibrium constant values of $\leq 10^{24}$ m^{-3} resulted in numerical instabilities and failed solutions. Given these considerations, the values $\widehat{K}_{V_{Al}} = 4.34 \times 10^{25}$ m^{-3}, $\widehat{K}_{V_O} = 1.04 \times 10^{25}$ m^{-3}, and $D_{V_{Al}} = D_{V_0} = 1 \times 10^{-14}$ m^2/s will be used in the numerical solutions. The diffusivities of the two defects are likely not the same. However, the specific values for the two defect diffusivities are unknown. The assumption that they are equivalent is used here to demonstrate the numerical approach.

5.2.6.2 Results

A numerical solution was performed using the input parameters shown in Table 26 and defect self-diffusivities values of $D_{V_{Al}} = D_{V_O} = 1 \times 10^{-14}$ m^2/s. The results of the numerical solution are shown in Figure 123. The dimensionless function ψ is plotted versus location at 10, 100, 1000, 2000, and 4000 hours in Figure 123(a), and the oxygen partial pressure P_{O_2} is plotted versus location at the same five times in Figure 123(b). Both the dimensionless function ψ and the oxygen partial pressure are initially uniform across the specimen thickness as a result of the imposed initial conditions. Early in the simulation, the partial pressure and dimensionless function are depleted at the interior of the specimen by a small amount of silicon particle oxidation. After the initial stages of oxidation, the only oxygen available for silicon oxidation is supplied by diffusion from the exterior surfaces. This causes an oxidation front that progresses inward with time from the two exterior surfaces. Figure 123(c) and (d) show the results for the oxygen fluxes J_p and J_n, respectively. J_p is significantly higher in magnitude than J_n, which is expected from the oxygen partial pressure of P_{O_2} = 1 atm at the exterior surfaces. The silicon particle radius and the extent of oxidation are plotted versus location in Figure 123(e) and 6(f), respectively. Figure 123(e) and (f) show the progression of the oxidation front from the exterior surface towards the interior as time progresses.

The extent of oxidation at 2000 hours in Figure 123(f) is replotted in Figure 124 to illustrate the thickness of the fully oxidized region and the transition region, which is the region between the fully oxidized region and unoxidized region. Note that the transition region is quite narrow. This numerical result is consistent with observations from micrographs of the oxidized pellets (J, Wan, [33]).

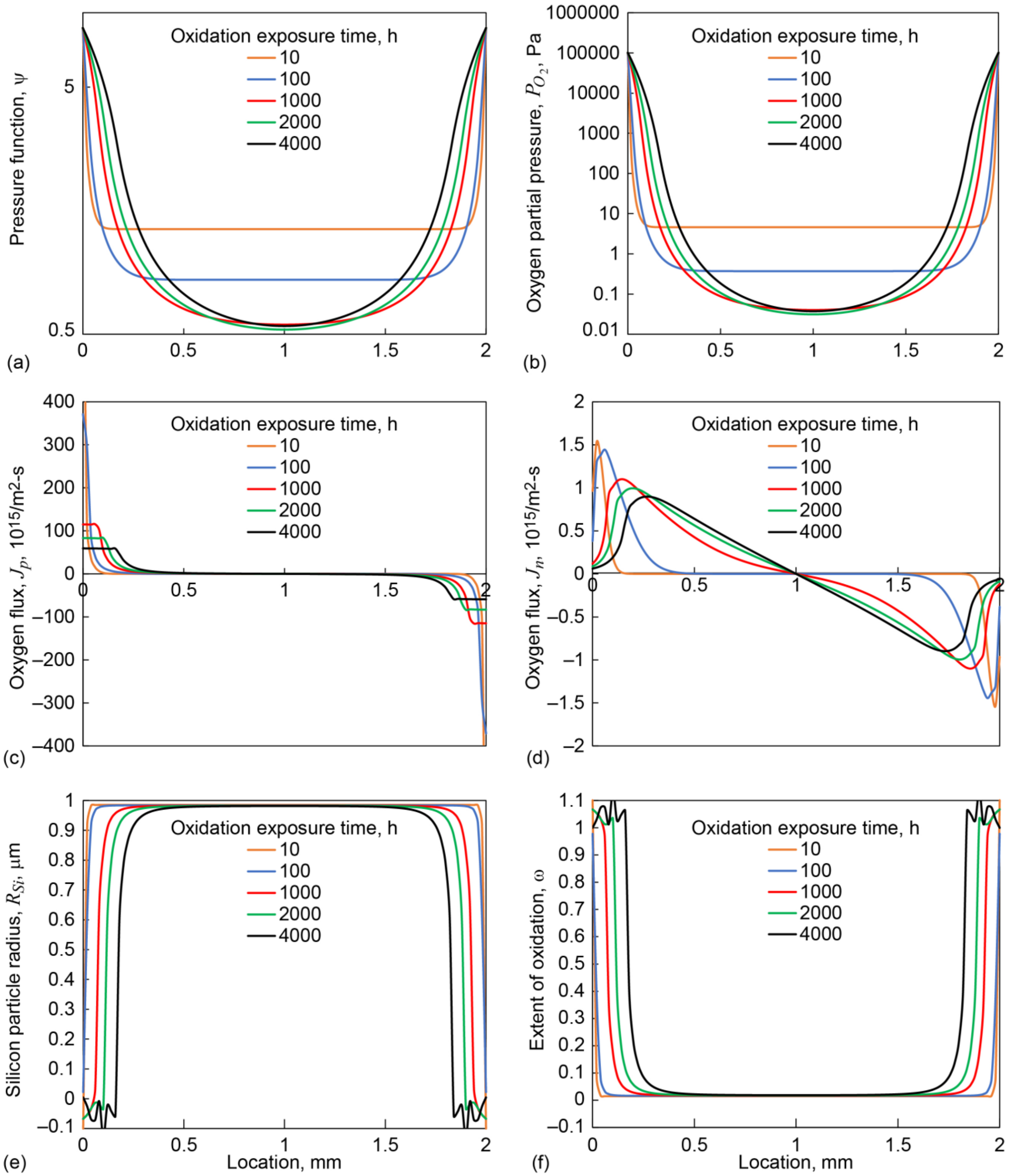

Figure 123: Numerical solution results plotted versus location at 10, 100, 1000, 2000 and 4000hrs.
(a) Dimensionless function ψ*. (b) Oxygen partial pressure* P_{O_2}*.*
(c) Oxygen flux J_p*. (d) Oxygen flux* J_n*.*
(e) Silicon particle radius R_{Si}*. (f) Extent of oxidation* ω*.*

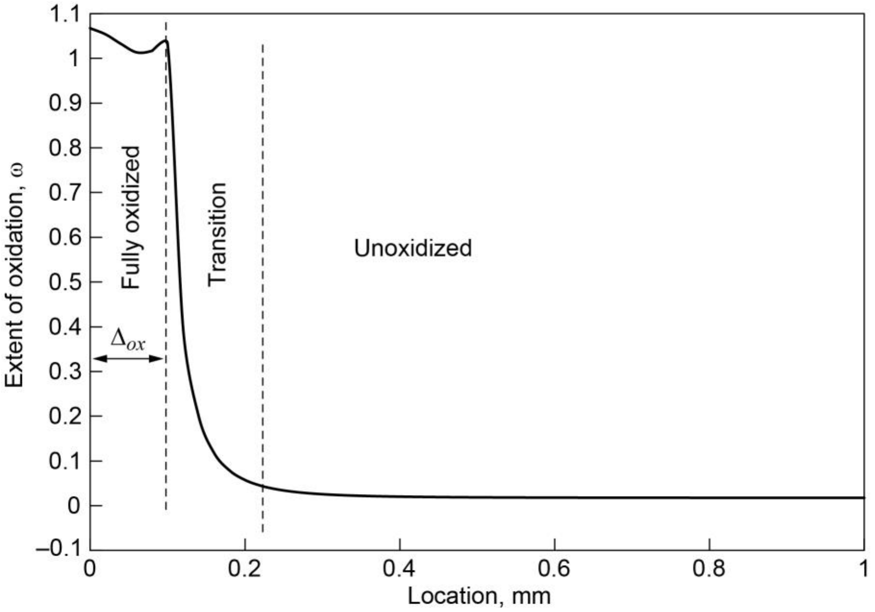

Figure 124: Extent of oxidation versus location at 2000hrs from numerical solution using input parameters in Table 26 and defect self-diffusivity of 1×10–14 m2/s. Fully oxidized, unoxidized, and transition regions are illustrated.

Numerical solutions were performed to investigate the effect of the defect diffusivity on the oxidation profiles. Two additional numerical solutions were performed using defect self-diffusivity values of 4×10^{-15} and 1×10^{-15} m^2/s. All other input parameters were the same as those listed in Table 26. The thicknesses of the fully oxidized region obtained from the numerical simulation using a vacancy diffusivity of 4×10^{-15} m^2/s are in close agreement with the fully oxidized thicknesses observed in the micrographs of the oxidized pellets at 1000 and 2000 hours. The comparison between the observed and the predicted fully oxidized thicknesses at 4000 hours is not as favorable. This discrepancy at 4000 hours might be due to grain growth in the mullite. If oxygen diffusion in mullite is primarily along the grain boundaries [25 and 27], then grain growth would cause a reduction in the diffusivity over time, resulting in less oxidation progression at 4000 hours than what would be predicted by a constant-diffusivity model.

An additional numerical solution was also performed to investigate the effect of the initial silicon particle radius R_0 on the oxidation. A numerical solution was performed with R_0 = 5 μm and $D_{V_{Al}} = D_{V_O} = 1 \times 10^{-14}$ m^2/s. All other input parameters were the same as those listed in Table 26. The intent of this analysis is to show the effect of increasing the initial particle radius while keeping the silicon volume fraction the same. To keep the silicon volume fraction the same while increasing the particle radius, one would need to increase the average particle spacing b. The extent of oxidation versus location for the solutions with R_0 = 1 and 5 μm is plotted in Figure 125. The results in Figure 125 show that a larger particle radius results in a slower progression of the oxidation front. The mullite/silicon particle interfacial area per unit volume ($8\pi R^2/b^3$) increases as the particle radius decreases. So, provided the local interfacial flux j_r is approximately equal in the two numerical solutions, the local oxygen consumption rate per unit volume (the right-hand side of Equation (3)) would be higher with the smaller particles.

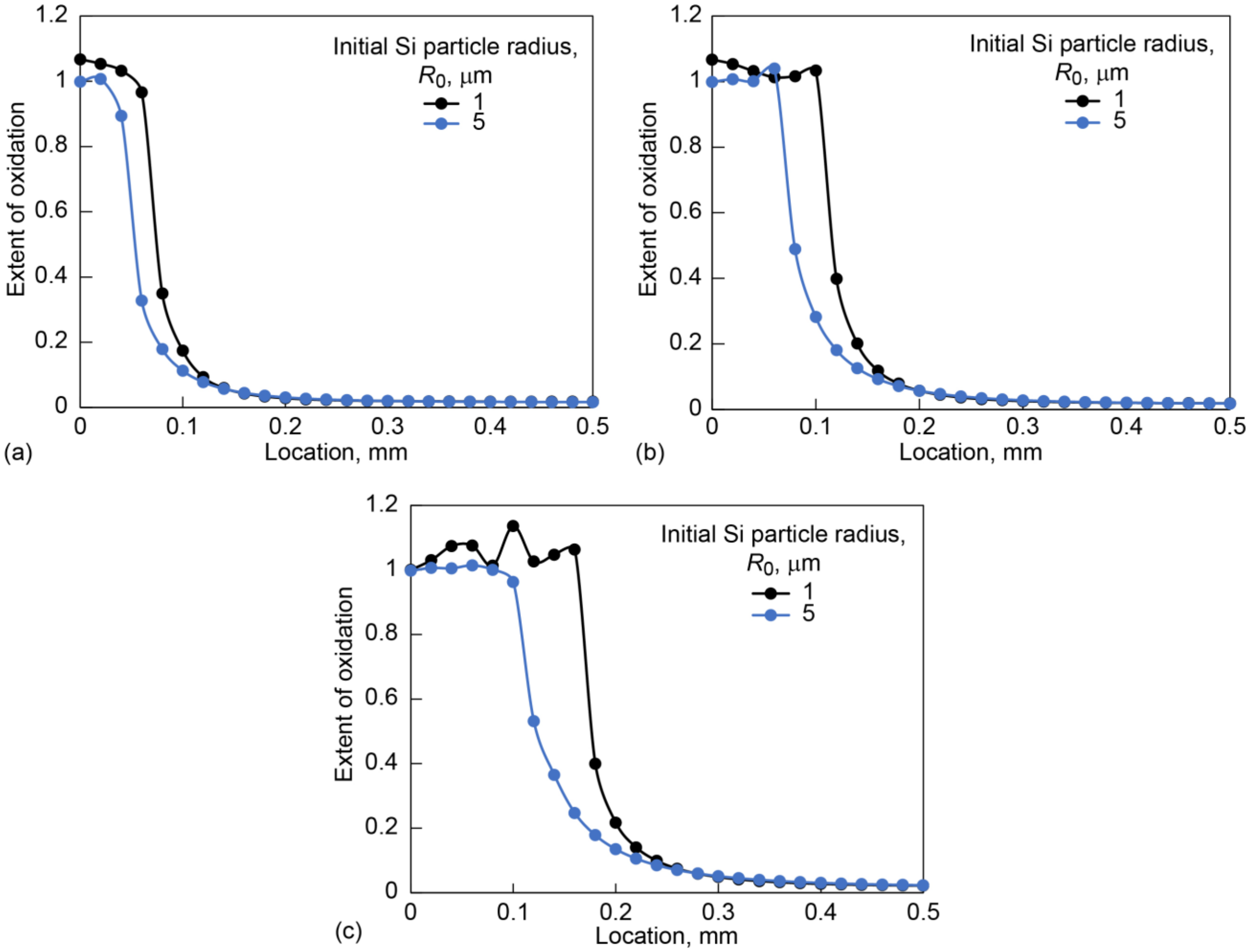

Figure 125: Numerical results showing effect of initial silicon particle size. Extent of oxidation versus location at different times for initial silicon particle sizes of R_0 = 1 and 5 μm. Both numerical solutions used self-diffusivity $D_{V_{Al}} = D_{V_O} = 1 \times 10^{-14}$ m^2/s and initial silicon volume fraction ϕ_{Si}^0 = 0.15. (a) 1000hrs. (b) 2000hrs. (c) 4000hrs.

Finally, the numerical tool was used to investigate the effect of varying the initial silicon particle volume fraction while keeping the initial particle radius R_0 constant. Physically, this would be achieved by varying the particle spacing. Numerical solutions were performed with ϕ_{Si}^0 = 0.05, 0.15, and 0.25; $D_{V_{Al}} = D_{V_O} = 1 \times 10^{-14}$ m^2/s; and all other input parameters the same as those listed in Table 26. The extent of oxidation versus location from these three numerical solutions are shown in Figure 126. The results in Figure 126 show that the oxidation progression increases with a decreasing silicon volume fraction. However, the relationship between the oxidation progression and the silicon particle volume fraction is not linear; that is, there is not as much difference in the oxidation progression between the ϕ_{Si}^0 = 0.25 and the ϕ_{Si}^0 = 0.15 solutions as there is between the ϕ_{Si}^0 = 0.15 and ϕ_{Si}^0 = 0.05 solutions.

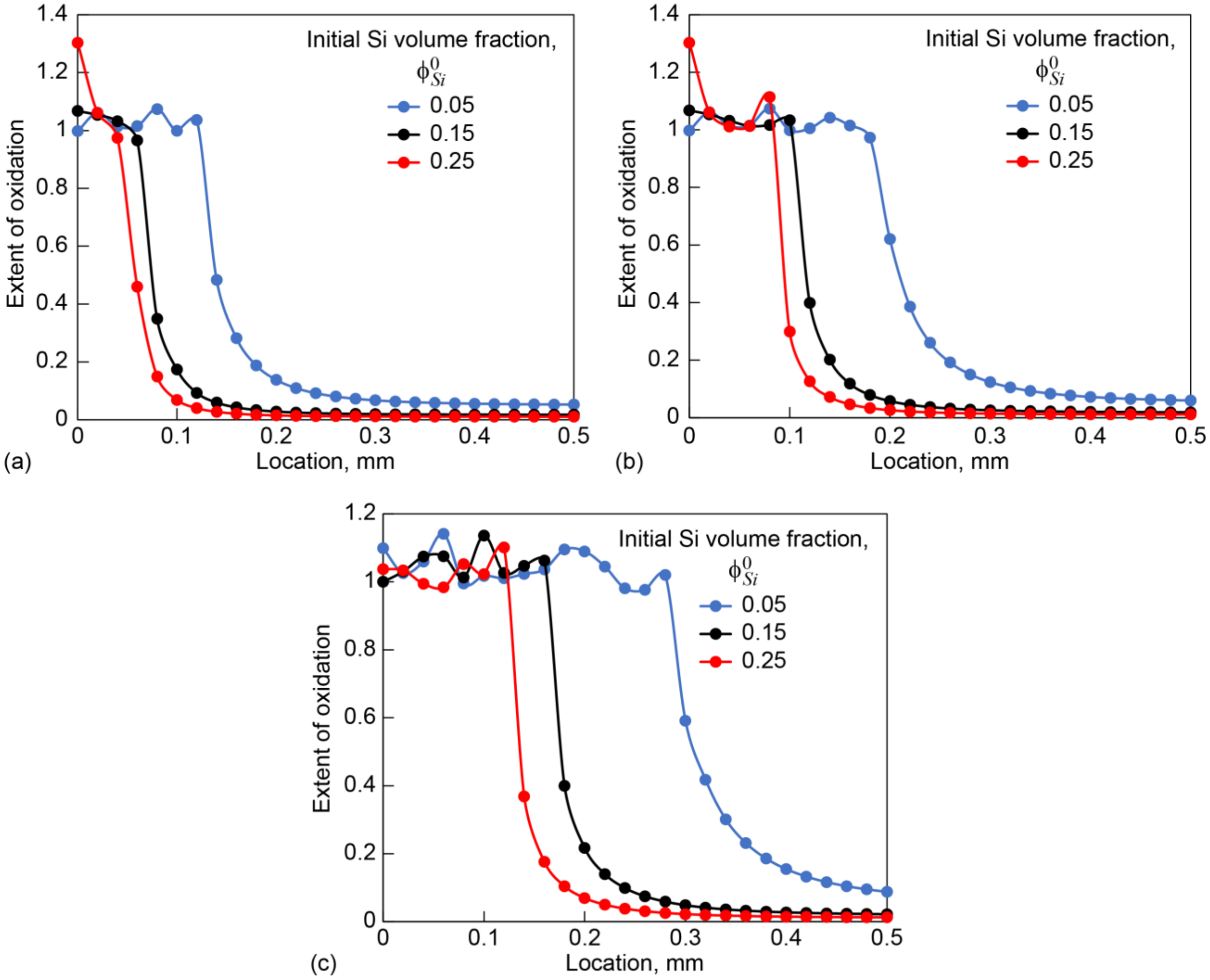

Figure 126: Numerical results showing effect of initial silicon volume fraction.
Extent of oxidation versus location for initial silicon volume fractions ϕ_{Si}^0 = 0.05, 0.15, and 0.25.
*All three numerical solutions used self-diffusivity $D_{V_{Al}} = D_{V_O} = 1 \times 10^{-14}$ m^2/s and initial silicon particle radius R_0 = 1 μm. (a) 1000hrs. **(**b) 2000hrs. (c) 4000hrs.*

5.2.7 Analysis of an Environmental Barrier Coating System with a mullite + silicon bond coat

In this section, an oxidation analysis of a SiC substrate with an environmental barrier coating (EBC) containing a mullite + silicon particle bond coat will be performed. The environmental barrier coating system consists of a layer of mullite with embedded silicon particles applied on a SiC substrate. A single layer of Yb$_2$Si$_2$O$_7$ is then applied on top of the bond coat. The substrate and EBC system are exposed to an oxygen environment $P_{O_2} = 1\ atm$ at a temperature of 1482^{o}C. Oxygen from the environment will diffuse through the topcoat and the mullite matrix of the bond coat, oxidizing the silicon particles and the SiC substrate. A layer of silica will form around each silicon particle as well as on the flat substrate surface. The thickness of the silica layer on the substrate will be denoted as x_o. Oxidation of the silicon particles will limit the amount of oxygen available for substrate oxidation and thus retard the substrate oxidation. The analysis will demonstrate the ability of the silicon particles to delay the oxidation of the substrate.

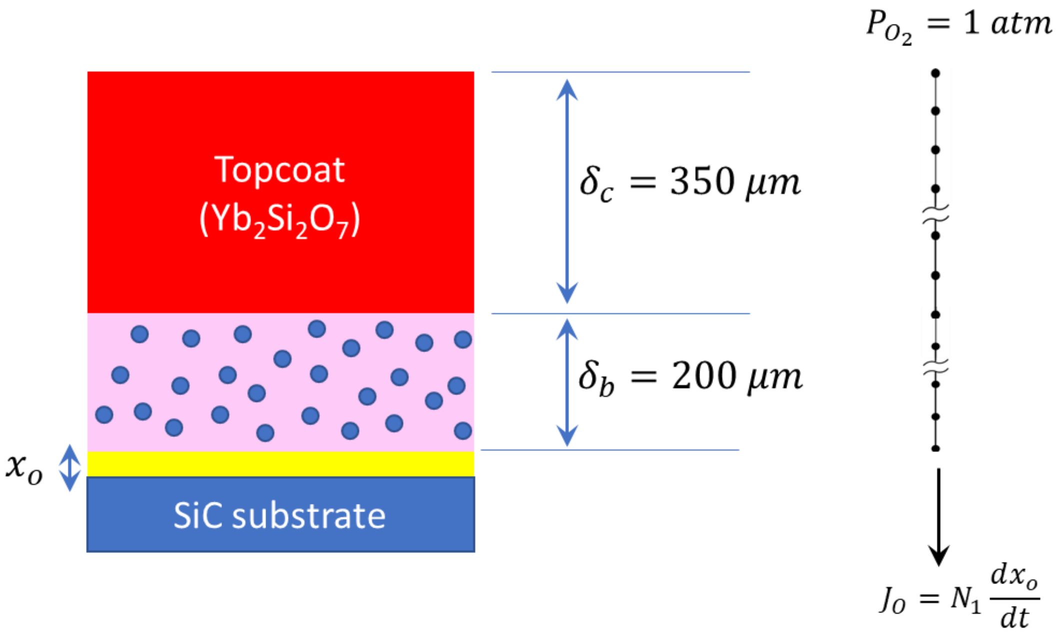

Figure 127: Sketch of environmental barrier coating system and SiC substrate with finite element mesh and imposed boundary conditions for numerical solution.

Diffusion of oxygen through the mullite matrix is assumed to occur by the two defect diffusion mechanisms described in the previous section of this report. Diffusion of oxygen through the $Yb_2Si_2O_7$ topcoat is assumed to occur by the two defect diffusion mechanisms described by Wada et al [32]. One oxygen diffusion mechanism involves the diffusion of Ytterbium vacancies and the other involves the diffusion of oxygen vacancies. A summary of the defect diffusion mechanisms for the diffusion of oxygen in both $Yb_2Si_2O_7$ and mullite and the values for the defect self-diffusivities and modified equilibrium constants that were used in these analyses are listed in Table 29. The values of the modified equilibrium constant were obtained by calculating the product $D_V\ \tilde{K}_V$ at 1482°C and by assuming a value for the defect self-diffusivity.

Table 27: Summary of oxygen diffusion mechanisms in topcoat and bond coat including defect self-diffusivities and modified equilibrium constants

	Transport mechanism	**Equ. Const. (m^{-3})**	**Diffusivity (m^2/s)**
Topcoat ($Yb_2Si_2O_7$)	$\frac{1}{2}O_2 \rightarrow O_O^x + 2h^{\cdot} + \frac{2}{3}V_{Yb}'''$	$\hat{K}_{V_{Yb}} = 3.36x10^{26}$	$D_{V_{Yb}} = 1x10^{-14}$
	$\frac{1}{2}O_2 + V_O^{\cdot\cdot} + 2e' \rightarrow O_O^x$	$\hat{K}_{V_O} = 4.39x10^{26}$	$D_{V_O} = 1x10^{-14}$
Mullite bond coat	$\frac{1}{2}O_2 \rightarrow O_O^x + 2h^{\cdot} + \frac{2}{3}V_{Al}'''$	$\hat{K}_{V_{Al}} = 4.34x10^{25}$	$D_{V_{Al}} = 1x10^{-14}$
	$\frac{1}{2}O_2 + (V_O^{\cdot\cdot} \cdot Al_{Si}')^{\cdot} + e' \rightarrow O_O^x + Al_{Al}^x$	$\hat{K}_{V_O} = 1.04x10^{25}$	$D_{V_O} = 1x10^{-14}$

The EBC and substrate oxidation analysis is performed with COMSOL by solving equation (17) in the bond coat domain and simultaneously solving a similar oxygen mass conservation equation in the topcoat domain. The local mass conservation equation for oxygen in the topcoat is

$$\left(\frac{3}{16}\widetilde{K}_{V_{Yb}}P_{O_2}^{-13/16}+\frac{1}{6}\widetilde{K}_{V_O}P_{O_2}^{-7/6}\right)\frac{dP_{O_2}}{dt}+\frac{\partial}{\partial x}\left(-\frac{3}{4}D_{V_{Yb}}\widetilde{K}_{V_{Yb}}P_{O_2}^{-13/16}\frac{dP_{O_2}}{dx}-\frac{1}{2}D_{V_O}\widetilde{K}_{V_O}P_{O_2}^{-7/6}\frac{dP_{O_2}}{dx}\right)=0 \tag{39}$$

Equation (39) includes terms that simulate the defect diffusion mechanisms proposed by Wada et al [32] for the diffusion of oxygen in $Yb_2Si_2O_7$. Note that the right-hand side of (39) is equal to zero since there is no consumption of oxygen due to oxidation in the topcoat. Solution of equation (39) in the topcoat domain and equation (17) in the bond coat domain yields the oxygen partial pressure at each spatial location within the topcoat and bond coat layers.

Figure 127 also shows a sketch of the one-dimensional finite element mesh with the imposed boundary conditions. There is a Dirichlet boundary condition of $P_{O_2} = 1\ atm$ at the exterior surface node and an oxygen flux boundary condition imposed at the opposite end of the mesh which coincides with the interface between the mullite bond coat and the growing silica layer on the substrate. This flux represents the flux of oxygen required to grow the silica on the substrate. For flat surfaces, the relationship between the oxidant flux and the rate of oxide growth is $J = N_1 \frac{dx_o}{dt}$.

As in the oxidation analyses described in the previous section, the silicon particle radius R_{Si}, the outer silica radius R and the local flux j_r are calculated at each spatial location within the bond coat using equations (30), (31) and (32), respectively. To distinguish between oxidation of the silicon particles and the SiC substrate, the rate constants for the oxidation of the silicon particles will be denoted A_{Si} and B_{Si} in the following discussion. The parabolic rate constant B_{Si} is calculated at each spatial location using the local oxygen partial pressure and the equation $B_{Si} = \frac{B_{o\,Si}}{1\,atm} P_{O_2}$, where $B_{o\,Si}$ is the parabolic rate constant for the oxidation of silicon at an oxygen partial pressure of 1 atm. The values of $B_{o\,Si}$ and A_{Si} used in this analysis were obtained by extrapolating the values of B and B/A listed in Deal and Grove for oxidation in dry oxygen to 1482°C.

From Deal and Grove [21], the expression for the rate of oxide growth on a flat surface has the form $\frac{dx_o}{dt} = \frac{B}{2x_o + A}$. To specify the oxide growth on the flat SiC surface, one may write

$$\frac{dx_o}{dt} = \frac{B_{SiC}}{2x_o + A_{SiC}} \tag{40}$$

where A_{SiC} and B_{SiC} are the oxidation constants for the SiC substrate. The parabolic rate constant B_{SiC} is calculated using the oxygen partial pressure at the mullite/silica interface $P_{O_2}(\delta_c + \delta_b)$ and the equation $B_{SiC} = \frac{B_{o\,SiC}}{1\,atm} P_{O_2}(\delta_c + \delta_b)$, where $B_{o\,SiC}$ is the parabolic rate constant for the oxidation of SiC at an oxygen partial pressure of 1 atm. The values of $B_{o\,SiC}$ and A_{SiC} were obtained by extrapolating the values of B and B/A for the "CVD Fast" data listed in Ramberg, et al. [30] to 1482°C.

Equation (40) was used to calculate the rate of substrate oxide growth and to update the flux boundary condition imposed on the finite element mesh at each time step. Note that the flux boundary condition varies with time as it is a function of the substrate oxide thickness and the value of B at the mullite/silica interface, which depends on the oxygen partial pressure at that location.

An oxidation analysis was performed with the bond coat attributes of $R_0 = 1\mu m$ and $\phi_{Si}^0 = 0.05$ and the values for the input parameters listed in Table 27. The numerical results are shown in Figure 128. Figure

128a is a plot of the oxygen partial pressure in the topcoat and bond coat at 500, 1000 and 2000 hours. Figure 128b is a plot of the silicon particle radius in the bond coat at 100, 500, 1000, 1500 and 1700 hours. Note the depletion of silicon particles in the bond coat as time progresses. The silicon particles are completely converted to silica at approximately 1700 hours. Figure 128c is a plot of the substrate oxide thickness versus time. The substrate oxide thickness remains low until 1700 hours. Once the silicon in the bond coat is completely oxidized then the oxygen partial pressure at the mullite/silica interface increases and oxidation of the substrate is accelerated. This point in time is referred to here as the “turning point.”

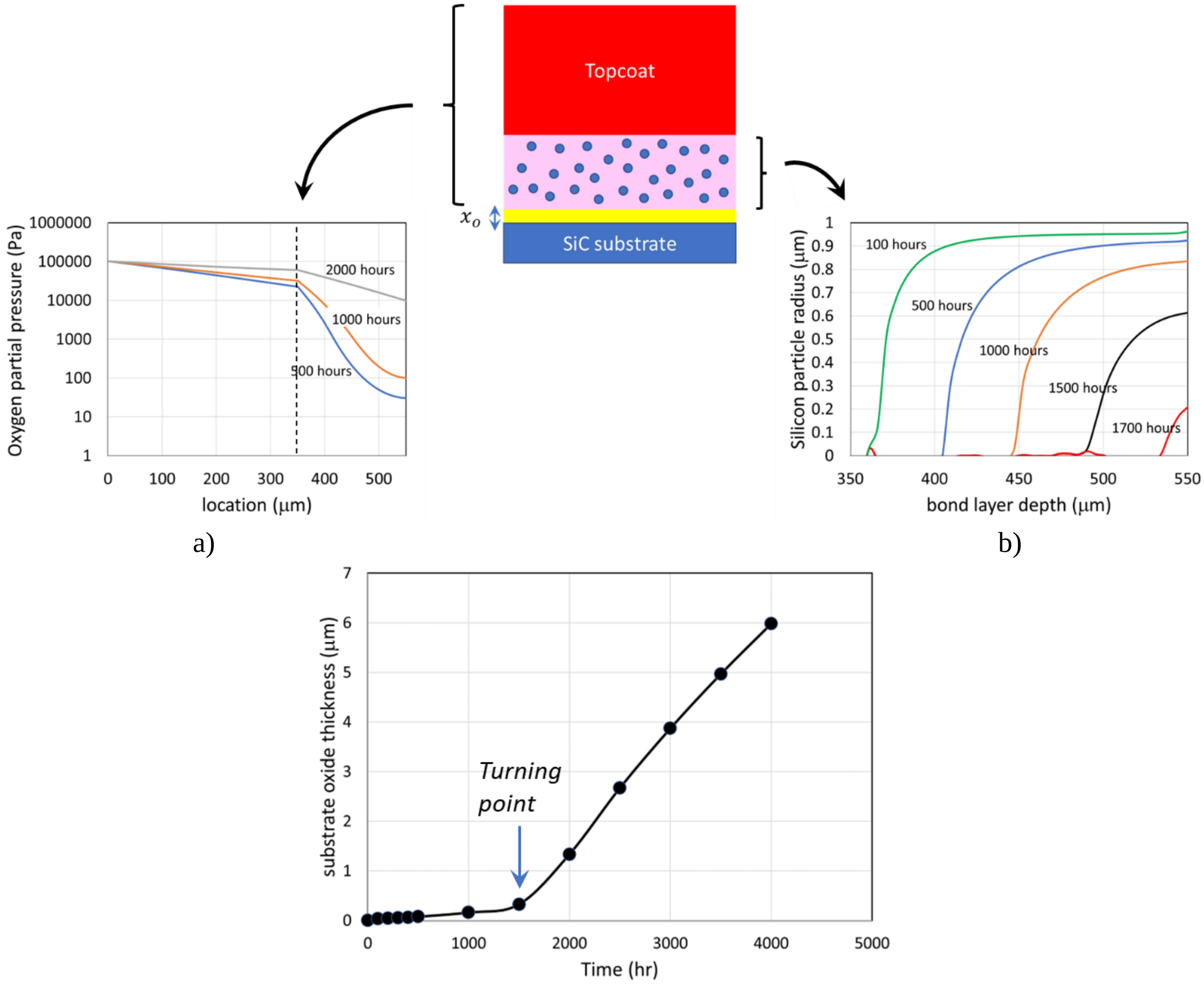

a)

b)

c)

Figure 128 Numerical results from solution using R_0=1μm and ϕ_{Si}^0=0.05. a) Oxygen partial pressure in topcoat and bond coat. b) Silicon particle radius in bond coat at various times. c) Substrate oxide thickness versus time

5.2.8 Concluding Remarks

A numerical method to calculate the oxidation of silicon particles embedded in a mullite matrix has been presented. The method simulates oxidant diffusion and oxidation of the silicon particles in a dry oxygen environment where the oxidant is presumably oxygen. The method includes transport of oxygen by two lattice defect diffusion mechanisms. The numerical method has been implemented using COMSOL Multiphysics® Program (2021).

The method has been applied here to simulate the silicon particle oxidation behavior in a mullite pellet during recent oxidation experiments. It has also been applied to simulate the oxidation of a SiC substrate coated with a generic EBC system with a mullite + silicon bond coat. The method can be used to study the effects of the various attributes of the bond coat on its ability to limit the substrate oxidation.

6. Technology Assessment

6.1 TRL-4 and TRL-5 Assessment

The goal for the program was to mature the HTEBC technology to a NASA TRL-5 level, including achieving TRL 4 if not already performed. Based on the HTEBC maturation activities under this program, TPM assessments for TRL-4 and TRL-5 are captured in the Table 28 against the criteria set forth in section 2.2.2.

Table 28 TPM assessment for TRL exit

Airfoil ID	Architecture	TRL-4 TPM		TRL-5 TPM		
		Steam Oxidation	QARE Rig	Steam Oxidation	JETS	Combustion Rig
0		PASS	PASS	PASS	PASS	PASS
1A	1i	PASS	PASS	PASS	PASS	PASS
1B		PASS	PASS	PASS	PASS	Not tested
2A	2ii	PASS	PASS	PASS	PASS	Not tested
2B		PASS	PASS	PASS	PASS	PASS

All 3 architectures (0, 1 and 2) have met KPP-4 criteria, as defined in Table 1, with considerable durability at temperatures beyond the capability of current SoA EBC coatings. Therefore, they are assessed at NASA TRL-5.

6.2 Lessons learned

EBCs are multilayer systems with complex structure engineered for very specific functionality assigned to each layer. Physical and chemical interactions between the EBC and CMC substrate, within and between the coating layers can be very complicated with time, temperature, and environment and, in some cases, hard to predict. The complexities of coating responses increase dramatically with increasing temperature and the resulting reactivity. GEA's high temperature EBC system has integrated many of the lessons from Gen2 EBC development and deployment efforts. Key lessons learned from developing such a complex high temperature coating system include:

1) Early integration of the entire system- CMC and EBC architecture- is important. Changing one component can often lead to unforeseeable consequences to other components. Therefore, key tests, especially long duration high-temperature exposures, or high-cost tests are best performed with all the components in place.
2) For the same reason as above, while fundamental thermodynamics, thermochemistry and kinetics guide the material selections, evolving material systems needs frequent and through experimental evaluations at all TRL stages to offer timely feedback to material and process design efforts. In this program, the addition of QARE rig test alongside steam and JETS test proved to lead to positive outcomes and hence encouraged for future efforts.
3) For reasons above, it has been proven to be a wise decision to prepare multiple backup articles for key tests such as CE-5 rig tests. This practice greatly reduced the risk associated with complex conditions in both fabrication and testing and has been one of the key factors that ensured the success of the program.

4) Allocations of time and planning resources to more complex test plans such as QARE and CE-5 rig are often underestimated. More than often, standing up the test facility and the need to perform shakedown test are forced to let go of because of limited time and resources. Future programs should plan such test conservatively or with pessimism built in.
5) Design of hardware with the complexity of the combustion test requires an immense amount of time and flexibility. The use of new manufacturing techniques such as additive processing provides significant design advantages but results in new and many times unforeseen challenges. As mentioned regarding the fabrication of backup articles, fabrication of additional test hardware components proved to be significantly helpful.
6) Basic material thermal and flow modeling are essential and should be included in the initial test development as well as throughout the test campaign. In this work, preliminary modeling would have provided a baseline for expectation and could have impacted the design of the test hardware to achieve higher interface temperatures.

6.3 Recommendations

6.3.1 HTEBC Development

Five future activities are recommended:

1) *Focus on Architecture 1 Advancement*
   GEA Architecture 1 high temperature EBC has the following general four constituting layers: a) mullite-Si baseline bondcoat, b) mullite based barrier layer, c) hafnon based intermediate layer and d hafnium oxide top-layer. This architecture is designed as the more refractory option out of the two architectures from GEA, both from the upper layer eutectic temperature point of view as well as from bondcoat high temperature durability point of view. Because of this high-temperature capability, this architecture needs to remain a focus of future development of high temperature CMC-EBC system at the component level.
2) *Optimize coating processes and application*
   One of the primary development needs for Architecture 1 EBC is further improvements in the deposition process and microstructure of the mullite-Si composite bondcoat to achieve lower porosity and a higher density. Therefore, developing improved processing methods to improve the density and/or methods to increase the Si content of the bondcoat layer would be warranted.
3) *Improve durability of top coat*
   Another development need for Architecture 1 EBC is the tendency for hafnia top-layer to delaminate or spall off along the interface with the hafnon intermediate layer. Improvement of top-layer durability via microstructural or compositional changes to decrease driving forces for the delamination or increase the adhesion strength would improve durability of the EBC system against recession water-vapor mediated recession.
4) *Explore further refinement of Architecture 2*
   GEA Architecture 2 high temperature EBC is composed of a mullite-Si bondcoat with or without modified composition modifications to the mullite matrix, a mullite-based barrier layer, a rare earth disilicate intermediate layer and a rare earth monosilicate top-layer. The primary shortcoming for this coating is the relatively inferior high temperature oxidation life than Architecture .1
5) *Mature HTCMC along with HTEBC*
   HTCMC and HTEBC are an integrated material system for end use. Therefore, TRL of HTCMC technology should be advanced in parallel with that of HTEBC to retire overall material risks and to avoid any delays in product introduction.

6) *Advance capabilities of Architecture 0*
The architecture 0 chemistry listed in this section are based on work mentioned under [41], [42], [43], [44], [45] and [46].
Arch 0 bond coat relies on the chemical bonding with CMC and slow TGO formation for a long life. Further optimization of the bond coat chemistry and the slurry process should be the focus to strengthen these areas. Recession resistant topcoat development is another future focus area. Rare earth monosilicates (Sc_2SiO_5, Lu_2SiO_5, Yb_2SiO_5) are most promising candidates due to their decent recession resistance, and the chemical compatibility with $Sc_2Si_2O_7$. Yb_2SiO_5 is most desirable from the economic standpoint, however, its viability is contingent upon keeping the eutectic phase below the $Sc_2Si_2O_7$ coat. HfO_2 is an excellent candidate from the recession resistance standpoint, however, the large CTE is its Achilles' heel. Keeping the layer compliant to mitigate the CTE mismatch-induced spallation is the key to its viability.

6.3.2 Rig Testing

6.3.2.1 QARE Rig Testing

Three future activities are recommended:

1) *Modeling of the rig test conditions*
Atmospheric QARE rig test is a relatively low cost and convenient way to test EBC architectures to fill the gaps between the conventional steam tests and a real simulated turbine engine environment. It combines the effect of high temperature, high temperature gradient, relatively high gas flow rate and the presence of water vapor. The geometry is relatively simple, but it is still too complicated for applying a 1D analytical model. Therefore, a 3D model that can map out the temperature field, temperature field along with gas composition field is highly desirable. In the presence of such a model, each point on the sample will serve as a unique data point that will generate a wealth of information much beyond what this report reflects. In addition, QARE rig could accept shaped feature specimens such as a leading edge or trailing edge geometry of an airfoil, hence extending modeling evaluation to non-planar flat coupons are highly recommended.

2) *Untested architectures*
Due to both rig availability and GEA's thermal spray cell availability, some critical samples could not be tested. Among these include the exact final architectures that are selected to go into CE-5 high-pressure combustor rig test. For Architecture 1, the intermediate layer is re-designed and therefore different response might emerge. For Architecture 2, the high-pressure combustor rig test article would likely bear a modified mullite matrix bondcoat. Both these subvariants can benefit from additional evaluations in the QARE rig test.

3) *Unique material observations*
The thermo-chemical environment associated with high velocity combustion gas flow on the surface at the extreme HTEBC surface temperatures studied in this program and QARE rig test campaigns can bring new insights into surface recession behavior and other chemical interactions driven by solid state diffusion under thermal and chemical gradient and vapor phase transport can bring about better understanding of EBC degradation modes in such environments. This can have profound effect on the material selection for ultra-high temperature EBC applications for turbine engine and other applications. NASA encourages continued investment in QARE rig and its utilization for EBC surface and subsurface degradation mode evaluations.

6.3.2.2 CE-5 Rig Testing

Five future activities are recommended:

1. The design of the large airfoil used to evaluate the coatings under the HyTEC HTEBC effort was predicated on the symmetric airfoil design used in the TTT test. There was a desire to incorporate more instrumentation into the HyTEC airfoil cavity, which increased the overall size to ~5.85”. An unintended effect of this larger airfoil was that the maximum temperature was limited given the large acreage that needed to be heated. Future testing in this facility should consider the upper temperature needed and perform baseline modeling to predict the temperature distribution and ranges on the test article.
2. Over the course of this testing, the CE-5 materials test rig provided over 315 hours of combustion testing with approximately 275 hours of testing at desired conditions. This testing was performed over 34 days within 3 months’ time. Borescope results indicated that the castable ceramic in the injector housing and in the Transition Section experienced degradation over the course of testing. Images of the injector in February and late May show significant degradation in the wall after ~300 hours of combustion are shown in Figure 25. Given these observations, at testing conditions of 3000F+, the castable should be changed after 250-300 hours of testing.

Figure 129: Images of the 9-point injector and the (white) transition section castable ceramic showing degradation over the 3 months of testing.

3. The test hardware would also benefit from the application of a bond coat and thermal barrier coating within the Test Section. While the modeling indicated that there would not be significant cooling on the center line, dark deposits on the airfoil top and bottom indicate the cooling effect of the water-cooled copper plates. This did not significantly affect the test, but the application of a metallic bond coat and ceramic topcoat on the copper would minimize the cooling and likely provide additional durability to the hardware.
4. Despite performing a significant number of testing hours with extensive data collection for both the rig and the airfoil, there were still many unknowns that should be considered in future testing. Measurement of temperature is always challenging. The thermal camera on the side of the test hardware provided excellent data but deposits that formed on the ZnSe lens obscured the viewport and interfered with the temperature measurement. There was a clear increase in the temperature after each cleaning for any of the airfoils.

5. The Inconel airfoil stalk was intended to provide a directed path for the T3 cooling air on the backside of the airfoil. However, it was determined with Airfoil 1A that the cooling air reduced the airfoil temperature too much, which further emphasizes the need for baseline thermal modeling of the hardware. The consequence of needing to reduce or eliminate the backside cooling was that the Inconel airfoil stalk became much hotter than anticipated. As mentioned above, although the gaps between the airfoil and the Inconel were expected to be more than sufficient, a combination of high Inconel temperatures, misalignment in the airfoil/stalk, and variation in the CMC could have played a significant role in splitting all four airfoils.

6.3.3 HTEBC Modeling

6.3.3.1 Bond Coat Oxidation Modeling

Prior to HyTEC program, GEA developed a 1D analytical model to describe the oxidation kinetics of its patented mullite-silicon bondcoat. This model was used to guide further development of the composite mullite-Si bondcoat and to predict the entitlement life of bondcoat with ideal bondcoat microstructures (fully dense, clean microstructure). It was also modified to be able to semi-quantitatively describe oxidation behavior when there is certain degree of porosity.

Under HyTEC program, a preliminary 1D numerical oxidation model was devised further for the composite mullite-Si bondcoat in COMSOL to lay the foundations to predict oxidation life based on more realistic microstructure features. The model was described in Section 5.2 and has the key building blocks for extension of a physics-based model of real microstructures. Additional improvement to this model is needed to capture with higher fidelity the 2D and 3D attributes and effects of real microstructures and the thermo-chemistry characteristics of the composite bondcoat. Such characteristics include porosity, grain size, particle size polydispersity, grain boundary phase composition change, etc.

As the first steps to develop this model into its intended form, five future activities are recommended:

1) *Incorporate oxygen diffusivity into model*
   Currently this model is not truly a first-principal model yet, due to the fact it needs an oxygen diffusivity input to fit experimental data. Oxygen diffusivity data is readily available in literature, it just needs to be evaluated and incorporated into the model.

2) *Explore option for wet oxidation in the model*
   The current model is applicable only to dry oxidation conditions (only oxygen as the oxidant). This is caused by the discrete distribution of silicon and silica particles in the model structure. A continuous silica TGO domain is needed for wet oxidation (water vapor as the primary oxidant) modeling

3) *Develop understanding for chemistry effects*
   Related to Point 2 above, glassy phase (or the silica phase, which is the oxidation product of Si getter phase) chemistry effect from contamination, can only be effectively studied when that phase is continuous.

4) *Develop porosity effect in the model*
   Introduction of porosity into the model needs to consider three phase equilibrium (Si, SiO and SiO_2). In the current model form, only 2 phase equilibrium is considered (Si, SiO_2).

5) *Explore options to validate model*
   There are some inconsistencies between the model predictions and experimental observations, when the “transition layer” (the layer at the interface between the TGO and the virgin bondcoat, in which silicon particles are partially oxidized) thickness is concerned. Current model predicts a very thick transition layer, on the order of 50-100 μm, even with monodispersed 1μm silicon particle. Experimental observations from metallographic analysis of steam tested coupons during

this program, however, show that this layer can be almost un-discernable (<10 μm). Further maturation of the model will require understanding of some of these inconsistencies to refine the predictions.

6) *Understand capabilities of model prediction*
   A valuable exercise seems to be warranted with the current model despite its early stage. It is to use the model to predict at which point in the oxidation life of the composite bondcoat oxidation of the CMC substrate starts. The more relevant characteristic to capture for such an event is the CO pressure generated, rather than the SiO_2 thickness

To summarize, the current COMSOL model is in good shape and ready to be modified towards its intended form as a comprehensive model. It can provide valuable parametric sensitivity studies. However, it needs further development in order to be used as a more comprehensive life model, as it was intended to be.

7. Conclusion

A comprehensive material development program was conducted in partnership with NASA Glenn to mature and advance the HTEBC technology from TRL-3 to TRL-5. The test campaigns meet the goals of the program and demonstrated improved durability of HTEBC system for temperatures beyond the capability of current SoA EBCs. Further TRL/MRL progress is needed for advancement to engine test. HTCMC/HTEBC is an enabling technology for hotter core and reduced fuel burn/emissions that GEA has committed to mature in collaboration with NASA and DoD partners.

References

[1] Presby, M.J., Endo, M., Fox, D.S., Harder, B.J., Lee, K.N., Hoffman, L.C., and Cuy, M.D. (2024) “The Development and Use of a Natural Gas/Oxygen Burner Rig for Environmental Barrier Coating and Ceramic Matrix Composite Technology Maturation,” ASME Journal of Engineering for Gas Turbines and Power, Vol. 146, No. 1.

[2] [1] D.S. Fox, E.J. Opila, Q.N. Nguyen, D.L. Humphrey, and S. M. Lewton, *J. Amer. Ceram. Soc.* **86** 1256-61 (2003); N.S. Jacobson, M.A. Kuczmarski, and B.A. Kowalski, *Oxid. Met.* **93**, 247-82 (2020).

[3] J. Steibel, Ceramic matrix composites taking flight at GE Aviation, Am. Ceram. Soc. Bulletin, 98(3), 2019, pp. 30–33.

[4] F.W. Zok, Ceramic-matrix composites enable revolutionary gains in turbine engine efficiency, Am. Ceram. Soc. Bulletin, 95(5), 2016.

[5] https://www.compositesworld.com/articles/a-new-era-for-ceramic-matrix-composites

[6] K.N. Lee, Environmental barrier coatings for CMCs in: N.P. Bansal, J. Lamon (Eds.) Ceramic Matrix Composites, Wiley, New York, 2015, pp. 433–451.

[7] Xiao S., Li J., Huang P., Zhang A., Tian Y., Zhang X., et al. Evaluation of environmental barrier coatings: A review. Int J Appl Ceram Technol. 2023; 1–22. https://doi.org/10.1111/ijac.14370

[8] M. Presby et al., The development and use of a natural gas/oxygen burner rig for environmental barrier coating and ceramic matrix composite technology maturation, Proc. ASME Turbo Expo 2023, Paper No. GT2023-101562, June 26–30, 2023, Boston, MA.

[9] K.N. Lee, Yb2Si2O7 Environmental barrier coatings with reduced bond coat oxidation rates via chemical modifications for long life. J. Am. Ceram. Soc., 102(3), 2018, pp. 1507–1521.

[10] T.M. Ricks et al., Coupled thermos-mechanical modeling of the influence of the thermally grown oxide in an environmental barrier coating system, Proc. 33rd Am. Soc. Of Composites Annual Technical Conf., Sep. 24–16, 2018, Seattle, WA.

[11] S.K. Mital et al., Modeling the influence of thermally grown oxide (TGO) layers on the driving forces in environmental barrier coating systems, NASA/TM-201210014094, April 2021.

[12] Richards et al., Mechanical Properties of Air Plasma Sprayed Environmental Barrier Coating (EBC) Systems: Preliminary Assessments,” Developments in Strategic Ceramic Materials – A Collection of Papers presented at 39th International Conference of Advanced Ceramics and Composites, Daytona Beach, FL, American Ceramic Society, Dec. 2015.

[13] A.A. Wereszczak, et al., Dimensional changes and creep of silica core ceramics used in investment casting of superalloys, J. of Materials Science, vol. 37, 2002, pp. 4235–4245.

[14] N.N. Nemeth et al., Stochastic simulation of mudcrack damage formation in an environmental barrier coating, NASA/TP-2020-220185, February 2020.

[15] https://github.com/nasa/pretrained-microscopy-models

[16] Stuckner, J.; Harder, B.; Smith, T.M. Microstructure segmentation with deep learning encoders pre-trained on a large micros-515 copy dataset. J. Comput. Mater. 2022, 8, pp. 1–12.

[17] Jinkang Du et al. Effect of the thermally grown oxide and interfacial roughness on stress distribution in environmental barrier coatings, J. of European Ceramic Society, vol. 43, issue 15, December 2023, pp. 7118–7133. https://doi.org/10.1016/j.jeauceramsoc.2023.07.074

[18] P. Naghipour, S. Arnold, S., et al. Multiscale Static Analysis of Notched and Unnotched Laminates Using the Generalized Method of Cells, NASA/TM-2016-219084, 2016.

[19] J. Salem et al., Design of an environmental barrier coating bond strength test coupon, Proc. ASME Turbo Expo 2023, GT2023, June 26–20, Boston, MA.

[20] B.J. Harder, M.J. Presby, et al. Environmental Barrier Coating Oxidation and Adhesion Strength, J. of Engineering for Gas Turbine and Power, vol. 143, March 2021.

[21] Deal, B.E.; and Grove A.S.: General Relationship for the Thermal Oxidation of Silicon. J. Appl. Phys., 1965, vol. 36, no. 12, pp. 3770–3778.

[22] Private communication, Roy Sullivan, NASA Glenn Research Center, Cleveland, Ohio, Dec. 2023

[23] Hexoloy® SA alpha silicon carbide, Carborandum/St. Gobain, Niagara Falls, NY
[24] COMSOL (2020): COMSOL Multiphysics User's Guide. Version 5.6.
[25] Fielitz, Peter, et al. (2004): Oxygen Grain-Boundary Diffusion in Polycrystalline Mullite Ceramics. J. Am. Ceram. Soc., vol. 87, no. 12, pp. 2232–2236.
[26] Fromhold, A.T. (1976): Theory of Metal Oxidation. North Holland Publishing Company, Amsterdam.
[27] Kitaoka, Satoshi, et al. (2017): Oxygen Permeation Mechanism in Polycrystalline Mullite at High Temperatures. J. Am. Ceram. Soc., vol. 100, no. 7, pp. 3217–3226.
[28] Luthra, Krishan L.; and Wan Julin (June 25, 2020): EBC With Mullite Bondcoat That Includes an Oxygen Getter Phase. U.S. Patent 2020/0199031 A1.
[29] Luthra, Krishan L.; and Wan Julin (Feb. 23, 2021): EBC With Mullite Bondcoat Having a Non-Oxide Silicon Ceramic. U.S. Patent 10,927,046 B2.
[30] Ramberg C.E., Cruciani G., Spear K.E., Tressler R.E., Ramberg C.F., Passive oxidation kinetics of high purity silicon carbide from 800 to 1000 ºC, *J. Am. Ceram. Soc.* **79** [11] 2897-2911 (1996).
[31] Sullivan, R.M. (2021): On the Oxidation of the Silicon Bond Coat in Environmental Barrier Coatings. J. Eur. Ceram., vol. 41, pp. 557–562.
[32] Wada M., Matsudaira T., Kawashima N., Kitaoka S., Takata M., Mass transfer in polycrystalline ytterbium disilicate under oxygen potential gradients at high temperatures, *Acta Materialia* **135** 372-381 (2017).
[33] Wan, J. (May 3, 2023): General Electric Aerospace Research, personal communication.
[34] K.L Luthra and H.D. Park, J. Amer. Ceram. Soc. 73, 1014-23 (1990).
[35] F.J. Klug, S. Prochazka, and R.H. Doremus, J. Amer. Ceram. Soc. 70, 750-59 (1987).
[36] J.C. Mauro,Y. Yue, A.J. Ellison, P.K. Gupta, and D.C. Allan, Proc. Natl. Acad. Sci. 106, 19780-19784 (2009)
[37] J.M. Jewell, C.M. Shaw, and J.E. Shelby, J. Non-Cryst. Sol. 152, 32-41 (1993).
[38] Sullivan Roy M., Oxidation of silicon particles suspended in mullite matrix with dual-mode vacancy diffusion of oxygen, NASA/TM-20230010839, December 2023
[39] Mital, Subodh K. and Arnold, Steven M, A Phenomenological Durability Model for Environmental Barrier Coating Systems Subjected to Steam Oxidation. NASA/TM-20240000936, March 2024
[40] E.Copland,D. Myers',E. J.Opilat nd. S.Jacobson NASA Glenn Research Center, https://ntrs.nasa.gov/api/citations/20020025451/downloads/20020025451.pdf
[41] Kang Lee and Deborah Waters, "Environmental Barrier Coatings for Improved Temperature Capabilities and Longevity," US Patent #: US 11,325,869 Bl, May 10, 2022.
[42] K. Lee, D. L. Waters, B. J. Puleo, A. Garg, W. D. Jennings, G. Costa, D. E. Sacksteder, "Development of oxide-based High temperature environmental barrier coatings for ceramic matrix composites via the slurry process," J. Euro. Ceram. Soc. 41, 1639-1653 (2021).
[43] Kang Lee, Rebekah Webster, Bernadette Puleo, Michael Presby, Bryan Harder, John Setlock, Leland Hoffman, "Recent Advancements in High Temperature Slurry Environmental Barrier Coatings for SiC/SiC Ceramic Matrix Composites," 48th International Conference and Expo on Advanced Ceramics and Composites (ICACC2024), Daytona Beach, FL, Jan 28 – Feb 2 2024
[44] Kang Lee, "Next Generation Environmental Barrier Coatings for SiC/SiC Ceramic Matrix Composites," NATO AVT-393 Research Workshop on "Environmental and Thermal Barrier Coatings for Military Aircraft Engines," Ottawa, Canada, May 15, 2024.
[45] Kang Lee, Rebekah Webster, Bernadette Puleo, Michael Presby, Bryan Harder, Josh Stuckner, John Setlock, Leland Hoffman, "Oxidation Kinetics of Slurry Environmental Barrier Coatings for SiC/SiC Ceramic Matrix Composites," 14th International Conference on Ceramic Materials and Components for Energy and Environmental Systems, Budapest, Hungary, Aug 18-22, 2024.
[46] Kang Lee, "Next Generation Environmental Barrier Coatings for SiC/SiC Ceramic Matrix Composites," McMahon Award Lecture, The Alfred University School of Engineering & New York State College of Ceramics, Alfred, NY, Nov 7, 2024.